Compact binary merger searches in the era of multimessenger high energy astrophysics

Cosmin Stachie

UNIVERSITÉ CÔTE D'AZUR

ÉCOLE DOCTORALE
SCIENCES FONDAMENTALES ET APPLIQUÉES

THÈSE DE DOCTORAT

Recherches de fusions d'objets compacts à l'ère de l'astrophysique multi-messagers des hautes énergies

Cosmin STACHIE

Laboratoire ARTEMIS, Observatoire de la Côte d'Azur

Présentée en vue de l'obtention du grade de docteur en Physique de l'Université Côte d'Azur
Dirigée par : Nelson Christensen
Soutenue le : 30 Août 2021

Devant le jury, composé de :
Marie-Anne BIZOUARD, Observatoire de la Côte d'Azur, Nice
Nelson CHRISTENSEN, Observatoire de la Côte d'Azur, Nice
Frédéric DAIGNE, Institut d'Astrophysique de Paris, Paris
Tito DAL CANTON, Laboratoire de Physique des 2 Infinis Irène Joliot-Curie, Orsay
Damien DORNIC, Centre de Physique des Particules de Marseille, Marseille
Susanna VERGANI, Observatoire de Paris - GEPI, Paris

Recherches de fusions d'objets compacts à l'ère de l'astrophysique multi-messagers des hautes énergies

Compact binary merger searches in the era of multimessenger high energy astrophysics

Jury :

Président du jury :
Marie-Anne BIZOUARD, Directrice de Recherche, Laboratoire Artemis, Observatoire de la Côte d'Azur, Université de la Côte d'Azur, Nice

Rapporteurs :
Damien DORNIC, Chargé de Recherche CNRS, Centre de Physique des Particules de Marseille, Marseille
Susanna VERGANI, Directrice de Recherche CNRS, Observatoire de Paris – GEPI, Université PSL, Paris

Examinateurs :
Frédéric DAIGNE, Professeur des Universités, Sorbonne Université, Institut d'Astrophysique de Paris, Paris
Tito DAL CANTON, Chargé de recherche CNRS, Laboratoire de Physique des 2 Infinis Irène Joliot-Curie, Orsay

Directeur de thèse :
Nelson CHRISTENSEN, Directeur de recherche CNRS, Laboratoire Artemis, Observatoire de la Côte d'Azur, Université de la Côte d'Azur, Nice

RESUMÉ

Les étoiles à neutrons et les trous noirs stellaires sont créés par l'effondrement gravitationnel qui survient à la fin des cycles de fusion nucléaire ayant lieu au sein des étoiles massives. Ils sont les plus petits et les plus denses objets stellaires, avec des masses allant de un à quelques dizaines de masses solaires, et des tailles similaires à celle d'une ville sur Terre. Ils se trouvent soit isolés gravitationnellement soit en systèmes binaires, formant des binaires d'étoiles à neutrons (BNS), des systèmes trou noir - étoile à neutrons (NSBH) et des trous noirs binaires (BBH). Dans le dernier cas, lorsque les objets compacts sont en orbite l'un autour de l'autre, le système perd du moment cinétique et de l'énergie de liaison par émission d'ondes gravitationnelles (GW). Ainsi la séparation diminue au cours du temps et, si la séparation initiale n'est pas trop grande, ceci peut conduire à une fusion dans un temps compatible avec l'âge de l'Univers. Les secondes juste avant et après la fusion, tout comme les jours suivant cet événement cataclysmique, sont spectaculaires. L'amplitude des GWs augmente avec l'approche du temps de la fusion, les rendant détectables par les interféromètres à GWs Advanced LIGO et Advanced Virgo. Si en plus, au moins un des membres de la binaire est une étoile à neutrons et l'autre objet compact pèse moins de 10 masses solaires, une émission électromagnétique (EM) à haute énergie sous la forme d'un jet relativiste, appelé sursaut gamma court (GRB), activé par la chute de matière dans le disque d'accrétion entourant le trou noir nouvellement né, est attendue dans les secondes suivant ou précédant la fusion. Une radiation plus isotrope dans le spectre optique et infrarouge proche, appelée kilonova et alimentée par la désintégration radioactive des éléments lourds synthétisés lors du processus r, est émise dans les jours qui suivent. Enfin, les contrecoups (afterglows) des GRBs courts, couvrant une large portion du spectre d'énergie allant des rayons X aux ondes radio, pourraient être détectés sur des échelles variant d'heures aux mois. GW170817 a été un événement astrophysique remarquable, montrant clairement l'existence de toutes ces signatures de GWs/EMs. En outre, des travaux théoriques prédisent également l'existence d'autres signaux lors de ces phénomènes violents, tels que l'émission des neutrinos et les précurseurs des GRBs.

De nos jours, l'un des objectifs de la communauté scientifique est de détecter de

plus en plus de fusions d'objets compacts, avec l'espoir d'identifier plusieurs messagers associés entre eux. Cette thèse de doctorat s'inscrit dans ce cadre. Ainsi, plusieurs procédures sont présentées, dont le but est d'augmenter les chances de la détection de certains signaux de GWs/EMs, liés à la fusion d'une binaire compacte. Je propose une méthode statistique pour la détection de l'association entre l'émission rapide du GRB, identifiable dans les données de Fermi-GBM, et le trigger de GWs, rapporté par Advanced LIGO et/ou Advanced Virgo. L'idée derrière cela est de tirer profit de l'avantage du faible taux de coïncidence des bruits présents dans deux détecteurs distincts. De cette façon, on pourrait espérer d'être capable d'inférer une association astrophysique entre deux signaux provenant de deux détecteurs différents, même si pris séparément ils sont en dessous du seuil de détection. J'introduis aussi un outil destiné à la recherche d'un signal gamma modulé, détectable par les scintillateurs de Fermi-GBM, antérieurement à l'identification de l'événement de GWs, par les interféromètres de seconde génération. Tandis que les émissions de rayonnement gamma et GWs devraient être presque simultanées, la contrepartie kilonova est postérieure à la fusion, peut durer des jours et, la plupart du temps, est détectée par les télescopes terrestres. Deux des difficultés les plus importantes pour un observateur de EMs sont: la largeur des cartes de ciel fournies à partir des données de GWs donnant peu d'informations concernant la direction dans le ciel où les télescopes devraient pointer et la distinction parmi plusieurs candidats identifiés tôt afin de décider la stratégie d'observation pour le suivi ultérieur. Je propose ici deux méthodes visant à aider la communauté d'observateurs de EMs, dans son but de surmonter ces obstacles. D'abord je suggère l'utilisation d'un algorithme à base d'apprentissage automatique pour distinguer parmi des courbes de lumière photométriques attribuées aux kilonovas ciblées, aux supernovas dominant la liste de candidats et aux autres transients optiques non desirés. En second lieu, des courbes de lumière photométriques, pour des kilonovas, sont proposées, avec des délais de l'ordre des minutes, à partir des données de GWs, de faible latence.

Toutes ces méthodes pourraient être ameliorées afin d'augmenter leurs efficacités. Cependant, ces méthodes pourraient représenter des points de départ pour des idées et des outils, qui seront employés dans les années à venir. En effet, le futur proche sera caractérisé par une multitude de signaux de natures différentes, rendant l'interprétation des données très difficile. Dans ce monde passionnant, il n'y aura de place que pour les

méthodes d'analyse de données les plus efficaces.

Mots clés: étoile à neutrons, trou noir, fusion de binaire compacte, sursaut gamma, kilonova, onde gravitationnelle, photon, analyse bayésienne, courbe de lumière, photometrie.

ABSTRACT

Neutron stars and stellar mass black holes are the remnants of massive stars, caused by the gravitational collapse taking place at the end of their nuclear fusion based life cycles. They are the smallest and densest known stellar objects, with masses ranging from one to a few tens times more the mass of the Sun, and sizes similar to that of an Earth city. They can be found gravitationally isolated or in binary systems, forming binary neutron stars (BNS), neutron star-black holes (NSBH) and binary black holes (BBH). In the latter case, when the compact objects orbit each other, the system loses angular momentum and binding energy by emission of gravitational waves (GW). Thus the orbital separation shrinks over time and, if the initial separation is not too high, it might lead to a merger during the lifetime of the Universe. The seconds right before and after the merger, as well as the days following this cataclysmic event, are spectacular. The amplitude of the GWs increases with the approach of the coalescence time, making them detectable by the GW interferometers Advanced LIGO and Advanced Virgo. If in addition, at least one of the binary components is a neutron star and the other compact object is below 10 solar masses, a relativistic beamed high energy electromagnetic (EM) emission, called a short gamma ray burst (GRB), activated by the infalling matter into the accretion disc surrounding the newly born black hole, is expected in the seconds following or preceding the merger. A more isotropic radiation in both the optical and near infrared spectrum, called a kilonova and powered by the radioactive decay of the synthesized r-process heavy elements, is emitted on days timescale. Finally the short GRB afterglows spanning a wide energy spectrum going from X-rays to radio wavelengths might be detectable on timescales varying from hours to months. GW170817 was a remarkable astrophysical event, showing clear evidence for all these GW/EM signatures. Moreover, theoretical work predicts the existence of some other signals emitted by these violent phenomena such as the emission of neutrinos or gamma-ray burst precursors.

Nowadays one goal of the scientific community is to detect the more and more compact binary coalescences, hopefully by tracking several messengers associated with it. The present thesis is within this framework. Thus, several procedures whose aim is to increase the chances of detecting some GW/EM signals linked to a compact binary

merger are presented. I propose a statistical method for the detection of the association between the prompt GRB emission, identifiable in the Fermi-GBM data, and the GW trigger, reported by Advanced LIGO and/or Advanced Virgo. The idea behind it is to take advantage of the low coincident rate of backgrounds in two distinct detectors. In this way, one may hope to be able to infer an astrophysical association of two different detector signals, even if separately they are subthreshold. I also introduce a tool aimed to search for a modulated gamma-ray signal detectable by the Fermi-GBM scintillators, prior to a GW event identified by the Advanced interferometers. Whereas the emissions of gamma-ray radiation and GWs are expected to be almost simultaneous, the kilonova counterpart follows the merger, can last for days and is tracked most of the time by the terrestrial telescopes. Two of the biggest difficulties for an EM observer are: the broad GW skymaps giving insufficient information concerning the direction in the sky where the telescopes should be pointing to and the discrimination between several early identified candidates in order to decide the observing strategy for the later follow-up. I propose here two methods aiming to help the EM observing community in trying to handle these difficulties. Firstly, I suggest the use of a machine learning based algorithm in order to distinguish between photometric lightcurves attributed to the desired kilonovae, the dominating background supernovae and other background optical transients. Secondly, GW low-latency based kilonovae photometric lightcurves are proposed with delays of the order of minutes.

All these methods might be improved in order to increase their efficiencies. However, they might represent starting points for future ideas and materialized tools that will be employed in the coming years. Indeed the near future will be characterized by a plethora of signals of different natures, making the data interpretation very challenging. In this exciting world, there will be a place only for the most efficient data analysis methods.

Keywords: neutron star, black hole, compact binary merger, gamma-ray burst, kilonova, gravitational wave, photon, Bayesian statistic, lightcurve, photometry.

ACKNOWLEDGEMENT

Sincere thanks to my supervisor Nelson Christensen who offered me the opportunity to work for a few years in this exciting field.

I am very grateful to Tito Dal Canton and Michael W. Coughlin without the help of who the progress of my research would have been considerably slowed down.

I want to extend my thanks to all the colleagues from the Fermi-GBM - LIGO/Virgo team. Also to the colleagues from the GRANDMA collaboration. Especially, I want to thank Sarah Antier, who was always very kind with me, even if my involvement in the collaboration was quite limited.

Equally I want to thank people I have met (almost) daily at the Observatory. Because the list is too long, here I just mention Thomas, Guillaume and Adrian with whom I shared the office. I also thank Khaled and his team for the canteen meals.

Finally I want to express my gratitude to the reviewers and the jury of this thesis for the time dedicated to improve this work.

TABLE OF CONTENTS

RESUMÉ i
ABSTRACT iv
ACKNOWLEDGEMENT vi
LIST OF FIGURES ix
LIST OF TABLES xxiii
LIST OF TERMS AND ABBREVIATIONS xxvi

1 Introduction **1**
1.1 Compact object binaries 1
1.1.1 Neutron stars and black holes 1
1.1.2 Formation channels 4
1.2 GW emission 9
1.3 EM radiation 14
1.3.1 GRB prompt and afterglow emission 16
1.3.2 Kilonova 23
1.4 Detectors 26
1.4.1 GW interferometers 26
1.4.2 γ-ray space observatories 33
1.4.3 Terrestrial telescopes 38

2 GWs and GRB prompt emission coincidence **42**
2.1 Existing searches in the literature 42
2.2 New search 44
2.2.1 *PyCBC* GW triggers and Fermi-GBM EM triggers 44
2.2.2 Statistical framework 52
2.2.3 O1 and O2 data analysis results 58
2.3 Upcoming analyses 66

3 Modulated gamma-ray precursors to GW mergers 67
3.1 Real GRBs with multiple emission peaks and proposed precursor signal models . . . 67
3.2 Search for signals modulated by the pre-merger BNS/NSBH orbital phase evolution . . . 73
3.2.1 Flaring characteristics and statistical analysis of the Fermi-GBM data . . . 73
3.2.2 Pipeline sensitivity . . . 75
3.2.3 Output results for the O2/O3 real BNS/NSBH events . . . 83

4 Photometric lightcurve discrimination between kilonovae, supernovae and other transient signals 86
4.1 Motivation and other proposals . . . 86
4.2 Machine-learning based method . . . 90
4.2.1 `astrorapid` output based discrimination . . . 96
4.2.2 Performance on real events . . . 100
4.2.3 Injections recovery efficiency . . . 102
4.2.4 The case of AT2019wxt . . . 108

5 Kilonova photometric lightcurve prediction based on low-latency GW data 110
5.1 Supra-nuclear density matter equation of state and kilonova lightcurve models . . . 110
5.2 Compact objects masses and spins conversion into photometric lightcurves 113
5.2.1 GW input data and neutron star matter properties prior . . . 113
5.2.2 Mass ejecta and EM lightcurve computations . . . 118
5.2.3 Method performance testing and outcome for some real events . . . 127

6 Conclusion 135
REFERENCES . . . 140

LIST OF FIGURES

1.1 The different steps of the formation, evolution and death of stars. Credit: NASA. 2

1.2 Common envelope based formation channel for isolated compact binaries. The different steps are: (a) two main sequence stars orbit each other; (b) one of the stars expands overfilling its Roche lobe; (c) the star consumes its nuclear reaction based fuel and detonates as a supernova; (d) new system containing a black hole/neutron star/white dwarf and a main sequence star; (e) X-ray binary, with accretion disc around the compact object; (f) the outer shells of the second star extend beyond the compact object, giving birth to the common envelope; (g) after the ejection of the common envelope, the second star dies in a supernova explosion; (h) a new system of compact objects in a tight binary; (i) coalescence. 5

1.3 Chemically homogeneous evolution as an alternative formation channel for the synthesis of compact object binaries. The different steps are: (a) two highly spinning stars in a tight binary; (b) system formed of two He cores after the loss of outer shells by the two highly evolved main sequence stars; (c) a first supernova explosion; (d) new system consisting of a new born black hole and the other He core; (e) second supernova detonation; (f) tight binary black hole; (g) merger. 7

1.4 On left, an active galactic nucleus, with its supermassive black hole at the center and its accretion disc (in brown) containing a binary black hole. On right, a binary-single interaction. The result of the encounter might be either a softening, i.e. remoteness of the compact object components, or a hardening, i.e. a tighter binary. 8

1.5 The evolution of a Oxy point particle distribution due to the passage of a GW. On top (the middle), there is highlighted the effect due to only the $\oplus$ ($\otimes$) polarization. On bottom, there is the evolution of the GW phase. 11

1.6 *Inspiral*, *merger* and *ringdown* for binary system, consisting of two black holes of 30 and 25 solar masses. The projected adimensional spins along the orbital angular momentum are 0.9 (for heavier black hole) and 0.1 (for the lighter black hole). The waveform used in this derivation is SEOBNRv2 [Pürrer, 2014]. 13

1.7 Fireball model in which a relativistic jet is powered by the accretion disc surrounding the new born black hole. The optically thick inner part of the jet represents a soup of electrons, positrons and γ-rays. Sufficiently far away from the black hole engine, the density is low enough such that the medium becomes optically thin. In this region, matter blast waves travelling at different speeds collide with each other giving birth to a burst of high energy photons, which is the prompt γ-ray emission our space observatories detect. Further still, the shock waves interact with the interstellar medium, giving rise to forward and reverse shocks. The interaction between the blast waves and the interstellar medium is responsible for longer wavelength radiation (X-ray, optical, infrared, radio), known as the afterglow. 17

1.8 From Bhat et al. [2016b], the histogram of GRBs, as a function of $\log_{10} T_{90}$. The duration T_{90} is calculated in the $50 - 300\,\mathrm{keV}$ energy range. The samples used here are the 1405 triggers included in the third Fermi-GBM GRB catalog. 19

1.9 From Bhat et al. [2016b], the logarithm of the hardness ratio versus the logarithm of T_{90}. The hardness ratio is defined as the burst fluence in the $50 - 300\,\mathrm{keV}$ over the fluence in $10 - 50\,\mathrm{keV}$ energy band. The two fluences are calculated during T_{90}. The sample includes 1376 GRBs from the third Fermi-GBM GRB catalog. 20

1.10 From Abbott et al. [2017c]. On left (respectively right), E_{iso} (respectively L_{iso}) versus redshift, for short and long GRBs. In both panels, the green dashed curve represents the redshift dependence of the Fermi-GBM detection threshold. 21
1.11 The Fermi-GBM high energy lightcurve of GRB 170817A. In blue, the sum of counts reported by half of the NaI detectors, assigned with estimed error bars. In red, there is the estimated background photon rate. On the x axis, 0 corresponds to the mission ellapsed time MET = 524666471.475. The signal is found by the tool presented in Goldstein et al. [2019] on a timescale of $512\,$ms, with a log likelihood ratio of 73. . 22
1.12 Kilonova containing two components: near the equator (in red), the dynamical ejecta and, at higher latitudes (in blue), the disc winds. The black hole appears in black, while the GRB relativistic jets are depicted in yellow. 24
1.13 Apparent magnitude versus time for AT 2017gfo. The photometric filters used here are u, g, r, i, z, y, J, H and K. The circles represent observations with finite error bars, while the triangles stand for upper limits. 25
1.14 GW and EM signals expected during the merger of a binary neutron star: a powerful release of GWs in seconds prior to the merger; the GRB prompt emission radiation is expected to be at most a few seconds away with respect to the coalescence time; the kilonova radiation occurs during the hours, days and even weeks after the merger; the GRB afterglow starts with X-ray photons in the hours following the merger, continues on the optical range in the days/weeks after the fusion of the two neutron star, and is expected to still be visible in the radio spectrum in the months/years following the cataclysmic event. Figure taken from Burns [2020]. 26
1.15 Joseph Weber and its aluminium bar detector. 27

1.16 Michelson interferometer consisting of: a laser providing monochromatic radiation; a beam splitter separating the initial wave packet into a reflected part and a transmitted part; two end arm mirrors situated far away from the beam splitter, on which reflect the two spatially separated light components; a photodetector measuring the power of the interference radiation output. 28

1.17 Fabry-Perot cavity containing two optical mirrors M_1 and M_2 separated by a distance L_{FP}. Outside the cavity, there is an incident signal $\vec{E}_{\mathrm{inc}}(t,x)$, partly reflected into $\vec{E}_{\mathrm{ref}}(t,\vec{x})$ and partly transmitted as $\vec{E}_{\mathrm{trans}}(t,x)$. Inside the cavity, two plane waves, $\vec{E}_{\mathrm{cav}}^{\mathrm{right}}(t,x)$ and $\vec{E}_{\mathrm{cav}}^{\mathrm{left}}(t,x)$, propagate in opposite directions. 30

1.18 On left, a scheme of a GW interferometer possessing: a laser emitting the monochromatic radiation with frequency ω_{laser}; an electro-optic modulator creating sidebands frequencies; an input mode cleaner and an output mode cleaner filtering out all the TEM modes except the gaussian component; a beam splitter; a Fabry-Perot cavity for each arm of the interferometer; a photodetector. On right, a real picture of the Virgo interferometer, located in Cascina, Italy. 32

1.19 Amplitude spectral density for Advanced Virgo and Advanced LIGO (Livingston and Hanford), during O3. The data used to generate these curves is the same data as in Abbott et al. [2021a]. 34

1.20 On the x axis, the particle moves with velocity $\vec{v}_{\mathrm{particle}}(t)$ and emits radial EM waves propagating in the medium with $\vec{v}_{\mathrm{light}}$. On top (bottom), the emitted wavefronts travel at velocities lower (higher) than v_{light} and for this reason there is (no) overlap/interference. When $v_{\mathrm{particle}}(t) > v_{\mathrm{light}}$, cone-like radiation results. 35

1.21 High energy photon counter containing a scintillator crystal, a photomultiplier tube and the read-out electronics. After the excitation by the incoming γ-ray, the inorganic crystal emits longer wavelength photons which reach the photocathode of the photomuliplier. The photocathode coverts the incident light into electrons, through the photoelectric effect. A series of intermediate electrodes, called dynodes, at different electrical potentials, increases the electronic cascade, by the creation of secondary electrons [Arifov, 2013; Bruining, 2016]. The overall electrons arrive finally on the last electrode, the anode. The corresponding electrical signals is measured by means of a read-out technique. 36

1.22 On right: the Fermi satellite with its solar panels and two instruments: GBM and LAT. On left: the spatial distribution of the NaI and BGO scintillators of the GBM instrument. The Fermi satellite was launched on 11 June 2008, aboard a Delta II 7920-H rocket. 37

1.23 The 77 cm refractor telescope (*la Grande Lunette*), located at the Nice Observatory. It started to be operational in 1886. 39

1.24 Optical/Infrared/Radio telescope working principle. The EM radiation arrives on Earth under the form of plane waves, because it is emitted by a distant source. The incoming photons are intercepted by a (primary) parabolic mirror which redirects them towards its focal plane. The secondary mirror (it is not a compulsory equipment component) reflects once again the photons and reorients them to the photon detector. Here the light energy is converted into electronic energy and the corresponding signal is read out by a computer. 40

2.1 On left: sky localization based on only the GWs (in green), only the Fermi-GBM detection (dark blue), only the arrival times difference of high energy photons at Fermi and *INTEGRAL* [Savchenko et al., 2017] satellites (annulus in light blue), as well as the NGC 4993 discovery images realized by *Swope* [Coulter et al., 2017] and *DLT40* [Yang et al., 2017]. On right: the arrival times of the GW/EM signals at LIGO Handford interferometer, Fermi and *INTEGRAL* satellites. The left panel is taken from [Abbott et al., 2017b]. 43

2.2 On left, the number of *PyCBC* GW single interferometer triggers possessing a statistic $\hat{\rho}_{gw}$ higher than 6 (in red), 7 (in green) and respectively 8 (in blue); the results for both LIGO Livingston (L1) and LIGO Hanford (H1) are shown. On right, the histogram of LLR of the *targeted-search* EM counterpart to the GW triggers. 47

2.3 Frequency versus time Omega Scan for four noise transients: blip glitch (top left), paired doves glitch (top right), scattered light glitch (bottom left) and radio frequency glitch (bottom right). The *gwdetchar-omega* SNRs are 8.5 (for the blip glitch), 29.8 (for the paired doves glitch), 21.3 (for the scattered light glitch), and respectively 14.3 (for radio frequency glitch). Strain data has been used for the derivation of these diagrams. The bottom right panel corresponds to a LIGO Livingston event, while the three others are associated to LIGO Hanford. 50

2.4 Skymaps (on top) and lightcurves (on bottom) for a solar flare (on left) and a long GRB (on right). On the skymaps, represented are the Earth (in blue), the galactic plane (the grey line), the satellite position (the dot on the grey line), the Sun (in yellow), the confident area of the EM trigger (in red), as well as the sky directions towards which the scintillation detectors point. Regarding the lightcurves, the red line represents the estimated photon background, while the vertical grey line indicates the position of the EM trigger. The solar flare (long GRB) generates a *targeted-search* trigger with $\mathrm{LLR} = 196.11$ (respectively $\mathrm{LLR} = 105.90$), a duration of $2.048\,\mathrm{s}$ (respectively $8.192\,\mathrm{s}$) and *soft* (respectively *normal*) spectrum. 51

2.5 Sky localizations (on top), NaI scintillator lightcurves (middle) and BGO detector lightcurves (bottom) for a phosphorescence event (left) and a BGO spike (right). The phosphorescece event (BGO spike) generates a *targeted-search* trigger with $\mathrm{LLR} = 425.53$ (respectively $\mathrm{LLR} = 86.03$), a duration of $0.064\,\mathrm{s}$ (respectively $0.064\,\mathrm{s}$) and *soft* (respectively *hard*) spectrum. 54

2.6 The stages employed in the derivation of $P(\mathrm{LLR}|H_G^N)$ (top left), $P(\mathrm{LLR}|H_G^S)$ (top right), and $P(\hat{\rho}_{gw}|H_L^N)$ for the LIGO Livingston (bottom left) and LIGO Hanford (bottom right) interferometers. The histograms of the data samples are on blue, the KDE fitting appears on red. In green, the interpolation of the fitting over the ranges $\mathrm{LLR} \in [5, 170]$ (for the Fermi-GBM backgrounds), $\mathrm{LLR} \in [5, 2000]$ (for the Fermi-GBM real signals) and $\hat{\rho}_{gw} \in [8.0, 10.6]$ (for the GW noise events) with the functions LLR^{-4} and $\hat{\rho}_{gw}^{-4}$ for $\mathrm{LLR} \geq 170$ (for the EM noise transients), $\mathrm{LLR} \geq 2000$ (for the short GRB transients) and respectively $\hat{\rho}_{gw} \geq 10.6$ (for the GW backgrounds). 60

2.7 On top, the LIGO Bayes factor Q_L as a function of $\hat{\rho}_{gw}$ for the LIGO Livingston (left) and the LIGO Hanford (right) interferometers, during O2. On bottom, the LLR dependence of the Fermi-GBM Bayes factor Q_G, over the same period of time. 61

2.8 $I_{\Delta t}$ versus Δt. 62

2.9 Background FAR versus joint ranking Λ, for O2. The distribution corresponding to the background pairs of Fermi-GBM triggers and LIGO-Livingston (respectively LIGO-Hanford) triggers is on left (respectively right). On the left panel, the red diamond illustrates the position of the most interesting foreground association. 63

2.10 On left, Q_L versus $\hat{\rho}_{gw}$ for both the uninformative case (on black) and the quantity obtained empirically from the distributions $P(\hat{\rho}_{gw}|H_L^S)$ and $P(\hat{\rho}_{gw}|H_L^N)$ (on green). On right, the corresponding O2 FAR distributions. These results concern the LIGO-Hanford data. 64

2.11 On left (right), the cumulative density function of the inverse false alarm rate for the background and the foreground associations when the LIGO-Livingston (respectively LIGO-Hanford) GW triggers are considered. For the background associations, the 1σ, 2σ and 3σ uncertainties are provided too. On the left plot, the diagram coordinates of the most interesting foreground association is equally provided. 64

2.12 On left, frequency-time diagram of the power measured at LIGO-Livingston near June 03, 2017 21:51:45 UTC. On right, the Fermi-GBM lightcurve (summation of all NaI detector photon counts with energies in between $12\,\mathrm{keV}$ and $38\,\mathrm{keV}$) of the *targeted-search* counterpart. 65

3.1 *Swift/BAT* and Fermi-GBM lightcurves of GRB 081024A, containing two statistical significant bursts of photons. The picture is taken from Troja et al. [2010]. 68

3.2 Normalized EM intensity versus orbital phase, for EM chirps obtained as the sum of the relativistic Doppler beaming and of the gravitational lensing effects. In all simulations, the x axis covers an orbit and has its origin at the maximum of intensity. The orbital separation is, in all simulations, ~ 10 gravitational radii ($G(m_{\mathrm{BH}}^{\mathrm{SCH}} + m_{\mathrm{NS}}^{\mathrm{SCH}})/c^2$). Top left: the inclination angle $\theta_{\mathrm{inc}}^{\mathrm{SCH}}$ is varied at constant $m_{\mathrm{NS}}^{\mathrm{SCH}} = 1.4\,M_\odot$, $m_{\mathrm{BH}}^{\mathrm{SCH}} = 10 M_\odot$ and $\alpha^{\mathrm{SCH}} = 0$; top right: the mass of the black hole $m_{\mathrm{BH}}^{\mathrm{SCH}}$ varies, while $m_{\mathrm{NS}}^{\mathrm{SCH}} = 1.4\,M_\odot$ and $\alpha^{\mathrm{SCH}} = 0$ are kept constant; bottom center: the binary components masses $m_{\mathrm{NS}}^{\mathrm{SCH}} = 1.4\,M_\odot$ and $m_{\mathrm{BH}}^{\mathrm{SCH}} = 10\,M_\odot$ are fixed, while the spectral index α^{SCH} varies. 72

3.3 The positions of I_0, I_1 and I_2, for $N_{\mathrm{bins}} = 3$. In blue, orbital phase Φ_{orbit} versus time. The origin of the x axis corresponds to the merger time. 74

3.4 The positions of the $[t_{\mathrm{start}}, t_{\mathrm{start}} + \Delta t_{\mathrm{dur}}]$ windows on the time axis. The time windows with $\Delta t_{\mathrm{dur}} = 0.256\,\mathrm{s}$ (as well as those with $\Delta t_{\mathrm{dur}} \in \{0.064\,\mathrm{s},\ 0.128\,\mathrm{s},\ 2.048\,\mathrm{s}\}$) are separated by $64\,\mathrm{ms}$. For the windows with $\Delta t_{\mathrm{dur}} = 1.024\,\mathrm{s}$ (as for those with $\Delta t_{\mathrm{dur}} \in \{2.048\,\mathrm{s},\ 4.096\,\mathrm{s},\ 8.192\,\mathrm{s}\}$), the application of the phase factor of 8 means that the time windows are separated by $\frac{1.024\,\mathrm{s}}{8} = 0.128\,\mathrm{s}$. 76

3.5 FAP (assigned with 1σ, 2σ and 3σ uncertainties) versus LLR for background noise, for the *chirp-search* (left) and the *targeted-search* (right). The distributions have been obtained by running the two searches on the same 1000 random times distributed along the month of April 2019. For the *chirp-search*, the setting $N_{\mathrm{bins}} = 10$ is used. 77

3.6 Time dependence of the normalized lightcurve. In blue: the *exotic-waveform* parameterized by $\theta_{\rm peak} = 270^\circ$ and $\theta_{\rm width} = 40^\circ$; in orange: the lightcurve modulated by the relativistic beaming and the gravitational lensing. For both cases, the binary compact objects components have masses $m_1 = 10\,M_\odot$ and $m_2 = 1.4\,M_\odot$. 79

3.7 Top left: CDF versus FAP, for the case of signals injected and recovered with the same binary parameters. Top right: CDF versus LLR for injected signals with $\sigma_{\Delta\mathcal{M}} = 0$ and different values of $\sigma_{\Delta t}$. Bottom left: CDF versus LLR for injected signals with $\sigma_{\Delta t} = 0$ and different values of $\sigma_{\Delta\mathcal{M}}$. Bottom right: CDF versus LLR for different values of $(\sigma_{\Delta t}, \sigma_{\Delta\mathcal{M}})$. For all the panels, except the top left, the setting $N_{\rm bins} = 10$ is used. 81

3.8 Increase of the signal-to-noise ratio by considering more and more orbital phase intervals I_k. On the left panel is the lightcurve in the time space. The middle panels show the same time space histogram of photons arrival times as well as the positions of the orbital phase intervals I_k. The right panels represent the lightcurves in the orbital phase space after: (i) the addition of the foreground photons corresponding to each orbital phase interval I_k and (ii) the estimation of the orbital phase space photon background rate. 82

4.1 On top: spectroscopic measurements of AT 2017gfo; on bottom: photometric measurements of AT 2017gfo. The panels are taken from Pian et al. [2017]. 87

4.1 AB magnitudes versus time for some examples of templates used in the training of `astrorapid`. The plots represent the following templates: "SNIa-91bg" (first column, first row), "SNIa-x" (second column, first row), "SNIa-norm" (first column, second row), "Kilonova" (second column, second row), "SNIbc" (first column, third row), "SNII" (second column, third row), "TDE" (first column, fourth row), "CART" (second column, fourth row), "PISN" (first column, fifth row), "ILOT" (second column, fifth row), "SLSN-I" (first column, sixth row) and "AGN" (second column, sixth row). 93

4.2 astrorapid input (top panel) and output (bottom panel) data for a kilonova object. On the x axis is the time, while the y axis represents the photon flux (top panel) and the probabilities assigned to the different transient object classes (bottom panel). In this example, astrorapid assigns high probability to "Pre-explosion" before the increase of the light intensity, then the curve corresponding to "Kilonova" goes to higher and higher probabilities. The input data consists in r and g photometric data. 95
4.3 Initial guess of the four main classes, obtained by the collapse of original astrorapid classes. 96
4.4 Histogram of the preferred templates after 2, 11 and 21 observations, when the initial naive guess collapse described in Equation 4.5 is used. On the left (right) panel, the results correspond to the situation in which the input is represented by the real ZTF "SN" (respectively "Others") type transients. 97
4.5 Histogram of the percentage probabilities of the preferred template after two observations, assuming the naive guess collapse described in Equation 4.5. The input data is represented by those real ZTF "Others" lightcurves misclassified as "SN" or "KN". 98
4.6 The success (left) and failure (right) probabilities versus β. The preferred event is reported after 2, 6, 11, 16, 21 and 26 observations. The top (bottom) panels correspond to "SN" (respectively "Others") type objects. 99
4.7 Flowchart showing the different steps of the analysis. The photometric multi filter input data is initially analyzed by astrorapid which offers, after each new observation, a probability distribution over fourteen templates. The astrorapid output is manipulated as described in this section in order to report, at each new observation, a preferred template from {"SN", "Others", "KN", "Indistinguishable"}. 100

4.8 On top left, the observations number histogram for the ZTF public data stream objects. On top right, the histogram of the time separation between two consecutive photon flux measurements realized by using the same r (on top) or g (on bottom) photometric filter. On bottom left (right), the histogram of "SN" type objects cosmological redshift (time difference between the first detection and measured global maximum). . 101

4.9 Classification results for ZTF real events. Both r and g (respectively only r) observations are considered for the top (respectively bottom) panels. On the top left (right), "SN" (respectively "Others") labelled objects are used as input data, while for the bottom panel only "SN" type events are considered. 103

4.10 On left, the g passband absolute magnitude for simulated kilonovae possessing $M_{ej} = 0.005\,M_{\odot}$, $v_{ej} = 0.15\,c$ and different lanthanide fractions. On right, g passband apparent magnitude for simulated supernovae with color index $c = 0$, redshift $z = 0.022$ and possessing different shape parameters x_1. 104

4.11 Top left: preferred event histogram when the input is a set of 1000 injected "SN"; top right: preferred event histogram when the input is the a of 1000 injected "KN"; bottom left: classification fraction at the end of two nights, for both redshift assigned and unassigned "KN" injections; bottom-right: histogram of durations during which the simulated "KN" are visible for a ZTF-like telescope. 105

4.12 Kilonovae injections classification results as a function of the lanthanide fraction X_{lan} (top left), cosmological redshift (top right), mass ejecta M_{ej} (bottom left) and ejecta velocity v_{ej} (bottom right). In each panel, the histogram of the number of times each template, in between {"SN", "KN", "Indistinguisha is selected by the pipeline. 107

4.13 The r (on top) and g (on bottom) apparent magnitude probability density at the moment of the first correct classification. The set of 1000 well-sampled simulated "KN" are used as input data. 107

4.14 Histogram of preferred templates when the I use the 100 realistically sampled "KN" injections. 108

4.15 The locations distribution of the GRANDMA network observatories. The picture is taken from Antier et al. [2020b]. 109

5.1 $m_{\rm ej}(m_1, m_2)$ is plotted in color, while the level lines designate the quantity $2(m_{\rm ej} - m_{\rm ej}^{\rm NEA})/(m_{\rm ej} + m_{\rm ej}^{\rm NEA})$, where $m_{\rm ej}^{\rm NEA}$ is the predicted mass ejecta according to Nedora et al. [2020]. For the left (right) panel, the equation of state parameterized by $\gamma_0^{\rm LIN} = 0.5485$, $\gamma_1^{\rm LIN} = 0.3767$, $\gamma_2^{\rm LIN} = -0.0690$ and $\gamma_3^{\rm LIN} = 0.0035$ (respectively $\gamma_0^{\rm LIN} = 1.4777$, $\gamma_1^{\rm LIN} = -0.3225$, $\gamma_2^{\rm LIN} = 0.0694$ and $\gamma_3^{\rm LIN} = -0.0046$), predicting $11.3\,$km ($13.0\,$km) radius and 232 (663) tidal deformability for a $1.4\,M_\odot$ neutron star, as well as a $2.00\,M_\odot$ ($2.43\,M_\odot$) TOV limit, has been used. . 121

5.2 In color: $m_{\rm ej}(\chi_{\rm eff}, m_2)$ at constant $1/q = 2$ (top left); $m_{\rm ej}(1/q, m_2)$ at constant $\chi_{\rm eff} = 0.6$ (top right); $m_{\rm ej}(1/q, \chi_{\rm eff})$ at constant $m_2 = 1.6\,M_\odot$ (bottom). The level lines designate the quantity $2(M^{\rm dyn} - M_{\rm KAW}^{\rm dyn})/(M^{\rm dyn} + M_{\rm KAW}^{\rm dyn})$, where $M_{\rm KAW}^{\rm dyn}$ is the dynamical ejecta predicted by the fitting formula from Kawaguchi et al. [2016]. For the generation of the three panels, I used the equation of state parameterized by $\gamma_0^{\rm LIN} = 0.3268$, $\gamma_1^{\rm LIN} = 0.4456$, $\gamma_2^{\rm LIN} = -0.0586$ and $\gamma_3^{\rm LIN} = 0.0016$, predicting a $12.4\,$km radius and 458 tidal deformability, as well as a $2.37\,M_\odot$ TOV limit. 122

5.3 Absolute magnitude versus time; top left: *Model II* lightcurves for $m_{\rm ej} = 0.05\,M_\odot$, $\theta_{\rm inc} = 45°$ and different values of Φ; top right: *Model II* lightcurves for $m_{\rm ej} = 0.95\,M_\odot$, $\Phi = 45°$ and different values of $\theta_{\rm inc}$; bottom: *Model I* lightcurves for $m_{\rm ej} = 0.05\,M_\odot$, $v_{\rm ej} = 0.15\,c$ and different values of $X_{\rm lan}$. 124

5.4 Time evolution of the absolute magnitude. The binary parameters are $(m_1^{\rm fixed}, m_2^{\rm fixed}, \chi_{\rm eff}) = (1.6\,M_\odot, 1.4\,M_\odot, 0.001)$, the ejecta is characterized by $X_{\rm lan}^{\rm fixed} = 10^{-4}$, while the neutron star equation of state is parameterized by $(\gamma_0^{\rm LIN}, \gamma_1^{\rm LIN}, \gamma_2^{\rm LIN}, \gamma_3^{\rm LIN}) = (1.4777, -0.3225, 0.0694, -0.0046)$. From the top to the bottom panel, the considered sources of uncertainty are: the low-latency inaccurate measurement only; the equation of state marginalization only; the errors assigned to the fitting formulae only; the ejecta chemical composition uncertainty only; all the error sources put together. For each panel, the black curve represents the case of perfect predictions, while the blue shades contour plots designate the 1σ, 2σ and 3σ prediction errors. 128

5.5 $\log_{10} m_{\rm ej}$ cumulative distribution function for GW170817 and GW190425. One should note that this plot is slightly different than the one appearing in Figure 6 of Stachie et al. [2021]. The reason for this is the fact that here I use the PE samples from Abbott et al. [2019a] (for GW170817) and Abbott et al. [2021a] (for GW190425), while in the published paper, I used, by mistake, the PE samples corresponding to the GW waveforms priors *IMRPhenomPv2_NRTidalv2* [Dietrich et al., 2019], for GW170817, and *Taylor F2* [Damour et al., 2001], for GW190425.131

5.6 Absolute magnitude versus time for GW170817 (on top) and GW190425 (on bottom), for the $u, g, r, i, z, y, J, H, K$ photometric filters. The *Model I* lightcurves appear in blue, while the *Model II* lightcurves are in red. For each lightcurve, the two solid lines are the upper (90th percentile) and lower (10th percentile) limits, while the dashed line corresponds to the median. Finally, regarding GW170817, the observational points appear in circles (finite uncertainty) and triangles (upper limits), and have been derived from apparent magnitude data by means of the mean Bayestar skymap luminosity distance. Only the low-latency data is used for these simulations. 133

5.7 Time evolution of the GW190425 apparent magnitude, based on the PE input data. The chemical composition ejecta priors are: $X_{\rm lan} = 10^{-4}$ for the red lightcurve and $\log_{10} X_{\rm lan}$ uniform in [-9, -1] for the blue lightcurve.134

6.1 An overview of the main projects I worked on during my PhD. 136

LIST OF TABLES

3.1 MET and $\mathcal{M}$ for the five O2/O3 real events. For GW170817, the posteriors from [Romero-Shaw et al., 2020] have been used, while the samples from Abbott et al. [2019a] have been preferred for both GW190814 and GW190425. Finally, for GW200105 (respectively GW200115) I have used *LALInference* with the prior waveform *SEOBNRv4 ROM NRTidalv2 NSBH* [Bohé et al., 2017] (respectively *IMRPhe- nomNSBH* [Thompson et al., 2020]). In the table, the reported values represent the median (50th percentile), the upper limit (90th percentile) and the lower limit (10th percentile). For the case of $\mathcal{M}$, a missing upper/lower limit means that this limit is away from the median value by less than $0.001 M_{\odot}$. . . 84

3.2 LLR and corresponding FAP, for the two searches, for the five O2/O3 real GW events. The *chirp-search* is used with $N_{\rm bins} = 10$. For the FAP, the mean as well as $\pm$ 3 standard deviations are provided. When the mean and/or the upper limit (-3σ) is (are) equal to 0, it means that the value(s) is (are) lower than 0.01. All the events reported in this table represent triggers with duration of 0.064 s and *hard* spectrum. 85

5.1 The true values of the binary parameters appear in the first three columns, as follows: $m_1^{\rm fixed} = m_{\rm chirp}^{\rm fixed}(1+q^{\rm fixed})^{1/5}/(q^{\rm fixed})^{3/5}$, $m_2^{\rm fixed} = m_{\rm chirp}^{\rm fixed}(1+q^{\rm fixed})^{1/5}(q^{\rm fixed})^{2/5})$ and $\chi_{\rm eff}^{\rm fixed}$. It is assumed that the exact lanthanide fraction is $X_{\rm lan}^{\rm fixed} = 10^{-4}$, while the exact supra-nuclear equation of state $\rm EOS^{fixed}$ is parameterized by $\gamma_0^{\rm LIN} = 1.4777$, $\gamma_1^{\rm LIN} = -0.3225$, $\gamma_2^{\rm LIN} = 0.0694$ and $\gamma_3^{\rm LIN} = -0.0046$, which associates to a $1.4\,M_\odot$ neutron star, a 13 km radius and a tidal deformability of 663, and predicts a TOV limit of $2.43\,M_\odot$. In column four, the different sources of uncertainty taken into account: (i) no uncertainty; (ii) MBTA imprecise measurement only; (iii) neutron star equation of state marginalization only; (iv) ejecta fitting errors only; (v) ejecta chemical composition ignorance only; (vi) all the previous sources of uncertainty together. In the fifth column, the value of *HasEjecta*. The last sixth columns show the absolute magnitude at the end of 1, 2 and 3 days, for the g and K photometric filters. The upper and lower absolute magnitude limits are defined by the 10th and 90th percentiles. 126

5.2 The parameters of the MBTA offline analysis preferred templates in the case of GW170817, GW190425, GW190814, GW200105 and GW200115. There are four independent parameters: the masses and the aligned/anti-aligned spins of the heavier (m_1 and s_1) and the lighter (m_2 and s_2) binary compact objects. The chirp mass $m_{\rm chirp}$, the mass ratio q and the effective spin $\chi_{\rm eff}$ might be expressed as functions of the previous parameters, as follows: $m_{\rm chirp} = (m_1 m_2)^{3/5}/(m_1+m_2)^{1/5}$, $q = m_2/m_1$ and $\chi_{\rm eff} = (m_1 s_1 + m_2 s_2)/(m_1+m_2)$. 129

5.3 Median (50th percentile), upper limits (90th percentile) and lower limits (10th percentile) of the binary parameters $m_{\rm chirp}$, q and $\chi_{\rm eff}$, for GW170817, GW190425, GW190814, GW200105 and GW200115. While the columns 2-3-4 present the MBTA output templates results weighted by w, the columns 5-6-7 illustrate the binary parameters obtained by sampling unweighted items from the parameter estimation (hereafter PE) posteriors [Veitch et al., 2015]. More precisely, the PE samples used here are the same as in [Abbott et al., 2019a, 2021a]. 130

5.4 *HasRemnant*, MBTA *HasEjecta* and PE *HasEjecta*. While the *HasRemnant* values appearing here are the same as the ones reported in LIGO Scientific Collaboration and Virgo Collaboration [2019a] (for GW190425), LIGO Scientific Collaboration and Virgo Collaboration [2019b] (for GW190814), LIGO Scientific Collaboration and Virgo Collaboration [2020a] (for GW200105), LIGO Scientific Collaboration and Virgo Collaboration [2020b] (for GW200115) and Abbott et al. [2019b] (for GW170817; actually in this case I use the value reported for *EM-Bright*), the PE samples used here are identical to those reported in Abbott et al. [2019a] (for GW170817) and Abbott et al. [2021a] (for GW190425 and GW190814). 130

CHAPTER 1

Introduction

1.1 Compact object binaries

1.1.1 Neutron stars and black holes

Among the theorized compact objects, the only ones detected to date are white dwarfs, neutron stars and black holes. Concerning the latter category, there is observational evidence for stellar mass, intermediate mass and supermassive black holes. Hereafter, unless specified, by black holes, I refer to those of stellar mass. The compact objects represent the endpoint evolution of the luminous stars populating our Universe. A sketch of the life cycle of stars is presented in Figure 1.1. The star-forming regions refer to domains in the interstellar space characterized by dense molecular clouds, containing principally hydrogen and helium but also traces of heavier elements. They have sizes ranging from tens to hundreds light-years and weights going from thousands to millions solar masses [Murray, 2010]. The formation of a star is triggered by a gravitational collapse. This process occurs when the outward internal gas pressure is overcome by the inward gravitational pressure, a phenomenon known as Jeans instability [Smith, 2004]. The contraction of matter continues until hydrostatic equilibrium is achieved. An initial protostar, surrounded by a protoplanetary disc, is formed [Stahler and Palla, 2004]. The stars spend the main part of theirs lives on the main sequence. This stage is characterized by the nuclear fusion reactions taking place in the core of the stars and which are responsible for the light emitted outside in the Universe. The nuclear reactions consist principally in conversion of hydrogen into helium. Inside the core of more massive stars, production of heavier elements is happening, the limit being the synthesis of iron. The fate of the low and intermediate mass stars is the following: at the end of the main sequence lifetime, they become a red giant, i.e. a cool and luminous star with large radius [Miglio et al., 2012]. The ionized gas from the outer shells is becoming less and less trapped by gravity, escaping thus in the surrounding area and enriching the interstellar medium with the new nucleosynthesized elements. At this stage the red giant becomes a planetary nebula, in the center of which an electron-degenerate carbon-oxygen core can be found [Kwok, 2005]. When the expanding cloud gas is

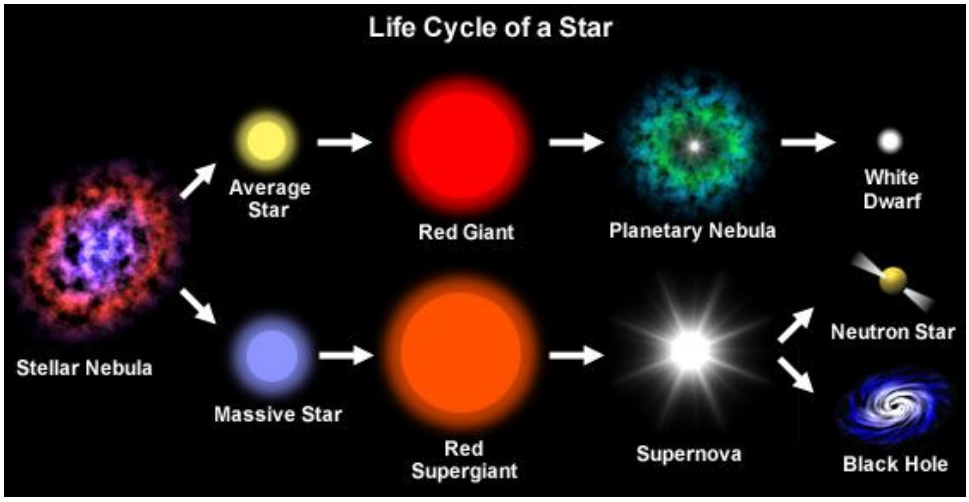

Fig. 1.1 The different steps of the formation, evolution and death of stars. Credit: NASA.

cold enough the life of the planetary nebula ends, leaving the room to the last stellar evolution phase, the white dwarf. This star remnant is believed to be formed of degenerate electrons [Fowler, 1926]. Because nuclear reactions are not taking place anymore inside a white dwarf, there is no more radiation pressure to balance the inward gravitational forces. The equilibrium is assured by the degeneracy pressure, at the base of which is the Pauli exclusion principle [Krane, 1987]. The first discovered white dwarf is represented by one component in the triple system *40 Eridani* [Holberg, 2009]. The destiny of massive stars, i.e. with masses more than eight times that of the Sun, is a bit different. First of all, during their main sequence period, they emit more light causing them to have a shorter lifespan. After the main sequence stage, they evolve into a supergiant, some of the largest objects populating the Universe. The stars exist as supergiants as long as there are still chemical elements to fuse. When this process is finished, what follows is a core-collapse explosion, a phenomenon called a supernova, in which gravitational binding potential energy is converted in far away ejected photons, neutrinos, cosmic rays and gravitational waves [Gilmore, 2004]. A core-collapse explosion is responsible for the expulsion of the outer layers of the supergiant, leaving behind a neutron star or a black hole, depending on the mass of the progenitor. Whereas this is considered to be the most common formation process, several other ways of producing neutron stars and black holes have been found. For example the mass of a white dwarf accreting matter from its binary companion can exceed the Chandrasekhar limit. At this point the electron degeneracy pressure is insufficient to oppose to the gravitational collapse, and thereby the white dwarf evolves into a neutron star or black hole [Nomoto, 1986]. Also a black hole can be the result of the merger of two smaller other compact objects [Abbott et al., 2019a].

Besides the general interest linked to the understanding of the Universe, neutron

stars and black holes are unique laboratories to test fundamental physics. Indeed, the interior of neutron stars contains matter exceeding the supra-nuclear density [Miller et al., 2019b]. At such overdensities, one might expect to find not (only) baryons, but also degenerate quarks [Alford et al., 2013; Han et al., 2019; Lindblom, 1998]. Equally some neutron stars, named pulsars, have magnetic fields which are much stronger than one could try to artificially generate on Earth [Makishima, 2003]. The black holes are objects that until recently have not even been imaginable. They are characterized by a barrier, named event horizon [Rindler, 1956], which delimits an area of the space-time inaccessible to an external observer. According to the non-hair theorem [Carter, 1971], for an external observer, a black hole is parameterized by its mass, angular momentum and electric charged. To date, there is no observational evidence of black holes possessing non zero electric charge. Space-time geometry for a non electrically charged and non-rotating black hole is contained in the Schwarzschild metric, whereas the Kerr metric describes the Riemannian geometry of a black hole with non-zero angular momentum, but still having no charge. An isolated black hole needs net charge to give rise to a magnetic field. However, if there is a disc of material orbiting a black hole, then a magnetic field might be formed. The gravitational field in the vicinity of both neutron stars and black holes is so strong that, when studying the physics around these objects, one needs to replace the Newtonian gravitation with the Einstein General Relativity. Thus the light passing in theirs neighbourhoods experiences non-negligible bending, making from these compact objects sources of microlensing [Wyrzykowski, Lukasz and Mandel, Ilya, 2020]. Likewise other extreme phenomena take place in the surroundings of these objects: the matter contained in theirs accretion discs radiates in X-rays [Narayan et al., 1997]; the outer shells of the neutron stars rotate at relativistic speeds [Hessels et al., 2006].

Most of the neutron stars and black holes detected yet are in our Milky Way. The vast majority of them are found in X-ray binaries. In such systems, matter is transferred from the companion star towards the black hole/neutron star [Lewin and van der Klis, 2006]. Gravitational potential energy is converted into X-rays. By the observation of such radiation, the first black hole (Cygnus X-1) was discovered in 1964 [Webster and Murdin, 1972; Bolton, 1972]. In addition to this technique, magnetized neutron stars, known as pulsars, emit detectable beams of radio EM radiation, the behavior being similar to that of a lighthouse [Abdo et al., 2013]. This is how PSR B1919+21, the first discovered pulsar, was detected [Hewish et al., 1968]. Although less numerous, extra-galactic compact objects [Cordes and Wasserman, 2016] have been equally detected by scientists. Even if it is not the focus topic of this dissertation, it is worth mentioning that there exists another class of black holes, weighing millions to billions solar masses and generally residing in the center of the galaxies: the supermassive black holes. They are

usually surrounded by heated accretion rings orbiting them. The accretion disc powers EM radiation, which can be measured by a distant observer [Event Horizon Telescope Collaboration et al., 2019].

1.1.2 Formation channels

Compact binary population synthesis is a very exciting and challenging topic of modern high energy astrophysics. The condition for a two black hole system to lead to merger in a Hubble time is to possess an initial binary separation not higher than a few tens of solar radii [Shapiro and Teukolsky, 1983]. In isolated binaries, it is expected that the majority of these black hole components to be formed at the end evolutionary stage of stars. And in particular, when a massive star leaves the main sequence and becomes a giant star, its radius might be of the order of several hundreds solar radii [van Belle et al., 2009]. So in order to address correctly the question of binary compact object formation, one needs to take into consideration physical processes such as mass transfer, common envelope, natal kicks and tidal interaction [Hurley et al., 2002]. The evolution of a massive star in a binary is different from the evolution it would have if it is born, grows up and dies alone, the reason for this fact being the interaction with its companion. Massive stars may lose an important part of their mass through stellar winds. The matter lost by radiation driven winds is accompanied by loss of star angular momentum. The amount of lost mass depends on metallicity [van Loon, 2006; Hainich et al., 2017; Vink, 2018], the stellar winds manifesting by the interaction of photons with millions of iron lines in the extreme ultra-violet EM spectrum. In a binary, the mass lost through the winds might be accreted by the companion [Burns Boyle, 1984; Lamers et al., 1976; Soker, 2004], causing thus a transfer of angular momentum too. Therefore, the mass transfer and the accretion might have an impact on the orbit, changing the orbital angular momentum and favoring circularization. Another important mechanism in binary systems is represented by the tidal interaction. Tidal-energy dissipation provokes synchronization between the star spins and the orbital angular velocities [Horedt, 1975; Campbell, 1984]. It also speeds up the circularization of the orbit [Rasio et al., 1996; Hut, 1981; Zahn, 2008]. Another mechanism allowing the loss of matter and spin angular momentum is magnetic braking. Indeed the magnetic field of stars plays the role of a trampoline for ionized matter which are transported far away from the originating system [Skumanich, 1971; Sun et al., 2019].

Illustrated in Figure 1.2 are the different steps taking place in the most common compact binary synthesis scenario for isolated binaries. The gravitational field in a binary system creates equipotential surfaces. Moreover, for each component star of the binary there is a Roche lobe, defined as the region inside which the matter is gravitationally bound to the star. At the end of the main sequence period, the star expands be-

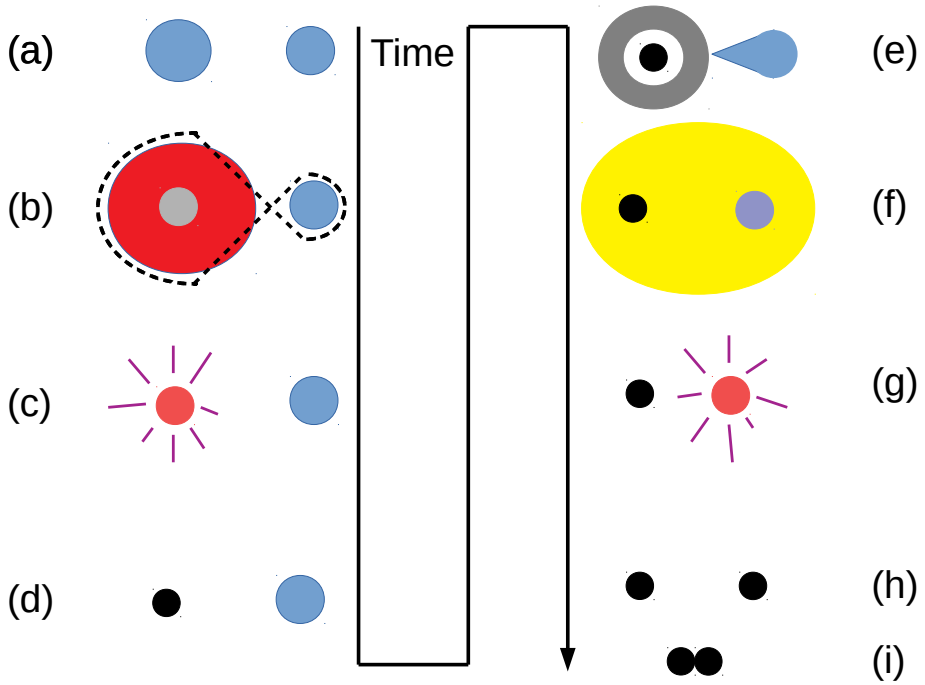

Fig. 1.2 Common envelope based formation channel for isolated compact binaries. The different steps are: (a) two main sequence stars orbit each other; (b) one of the stars expands overfilling its Roche lobe; (c) the star consumes its nuclear reaction based fuel and detonates as a supernova; (d) new system containing a black hole/neutron star/white dwarf and a main sequence star; (e) X-ray binary, with accretion disc around the compact object; (f) the outer shells of the second star extend beyond the compact object, giving birth to the common envelope; (g) after the ejection of the common envelope, the second star dies in a supernova explosion; (h) a new system of compact objects in a tight binary; (i) coalescence.

coming a giant, and its outer envelopes overfill the Roche lobe. The outer shell unbound matter might be accreted by the companion through the Lagrangian inner point [Eggleton, 1983; Tout et al., 1997; Webbink, 1988; Jackson et al., 2017]. At the end of its life, the primary star explodes as a supernova thus giving to the new born compact object a velocity kick [Lyne and Lorimer, 1994; Hansen and Phinney, 1997; Fryer and Kalogera, 1997; Kaspi et al., 1996; Shao and Li, 2018]. The recoil impulsion changes the parameters of the binary such as the eccentricity and the orbital separation [Martin et al., 2009], and sometimes may turn out to be fatal leading to the disruption of the binary system [Belczynski and Bulik, 1999]. If the binary survives the supernova kick, the new system is formed of a compact object and a companion star. The strong gravitational field of the compact objects rips matter out from the star, an accretion disc being formed around it [Migliari and Fender, 2006]. This new system is known as a X-ray binary [Chen and Podsiadlowski, 2016]. Later the secondary binary expands, its outer shells extending beyond the neutron star/black hole companion. This physical process is known as the common envelope phase [Bond et al., 1978; Rasio and Livio, 1996; Law-Smith et al., 2020]. During this phase, unstable processes of mass transfer and loss of angular momentum occur. The consequence of the common envelope is the orbital separation narrowing, or even a premature merger [Taam and Sandquist, 2000; Soker, 2013; Schrøder et al., 2019]. At the same time energy extracted from the binary accumulates in the common envelope, causing its ejection through dust-driven winds [Glanz and Perets, 2018; Kruckow, M. U. et al., 2016; Davis et al., 2012]. The result of the common envelope phase is a remnant short-period binary. Then follows the supernova explosion of the secondary component. If the binary survives again the new supernova natal kick, the new system is formed of two compact objects separated by a sufficiently small distance. Finally, the end life of the binary is marked by the coalescence of the compact objects.

The reason for which the existence of the common envelope seems inevitable is the simultaneous large radius of giant stars and the small orbital separation of short-period compact binaries. However, for the case of the massive black hole binaries, one can envisage formation channels which avoid the stage of the common enveloppe. Indeed it turns out that the tidal interaction of extremely massive stars might induce a large spin, aligned with the orbital angular momentum, for each component of the binary. And this causes the chemical mixing inside the star core, which has a non-negligible impact on the pre-supernova evolution of the star. Indeed if the chemical composition of the core is radially uniform, contrary to the traditional case of an outermost shell of hydrogen, followed by a shell of helium etc, the star avoids the dramatic expansion during the last stage of its life [de Mink, S. E. et al., 2009; Heger and Langer, 2000; Walborn, 1976; Maeder and Meynet, 2000]. Thus two highly spinning massive stars

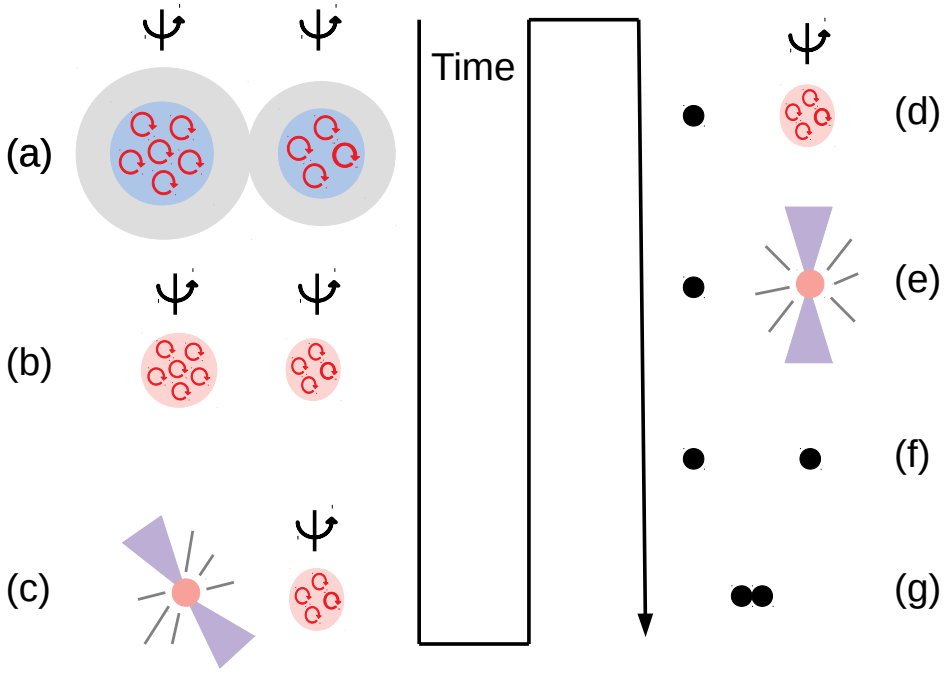

Fig. 1.3 Chemically homogeneous evolution as an alternative formation channel for the synthesis of compact object binaries. The different steps are: (a) two highly spinning stars in a tight binary; (b) system formed of two He cores after the loss of outer shells by the two highly evolved main sequence stars; (c) a first supernova explosion; (d) new system consisting of a new born black hole and the other He core; (e) second supernova detonation; (f) tight binary black hole; (g) merger.

might be present in a tight binary, without physical mechanisms, such as mass transfer or accretion [de Mink, S. E. et al., 2009; Song et al., 2016], taking place. This new formation channel is named chemically homogeneous evolution [Maeder, 1987] and its different steps are highlighted in Figure 1.3. In a few words the binary synthesis takes place as follows: two highly spinning massive stars are in a tight binary; by the end of their lives, the radius of each star, even if increases, avoids the dramatic elongation which occurs traditionally for low spinning stars; the two stars lose their outer layers, leaving two He (or other heavier chemical elements up to Fe) cores. The two cores explode as supernovae, leaving behind the remnant black holes. As before, if the binary survives the two supernova kicks, the compact objects prepare for the last stage, the coalescence.

Although the preceding formation channels might account for an important part of binaries detected by Advanced LIGO [Aasi et al., 2015b] and Advanced Virgo [Acernese et al., 2015] (LIGO/Virgo), there are places in the Universe where the scenario of an isolated binary seems improbable. Indeed, high stellar/gas densities can be found in several places, such as the globular clusters [Harris, 1996] and the active galactic nuclei [Shields, 1999]. The large number of stars implies a high number of black holes

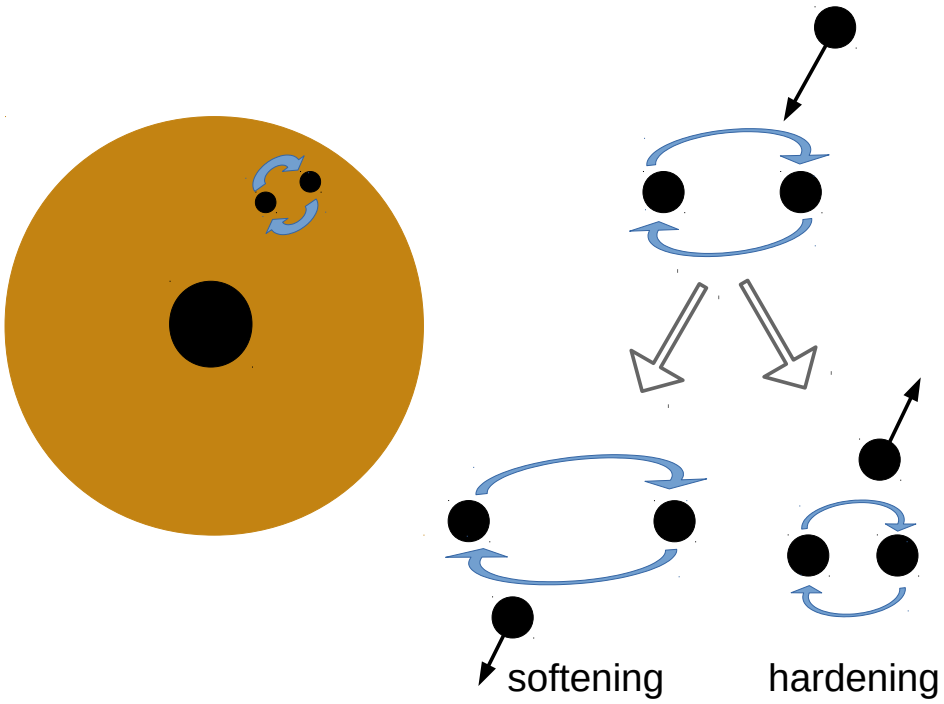

Fig. 1.4 On left, an active galactic nucleus, with its supermassive black hole at the center and its accretion disc (in brown) containing a binary black hole. On right, a binary-single interaction. The result of the encounter might be either a softening, i.e. remoteness of the compact object components, or a hardening, i.e. a tighter binary.

too. And presumably, many of them can be found in binaries. Even if the two compact objects are initially too distant one from another in order for the binary to merge through GW radiation in a Hubble time, the richness of the surrounding environment offers new opportunities to reduce the orbital separation. For example drag forces exercised by the active galactic nuclei disc gas might extract gravitational binding energy, leading to a tighter binary; also three-body (binary-single) interaction might dynamically harden the system [Leigh et al., 2018; Stone et al., 2017; Tagawa et al., 2020b; O'Leary et al., 2009; Kremer et al., 2018; Bartos et al., 2017]. Both mechanisms are scarcely highlighted in Figure 1.4. This class of binary systems, formed in dynamical environments, might be distinguished from the isolated systems category, by measuring some parameters of the binary. Indeed, in dynamical environments, one should expect interaction with the local surrounding regions, which might translate in large eccentricities and highly non-aligned spin components [Tagawa et al., 2021, 2020a; Trani et al., 2021], contrary to the isolated binary case which favors circular orbits and individual aligned spins.

1.2 GW emission

GWs have been predicted since the beginning of the $\mathrm{XX}^{\mathrm{th}}$ century firstly by Henri Poincaré [Poincaré, 1906] by taking advantage of the Lorentz invariance, and later by Albert Einstein [Einstein, 1916, 1918] in the frame of General Relativity. A system of two compact objects orbiting each other emits GWs, causing thus the decrease of the orbital separation. This leads inevitably towards merger, if the binary has no other contact with the external world. The detection of GW signals associated with the merger of compact objects is important for a variety of reasons. GWs give information related to the parameters and spins of the binary components [Vishveshwara, 1970; Press, 1971; Chandrasekhar and Detweiler, 1975; Blanchet et al., 1995; Blanchet, 2014; Buonanno and Damour, 1999b; Pretorius, 2005; Campanelli et al., 2006a; Baker et al., 2006b]. The reason for which the binary parameters can be estimated with extraordinary precision is that GWs interact very quickly with the surrounding matter and thus arrive on Earth almost unaltered, the only limitation being represented by the amplitude decrease with the distance.

In General Relativity, a gravitational field does not act instantaneously on a far away mass distribution, the information travelling at the speed of light. For this reason, General Relativity does predict the existence of GWs. I derive here, following Moore [2013], the 0^{th} order GWs emitted by two point masses orbiting each other, during the early inspiral, i.e. when the orbital separation is high enough in order for the particles to be considered non-relativistic. The assumption of an observer on Earth, far away from the GW astrophysical source, allows us to write the Riemannian metric $g_{\mu\nu}$ as the sum the flat spacetime metric $\eta_{\mu\nu} = \mathrm{diag}(-1, 1, 1, 1)$ and some metric perturbation $h_{\mu\nu}$:

$$g_{\mu\nu} = \eta_{\mu\nu} + h_{\mu\nu}, \tag{1.1}$$

where $h_{\mu\nu} = h_{\nu\mu}$ and $|h_{\mu\nu}| \ll 1$. The advantage of the weak-field limit prior is that it permits to write the field equations in linear form. The Einstein equation is

$$G^{\gamma\sigma} = \frac{8\pi G}{c^4} T^{\gamma\sigma}, \tag{1.2}$$

where $G_{\gamma\sigma}$ and $T_{\gamma\sigma}$ are the Einstein and the stress-energy tensors. It deserves to be mentioned that the cosmological constant does not appear in the previous equation because its impact is negligible for GW sources covering distances lower than a typical galaxy size, which is the case of our considered system. While $T_{\gamma\sigma}$ contains information relative to the density of matter and energy, $G_{\gamma\sigma}$ embeds everything having to do with the spatial curvature. In order to simplify calculations, I define the trace-reversed

metric perturbation by

$$H_{\mu\nu} \equiv h_{\mu\nu} - \frac{1}{2}\eta_{\mu\nu}h, \tag{1.3}$$

with $h \equiv \eta^{\mu\nu}h_{\mu\nu}$ the trace of the initial metric perturbation. By means of the Lorentz gauge, defined by $\partial_\mu H^{\mu\nu} = 0$, the Einstein equation becomes

$$\Box H^{\mu\nu} = -\frac{16\pi G}{c^4}T^{\mu\nu}. \tag{1.4}$$

In the preceding equation, $\Box \equiv \eta^{\alpha\beta}\partial_\alpha\partial_\beta$ is the d'Alembert operator. The wave equation can be recognized in the previous formula. Therefore, I search plane-wave solutions that can be written as

$$H^{\mu\nu}(t, x, y, z) = A^{\mu\nu}\cos\left(k_\sigma x^\sigma\right), \tag{1.5}$$

where $A^{\mu\nu}$ and $k_\sigma = [-\omega, k_x, k_y, k_z]$ represent a constant matrix and a constant covector. The Einstein equation, the Lorentz gauge, the symmetry of $A^{\mu\nu}$ and the addition of the transverse-traceless gauge, denoted by $h^{TT}_{\mu\nu} = A_{\mu\nu}\cos\left(k_\sigma x^\sigma\right)$ (which is equal to $H^{TT}_{\mu\nu}$), implies that a plane-wave solution, propagating in the +z direction, possesses a wave-vector $k_\sigma = [-\omega, 0, 0, \omega]$ and an amplitude matrix

$$A^{\mu\nu} = A_+ \begin{pmatrix} 0 & 0 & 0 & 0 \\ 0 & 1 & 0 & 0 \\ 0 & 0 & -1 & 0 \\ 0 & 0 & 0 & 0 \end{pmatrix} + A_\times \begin{pmatrix} 0 & 0 & 0 & 0 \\ 0 & 0 & 1 & 0 \\ 0 & 1 & 0 & 0 \\ 0 & 0 & 0 & 0 \end{pmatrix}, \tag{1.6}$$

with A_+ and $A_\times$ two constants. The two components of the amplitude matrix are called $\oplus$ and $\otimes$ polarizations. The physical effect of each polarization on a ring distribution of point particles, placed on the Oxy plane, is illustrated in Figure 1.5. At a given time, the $\oplus$ polarization changes by the same factor, for any two distinct points, only the separating distance component parallel to Ox (Oy) axis. On the other side, the $\otimes$ polarization changes only the separating distance component parallel to the first bisector or the line perpendicular to it. Moreover, by analogy with electromagnetism, one has

$$H^{\mu\nu}(t, \vec{R}) = \frac{4G}{c^4}\int_{\text{source}} \frac{T^{\mu\nu}\left(t - \frac{|\vec{R}-\vec{r}|}{c}, \vec{r}\right) d^3\vec{r}}{|\vec{R} - \vec{r}|}, \tag{1.7}$$

where $\vec{R}$ and $\vec{r}$ are the positions of the observer and mass-energy source respectively. I also define the reduced mass quadrupole moment 3-tensor, as

$$Q^{jk}(t) = \int_{\text{source}} \rho(t, \vec{r})(x^j x^k - \frac{1}{3}\eta^{jk}r^2)d^3\vec{r}, \tag{1.8}$$

where $\rho(t, \vec{x})$ is the mass density, $\vec{r} = (x^1, x^2, x^3)$ is the mass position and the integral

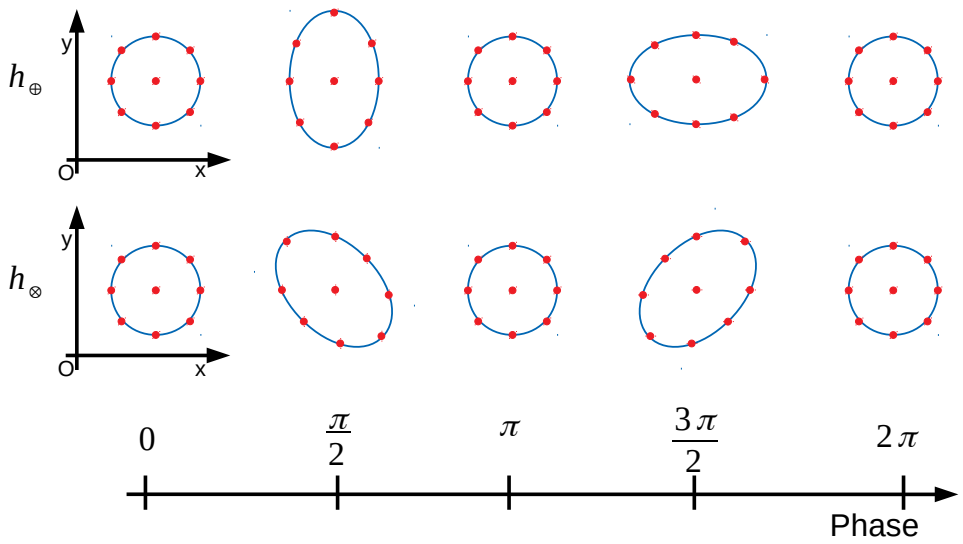

Fig. 1.5 The evolution of a Oxy point particle distribution due to the passage of a GW. On top (the middle), there is highlighted the effect due to only the $\oplus$ ($\otimes$) polarization. On bottom, there is the evolution of the GW phase.

is made over the three dimensional volume. The utility of this quantity comes from the fact that the spatial components of the transverse-traceless perturbation metric can be expressed as $h^{jk}_{TT} = \frac{2G}{Rc^4}\ddot{Q}^{jk}_{TT}$. Moreover, the gravitational energy radiated by a system, defined by

$$\frac{dE}{dt} = -\frac{R^2c^3}{32\pi G}\int_{\theta=0}^{\theta=\pi}\int_{\phi=0}^{\phi=2\pi}\left\langle \dot{h}^{jk}_{TT}\dot{h}^{TT}_{jk}\right\rangle \sin\theta d\theta d\phi, \tag{1.9}$$

has the following form

$$\frac{dE}{dt} = -\frac{G}{5c^5} < \dddot{Q}_{jk}\dddot{Q}^{jk} > . \tag{1.10}$$

The only remaining thing that needs to be considered is the astrophysical system at the origin of the GWs. For two point particles with masses m_1 and m_2, separated by a distance D, orbiting each other in the Oxy plane with the pulsation ω, the reduced quadrupole moment is

$$Q^{jk} = \frac{m_1m_2D^2}{m_1+m_2}\begin{pmatrix} \cos^2\omega t - \frac{1}{3} & \cos\omega t\sin\omega t & 0 \\ \cos\omega t\sin\omega t & \sin^2\omega t - \frac{1}{3} & 0 \\ 0 & 0 & -\frac{1}{3}\end{pmatrix}. \tag{1.11}$$

I consider only the case of circular orbits. It has been demonstrated that binary orbits of an isolated system circularize early [Peters, 1964]. Thus, the spatial metric part of the

perturbation for radiation in the +z direction is

$$h_{TT}^{jk}(t,\vec{R}) = -\frac{4Gm_1m_2D^2\omega^2}{r(m_1+m_2)c^4}\begin{pmatrix}\cos\left[2\omega(t-R/c)\right] & \sin\left[2\omega(t-R/c)\right] & 0\\ \sin\left[2\omega(t-R/c)\right] & -\cos\left[(2\omega(t-R/c)\right] & 0\\ 0 & 0 & 0\end{pmatrix} \tag{1.12}$$

and the energy released by the binary is

$$\frac{dE}{dt} = -\frac{32G(m_1m_2)^2D^4\omega^6}{5c^5(m_1+m_2)^2}. \tag{1.13}$$

But for a binary system, it is known that $D^3\omega^2 = G(m_1+m_2)$ (Kepler's third law) and $E = -\frac{Gm_1m_2}{2D}$, thus I deduce that

$$\omega(t) = \left(\frac{5}{256}\frac{1}{-t}\right)^{3/8}\left(\frac{G}{c^3}m_{\text{chirp}}\right)^{-5/8}. \tag{1.14}$$

In the previous expression $t = 0$ corresponds to the coalescence time. The equation 1.14 shows that the frequency increases over time, and thus the orbital separation shrinks. This behaviour is known in the literature with the name of chirp. There is observational evidence for such an evolution of the orbital separation with time [Weisberg et al., 2010; Burgay et al., 2003; Hermes et al., 2012].

The derivation realized above is approximately valid during the early *inspiral* phase, i.e. as long as the distance between the point particles is high enough, in order for the dynamics to remain stable. More specifically, given a massive object, the trajectory of a test particle, orbiting the massive object, is stable if its distance from the central object is higher than the radius of the innermost stable circular orbit [Jefremov et al., 2015]. If one notes by M_{ISCO} and χ_{ISCO} the mass and the dimensionless spin of the massive object, then this minimal distance can be expressed as

$$r_{\text{ISCO}} = \frac{GM_{\text{ISCO}}}{c^2}\left(3 + Z_{2,\text{ISCO}} \pm \sqrt{(3-Z_{1,\text{ISCO}})(3+Z_{1,\text{ISCO}}+2Z_{2,\text{ISCO}})}\right), \tag{1.15}$$

with $Z_{1,\text{ISCO}} = 1+\sqrt[3]{1-\chi_{\text{ISCO}}^2}\left(\sqrt[3]{1+\chi_{\text{ISCO}}}+\sqrt[3]{1-\chi_{\text{ISCO}}}\right)$ and $Z_{2,\text{ISCO}} = \sqrt{3\chi_{\text{ISCO}}^2+Z_{1,\text{ISCO}}^2}$. In addition, in the previous equation, $\pm$ stands for a prograde/retrograde orbit. One should note that the notion of innermost stable circular orbit might be generalized to the case of two objects of comparable masses. The next step in the evolution of the binary is the *plunge* phase which starts at the end of the adiabatic *inspiral* phase [Buonanno and Damour, 2000]. During the *plunge* phase, the two compact objects continue to have distinct apparent horizons. It is worth noting that the apparent horizon is not the same as the event horizon, and is defined as the boundary separating the two regions for which light rays directed outward moves outward and respectively inward. The *merger*,

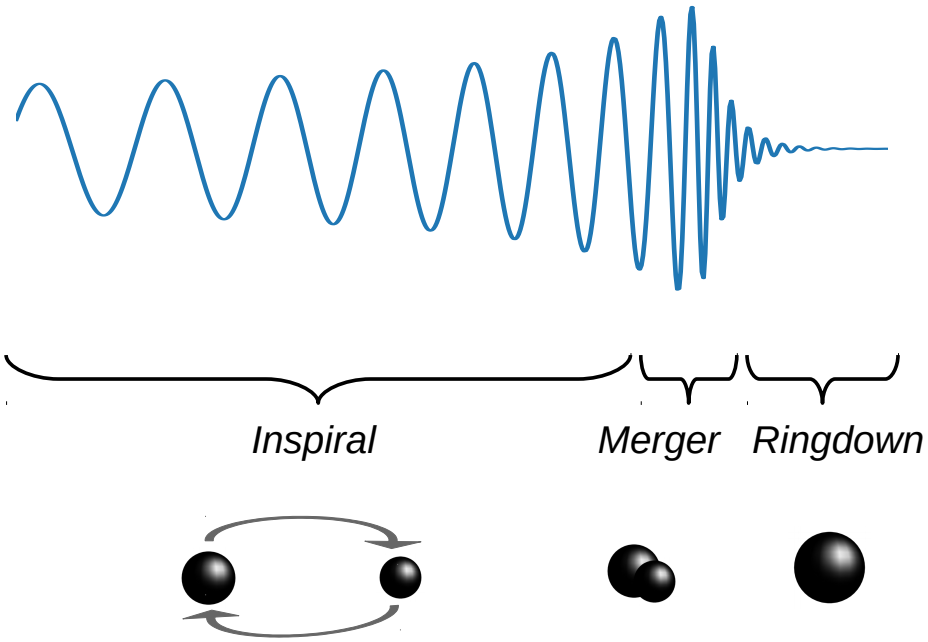

Fig. 1.6 *Inspiral*, *merger* and *ringdown* for binary system, consisting of two black holes of 30 and 25 solar masses. The projected adimensional spins along the orbital angular momentum are 0.9 (for heavier black hole) and 0.1 (for the lighter black hole). The waveform used in this derivation is SEOBNRv2 [Pürrer, 2014].

the next binary evolution phase, occurs when the two apparent horizons coincide, giving rise to what is named a common apparent horizon [Lovelace et al., 2015]. Finally, after the *merger*, the newly formed perturbed black hole starts a phase of relaxation, known as *ringdown*, during which is emitted GW radiation, whose set of frequencies and damping times are named quasinormal mode [Kelly and Baker, 2013; Brügmann et al., 2009; Bhagwat et al., 2018]. The different steps of the binary evolution are pictured in Figure 1.6.

One way to solve the late *inspiral* phase is to continue the development to next orders in v/c, where $\vec{v}$ is the relative velocity of the binary compact objects components. This procedure, named post-Newtonian theory, provides analytical approximations of the exact solution. The different terms appearing in the expansion depend on the binary system parameters, such as the masses and spins [Poisson and Will, 2014; Blanchet, 2014; Schäfer and Jaranowski, 2018; Futamase and Itoh, 2007]. The prediction of the last orbits can also be addressed by means of numerical relativity. This way, computers solve the full Einstein field equations, very often at the expense of huge computational cost [Pretorius, 2005; Campanelli et al., 2006a; Baker et al., 2006a]. Numerical relativity turns out to be very useful in the case of the *merger* and the *ringdown*. Indeed, in this regime of strong gravity field and relativistic motions, the post-Newtonian expansion is no more valid. Other ways to model the GWs have been proposed. For example, the

Effective-One-Body method reformulates the two-body problem. In this framework, a test particule is considered in an effective metric and its dynamics are derived from an effective Hamiltonian [Buonanno and Damour, 1999a; Damour and Nagar, 2011; Bini et al., 2017]. Is is worth noting that this approach is not independent from the previous methods (post-Newtonian expansion and black hole perturbation theory), but makes use of them. Another different method to model GWs is represented by the phenomenological templates. In this case, results from post-Newtonian theory, black hole perturbation and/or calibration to numerical relativity are used to parameterized GW signal based on a set of coefficients [Hannam et al., 2014; Santamaría et al., 2010; Husa et al., 2016; Khan et al., 2016; Sturani et al., 2010]. It is worth mentioning that both the Effective-One-Body and the phenomenological methods are appropriate for the description of all final stages of the binary life. Moreover, when at least one of the binary objects is a neutron star, the GW signal might contain information related to tidal deformabilities, which in turn depend on the supra-nuclear density matter equation of state [Poisson, 1998; Read et al., 2009; Hinderer et al., 2010; Damour et al., 2012; Del Pozzo et al., 2013; Read et al., 2013; Wade et al., 2014; Lackey and Wade, 2015]. In addition, for highly rotating neutron stars, deformations of the compact objects might also arise because of the spin-quadrupole effects [Harry and Hinderer, 2018].

1.3 EM radiation

Gamma-ray bursts (GRBs) have been an enigmatic phenomenon for decades. The detection of the firsts GRB prompt emissions was realized in 1967 by the Vela nuclear test detection satellites [Klebesadel et al., 1973]. It happened in the context of the Cold War, and more precisely after the Nuclear Test Ban Treaty in 1963. Indeed USA suspected USSR of making nuclear tests in space, outside the atmosphere where a fireball could have been avoided, the only detectable traces being the presence of high-energy photons. In spite of intensive calculations [Fowler and Hoyle, 1964; Colgate and White, 1966; Arnett, 1967; Wilson, 1971], the questions concerning the GRB progenitors and/or sky origin had not been determined. The BATSE satellite [Fishman et al., 1989] made the first step forward in understanding these violent events. A partition in two classes, short and long GRBs, has been derived based on their time durations [Kouveliotou et al., 1993]. Moreover, the isotropic distribution of the GRB sky locations definitely tilted the scale in favor of an extragalactic origin [Meegan et al., 1992]. Another debate inside the scientific community concerned the possible existence of a longer wavelength radiation (the afterglow), following the GRB prompt emission. A key role in accomplishing this task was played by the Italian-Dutch BeppoSAX satellite [Boella, G. et al., 1997]. Thus GRB 970228 was the first event for which a afterglow emission was detected [Costa et al., 1997; van Paradijs et al., 1997]. It followed GRB 970508,

the first event with a measured redshift afterglow [Metzger et al., 1997; Reichart, 1998; Waxman et al., 1998] and GRB 980425, the first event having a clear association with a supernova [Galama et al., 1998]. All these together consolidated the idea that long GRB progenitors are core collapse supernovae [Paczyński, 1998]. But short GRBs are fainter as well as theirs afterglows. Consequently the detection of such afterglows is more challenging. It was the turn of the Swift telescope [Gehrels et al., 2004] to overcome this difficulty. The detection of GRB 050509B and its X-ray afterglow [Gehrels et al., 2005] represented a breakthrough. Indeed the position measurement was accurate enough in order to infer an elliptical galaxy origin, which is another clue in the favor of compact binary mergers progenitors [Eichler et al., 1989; Nakar, 2007]. It should be noted that long GRBs associated with broad-line Type Ic supernovae are generally characteristic of star forming regions, being found in spiral galaxies.

Also theoretical work associated kilonovae to compact binary mergers [Metzger et al., 2010a; Lattimer and Schramm, 1974; Li and Paczynski, 1998]. And the association of a kilonova with GRB 130603B [Tanvir et al., 2013] strengthened this idea. To complete the picture scientists understood the necessity of the coincident detection of GWs and EM emission from compact binary mergers. Since the advent of the second generation GW interferometers, Advanced LIGO [Aasi et al., 2015b] and Advanced Virgo [Acernese et al., 2015], compact binary coalescences can be detected unambiguously [Abbott et al., 2019a, 2021a]. GW170817 is an exceptional binary neutron star merger event. For the first time, there was clear evidence for association between GW [Abbott et al., 2017e], short GRB 170817A [Goldstein et al., 2017; Savchenko et al., 2017], ultra-violet, optical and near infrared kilonova AT 2017gfo [Coulter et al., 2017; Smartt et al., 2017], and finally X-ray [Nynka et al., 2018; D´Avanzo, P. et al., 2018] and radio [Hallinan et al., 2017] afterglow. Since then, based on its similarity to AT 2017gfo, Troja et al. [2018] inferred a kilonova associated to GRB150101B [Fong et al., 2016].

Photons highly interact with the surrounding medium, being precious witnesses of the behaviour of matter in extreme environments [Zhang and Meszaros, 2004; Meszaros, 2006; Piran, 2005; Nakar, 2007; Fan and Piran, 2008; Daigne, 2021; Zhang, 2014; Kumar and Zhang, 2014; Berger, 2014; Meszaros et al., 1993]. The GRB afterglows provide information concerning the matter existing in between the EM source and the Earth observer. Thus they might validate theories about the massive stars' birth place, as well as the features of galaxies hosting them [Akerlof et al., 1999; Castro-Tirado, A. J. et al., 2010; Christensen et al., 2004; Frail et al., 2002; Jakobsson et al., 2006; Hjorth et al., 2003]. Finally the kilonova offers indications regarding the equation of state of ultra-dense matter, the composition of the ejected material or the velocity of the expelled matter [Bauswein et al., 2013a; Piran et al., 2013; Bauswein et al., 2017; Dietrich and

Ujevic, 2017; Radice et al., 2018b; Abbott et al., 2018a]. Additionally, multimessenger astronomy brings new opportunities. GWs and EM radiation together might be used to address questions related to the speed of gravitons [Abbott et al., 2017d; Green et al., 2018], the measurement of the Hubble constant [Abbott et al., 2017a; Hotokezaka et al., 2019; Coughlin et al., 2020b], the nucleosynthesis of elements in the Universe [Watson et al., 2019; Drout et al., 2017; Pian et al., 2017; Kasen et al., 2017], and alternative gravity theories [Jana and Mohanty, 2019; Langlois et al., 2018; Bahamonde et al., 2020; Sakstein and Jain, 2017; Nojiri and Odintsov, 2018]. According to Burns [2020], with the actual γ-ray observatories, at the moment when the already existing GW interferometers reach the design sensitivity, one should expect more than 0.8–4.4 joint GW-GRB detections per year. Equally, joint detections of GW and associated kilonovae are possible, but the rate of such events strongly depend on the quality of the EM follow-up done by the terrestrial telescopes [Mochkovitch et al., 2021].

1.3.1 GRB prompt and afterglow emission

Since the detections of the first GRBs by the Vela satellite [Klebesadel et al., 1973], much controversy has occurred in attempting to explain the origin and the mechanism of these cataclysmic events. While the progenitors are not the same for all GRBs, the radiation production mechanism is common. Moreover, the physical mechanism powering the wide wavelength emission is equally at the origin of the EM radiation coming to us from other high energy astrophysical phenomena: supermassive black holes at the centers of active galaxies like quasars and radio galaxies [Punsly, 2015; Taylor et al., 2009], cataclysmic variable stars [Shahbaz et al., 1997], X-ray binaries [Fender, 2001], or post-asymptotic giant branch stars [Pérez-Sánchez et al., 2013]. The physical process consists of a relativistic jet fed by an accretion disc.

In Figure 1.7, a diagram of the relativistic jet stemming from the new born black hole, and powered by the accretion disc, is provided. The compactness of the engine is necessary to explain the short-time scale variability. Nevertheless, the black hole engine does not emit energy far away, directly in the form of high energy photons. This is impossible as was noted a few decades ago [Ruderman, 1975; Schmidt, 1978]. Indeed an emitter area possessing a size similar to that of the remnant diameter would imply a too high density of high energy photons. In such a case, the electron-positron pair production reaction $\gamma\gamma \rightarrow e^+e^-$ will be very efficient, rendering the outflow optically thick, i.e. opaque for the gamma rays [Guilbert et al., 1983; Carrigan and Katz, 1992]. Therefore, if the radiation reaching us is the same as the radiation trapped in this initial opaque medium, it will undergo thermalization. Although, the spectra of the detected GRBs have not blackbody shape [Ghirlanda et al., 2004; de Ugarte Postigo et al., 2012], proving that the radiation is produced in a optically thin region. In addition, during this early

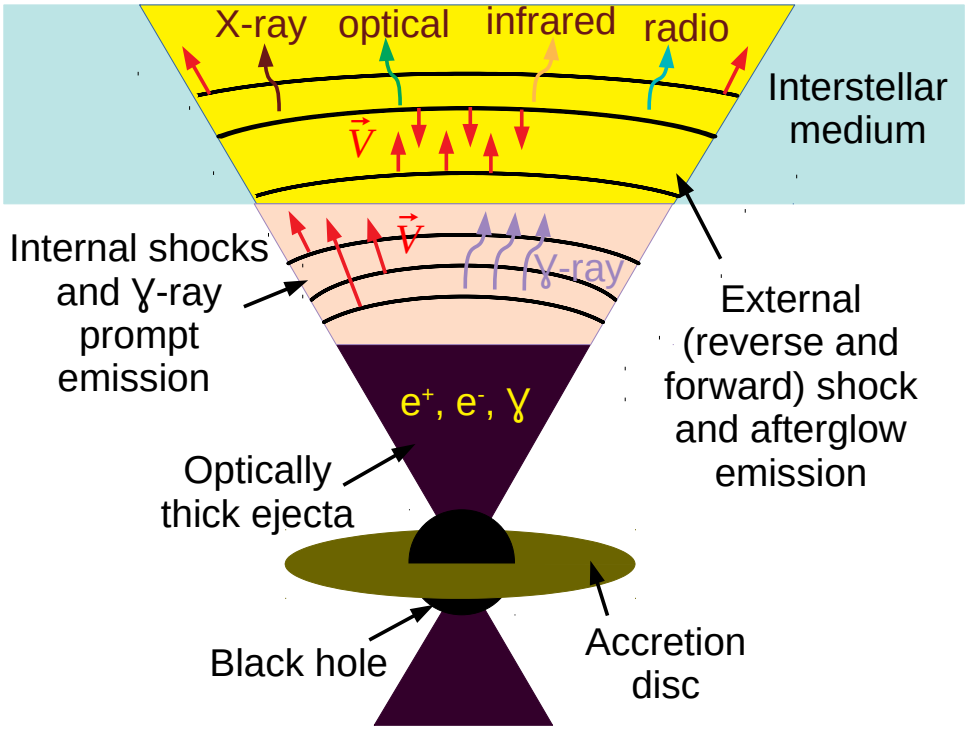

Fig. 1.7 Fireball model in which a relativistic jet is powered by the accretion disc surrounding the new born black hole. The optically thick inner part of the jet represents a soup of electrons, positrons and γ-rays. Sufficiently far away from the black hole engine, the density is low enough such that the medium becomes optically thin. In this region, matter blast waves travelling at different speeds collide with each other giving birth to a burst of high energy photons, which is the prompt γ-ray emission our space observatories detect. Further still, the shock waves interact with the interstellar medium, giving rise to forward and reverse shocks. The interaction between the blast waves and the interstellar medium is responsible for longer wavelength radiation (X-ray, optical, infrared, radio), known as the afterglow.

phase of the jet the energy becomes baryon loaded based high Lorentz factor [Mirabel and Rodriguez, 1997] kinetic energy (there have been proposed versions in which the energy is carried by Poynting flux [Thompson, 1994; Usov, 1994; Smolsky and Usov, 1996; Katz, 1997]), while an Earth observer receives EM radiation energy. This apparent problem is solved by the fireball model [Paczynski, 1986; Goodman, 1986; Shemi and Piran, 1990; Paczynski, 1990]. The conversion of the kinetic energy into EM energy is realized through shocks. There are two types of shocks: internal and external. The internal shocks are due to baryons flying with different Lorentz factors. Within this picture, two matter waves are released by the central engine at two distinct times. If the wave starting the along jet journey lastly has a higher velocity, after a period of time, it will overtake the other wave, thus generating a collision [Rees and Mészáros, 1992; Rees and Meszaros, 1994; Meszaros and Rees, 1993; Sari and Piran, 1995]. This mechanism is responsible for the prompt γ-ray emission. More precisely, supported by the presence of the magnetic fields, the radiation processes that are most probably at play are synchrotron emission and inverse Compton scattering [Meszaros et al., 1993; Katz, 1994; Sari et al., 1996; Rybicki and Lightman, 1979; Schaefer et al., 1998], even if there is no absolute understanding of the GRB spectrum [Band et al., 1993]. The longer wavelength photons, forming the afterglow, are created through the external shock, the deceleration of the blast wave by the interstellar medium [Paczynski and Rhoads, 1993; Meszaros and Rees, 1997; Wijers et al., 1997; Waxman, 1997b,a; Meszaros et al., 1998]. As emphasized in Figure 1.7, the external shock might comprise two components: a long-lived forward- and a short-lived reverse-shock. The two components could be distinguished by an analysis of the well-sampled GRB lightcurves [Lamb, 2020; Gao and Mészáros, 2015].

When a short or long GRB occurs, the system loses rotational energy, by the fall of matter from the accretion disc into the newly formed black hole. This process powers two opposite relativistic jets, perpendicular to the accretion disc. The subsequent shock wave internal collisions lead to the production of high energy photons, which propagate far away through space. On the other hand, the Earth space observatories are equipped with high energy photon counters, which detect the incoming radiation. The γ-ray prompt emission, in the Earth observer frame, might last from milliseconds to thousands of seconds. If T_{90} defines the time interval whose extremities correspond to 5% and 95% of the total fluence, one can remark that two categories of GRBs arise: short with $T_{90} < 2\,\mathrm{s}$ and long with $T_{90} > 2\,\mathrm{s}$ [Bromberg et al., 2013]. More specifically, in Figure 1.8 appears the T_{90} distribution, according to the third Fermi-GBM GRB catalog [Bhat et al., 2016b]. One can easily remark that the detection frequency is higher for longer duration bursts. Although Figure 1.8 suggests the existence of two duration GRB components (short and long), the discrimination seems to be less than

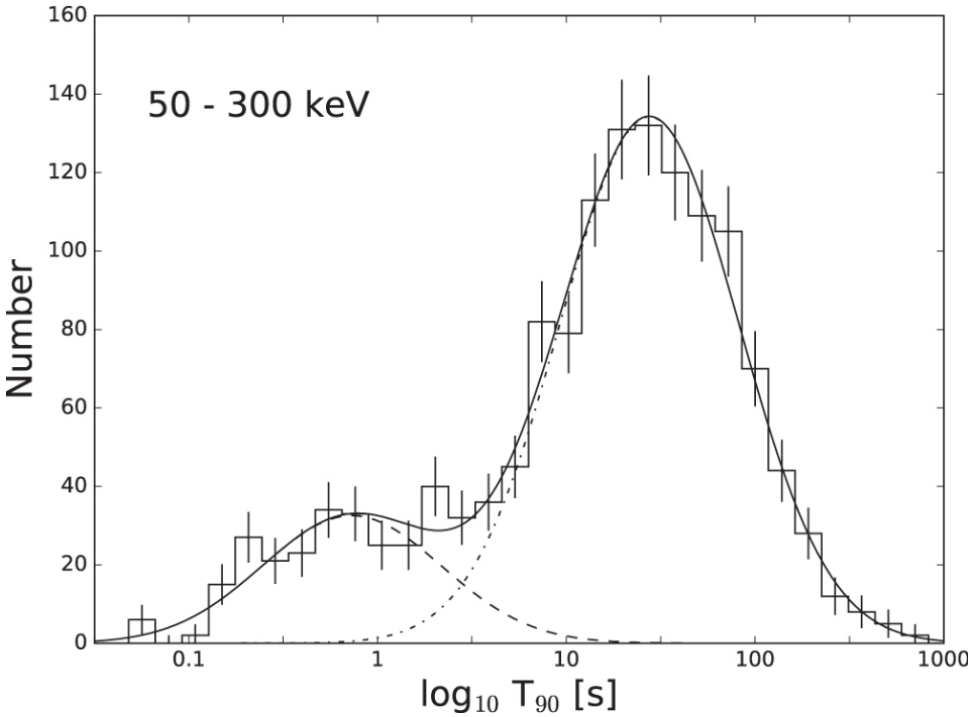

Fig. 1.8 From Bhat et al. [2016b], the histogram of GRBs, as a function of $\log_{10} T_{90}$. The duration T_{90} is calculated in the $50-300\,\mathrm{keV}$ energy range. The samples used here are the 1405 triggers included in the third Fermi-GBM GRB catalog.

obvious. Moreover, it is worth mentioning that the measured duration of a burst might be insufficient to correctly assign its progenitor system. Indeed, a long GRB, viewed off-axis, might look like a short burst for an external observer [Rossi et al., 2021]. The spectra of GRBs are non-thermal (or have a non-thermal components [Kawakubo et al., 2018]) and traditionally are fitted by Band functions of type

$$\frac{dN}{dE} \propto \begin{cases} \left(\frac{E}{100\mathrm{keV}}\right)^{\alpha_{\mathrm{spec}}} e^{-\frac{(\alpha_{\mathrm{spec}}+2)E}{E_{\mathrm{peak}}}} & \text{if } E \leq \frac{\alpha-\beta}{\alpha+2} E_{\mathrm{peak}} \\ \left(\frac{E}{100\mathrm{keV}}\right)^{\beta_{\mathrm{spec}}} \left[\frac{E_{\mathrm{peak}}}{100\mathrm{keV}} \frac{(\alpha_{\mathrm{spec}}-\beta_{\mathrm{spec}})}{(\alpha_{\mathrm{spec}}+2)}\right]^{(\alpha_{\mathrm{spec}}-\beta_{\mathrm{spec}})} e^{(\beta_{\mathrm{spec}}-\alpha_{spec})} & \text{otherwise} \end{cases}, \tag{1.16}$$

where α_{spec} and β_{spec} are two fitting coefficients , while E_{peak} is the peak energy. According to Ghirlanda et al. [2009], E_{peak} is generally around $500\,\mathrm{keV}$ (respectively $350\,\mathrm{keV}$) for short (respectively for long) GRBs, which is a proof of the fact that the shorter bursts are spectrally harder. This dichotomy between short-hard and long-soft GRBs is also emphasized by Figure 1.9. One can easily see that the shorter (longer) duration GRBs have higher (smaller) hardness ratios. Another observable accessible by means of the high energy detector measurements is the bolometric fluence, defined as

$$S_{\mathrm{bolo}} = T_{90} \int EN(E)dE. \tag{1.17}$$

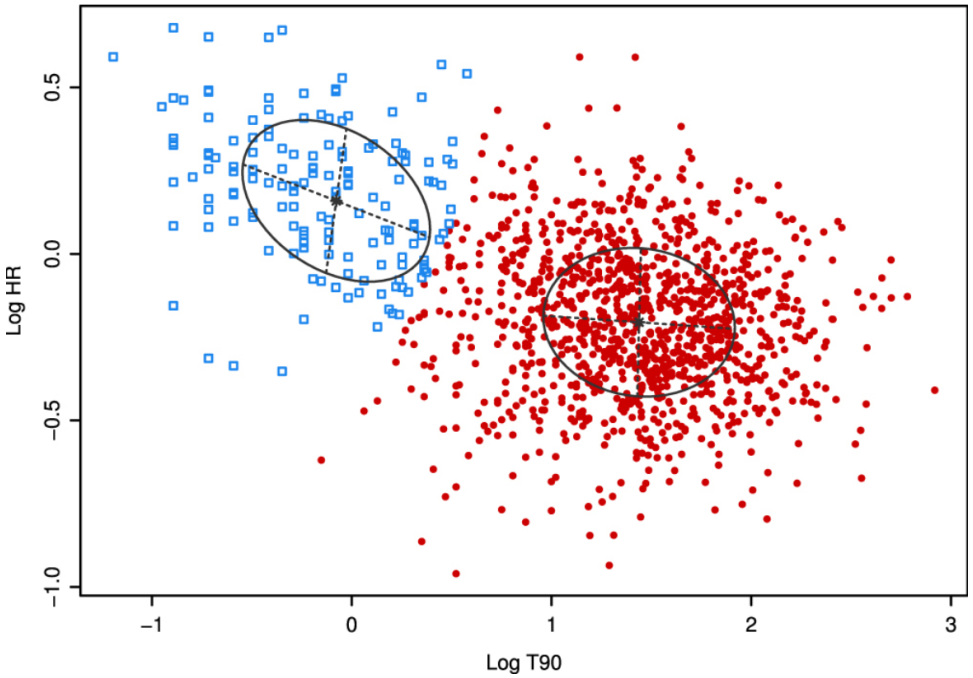

Fig. 1.9 From Bhat et al. [2016b], the logarithm of the hardness ratio versus the logarithm of T_{90}. The hardness ratio is defined as the burst fluence in the $50-300\,\mathrm{keV}$ over the fluence in $10-50\,\mathrm{keV}$ energy band. The two fluences are calculated during T_{90}. The sample includes 1376 GRBs from the third Fermi-GBM GRB catalog.

The order of magnitude of the bolometric fluence is a few tens of $\mathrm{erg/cm^2}$ [Dirirsa et al., 2019]. If in addition, the host galaxy is identified and/or the redshift z is derived [Le and Mehta, 2017], using the afterglow radiation, a luminosity distance d_L might be calculated. In order to do this, a cosmology needs to be assumed. For example, in the approximation of a flat ΛCDM cosmology, with matter and dark energy densities Ω_m and Ω_Λ, respecting the relation $\Omega_m = 1-\Omega_\Lambda$, the distance luminosity can be expressed as

$$d_L = (1+z)\frac{c}{H_0}\int_0^z \frac{dz'}{\sqrt{(1-\Omega_\Lambda)(1+z')^3+\Omega_\Lambda}}, \tag{1.18}$$

c and H_0 being here the light speed and the Hubble constant. If the redshift is measured, one might derive the isotropic radiated energy E_{iso} and the isotropic luminosity L_{iso} defined by

$$E_{\mathrm{iso}} = \frac{4\pi d_L^2}{1+z} S_{\mathrm{bolo}} \qquad \text{and} \qquad L_{\mathrm{iso}} = \frac{(1+z)E_{\mathrm{iso}}}{T_{90}}. \tag{1.19}$$

Tsvetkova et al. [2021] show, by studying a large sample of GRBs, that the isotropic luminosity and isotropic energy range from $\sim 2\times10^{48}\,\mathrm{erg/s}$ to $\sim 5\times10^{54}\,\mathrm{erg/s}$, respectively from $\sim 3\times10^{49}\,\mathrm{erg}$ to $\sim 6\times10^{54}\,\mathrm{erg}$. Also, in Figure 1.10 are the distributions of E_{iso}, L_{iso} as well as of the redshift for a sample of GRBs [Abbott et al., 2017c]. From Figure 1.10, one can conclude that long GRBs are more energetic and are situated at higher distances. Concerning the isotropic luminosity, even if the higher values are

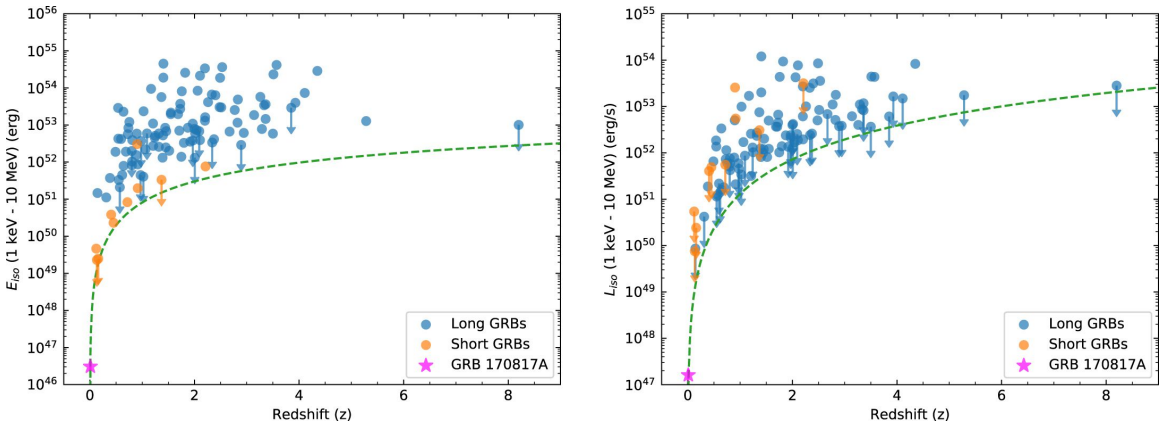

Fig. 1.10 From Abbott et al. [2017c]. On left (respectively right), E_{iso} (respectively L_{iso}) versus redshift, for short and long GRBs. In both panels, the green dashed curve represents the redshift dependence of the Fermi-GBM detection threshold.

generally assigned to long GRBs, the discrepancy is less obvious. One should also note, based on Figure 1.10, the peculiarity of GRB 170817A, which is much less energetic that the majority of the other observed GRBs. It is believed that this is due to the fact that, from the Earth, the GRB 170817A jet was viewed off-axis [Granot et al., 2018]. However, one should note that GRBs are not isotropic. More precisely, if one notes by $\theta_{\rm jet}$, the opening angle of the relativistic jets, then the relation between the real emitted energy $E_{\rm GRB}$ and the isotropic energy is

$$E_{\rm GRB} \approx \theta_{\rm jet}^2 E_{\rm iso}. \tag{1.20}$$

In Figure 1.11, there is the lightcurve of GRB 170817A, showing the counts reported by half of the Fermi-GBM NaI detectors, at energies going from 50 to 294 keV.

The GRB afterglow consists in photons emitted over the entire EM spectrum. Following Sari et al. [1999], I present here a few characteristics of this type of EM transient. The afterglow is not isotropic, but it might be observed if the GRB relativistic jet is oriented towards the Earth. Indeed for a jet with angular width $\theta_{\rm jet}$, as long as the Lorentz factor $\Gamma \gg \theta_{\rm jet}^{-1}$, the entire emission will be included in a cone with opening angle equal to Γ^{-1}. But as long as the fireball expands, the Lorentz factor decreases, following the law

$$\Gamma(t) = 6 \left(\frac{E_{\rm iso}}{10^{52}{\rm erg}} \cdot \frac{1{\rm cm}^{-3}}{n_{\rm ISM}} \right)^{\frac{1}{8}} \left(\frac{t}{1{\rm day}} \right)^{-\frac{3}{8}}, \tag{1.21}$$

where $E_{\rm iso}$ and $n_{\rm ISM}$ are the ejecta isotropic energy and particle density of the surrounding interstellar medium. When the Lorentz factor goes below $\theta_{\rm jet}^{-1}$, the material spreads sideways, the afterglow being visible off-axis, if still bright enough. The dura-

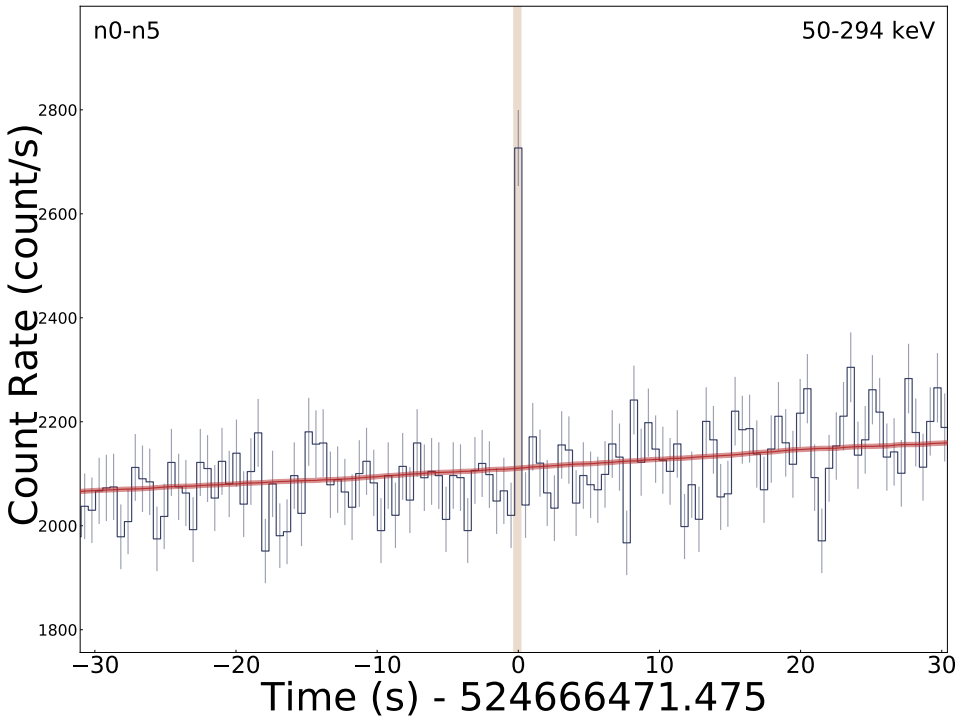

Fig. 1.11 The Fermi-GBM high energy lightcurve of GRB 170817A. In blue, the sum of counts reported by half of the NaI detectors, assigned with estimed error bars. In red, there is the estimated background photon rate. On the x axis, 0 corresponds to the mission ellapsed time MET = 524666471.475. The signal is found by the tool presented in Goldstein et al. [2019] on a timescale of $512\,\mathrm{ms}$, with a log likelihood ratio of 73.

tion needed to reach this second phase is estimated by the formula

$$\Delta t_{\rm trans} = 6.2\,{\rm hours} \times \left(\frac{E_{\rm iso}}{10^{52}{\rm erg}} \cdot \frac{1{\rm cm}^{-3}}{n_{\rm ISM}}\right)^{\frac{1}{3}} \left(\frac{\theta_{\rm jet}}{0.1{\rm rad}}\right)^{\frac{8}{3}}. \tag{1.22}$$

Moreover, the GRB spectra distributions present power laws, which most presumably are due to synchrotron radiation and inverse Compton scattering. In the observer frame, the typical frequency is expected to be $\nu_m^{\rm aft} \propto t^{-2}$, while the cooling frequency is constant over time ($\nu_c^{\rm aft} \propto t^0$). At late times (after a few hours), one has $\nu_c^{\rm aft} \gg \nu_m^{\rm aft}$. Finally, the flux per unit frequency, at a given time, has the expression

$$F(\nu|t) \propto \begin{cases} \nu^{-0.7} & \text{for } \nu \leq \nu_c^{\rm aft} \\ \nu^{-1.2} & \text{otherwise} \end{cases}, \tag{1.23}$$

while the flux per unit time, at a given frequency, i.e. the lightcurve, has the following power law

$$F(t|\nu) \propto t^{-2.4}. \tag{1.24}$$

1.3.2 Kilonova

Another EM counterpart to compact binary mergers, predicted a few decades ago, is the kilonova [Lattimer and Schramm, 1974, 1976; Lattimer et al., 1977; Symbalisty and Schramm, 1982; Eichler et al., 1989; Meyer, 1989; Davies et al., 1994]. This is due to the synthesis of heavy elements through r-process neutron capture. Subsequently, the newly formed high atomic number chemical elements radioactively disintegrate. Recently more and more nucleosynthesis arguments have been provided to support the idea that compact binary coalescences might be the principal site production of the heaviest elements in the Universe, putting aside the initial idea according to which these r-process chemical elements should mainly be created during supernovae [Freiburghaus et al., 1999; Rosswog et al., 1999; Oechslin et al., 2007; Metzger et al., 2010b; Roberts et al., 2011; Goriely et al., 2011b,c; Korobkin et al., 2012; Bauswein et al., 2013b]. The most believable structure of a kilonova is pictured in Figure 1.12. There are two principal components: the dynamical ejecta and the disc winds [Fernández et al., 2015]. The dynamical ejecta represents the matter which, during the merger, becomes unbound due to gravitational torques and hydrodynamic processes [Rosswog et al., 1999; Metzger et al., 2010a; Roberts et al., 2011; Rosswog, 2013; Barnes and Kasen, 2013; Tanaka and Hotokezaka, 2013; Hotokezaka et al., 2013; Bauswein et al., 2013b; Sekiguchi et al., 2016; Radice et al., 2016; Dietrich et al., 2017; Dietrich and Ujevic, 2017; Bovard et al., 2017]. But also the gravitationally bound matter forming the accretion disc is responsible for the EM radiation. Indeed physical processes such as neutrino cooling, angular momentum transport and nuclear recombination, generate emission, known in

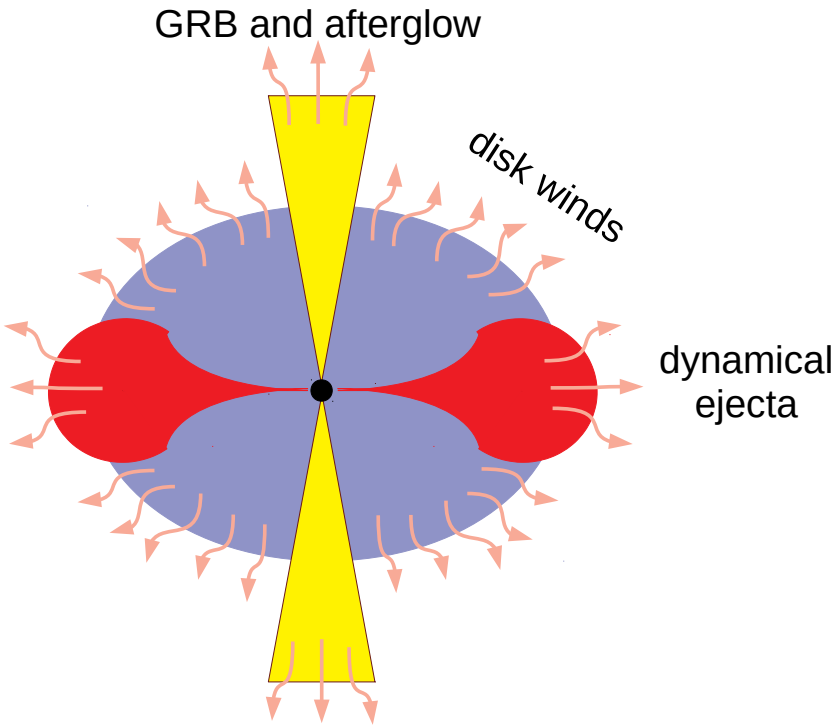

Fig. 1.12 Kilonova containing two components: near the equator (in red), the dynamical ejecta and, at higher latitudes (in blue), the disc winds. The black hole appears in black, while the GRB relativistic jets are depicted in yellow.

the literature as disc wind [McLaughlin and Surman, 2005; Surman et al., 2008, 2006; Dessart et al., 2009; Wanajo and Janka, 2012; Metzger and Fernández, 2014; Perego et al., 2014; Metzger et al., 2009; Lee et al., 2009; Fernández and Metzger, 2013; Metzger and Fernández, 2014; Just et al., 2015; Fernández et al., 2014]. Concerning the spatial position, the dynamical ejecta is found at lower latitudes, while the disc winds are closer to the poles. Additionally, the photometric lightcurve kilonova is supposed to be formed from a blue (ultra-violet and optical) component due to the lanthanide free material in the composition of disc winds, and a red (optical and infrared) component due to the more neutron-rich dynamical ejecta.

During the merger process, once the outflow is sufficiently expanded, and so the matter density as well as the optical depth are sufficiently low, in order for the light to escape, the spectrum is thermalized. The key parameters determining the lightcurve of a kilonova are: the amount of ejected mass $m_{\rm ej}$, the velocity of the ejecta $v_{\rm ej}$ and the chemical composition of the ejecta which determines the light opacity $\kappa_{\rm KN}$. Following Kasen et al. [2017], which makes use of numerical resolution of the Boltzmann equation for relativistic radiation transport in a radioactive plasma, the timescale of the kilonova might be expressed

$$t_{\rm KN} \approx 2.7{\rm days} \times \left(\frac{m_{\rm ej}}{0.01 M_\odot}\right)^{\frac{1}{2}} \left(\frac{v_{\rm ej}}{0.01c}\right)^{\frac{-1}{2}} \left(\frac{\kappa_{\rm KN}}{1{\rm cm}^2{\rm g}^{-1}}\right)^{\frac{1}{2}}, \tag{1.25}$$

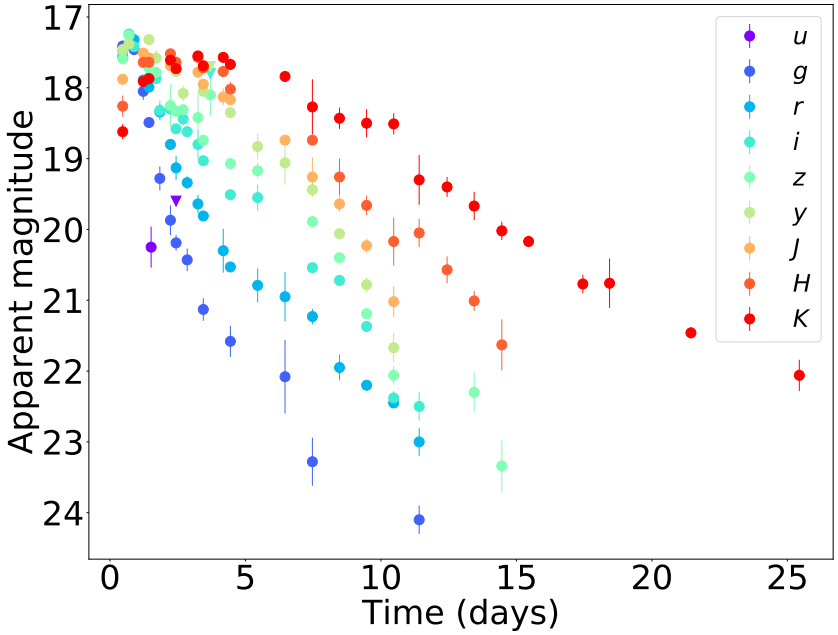

Fig. 1.13 Apparent magnitude versus time for AT 2017gfo. The photometric filters used here are u, g, r, i, z, y, J, H and K. The circles represent observations with finite error bars, while the triangles stand for upper limits.

while the characteristic luminosity has the following form

$$L_{\rm KN} \approx 5 \times 10^{40} {\rm ergs}^{-1} \times \left(\frac{m_{\rm ej}}{0.01 M_\odot} \right)^{1-\frac{\alpha_{\rm KN}}{2}} \left(\frac{v_{\rm ej}}{0.1c} \right)^{\frac{\alpha_{\rm KN}}{2}} \left(\frac{\kappa_{\rm KN}}{1 {\rm cm}^2 {\rm g}^{-1}} \right)^{-\frac{\alpha_{\rm KN}}{2}} . \quad (1.26)$$

In those two previous equations, $M_\odot$ and c designate the solar mass and the light speed, while $\alpha_{\rm KN} = 1.3$ is a constant. Based on these two formulas, one can conclude that the higher the amount of the expelled neutron-rich material, the brighter and longer-lasting is the kilonova. Similarly, the higher the velocity, the higher the brightness and the shorter the duration of the EM counterpart. Finally, the heavier the composition of the ejecta, the higher the light opacity, which in turns will imply a longer and dimmer transient, causing the reddening of the corresponding lightcurve. The observational points of AT 2017gfo are illustrated in Figure 1.13. One can easily remark that the maximum of emission takes place at around 1 day after the merger. Also, it is clearly highlighted that the longer wavelength radiations (due to higher opacities) decay on longer timescales.

It is worth mentioning that sometimes, in the case of binary compact coalescences, it is difficult to decide, based on uniquely photometric observations, if the measured radiation corresponds to only the kilonova, only the short GRB afterglow or the superposition of two EM transients [Ascenzi et al., 2019]. But in some cases the discrimination

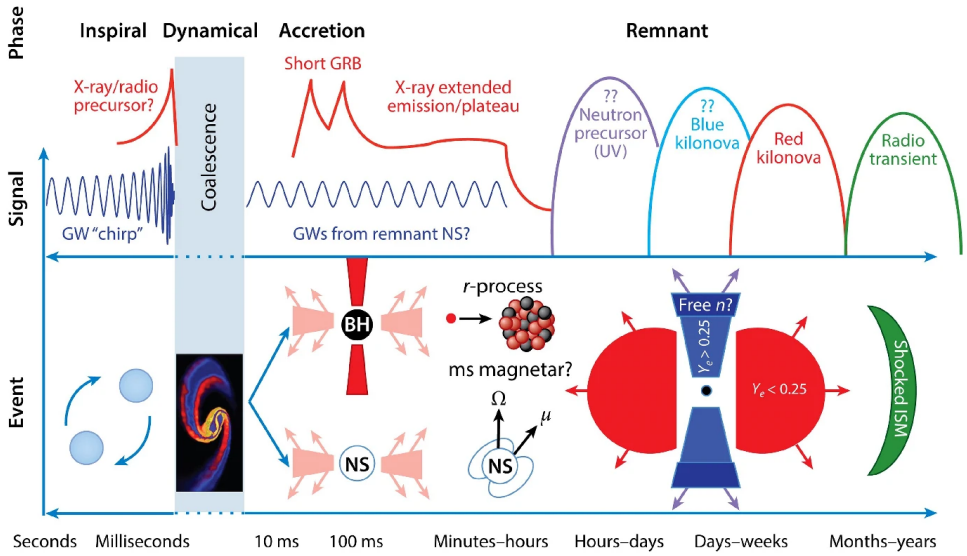

Fig. 1.14 GW and EM signals expected during the merger of a binary neutron star: a powerful release of GWs in seconds prior to the merger; the GRB prompt emission radiation is expected to be at most a few seconds away with respect to the coalescence time; the kilonova radiation occurs during the hours, days and even weeks after the merger; the GRB afterglow starts with X-ray photons in the hours following the merger, continues on the optical range in the days/weeks after the fusion of the two neutron star, and is expected to still be visible in the radio spectrum in the months/years following the cataclysmic event. Figure taken from Burns [2020].

is possible. For example Gompertz et al. [2018] show that the longer wavelength counterpart to short GRB 140903A is too bright to account for a kilonova. As an example, the photon flux in the i-band is almost 15 times higher than the corresponding kilonova fluence expectation.

A sketch of the different multimessenger signals, that are expected in the case of a compact binary neutron stars merger, is presented in Figure 1.14.

1.4 Detectors

1.4.1 GW interferometers

It was shown in the section 1.2 that a passing GW stretches and elongates the distance separation between freely falling points. Scientists tried to put into evidence such effects. A first attempt was done in the 1960s by Joseph Weber (see Figure 1.15) who tried to detect the fundamental mode excitation of an aluminium cylinder [Weber, 1960]. This excitation is due to the restoring force acting as a response to the elongation/stretching effect of the GW passing through it. Weber even claimed the detection of GWs [Weber, 1968], but we know today that his experimental setup was not sensitive enough for such observations.

The first device which turned out to be appropriate for the measurement of such

Fig. 1.15 Joseph Weber and its aluminium bar detector.

small displacements is the large arm interferometer. In Figure 1.16 there is a scheme of such an experimental setup. A monochromatic EM source (in our case a laser) is incident on a beam splitter. Some part of the initial radiation is reflected, some other part is transmitted, and for real case one should consider energetic losses which consists in light absorption. Unless clearly specified, hereafter I will consider no energy dissipation. Afterwards, the reflected and transmitted wave packets travel along separate trajectories, reflect on end arm mirrors and return back to the beam splitter. Once the wave packets arrive at the beam splitter, interference phenomena occur. Thus, depending on the interferometer arm length difference, the phase difference might account for a more or less pronounced constructive or destructive interference. The interference pattern is put into evidence by a photodetector measuring incoming light power. Following Maggiore [2007], I present here the way a GW interacts with a ground-based interferometer and the measurement principle. Thus I consider ω_{laser}, $k_{\text{laser}} = \frac{\omega_{\text{laser}}}{c}$ and $\lambda_{\text{laser}} = \frac{2\pi}{k_{\text{laser}}}$ the angular frequency, the wavenumber and the wavelength respectively of the laser. Thus, for some wave packet emitted at some time t, and having traveled over some distance $\vec{x}$, the electric field can be expressed as $E_0 e^{-i\omega_{\text{laser}}t + i\vec{k}_{\text{laser}}\cdot\vec{x}}$, where E_0 is the amplitude of plane wave. In addition, L_x and L_y designate the lengths of the interferometers arms in the x and respectively y direction. I also note by ω_{GW} the angular frequency of the GW signal. Therefore the two light components interfering at the beam splitter, after a round trip in the arms of the interferomenters, are $E_x = -\frac{1}{2}E_0 e^{i\omega_{\text{laser}}t + 2ik_{\text{laser}}L_x}$ and $E_y = \frac{1}{2}E_0^{-i\omega_{\text{laser}}t + 2ik_{\text{laser}}L_y}$, while the electric field at the output of the beam splitter, after the interference, is $E_{\text{out}} = E_1 + E_2$. The power measured by the photodetector is proportional to the square of the electric field, which can be put under the form

$$|E_{\text{out}}|^2 = E_0^2 \sin^2 [k_{\text{laser}}(L_y - L_x)]. \tag{1.27}$$

The preceding formula shows that the output power depends on the arm length difference. Thus one may intuitively anticipate that the passage of a GW will have a similar effect on the output measurement. For illustrative purposes, I consider in the tranverse

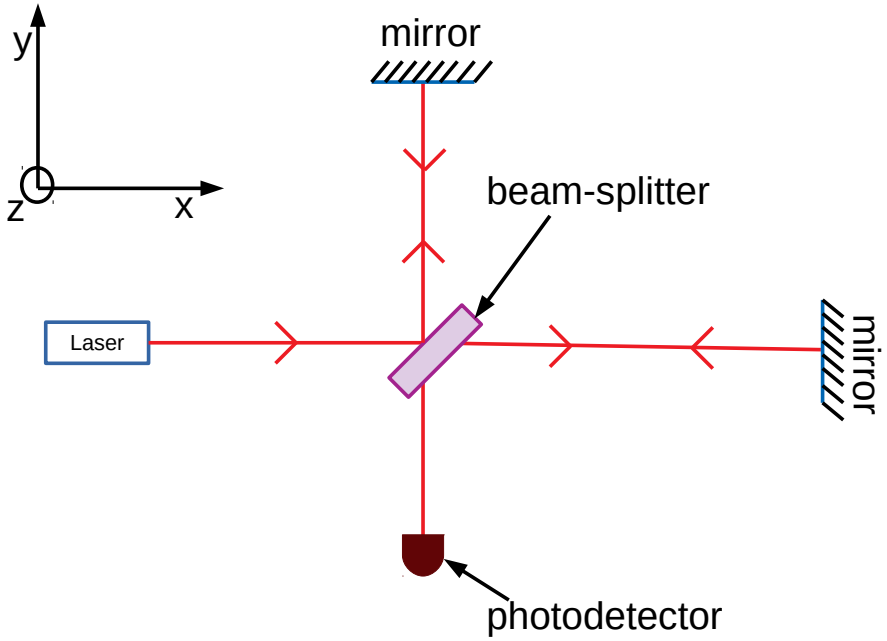

Fig. 1.16 Michelson interferometer consisting of: a laser providing monochromatic radiation; a beam splitter separating the initial wave packet into a reflected part and a transmitted part; two end arm mirrors situated far away from the beam splitter, on which reflect the two spatially separated light components; a photodetector measuring the power of the interference radiation output.

traceless gauge, a GW propagating in the z direction with the $\oplus$ polarization. The time dependent strain thus can be written $h_+(t) = h_0 \cos(\omega_{\rm GW} t)$, with h_0 the maximum amplitude. After calculations of the photon geodesic paths, one arrives at the conclusion that the wave packets interfering at the beam splitter at time t, should start their round trip journeys at times

$$t_0^{(x)} = t - \frac{2L_x}{c} - \frac{L_x}{c} h(t - L_x/c) \text{sinc}(\omega_{\rm GW} L_x/c), \tag{1.28}$$

$$t_0^{(y)} = t - \frac{2L_y}{c} - \frac{L_y}{c} h(t - L_y/c) \text{sinc}(\omega_{\rm GW} L_y/c), \tag{1.29}$$

where $\text{sinc}(\zeta) = \frac{\sin\zeta}{\zeta}$. And the power measured by the photodetector is proportional to

$$1 - \cos\left[2\phi_0 + \Delta\phi_{\rm Mich}(t)\right], \tag{1.30}$$

where ϕ_0 is the phase of the chosen working point and $\Delta\phi_{\rm Mich}$ is the total phase induced by the GWs and which, under the approximation $L_x \approx L_y$, has the following expression

$$\Delta\phi_{\rm Mich} = 2h_0 k_{\rm laser} \frac{L_x + L_y}{2} \text{sinc}\left(\omega_{\rm GW} \frac{L_x + L_y}{2c}\right) \cos\left[\omega_{\rm GW}\left(t - \frac{L_x + L_y}{2}\right)\right]. \tag{1.31}$$

In the preceding expression, one can remark the appearance of the term $x \mapsto x\text{sinc}(\omega_{\rm GW} x/c) = \frac{c}{\omega_{\rm GW}} \sin(\omega_{\rm GW} x/c)$. Thus for an optimal sensitivity one needs $L_x, L_y \approx \frac{\pi c}{2\omega_{\rm GW}} = 750\,\text{km}\left(\frac{100\,\text{Hz}}{f_{\rm GW}}\right)$, with $f_{\rm GW}$ the frequency of the GWs. In conclusion, in order to detect compact binary mergers radiating GWs with frequencies ranging from tens to a few thousands Hz one needs an interferometers with arm lengths of the order of hundreds of kilometers, which is of course impossible for both financial and technical reasons. In order to handle this issue, scientists made use of Fabry-Perot cavities. Such an optical cavity is made of two parallel mirrors. Inside it, at resonance, the light is doing lots of round trips, increasing thus the optical path length without the necessity of a too spatial wide experimental setup. A scheme of the Fabry-Perot cavity is offered in Figure 1.17. As in Figure 1.17, I consider a right moving incoming field $\vec{E}_{\rm inc}(t,x)$ which gives birth to a left moving reflected field $\vec{E}_{\rm ref}(t,x)$ and a right moving transmitted field $\vec{E}_{\rm trans}(t,x)$, as well as two cavity trapped plane waves $\vec{E}_{\rm cav}^{\rm right}(t,x)$ and $\vec{E}_{\rm cav}^{\rm left}(t,x)$ propagating in opposite directions. As in Maggiore [2007], I consider (r_1, t_1, p_1) (respectively $(-r_1, t_1, p_1)$) the reflection, transmission and energy loss coefficients for a right (respectively left) moving wave incident on the first mirror. The coefficients respect the relation $r_1^2 + t_1^2 = 1 - p_1$. For the second mirror I consider similar coefficients, by replacing index 1 with index 2. The resulting fields are obtained by summing up the corresponding wave packets having done different number of round trips inside the

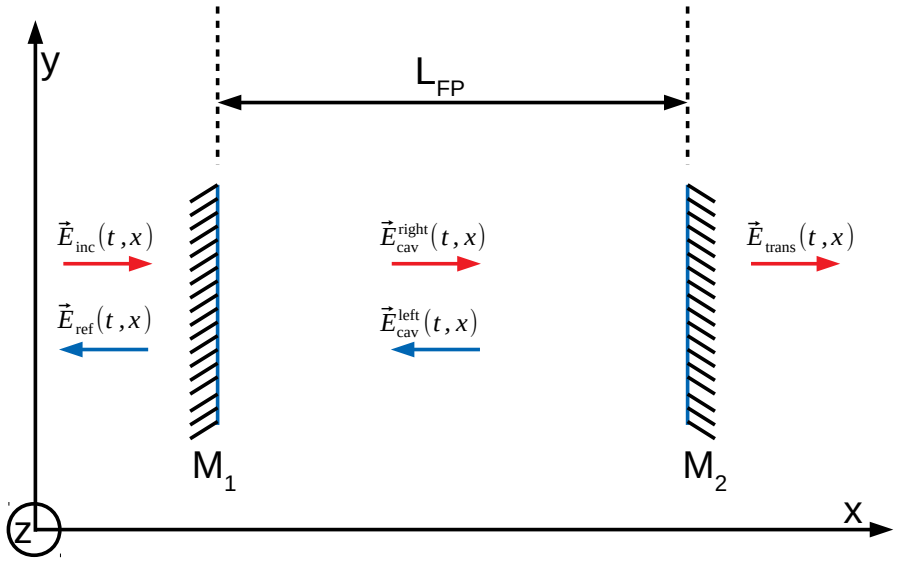

Fig. 1.17 Fabry-Perot cavity containing two optical mirrors M_1 and M_2 separated by a distance L_{FP}. Outside the cavity, there is an incident signal $\vec{E}_{\mathrm{inc}}(t,x)$, partly reflected into $\vec{E}_{\mathrm{ref}}(t,\vec{x})$ and partly transmitted as $\vec{E}_{\mathrm{trans}}(t,x)$. Inside the cavity, two plane waves, $\vec{E}^{\mathrm{right}}_{\mathrm{cav}}(t,x)$ and $\vec{E}^{\mathrm{left}}_{\mathrm{cav}}(t,x)$, propagate in opposite directions.

cavity. Thus the reflected field evaluated at the origin of the x axis is

$$E_{\mathrm{ref}}(t,x=0) = E_0 e^{-i\omega_{\mathrm{laser}}t} \cdot \frac{r_1 - r_2(1-p_1)e^{2ik_{\mathrm{laser}}L_{\mathrm{FP}}}}{1 - r_1 r_2 e^{2ik_{\mathrm{laser}}L_{\mathrm{FP}}}}. \tag{1.32}$$

For high reflective mirrors ($r_1, r_2 \approx 1$), there are resonances for L_{FP} being an integer of π/k_{laser}. Also if I define the finesse of the cavity by $\mathcal{F} = \frac{\pi\sqrt{r_1 r_2}}{1-r_1 r_2}$ and the phase of the reflective field ϕ_{ref} by $E_{\mathrm{ref}}(t,x) = |E_{\mathrm{ref}}|e^{-\omega_{\mathrm{laser}}t}e^{i\phi_{\mathrm{ref}}}$, then one has

$$\frac{\partial\phi_{\mathrm{ref}}}{\partial\epsilon} \approx \frac{2\mathcal{F}}{\pi}, \tag{1.33}$$

where $\epsilon/(2k_{\mathrm{laser}})$ is a small deviation of the resonant chosen value L_{FP}. So the finesse is the quantity characterizing the displacement measurement sensitivity of the Fabry-Perot quantity when the setup is fixed near the resonance. Indeed if I consider again the only $\oplus$ polarization GW strain $h_+(t) = h_0 \cos(\omega_{\mathrm{GW}}t)$, as long as the the length of the interferometer is small compared to the GW wavelength (i.e. $\frac{(L_x+L_y)f_{\mathrm{GW}}}{2c} \ll 1$), the phase shift induced by the passage of the GW on the Fabry-Perot based experimental

setup, can be written as

$$\Delta\phi_{\mathrm{FP}}(t) = h_0 \frac{4\mathcal{F}}{\pi} k_{\mathrm{laser}} \frac{L_x + L_y}{2} \mathrm{sinc}\left(\omega_{\mathrm{GW}} \frac{L_x + L_y}{2c}\right) \frac{1}{\sqrt{1 + (f_{\mathrm{GW}}/f_p)^2}} \cos\left(\omega_{\mathrm{GW}} t\right), \tag{1.34}$$

where $f_p \approx \frac{c}{2\mathcal{F}(L_x+L_y)}$. $1/f_p$ is a quantity accounting for the time spent by the light in the cavity. One can easily remark that if the light spends too much time stored inside the Fabry-Perot cavity, a degradation of the sensitivity appears because, during the photons' travel time, the GW not only elongates or only stretches the optical path but does oscillate between the stretching and contracting. In contrary, if $f_{GW} \ll f_p$, the new value of the phase shift is, at first order, a factor $2\mathcal{F}/\pi$ higher than the previous value, i.e. $|\Delta\phi_{\mathrm{FP}}| \approx \frac{2\mathcal{F}}{\pi} |\Delta\phi_{\mathrm{Mich}}|$. In conclusion, an optimal experimental setup requires a cavity with a finesse in $\mathcal{O}(100)$.

Although the important features have been mentioned, a real GW interferometer is more complicated than even a Fabry-Perot cavity based Michelson interferometer. For example, up to now I considered that the laser output radiation is represented by plane waves. But this is obviously just an approximation, as the component perpendicular to the propagation direction of the EM signal has a finite extent. For this reason, the spatial distribution of the radiation can be expressed as a sum of transverse electromagnetic (TEM) modes, whose predominant component, named TEM_{00}, is Gaussian. As mentioned previously, for an optimal sensitivity, both Fabry-Perot cavities should be resonant. But different TEM_{ij} need different adjustments in order to be at resonance. This is why, in real GW interferometers, before entering the beam-splitter, the TEM_{ij} modes, with $i \neq 0$ or $j \neq 0$, are filtered out. This process is realized by means of an input mode cleaner [Araya et al., 1997; Romero-Rodríguez et al., 2021]. A similar apparatus, called output mode cleaner [Kumeta et al., 2015; Prijatelj et al., 2012], exists at the output of the beam-splitter, once the interference had taken place, in order to filter out the junk light from the GW signal before the EM radiation power is measured by the photodetector. Moreover, the best working points for the actual GW interferometers correspond to dark fringe settings [Maggiore, 2007]. But, when the interferometer is set on such a position, the first derivative of the photodetector measured power with respect to GW strain is zero. In order to handle this issue, the frequency of the laser is modulated in order to make appear frequency sidebands, in addition to the already existing ω_{laser}. This procedure is realized by means of an electro-optical modulator [Canuel et al., 2011; Quetschke, 2008]. Furthermore, given that the working point of the interferometer corresponds to a dark fringe position, it means that when there is no GW signal, the input laser light is not exiting the setup, but it is reflected back. In order to not lose this radiation, a power recycling mirror is positioned before the beam-splitter, whose role is to resend the photons towards the Fabry-Perot cavities. A sketch of a real

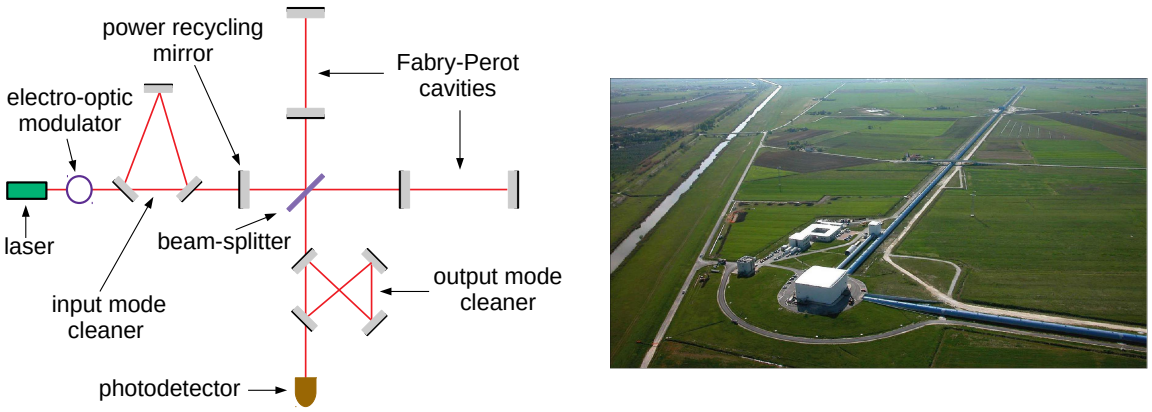

Fig. 1.18 On left, a scheme of a GW interferometer possessing: a laser emitting the monochromatic radiation with frequency $\omega_{\rm laser}$; an electro-optic modulator creating sidebands frequencies; an input mode cleaner and an output mode cleaner filtering out all the TEM modes except the gaussian component; a beam splitter; a Fabry-Perot cavity for each arm of the interferometer; a photodetector. On right, a real picture of the Virgo interferometer, located in Cascina, Italy.

GW interferometer, as well as a real image of the Virgo detector, are presented in Figure 1.18. Also the main parameters of the Advanced LIGO interferometers, at design sensitivity, are shown in Table 1.1.

I end this subsection with a succinct presentation of the noise sources limiting the performances of a GW interferometer. One source of uncertainty comes from the intrinsic quantum nature of light. Indeed the light is formed of discrete quanta, named photons, which possess energy and carry momentum. Thus when a photodetector measures light power, it actually counts photons. Given that the arrival rate of photons follows the Poisson distribution, the state of $N_{\rm photons}$ fluctuates, with an uncertainty in $N_{\rm photons}$ of $N_{\rm photons}^{1/2}$. This source of uncertainty is the shot noise. It is more important at higher frequencies and can be reduced by increasing the laser power. Another noise due to the quantum nature of light is the radiation pressure. It is created by the stochastic force exerted by the stochastic number of photons bouncing mainly on the Fabry-Perot cavities. Unlike the shot noise, the radiation pressure noise decreases with the frequency and increases with the laser power. The shot noise and the radiation pressure form the optical readout noise [Nishizawa et al., 2007; Buonanno and Chen, 2001]. Attempts to reduce the quantum noise by means of squeezed light injections have been done [Yap et al., 2020; McCuller et al., 2020; Aasi et al., 2013]. The motion of the Earth ground also represents an important source of noise, especially at low-sensitivity. It is named the seismic noise, and it represents the most important limitation for the detection of GW astrophysical sources below 1Hz [Accadia et al., 2012; Badaracco et al., 2021; Daw et al., 2004]. For instance, in order to detect tight binaries of supermassive black holes, one needs to conceive an interferometer suspended in the air, as

Parameter	Value
Arm cavity length	$3994.5\,\mathrm{m}$
Arm cavity finesse	450
Laser type	Nd:YAG
Laser wavelength	$1064\,\mathrm{nm}$
Input power at the power recycling mirror	up to $125\,\mathrm{W}$
Beam polarization	linear, horizontal
Test mass material	Fused silica
Test mass size	$34\,\mathrm{cm}$ diameter $\times$ $20\,\mathrm{cm}$ height
Test mass mass	$40\,\mathrm{kg}$
Beam radius at the input test mass	$5.3\,\mathrm{cm}$
Beam radius at the end test mass	$6.2\,\mathrm{cm}$
Radius of curvature at the input test mass	$1934\,\mathrm{m}$
Radius of curvature at the end test mass	$2245\,\mathrm{m}$
Input mode cleaner length	$32.9\,\mathrm{m}$ (round trip)
Input mode cleaner finesse	500
Recycling cavity length at the power recycling cavity	$57.6\,\mathrm{m}$
Recycling cavity length at the signal recycling cavity	$56.0\,\mathrm{m}$

Table 1.1 Advanced LIGO interferometer parameters, at design sensitivity. The values are taken from Aasi et al. [2015a].

it is will be the case for LISA [Amaro-Seoane et al., 2017]. The local changes of the gravitational field due to either seismic or atmospheric displacements, responsible for the Newtonian noise, have a non-negligible impact on the sensitivity of ground-based GW interferometers [Beker et al., 2012; Badaracco and Harms, 2019]. Thermal noise (mirror coatings, mirror substrates, suspension system) is another limitation of the actual detectors. Stochastic movement, due to the temperature, is related to the internal energy of the GW interferometer components (such as mirrors), which impacts the sensitivity of the setup [Tugolukov et al., 2018; Granata et al., 2020; Brif, 1999]. Finally, in Figure 1.19, there is an representative illustration of the noise spectrum during O3 in Advanced LIGO and Advanced Virgo.

1.4.2 γ-ray space observatories

γ-rays represent the highest energy EM radiation, whose spectrum is above $100\,\mathrm{keV}$. In the Universe, they are generated by the most energetic objects and phenomena, such as pulsar magnetic flares [Palmer et al., 2005; Grenier and Harding, 2015; Cerutti et al., 2014], supernova explosions [Siegert, 2018], compact binary neutron stars, blazar relativistic jets [Ackermann et al., 2017; Rajput et al., 2020]. On Earth, they are produced either naturally, as in terrestrial gamma-ray flashes [Mailyan et al., 2020; Neubert et al., 2019], or artificially, like in the case of nuclear reactors [Roos, 1959; Nakashima et al., 1971], nuclear bombs [Straume, 1995; Shimizu, Mar 1987], high energy physics experiments [Tracz, 2017; Gonzalez, 2020]. Luckily for our health and unfortunately for our

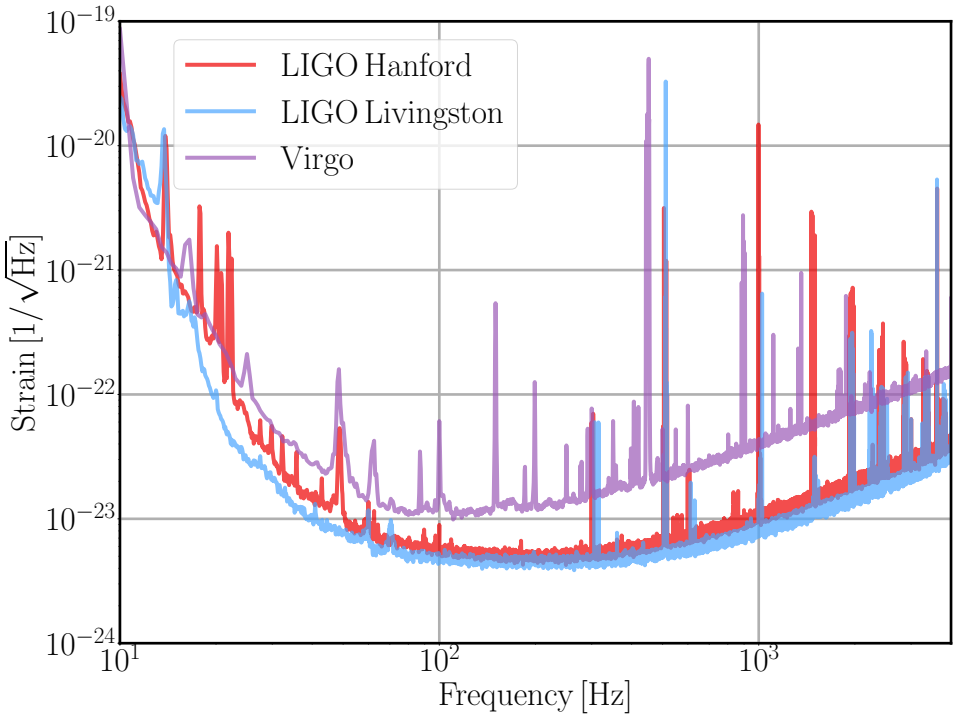

Fig. 1.19 Amplitude spectral density for Advanced Virgo and Advanced LIGO (Livingston and Hanford), during O3. The data used to generate these curves is the same data as in Abbott et al. [2021a].

Universe understanding ease, the Earth atmosphere blocks the γ-rays originating from outer space and propagating towards us [Allison, 1958; Grasty, 1975]. Indeed the high energy photons interact with the upper layers of the atmosphere through the following phenomena: photoelectric effect, Compton scattering and pair production. Thus the γ radiation does not reach us on the surface of the Earth. In order to detect it, two solutions can be envisaged: either to measure, by means of ground-based detectors, the effect of the interaction between the high energy radiation and the atmosphere; or to make use of space observatories situated at altitudes, high enough such that the photons reach them before interacting with the atmospheric molecules. Although for this thesis the interest is focused on the latter option, it is worth mentioning a few words about the former solution.

When high energy photons enter the atmosphere, they interact with it, producing a cascade of relativistic subatomic particles. Therefore, the newly formed particles travel at speeds close to the velocity of light. Also, a particle in acceleration emits EM radiation. On the other hand, the atmosphere, contrary to the vacuum, has a refractive index higher than 1, slowing down an EM signal. As a consequence, in these upper layers of the atmosphere, the interaction resulting particles might travel faster than light. Therefore, the wavefronts emitted by a particle at distinct times overlap, leading to constructive interference. An external observer sees this emitted radiation

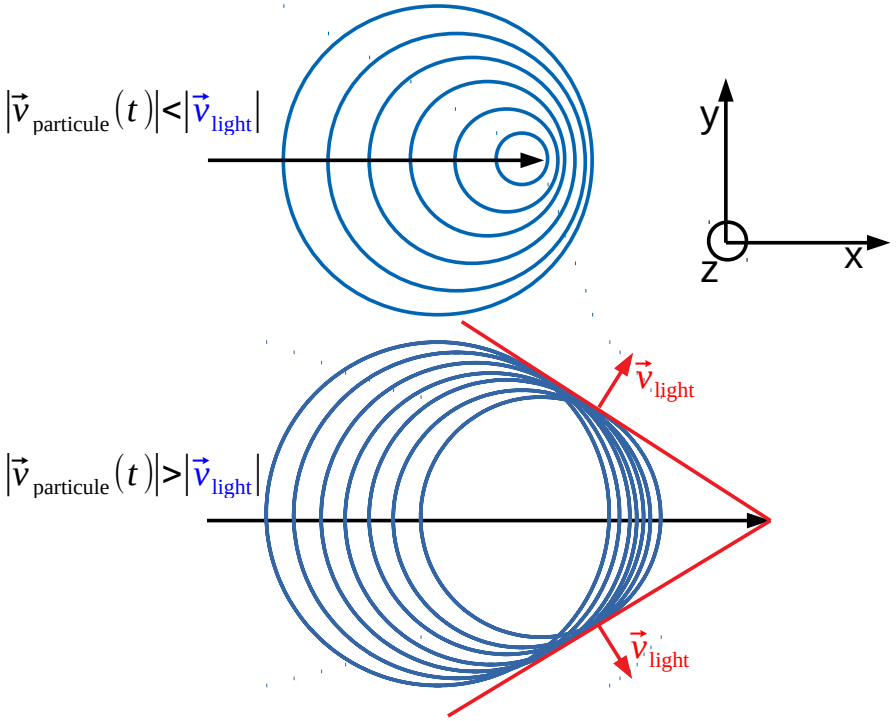

Fig. 1.20 On the x axis, the particle moves with velocity $\vec{v}_{\text{particle}}(t)$ and emits radial EM waves propagating in the medium with $\vec{v}_{\text{light}}$. On top (bottom), the emitted wavefronts travel at velocities lower (higher) than v_{light} and for this reason there is (no) overlap/interference. When $v_{\text{particle}}(t) > v_{\text{light}}$, cone-like radiation results.

as a cone-like signal with a characteristic angle [Mirzoyan, 2021]. This is named Cherenkov radiation, after the Soviet physicist Pavel Cherenkov who discovered this phenomenon [Cherenkov, 1934]. Figure 1.20 offers an illustrative explanation of the Cherenkov light. Several Cherenkov telescopes have been built [Abramowski et al., 2016; Cortina et al., 2009; Bradbury et al., 2000] and ambitious projects are planned for the near future [Knödlseder, 2020].

Concerning the space observatories, one needs to conceive a device which interacts with the incoming high energy photons. Traditionally scientists use scintillation counters. The main component of such a device is the scintillator, a material which, when is excited by ionizing radiation, produces a flash of low-energy photons [Leo, 2012]. The scintillators used for the purposes of the high energy astrophysics community are generally inorganic crystals, the most common of them being the thallium-doped sodium iodide [Cuesta et al., 2013; Sailer et al., 2012]. The counter apparatus also contains a photodetector, whose purpose is to convert the generated light to electrical signal, which is amplified before being measured. A scheme representing a scintillator counter is presented in Figure 1.21. As a matter of example, the Fermi-GBM instrument uses 12 NaI and 2 BGO scintillator detectors. The distribution of the scintillators on Fermi satellite is shown in Figure 1.22. The conversion of shorter wavelength photons into smaller energy radiation, taking place inside scitillators, represents the Compton scat-

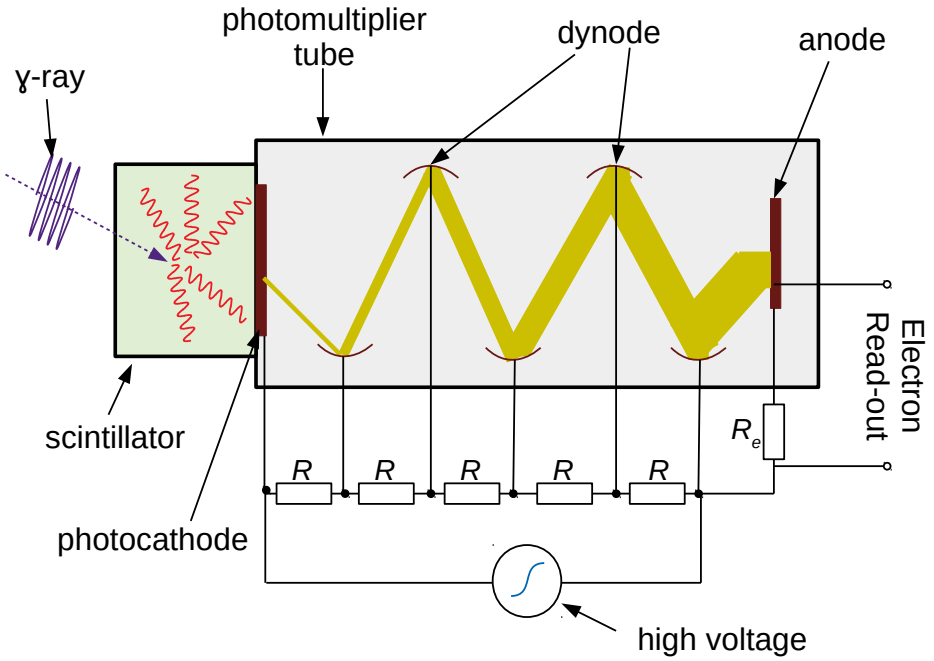

Fig. 1.21 High energy photon counter containing a scintillator crystal, a photomultiplier tube and the read-out electronics. After the excitation by the incoming γ-ray, the inorganic crystal emits longer wavelength photons which reach the photocathode of the photomuliplier. The photocathode coverts the incident light into electrons, through the photoelectric effect. A series of intermediate electrodes, called dynodes, at different electrical potentials, increases the electronic cascade, by the creation of secondary electrons [Arifov, 2013; Bruining, 2016]. The overall electrons arrive finally on the last electrode, the anode. The corresponding electrical signals is measured by means of a read-out technique.

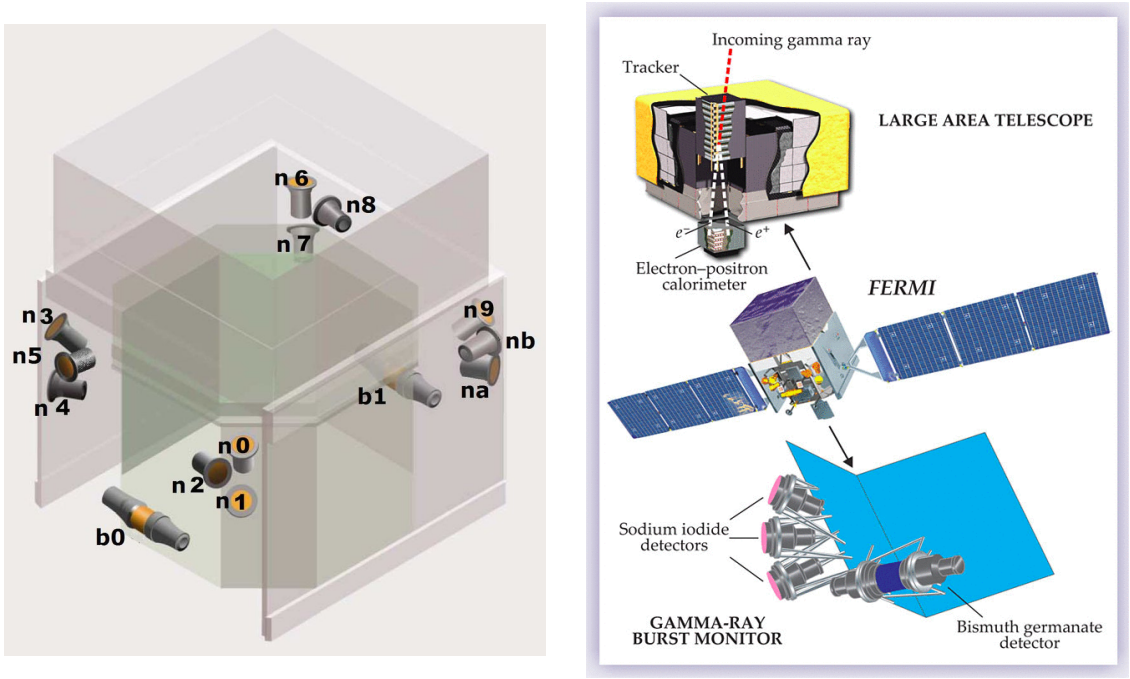

Fig. 1.22 On right: the Fermi satellite with its solar panels and two instruments: GBM and LAT. On left: the spatial distribution of the NaI and BGO scintillators of the GBM instrument. The Fermi satellite was launched on 11 June 2008, aboard a Delta II 7920-H rocket.

tering [Compton, 1923]. The Compton effect is the predominant interaction of intermediate energy range γ photons with matter.

When the incident radiation is composed of soft γ- and/or hard X-rays, the EM waves interact principally through photoelectric effect [Hertz, 1887; Elster and Geitel, 1889; Einstein, 1905]. And in this case, other technology devices might be preferred. For example semiconductor based detectors convert directly the incoming EM radiation into electrical signal. The Burst Alert Telescope (BAT) instrument aboard the Neil Gehrels Swift Observatory, uses CdZnTe hard X-ray detector tiles. Also the ECLAIR instrument aboard the future SVOM (Space Variable Objects Monitor) mission, plans to use CdTe detectors [Remoue et al., 2009]. It is worth mentioning that X-rays, emitted during the afterglow flaring, are detected by means of similar technology. For example, the primary instruments of XMM-Newton [Aschenbach et al., 2000] and the Chandra X-ray Observatory [Weisskopf et al., 2000] use silicon based chips which convert the high energy incoming photons into free pairs of electrons and holes. The newly created charge carriers are finally transformed into an electric signal by read-out electronics.

On the other hand, when a γ-ray is highly energetic, pair production phenomena might occur. More specifically, if a photon has an energy higher than twice the electron rest mass of $0.511\,\mathrm{MeV}$, it might be converted into an electron-positron pair [Hubbell, 2006]. Thereby, for the detection of photons in the highest energy spectrum, a pair conversion telescope [Hunter, 2018] might turn out to be the most appropriate choice. This is the case for the Fermi-LAT instrument [Atwood et al., 2009]. There are also proposals for future space missions equipped with pair telescopes [Tatischeff et al., 2016; Bernard et al., 2014].

1.4.3 Terrestrial telescopes

If for far ultra-violet, X- and γ-rays, the atmosphere is almost opaque, due essentially to the ozone layer [Hartley, 1881], the situation is different for some ranges in the longer wavelength EM radiation spectrum [Horvath, 1993]. For example, the visible radiation reaches us even if affected by the atmospheric distortion [Ackerman and Toon, 1981] due essentially to the absorption by the natural [Viana et al., 2014] and anthropogenic [Shen et al., 2020] air aerosols. Most of the incident infrared photons are absorbed by the atmospheric greenhouse gases [Sinha and Harries, 1995]. Finally a wide range of the microwave and radio wave spectrum is observable from the Earth surface [Shi et al., 2017; Kobayashi, 1980]. To summarize, the viewing conditions are always better for a telescope on a satellite in the outer space. This explains the existence of numerous space missions, aiming to observe the Universe in EM spectrum windows going from optical [Chaisson and Villard, 1990; Borucki et al., 2010; Collaboration et al., 2016], to radio [Dodson et al., 2004], and passing through infrared [Werner et al.,

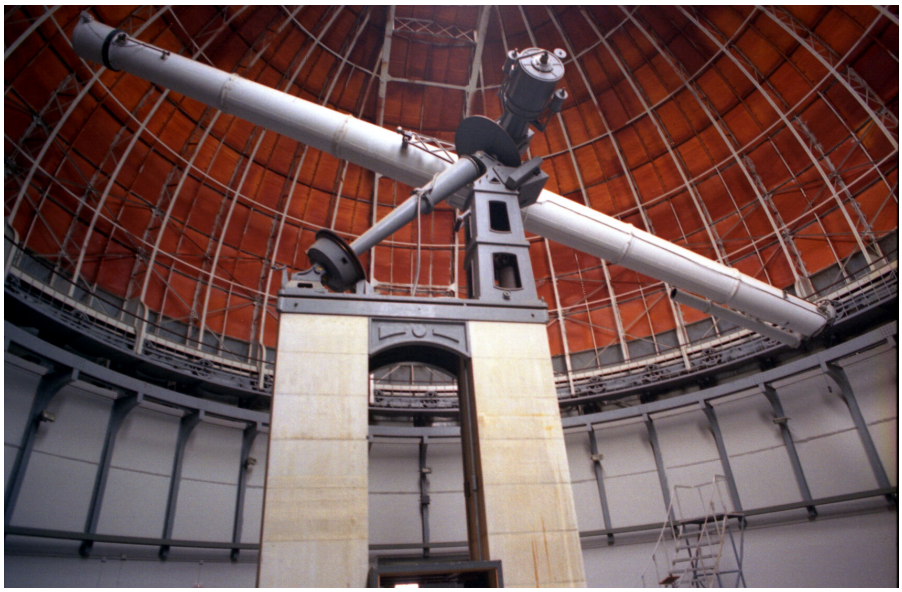

Fig. 1.23 The 77 cm refractor telescope (*la Grande Lunette*), located at the Nice Observatory. It started to be operational in 1886.

2004; Pilbratt et al., 2010; Wright et al., 2010] and microwave [Bennett et al., 1996, 2003; Collaboration et al., 2006] ranges.

Traditionally, there exist two types of such instruments: refractors, whose principal component is an objective lens, and reflectors, where the main constituent is a curved mirror. The former category of instruments enjoyed success at the beginning of Cosmos Study with the optical telescopes. The most famous example is probably the Galileo Galilei refracting telescope. The lens based instruments were very popular in the second half of the 19^{th} century [Launay, 2007; Hale, 1897; Scharmer et al., 2003; Neubauer, 1950]. A picture of the 77 cm refractor, at Nice Observatory, appears in Figure 1.23.

However, when physicists and engineers became able to build large aperture mirrors, the reflectors became the new favourite devices. A scheme of a real mirror-based telescope is presented in Figure 1.24. The main components of such instrument are: the parabolic mirror, collecting the EM energy from a distant source, and the photon detector, converting the incoming photons into electrical signal. The parabolic mirror needs to fulfill shape and micro-roughness requirements in order to send an incoming plane wavefront towards its focal point. For example, the surface of the mirror should be smoother than a small fraction of the wavelength of the photons one wants to collect. To this end, high quality polishing processes are required. Also the surface necessitates high reflectivity. For the radio telescopes, a polished metal, like the steel or the aluminum, is an appropriate choice. For the optical and near infrared range, generally the mirror surface are covered with a thin metallic layer, named coating; aluminum is an

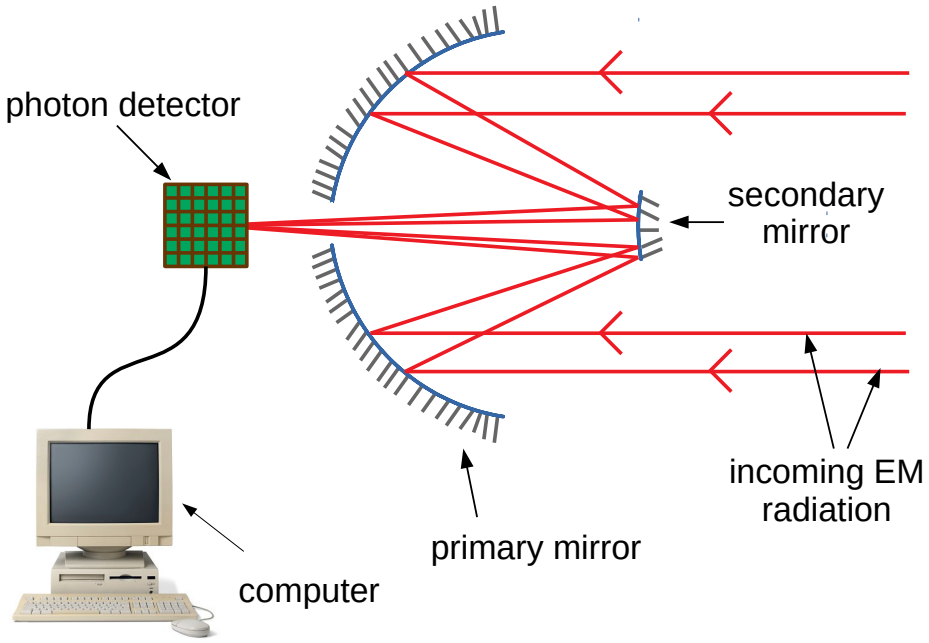

Fig. 1.24 Optical/Infrared/Radio telescope working principle. The EM radiation arrives on Earth under the form of plane waves, because it is emitted by a distant source. The incoming photons are intercepted by a (primary) parabolic mirror which redirects them towards its focal plane. The secondary mirror (it is not a compulsory equipment component) reflects once again the photons and reorients them to the photon detector. Here the light energy is converted into electronic energy and the corresponding signal is read out by a computer.

appropriate choice for the optical wavelength; gold is convenient for infrared radiation; silver is suitable in both cases. Despite the progress achieved to handle these technical conditions, other limitations need to be taken into account. The wave nature of light, more specifically the physics of diffraction, imposes a lower limit on the angular resolution a telescope might can obtain. Thus, a mirror with aperture D_{mirror}, collecting photons at wavelengths λ, cannot distinguish two points separated by an angular displacement smaller than $1.22\frac{\lambda}{D_{\mathrm{mirror}}}$. Nevertheless, one can go beyond this lower limit, by means of astronomical interferometry. Indeed with an array of separate telescopes, by taking advantage of the optical path difference between them, one might get performances similar to those of a huge telescope whose aperture is equal to the spatial distance between the telescope array components. This procedure is commonly used in radio astronomy [Brown et al., 2004; Napier et al., 1994], but there are also examples at shorter wavelength EM spectrum [Lopez et al., 2014; Armstrong et al., 2013; Haguenauer et al., 2010]. Another light detection limitation is the astronomical seeing. It accounts for the atmospheric turbulence, causing refractive index perturbations, which affects the optical path of outer space originating photons. Therefore, photons, which belong to a same wave plane, do not arrive simultaneously at the telescope. Recently adaptive optics have been developed to remedy to this problem [Beckers, 1993]. Equally, other methods have been proposed, such as speckle imaging [Jacquot, 2008] and lucky imaging [Fried, 1978]. As mentioned previously, the second main component of a telescope is the photon detector. Since the time of Galileo up to the second half of the 19^{th} century, astronomers used their eye to see the astrophysical objects. Later, they used photographic plates [Abell, 1959]. Nowadays, new devices are used. For the detection of optical and near infrared photons, the technique is quite similar. First, one needs an anti-reflective coating in order to reduce the loss of incoming photons. Then, a photoactive layer (silicon for visible light [Kamata et al., 2004]; HgCdTe or InSb for near infrared light [Borrello et al., 1980; Shirouzu et al., 1986]) interacts with the photons generating electrons through the photoelectric effect. The resulting electrons are collected pixel by pixel by means of applied electrical fields. In the case of optical radiation detection, a transfer of electrons is needed. Finally, charge amplification and digitization is realized. The most common detectors using this technique are the CCD (charge-coupled device) [Tompsett et al., 1970] and the CMOS (Complementary metal–oxide–semiconductor) [Chih-Tang, 1988]. For mid- and far-infrared radiation, thermal detectors might be used. Indeed, bolometers [Nishimura, 1989], measuring the resistance change, and thermocouples, based on the thermoelectric effect, turn out to be good choices [Rogalski, 2012]. Radio photons are measured by means of radio antennas [Gancio et al., 2020]. When an oscillating EM signal arrives, the electrons inside the wire oscillate, generating an electrical signal which is measured.

CHAPTER 2

GWs and GRB prompt emission coincidence

This Chapter summarizes the work from [Stachie et al., 2020a].

2.1 Existing searches in the literature

Each black hole defines a border, named event horizon, beyond which no information can escape, so it is invisible for an external observer. This is why, GRB prompt emission is not expected to be associated with BBH, unless baryon matter exists in the vicinity (e.g. the accretion discs) [Loeb, 2016; Janiuk et al., 2013]. On the other hand, NSBHs, for which the binary components mass ratio and the spin of the black hole would allow the disruption of the neutron star component before entering the black hole horizon, are expected to generate γ-ray flaring [Barbieri et al., 2020]. Finally BNSs are the most probable sources of this field of the multimessenger astronomy. GW signals originating from the coalescence of two compact objects are detected with ground based GW interferometers, while the high energy photons released during the merger of binaries are observed and recorded by the γ-ray space observatories. Thus, the different messengers are detected by different instruments. Once photon counts and GW strain are measured, their common astrophysical origin might be investigated. There are different clues which can bring conclusive answers to this issue. Generally, GW and GRB events produce sky localization estimations. Thereby, if the two signals are from the aftermath of the same astrophysical phenomenon, the two skymaps should be consistent with each other. Also, theoretical modeling predicts that the separation between the arrival times, on Earth, of two such signals should not be higher than a few tens of seconds. Both sky localizations overlap and similarities in the arrival times of photons and GWs have been verified for the case of GW170817 - GRB 170817A multimessenger detection [Abbott et al., 2017b], as can be remarked from Figure 2.1.

Nevertheless, one can imagine the other way around. If a GW trigger and a high energy photon excess have not sufficient statistical significance to be claimed separately as confident astrophysical events, a small amount of Earth arrival time offset, similarities between their sky localizations, as well as a BNS/NSBH binary type inference, might raise enough the statistical ranking of the association in order to claim an astrophysical

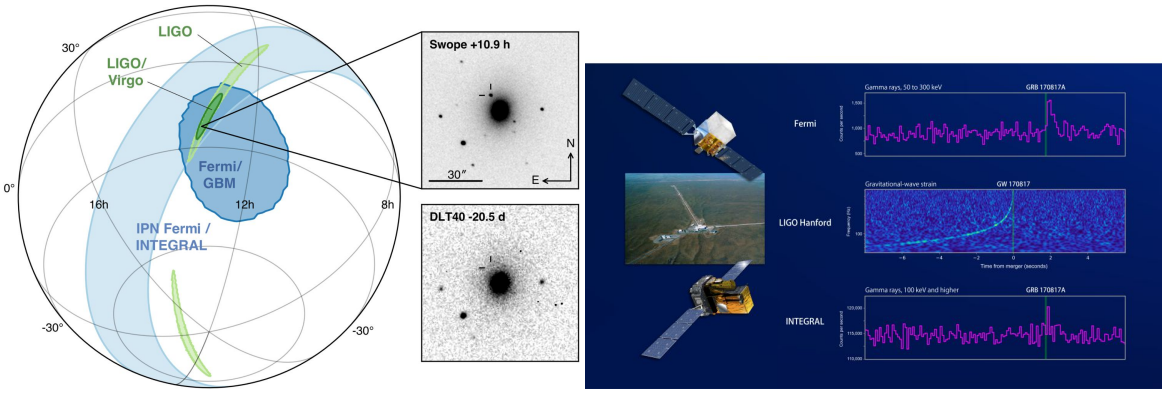

Fig. 2.1 On left: sky localization based on only the GWs (in green), only the Fermi-GBM detection (dark blue), only the arrival times difference of high energy photons at Fermi and *INTEGRAL* [Savchenko et al., 2017] satellites (annulus in light blue), as well as the NGC 4993 discovery images realized by *Swope* [Coulter et al., 2017] and *DLT40* [Yang et al., 2017]. On right: the arrival times of the GW/EM signals at LIGO Handford interferometer, Fermi and *INTEGRAL* satellites. The left panel is taken from [Abbott et al., 2017b].

common origin. Therefore searching for associations between sub-threshold triggers has an interest in both the enlargement of the GW and GRB events catalog, and the realization of new multimessenger detections, which, to date, are very rare: GW 170817 (GWs) - GRB 170817A (photons)- AT 2017fgo (photons) [Abbott et al., 2017b] and SN 1987A (photons and neutrinos) [Arnett et al., 1989] are the only unambiguous events, while IceCube-170922A (neutrinos) - TXS0506+056 (photons) [Aartsen et al., 2018] is very convincing. In the literature, there have been proposed several attempts to search for such associations. For example, Burns et al. [2019] investigate the possible existence of signals, released by the same astrophysical source, in both the Fermi-GBM and LIGO/Virgo O1 data, by making use of three methods (a "blind", a "targeted" and a "joint analysis" search), as follows. The GW data sample is represented by the trigger set output of offline LIGO/Virgo GW search pipelines, *PyCBC* [Dal Canton et al., 2014; Usman et al., 2016] and *GstLAL* [Privitera et al., 2014; Messick et al., 2017], which identify template-based compact binary coalescence signals, by matching the GW observational data with a template bank of simulated signals. More precisely, they consider as foreground (respectively background) data sample the triggers possessing a false alarm rate $\mathrm{FAR}_{\mathrm{GW}}^{\mathrm{BUR}}$ lower (respectively higher) than 10^{-5} Hz (respectively 10^{-3} Hz). For the "blind" search, both the on-board triggers generated by the Fermi-GBM flight software [Meegan et al., 2009; von Kienlin et al., 2014; Bhat et al., 2016a] and the output triggers of an offline all-time all-sky pipeline [Hui et al., 2020] occurring during the same O1 period, have been used as Fermi-GBM data sample. The triggering time lists of the GW and EM data samples have been compared, while the association ranking statistic is assumed to be the shortest absolute time offset between two triggers

belonging to the two distinct sets. For the "targeted" search, the counterpart to a GW trigger is considered to be the highest statistical significant Fermi-GBM output trigger, with detection statistic Λ^{BUR}, reported by an offline targeted pipeline [Blackburn et al., 2015], taking as input the GW time trigger and analyzing the $\pm 30\,\mathrm{s}$ around it. In this case the association ranking statistic is the same as Λ^{BUR}. Regarding the "joint" analysis, the EM counterpart is the same as in the case of the "targeted" analysis, while the association ranking statistic is the quantity $\frac{1}{\mathrm{FAR}^{\mathrm{BUR}}_{\mathrm{GBM}}|\Delta T|}$, where $\mathrm{FAR}^{\mathrm{BUR}}_{\mathrm{GBM}}$ and $|\Delta T|$ are the false alarm rate of the EM trigger and the absolute offset value of the two signal arrival times. Finally, for each of the three methods, a comparison between the ranking statistic distributions of background and foreground associations allows one to infer the non-existence of a multimessenger event, in the two data samples. Similar methods have been used by Hamburg et al. [2020] in the joint LIGO/Virgo - Fermi-GBM O2 search. In this case, the "joint" analysis association ranking statistic is the quantity $\frac{p^{\mathrm{HAM}}_{\mathrm{astro}} p^{\mathrm{HAM}}_{\mathrm{visible}}}{|\Delta t|\mathrm{FAR}^{\mathrm{HAM}}_{\mathrm{GBM}}}$, where $p^{\mathrm{HAM}}_{\mathrm{astro}}$, p_{visible} and $\mathrm{FAR}^{\mathrm{HAM}}_{\mathrm{GBM}}$ are the astrophysical probability of the GW trigger, the fraction of the GW skymap visible by Fermi-GBM at the time of the GW trigger time, and respectively the false alarm rate of the Fermi-GBM trigger.

2.2 New search

During my thesis, I contributed to the development of an event association search pipeline, which combines ideas presented in Burns et al. [2019]; Hamburg et al. [2020] with coincident detection concepts used for the identification of GW signals presented in the data sets of two distinct interferometers. The choice of the association ranking statistic utilizes the separate statistical significance of each trigger, as well as the arrival times offset and the overlap of the two sky localization. This method is used for the search of Fermi-GBM EM counterpart to LIGO GW single interferometer triggers, from O1 and O2 data. No statistical significance association has been found. These results are part of the outcome presented in Hamburg et al. [2020]. Moreover, an independent paper is dedicated to this analysis method [Stachie et al., 2020a].

2.2.1 *PyCBC* GW triggers and Fermi-GBM EM triggers

Like in the analyses summarized above, here also a set of LIGO GW triggers and a set of Fermi-GBM EM triggers are needed. The GW data input is generated by means of *PyCBC*. More precisely, the O1 and O2 LIGO data is analyzed offline. Thus, the strain time series is matched filtered against the modelled waveforms from the template bank introduced in Dal Canton and Harry [2017], giving rise to a list of GW triggers, assigned with statistic $\hat{\rho}_{gw}$, which is a function of the signal to noise ratio and two chi-squared signal-based vetoes [Allen, 2005; Nitz, 2018]. I present here a summary of the *PyCBC* mathematical framework, following [Dal Canton et al., 2014; Usman et al.,

2016; Allen, 2005; Nitz, 2018]. Let $n^{\mathrm{PyC}}(t)$ and $h^{\mathrm{PyC}}(t)$ be the time series noise and GW signal. Hence, the GW detector data stream is $s_{\mathrm{PyC}}(t) = n_{\mathrm{PyC}}(t) + h_{\mathrm{PyC}}(t)$. For a given time function $x(t)$, its Fourier transform, defined by $\tilde{x}(f) = \int_{-\infty}^{+\infty} x(t)e^{-2\pi i f t}dt$, is associated. Thus, the stationary noise single-sided power spectral density becomes $\langle \tilde{n}(f)\tilde{n}^*(f')\rangle = \frac{1}{2}S_n(|f|)\delta(f-f')$, where $\langle\rangle$ denotes the average over the ensemble of different time series. The SNR is defined by

$$\rho_{\mathrm{PyC,init}} = \frac{|4\int \frac{\tilde{s}_{\mathrm{PyC}}(f)\tilde{h}^*_{\mathrm{PyC}}(f)}{S_n(f)}e^{-i2\pi f t_{GW}}df|}{\sqrt{|4\int \frac{\tilde{h}_{\mathrm{PyC}}(f)\tilde{h}^*_{\mathrm{PyC}}(f)}{S_n(f)}df|}}. \tag{2.1}$$

In the preceding expression, t_{GW} is the coalescence time. If the GW detectors had only Gaussian noise, $\rho_{\mathrm{PyC,init}}$ would be an appropriate statistic to rank the triggers. But the GW data contain spurious non-Gaussian and non-stationary noise which possess high $\rho_{\mathrm{PyC,init}}$ values. This behavior degrades the sensitivity of the detector. In order to mitigate these inauspicious effects, a first reduced chi-squared, noted $\chi^2_{1,\mathrm{PyC}}$, is introduced. Initially the frequency range, over which the integrals from Equation 2.1 have been done, are split into p_{PyC} non-overlapping bands. These bands are chosen in such a way that the modelled waveform h_{PyC} has a SNR equal to $\frac{\rho_{\mathrm{PyC,init}}}{p_{\mathrm{PyC}}}$ in each band. The purpose of this first chi-squared is to compare the power of the signal (noted $\rho_{\mathrm{PyC,l}}$) in each of the non-overlapping bands with the power expected from the theoretical model, and so it has the following expression

$$\chi^2_{1,\mathrm{PyC}} = \frac{p_{\mathrm{PyC}}}{2p_{\mathrm{PyC}}-2}\sum_{l=1}^{p_{\mathrm{PyC}}}\left(\rho_{\mathrm{PyC,l}} - \frac{\rho_{\mathrm{PyC,init}}}{p_{\mathrm{PyC}}}\right). \tag{2.2}$$

Therefore, if $\chi^2_{1,\mathrm{PyC}} \gg 1$, it is an indication of the presence of a noise glitch in the data. Hence, this chi-squared behaves like a signal-based veto destined to filter out the output trigger list of undesired candidates. $\chi^2_{1,\mathrm{PyC}}$ is used to define a temporary reweighted SNR (noted $\rho_{\mathrm{PyC,temp}}$), as follows

$$\rho_{\mathrm{PyC,temp}} = \begin{cases} \rho_{\mathrm{PyC,init}}\left[\left(1+\left(\chi^2_{1,\mathrm{PyC}}\right)^3\right)/2\right]^{-\frac{1}{6}} & \text{if } \chi^2_{1,\mathrm{PyC}} > 1 \\ \rho_{\mathrm{PyC,init}} & \text{otherwise} \end{cases}. \tag{2.3}$$

Despite the sensitivity improvement brought by the $\chi^2_{1,\mathrm{PyC}}$ based signal veto, there are still non-Gaussian noises surviving. In particular, the short duration blip glitches, mimicking high mass binaries, are very numerous [Nitz, 2018]. One particularity of these spurious events is that they contain more power than the true GW waveforms, at high frequency. The second chi-squared veto, noted $\chi^2_{2,\mathrm{PyC}}$, is aimed to detect this excess power. This is realized by measuring the reweighted SNR $\rho_{\mathrm{PyC,init}}$ of the detector sig-

nal on a series of N_{PyC} sine-Gaussian tiles, defining tight frequency ranges over which the true GW signal is not expected to contain power. Thus, if one notes by $\rho^{\mathrm{tile}}_{i,\mathrm{PyC}}$ the SNR of the signal when matched against the i^{th} sine-Gaussian tile, the expression of the second chi-squared veto becomes

$$\chi^2_{2,\mathrm{PyC}} = \frac{1}{2N} \sum_{i=1}^{N_{\mathrm{PyC}}} \left(\rho^{\mathrm{tile}}_{i,\mathrm{PyC}}\right)^2. \tag{2.4}$$

As previously, $\chi^2_{2,\mathrm{PyC}} \gg 1$ means a more likely noise glitch transient. This indicator is used for the derivation of the final expression of the *PyCBC* statistic, as follows

$$\hat{\rho}_{gw} = \begin{cases} \rho_{\mathrm{PyC,temp}} \left(\chi^2_{2,\mathrm{PyC}}/4\right)^{-\frac{1}{2}} & \text{if } \chi^2_{2,\mathrm{PyC}} > 4 \\ \rho_{\mathrm{PyC,temp}} & \text{otherwise} \end{cases}. \tag{2.5}$$

The coincident triggers, i.e. those appearing simultaneously in both LIGO Livingston and LIGO Hanford data, have been the subject of the main analysis presented in Hamburg et al. [2020]. Therefore, the actual study concerns only the single interferometer triggers, i.e. those appearing in and only in the LIGO Livingston data or in and only in the LIGO Hanford data. Henceforth in this chapter, by *PyCBC* trigger it is meant a tuple $(m_1, m_2, S_{1,z}, S_{2,z}, t_{GW}, \hat{\rho}_{gw})$. m_1 (respectively m_2) is the mass of the heavier (respectively lighter) compact object. $S_{1,z}$ (respectively $S_{2,z}$) is the heavier (respectively lighter) object dimensionless spin component, parallel to the orbital angular momentum. More precisely, if $J_{1,z}$ is the angular momentum of the primary compact object, then $S_{1,z} = \frac{cJ_{1,z}}{Gm^2}$. Besides the binary parameters and the statistical significance value, each GW trigger has an associated skymap, by means of the Bayestar algorithm [Singer and Price, 2016]. An overview of the size of this trigger list is presented in the left panel of Figure 2.2. For computational cost reasons, only those triggers with $\hat{\rho}_{gw} \geq 8$ have been considered. Additionally, this choice is supported by the fact that the quasistationary noise of the detector is already above this threshold. Concerning my role, I want to mention that I did not need to generate by myself the list of triggers, because available for LIGO/Virgo members at `https://git.ligo.org/tito-canton/o2-ligo-fermi-search/-/tree/master/pycbc`. On the other hand I was in charge of the production of Bayestar skymaps for each *PyCBC* trigger used in this analysis.

I obtained the list of Fermi-GBM triggers as follows: for each GW candidate, I used the *targeted-search* [Blackburn et al., 2015; Kocevski et al., 2018; Goldstein et al., 2019] which gives a list of EM triggers occurring in the window $[-30\,\mathrm{s}, 30\,\mathrm{s}]$ with respect to the GPS time of the GW candidate. More specifically, the *targeted-search* initially estimates a photon rate background, and then searches for an excess of photons over different timescales ($0.064\,\mathrm{s}$, $0.128\,\mathrm{s}$, $0.256\,\mathrm{s}$, $0.512\,\mathrm{s}$, $1.024\,\mathrm{s}$, $2.048\,\mathrm{s}$, $4.096\,\mathrm{s}$ and

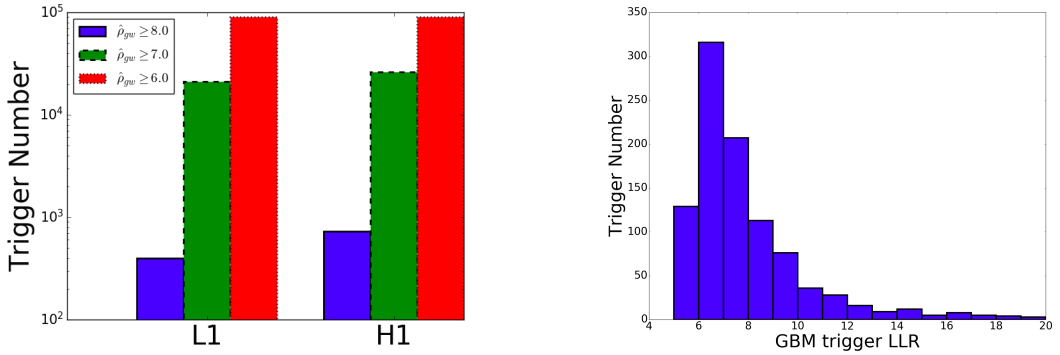

Fig. 2.2 On left, the number of *PyCBC* GW single interferometer triggers possessing a statistic $\hat{\rho}_{gw}$ higher than 6 (in red), 7 (in green) and respectively 8 (in blue); the results for both LIGO Livingston (L1) and LIGO Hanford (H1) are shown. On right, the histogram of LLR of the *targeted-search* EM counterpart to the GW triggers.

8.192 s), the phase shift being of 64 ms for durations smaller or equal to 1.024 s. For the longer durations a phase shift of factor 8 is used (e.g. the 4.096 s windows are separated by 0.512 s). It is worth mentioning that the search is realized over a grid obtained by the cartesian product of a set of sky locations and a set of three Band function based spectra, named *soft* (the lowest energy), *normal* (the medium energy) and *hard* (the highest energy). Each such candidate is assigned a log-likelihood ratio (LLR), measuring the statistical significance of the trigger. I remember here the statistical method used to derive the LLR, following Kocevski et al. [2018]; Blackburn et al. [2015] . An index i defines a pair formed of a detector and an energy channel, so there are 112 (14 detectors $\times 8$ energy channels) such indices. For each pair, d_i^{ts}, n_i^{ts}, $\sigma_{d_i}^{ts}$, $\sigma_{n_i}^{ts}$ and r_i^{ts} represent the observed data counts, the background counts, the standard deviation of the expected data, the standard deviation of the background and respectively the location and spectrally dependent detector response. Also noted by H_1^{ts} (H_0^{ts}) is the hypothesis of the presence of both signal and noise (only noise) in the data. Therefore, under the prior of Gaussian noise, the probability of measuring the data $d^{ts} = \{d_i^{ts}\}$, given the assumption of the presence of a signal of amplitude $s > 0$, can be written as

$$P(d^{ts}|H_1^{ts}, s) = \prod_i \frac{1}{\sqrt{2\pi}\sigma_{d_i}^{ts}} \exp\left(-\frac{(\tilde{d}_i^{ts} - r_i^{ts}s)^2}{2(\sigma_{d_i}^{ts})^2}\right), \tag{2.6}$$

while the probability to have the same data, given the assumption of only noise in the data, can be expressed as

$$P(d^{ts}|H_0^{ts}) = \prod_i \frac{1}{\sqrt{2\pi}\sigma_{n_i}^{ts}} \exp\left(-\frac{(\tilde{d}_i^{ts})^2}{2(\sigma_{n_i}^{ts})^2}\right). \tag{2.7}$$

In Equations 2.6 and 2.7, $\tilde{d}_i^{ts} = d_i^{ts} - \langle n_i^{ts} \rangle$ is the background-subtracted data. The likelihood ratio (LR), under the assumption of amplitude signal s, is defined by the quantity $\Lambda^{ts}(d|s) = \frac{P(d^{ts}|H_1^{ts},s)}{P(d^{ts}|H_0^{ts})}$. By replacing the two probabilities with the expressions obtained above, one has

$$\Lambda^{ts}(d^{ts}|s) = \exp\left\{\sum_i \left[\ln \frac{\sigma_{n_i}^{ts}}{\sigma_{d_i}^{ts}} + \frac{(\tilde{d}_i^{ts})^2}{2(\sigma_{n_i}^{ts})^2} - \frac{(\tilde{d}_i^{ts} - r_i^{ts}s)^2}{2(\sigma_{d_i}^{ts})^2}\right]\right\}. \tag{2.8}$$

Before taking the logarithm of the LR, one needs to marginalize, i.e. $\Lambda^{ts}(d) = \int \Lambda(d|s)P(s)ds$. By considering the prior

$$P(s) = \left[1 - \exp\left(-\left(\frac{s}{\gamma^{ts}\sigma_{\mathcal{L}}^{ts}}\right)^{\beta^{ts}}\right)\right] s^{-\beta^{ts}}, \tag{2.9}$$

with $\gamma^{ts} = 2.5$ and $\beta^{ts} = 1$, one obtains for the LLR, defined here by $\mathcal{L}^{ts}(d^{ts}) = \ln \Lambda^{ts}(d^{ts})$, the following expression

$$\begin{aligned}\mathcal{L}^{ts}(d^{ts}) &= \ln \sigma_{\mathcal{L}}^{ts} + \ln\left[1 + \text{erf}\left(\tfrac{s_{\text{best}}^{ts}}{\sqrt{2}\sigma_{\mathcal{L}}^{ts}}\right)\right] + \ln \Lambda^{ts}(d^{ts}|s_{best}^{ts}) + \\ &\begin{cases} \ln\left[1 - \exp\left(-\frac{s_{\text{best}}^{ts}}{\gamma^{ts}\sigma_{\mathcal{L}}^{ts}}\right)\right] - \beta^{ts}\ln s_{\text{best}}^{ts} & \text{if } s_{\text{best}}^{ts} \geq 0 \\ -\beta^{ts}\ln(\gamma^{ts}\sigma_{\mathcal{L}}^{ts}) & \text{if } s_{\text{best}}^{ts} \leq 0 \end{cases}.\end{aligned} \tag{2.10}$$

In Equations 2.10 and 2.9, $\sigma_{\mathcal{L}}^{ts} = \frac{1}{\sum_i \frac{(r_i^{ts})^2}{(\sigma_{d_i}^{ts})^2}}$, while s_{best}^{ts} is the amplitude value maximizing $\ln \Lambda^{ts}(d^{ts}|s)$. It is derived by means of the iterative Newton's method. One starts with $s_0^{ts} = \frac{\sum_i r_i^{ts}\tilde{d}_i^{ts}/(\sigma_{d_i}^{ts})^2}{\sum_i (r_i^{ts})^2/(\sigma_{d_i}^{ts})^2}$, while the k^{th} iteration step consists in the procedure $s_{k+1}^{ts} \approx s_k^{ts} - \frac{\partial\mathcal{L}/\partial s}{\partial^2\mathcal{L}/\partial s^2}$. For this study, I kept only the candidate assigned by the highest LLR. Henceforth in this chapter, by a *targeted-search* trigger, it is meant a tuple $(\text{LLR}, t_{EM}, \text{dur}_{EM}, \text{spec}_{EM})$, where t_{EM} is the central time of the trigger, $\text{dur}_{EM} \in \{0.064\,\text{s}, 0.128\,\text{s}, 0.256\,\text{s}, 0.512\,\text{s}, 1.024\,\text{s}, 2.048\,\text{s}, 4.096\,\text{s}, 8.192\,\text{s}\}$ is the duration of the trigger. $\text{spec}_{EM} = 0, 1, 2$ stands for a *soft*, *normal* or *hard* spectrum. Moreover, the *targeted-search* provides, for each EM trigger, a sky localization. Like in the case of the GW trigger list, a cutoff of $\text{LLR} \geq 5$ is chosen. As emphasized by the right panel of Figure 2.2, this cutoff is almost equivalent to the choice where no restriction is considered, because almost all the most significant Fermi-GBM triggers have LLR higher than 5.

One could naively consider that a GW (EM) trigger assigned with a high reweighted SNR (LLR) is necessarily a real GW (EM) event. Actually, the GW (EM) background data is far from being Gaussian. For example in the strain data, measured by the GW interferometers, non-Gaussianity often arises under the form of glitches. In order to

confidently detect the GW emitted by a binary source, situated at millions to billions of light years, one needs sensitivities in measuring fractional length difference, on the order of 10^{-21}. Thus, given that the arms of the actual GW interferometers have lengths of $3/4$km, and the Fabry-Perot cavities are responsible for $\mathcal{O}(100)$ laser pulse round-trips, it means that one needs to measure length differences which are still much smaller than the atomic size. In these conditions, the instrumental noise, as well as the environmental perturbations, might produce excess power at the output of the interferometer. These external disturbances account for high SNR triggers, of non-astrophysical origin. The advantage of the coincident triggers, i.e. measured by distinct interferometers separated by thousands of km, is that, in general, the environmental disturbances have an impact only locally. Thus, it is unlikely to have two non-astrophysical GW candidates occurring at so large distances, and separated in time by at most a few milliseconds. On the other hand, for the single interferometer triggers, the same method cannot be applied. So one needs to envisage another way to address the question of the astrophysical origin of the GW candidates appearing when only one of the detectors is in the observing mode. In the LIGO and Virgo data, there are a multitude of glitch types. A citizen program dedicated to the classification of these non-Gaussian noises is *Gravity Spy*[1], hosted by the *Zooniverse* platform [Borne and Team, 2011]. Several efforts have been made in order to characterize and classify these background transients [Mukherjee et al., 2010; Mukund et al., 2017; Powell et al., 2015; Rampone et al., 2013; Bahaadini et al., 2018]. The identification and the filtering out of these background transients is important in order to increase the sensitivity of the actual GW detectors. Even if some of the sources of noise (scattered light, EM coupling between external instruments and the detector, vibrations of the external instruments, earthquakes etc) are known, there are still many glitches for which the origin of noise has not been associated yet. A few examples of Omega Scans [Chatterji et al., 2004] of glitches, as well as the associated *gwdetchar-omega*[2] SNRs, is offered in Figure 2.3. One of the most common non-Gaussian transient noise is the blip glitch [Torres-Forné et al., 2020; Cabero et al., 2019; Nitz, 2018]. They are short and, in a Time-Frequency diagram, they appear as a sharp increase of the frequency. Thus, they resemble high mass binaries. The presence of these types of glitches has as effect the degradation of the search pipelines sensitivity in the range of high mass BBH.

A similar situation happens when one tries to look for an excess of photons in the Fermi-GBM data. Any increase of photon counts in the scintillation detectors should not be associated to a short GRB event, even if assigned with high LLR by the *targeted-search*. Indeed other astrophysical sources are also responsible for the flashes of γ-rays reaching the Fermi satellite. In our solar system, the solar flares represent releases of

[1] `https://www.zooniverse.org/projects/zooniverse/gravity-spy`
[2] `https://gwdetchar.readthedocs.io/en/stable/omega/`

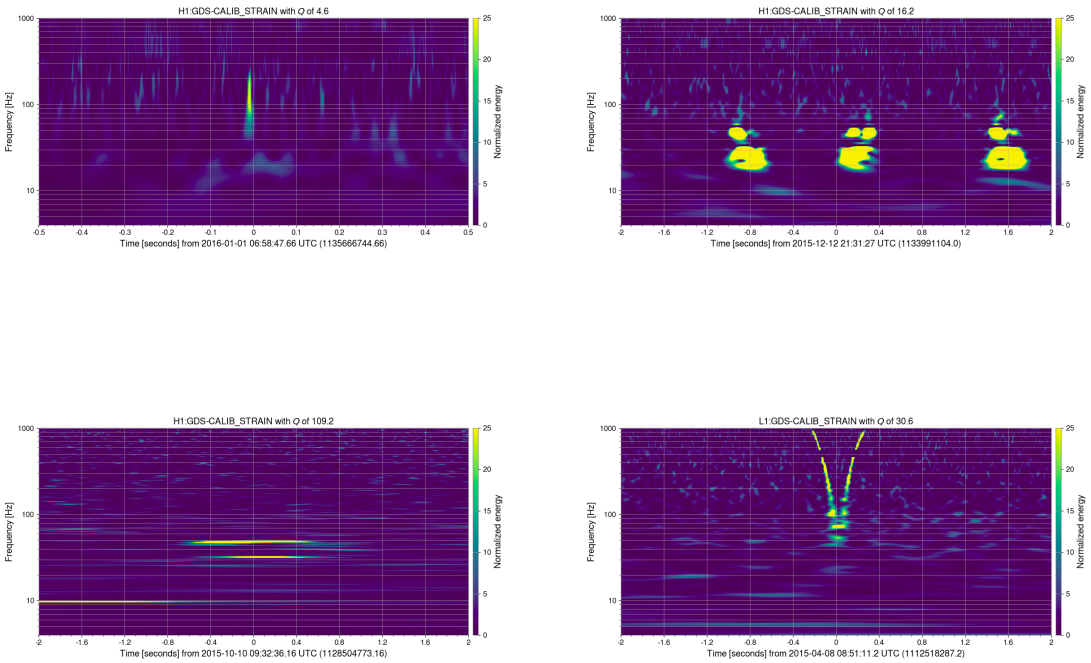

Fig. 2.3 Frequency versus time Omega Scan for four noise transients: blip glitch (top left), paired doves glitch (top right), scattered light glitch (bottom left) and radio frequency glitch (bottom right). The *gwdetchar-omega* SNRs are 8.5 (for the blip glitch), 29.8 (for the paired doves glitch), 21.3 (for the scattered light glitch), and respectively 14.3 (for radio frequency glitch). Strain data has been used for the derivation of these diagrams. The bottom right panel corresponds to a LIGO Livingston event, while the three others are associated to LIGO Hanford.

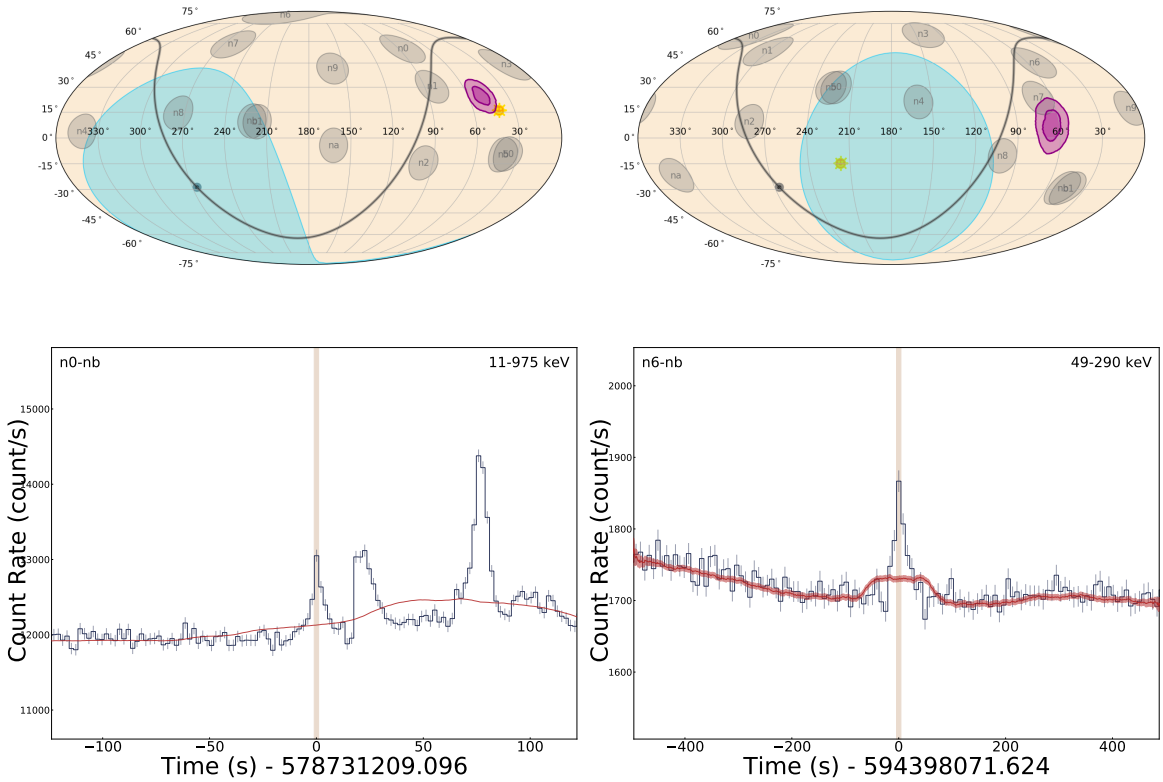

Fig. 2.4 Skymaps (on top) and lightcurves (on bottom) for a solar flare (on left) and a long GRB (on right). On the skymaps, represented are the Earth (in blue), the galactic plane (the grey line), the satellite position (the dot on the grey line), the Sun (in yellow), the confident area of the EM trigger (in red), as well as the sky directions towards which the scintillation detectors point. Regarding the lightcurves, the red line represents the estimated photon background, while the vertical grey line indicates the position of the EM trigger. The solar flare (long GRB) generates a *targeted-search* trigger with $\mathrm{LLR} = 196.11$ (respectively $\mathrm{LLR} = 105.90$), a duration of $2.048\,\mathrm{s}$ (respectively $8.192\,\mathrm{s}$) and *soft* (respectively *normal*) spectrum.

magnetic energy under the form of high energy photons, accelerated particles, magnetohydrodynamic waves and plasma heating. In particular, the Fermi-GBM detectors are sensitive to the photons and particles originating from the Sun [Kafexhiu et al., 2018; Knuth and Glesener, 2020]. Equally, in the Milky Way, X-ray binaries, i.e. a compact object (black hole or neutron star) accreting matter from its companion star, emit high energy radiation intercepted by the Fermi satellite [Grinberg et al., 2013; Malacaria et al., 2021; Sugizaki et al., 2020]. At cosmological distances, long GRBs, generally associated with the collapse of massive stars, send γ-ray photons towards the Earth [Gruber et al., 2011]. Figure 2.4 provides sky localizations and EM lightcurves for a solar flare event and a long GRB. Manual analysis of both the skymap and the lightcurve might allow the filtering out of the non short GRB events. Indeed high energy radiation associated with a solar flare is assigned with a skymap suggesting the

same position as the Sun. Also solar flare events have an excess of low energy photons, several episodes close in time being possible as depicted in the bottom left panel of Figure 2.4. Similarly, a flash of photons originating from a X-ray binary can be identified by a sky localization indicating a galactic plane position. Likewise, long GRBs might be distinguished from short GRBs, by studying the spectrum and especially the timescale. Effectively, the long GRBs have softer spectra, while their durations are longer than $2\,\mathrm{s}$ (bottom right panel of Figure 2.4). Other kinds of high LLR events, not associated with short GRB exist. An example is the long lasting phosphorescence due to the interaction of cosmic rays with one of the NaI crystal scintillators [Fishman and Austin, 1977; Kouveliotou et al., 1992; Hurley, 1978]. The subsequent cosmic ray scintillation has similar shape and duration as the γ-ray scintillation, but it generates lower energy counts. A similar process may take place in a BGO crystal. In this case, a high energy cosmic ray can hit the scintillator, giving birth to a short lived radioactive isotope, which afterwards decays to stability by releasing γ-rays [Grigoriev et al., 2009; Reedy, 2010]. Figure 2.5 provides skymaps and single detector lightcurves for each of these two types of noise transients. A filtering procedure is possible here, either with an automatic implementation or manually. Indeed, regarding the phosphorescence backgrounds, the excess of counts present in only one NaI detector is not characteristic of a flash of γ-ray coming from a distant source, but it denotes a physical process taking place locally, at the place of a single detector. A high energy wave packet coming from outside the satellite, whatever the non occulted (by the Earth) direction, determines a increase of counts on several detectors. Similarly, the excess of photons in only one BGO detector necessitates an EM radiation with only one very high energy component and positioned in the sky in such a particular place that is invisible to the other BGO detector, which is of course unrealistic. One should note from Figure 2.5, that, in the case of phosphorescence events, the *targeted-search* skymap clearly indicates the NaI detector on which the cosmic ray is incident, while, for BGO skymaps, it is quite uninformative. This is due to the fact that the NaI scintillators have a directional dependent response, whereas the BGO scintillator do not.

2.2.2 Statistical framework

It is worth mentioning that ideas contained in this subsection have been proposed by Tito Dal Canton in the regular meetings of the LIGO/Virgo - Fermi-GBM team. While in the previous subsection, I presented the way each messenger is separately assigned a statistical significance, i.e. the $\hat{\rho}_{gw}$ value for the GW candidates and the LLR for the EM triggers, here I introduce the mathematical method allowing to assign significance to an association, i.e. the pair formed of a *PyCBC* trigger and its *targeted-search* counterpart. The method is inspired from Ashton et al. [2018] and is based on a Bayesian formalism.

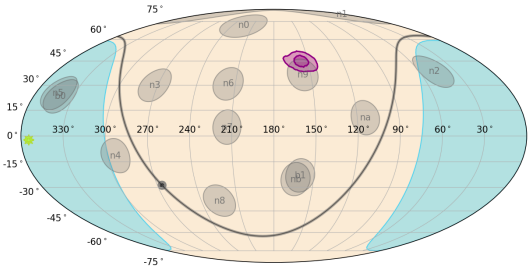

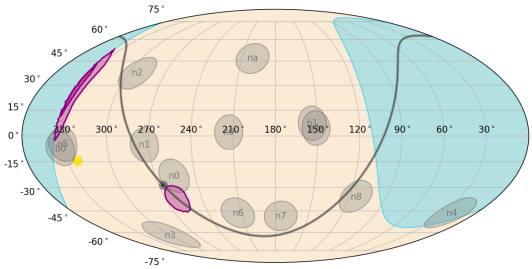

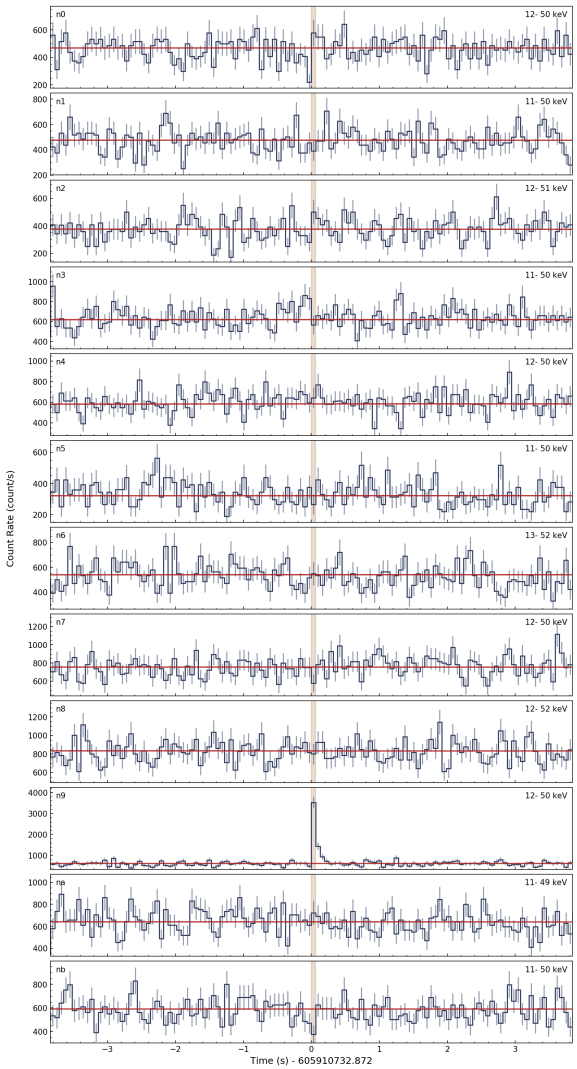
Count Rate (count/s)
Time (s) - 605910732.872

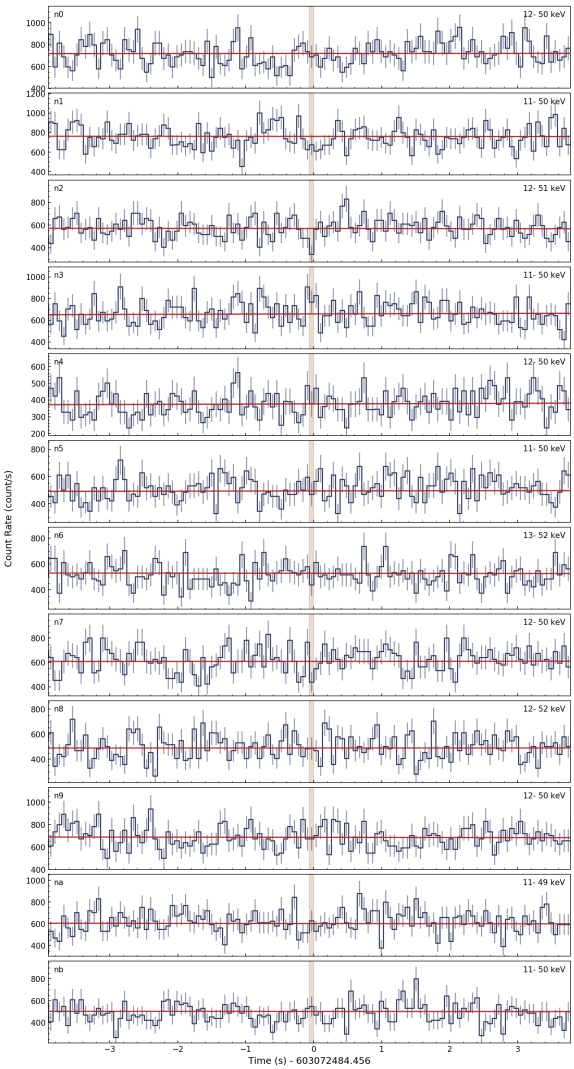
Count Rate (count/s)
Time (s) - 603072484.456

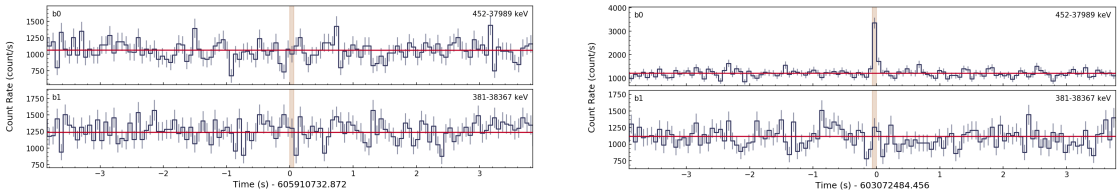

Fig. 2.5 Sky localizations (on top), NaI scintillator lightcurves (middle) and BGO detector lightcurves (bottom) for a phosphorescence event (left) and a BGO spike (right). The phosphorescece event (BGO spike) generates a *targeted-search* trigger with $\mathrm{LLR} = 425.53$ (respectively $\mathrm{LLR} = 86.03$), a duration of $0.064\,\mathrm{s}$ (respectively $0.064\,\mathrm{s}$) and *soft* (respectively *hard*) spectrum.

The notations are the same as in Stachie et al. [2020a]. Hereafter D_L and D_G represent the *PyCBC* and the *targeted-search* trigger data. Also noted by H^C, H^{NN}, H^{SN}, H^{NS} and H^{SS} are the hypothesis that the two triggers have a common astrophysical source, the hypothesis that the two triggers are noise events, the hypothesis that the GW (EM) candidate is of astrophysical origin (a background event), the hypothesis that the GW (EM) trigger is a transient noise (short GRB event), and respectively the hypothesis that two triggers are compact binary merger and short GRB events, but non-related. Of particular interest is the comparison of the likelihoods of measuring the observed data D_L and D_G, given H^C or $(H^{NN} \vee H^{SN} \vee H^{NS} \vee H^{SS})$. Therefore, the joint ranking statistic is defined by

$$\Lambda = \frac{P(D_L, D_G|H^C)}{P(D_L, D_G|H^{NN} \vee H^{SN} \vee H^{NS} \vee H^{SS})}. \tag{2.11}$$

In addition, the Bayes theorem allows the writing

$$P(D_L, D_G|H^{NN} \vee H^{SN} \vee H^{NS} \vee H^{SS}) = \frac{P(H^{NN} \vee H^{SN} \vee H^{NS} \vee H^{SS}|D_L, D_G)P(D_L, D_G)}{P(H^{NN} \vee H^{SN} \vee H^{NS} \vee H^{SS})}. \tag{2.12}$$

But the H^{XY}, for $X, Y \in \{N, S\}$, are disjoint hypotheses, so $P(H^{NN} \vee H^{SN} \vee H^{NS} \vee H^{SS}|D_L, D_G)P(D_L, D_G) = \sum_{X,Y\in\{N,S\}} P(H^{XY}|D_L, D_G)$ and $P(H^{NN} \vee H^{SN} \vee H^{NS} \vee H^{SS}) = \sum_{X,Y\in\{N,S\}} P(H^{XY})$. Therefore one can write

$$\Lambda = \frac{P(D_L, D_G|H^C) \sum_{X,Y\in\{N,S\}} P(H^{XY})}{\sum_{X,Y\in\{N,S\}} P(H^{XY}|D_L, D_G)P(D_L, D_G)}. \tag{2.13}$$

Once again the Bayes theorem is used, for each $(X, Y) \in \{(N, N), (N, S), (S, N), (S, S)\}$, as follows

$$P(H^{XY}|D_L, D_G)P(D_L, D_G) = P(D_L, D_G|H^{XY})P(H^{XY}). \tag{2.14}$$

Hence, the joint ranking statistic becomes

$$\Lambda = \frac{P(D_L, D_G|H^C)\sum_{X,Y\in\{N,S\}} P(H^{XY})}{\sum_{X,Y\in\{N,S\}} P(D_L, D_G|H^{XY})P(H^{XY})}. \tag{2.15}$$

In order to simplify even more this expression one can use the prior $P(H^{NN}) = P(H^{SN}) = P(H^{NS}) = P(H^{SS})$. This assumption seems unrealistic, as the GW and the EM trigger lists are dominated by background events, so $P(H^{NN}) \gg P(H^{SN}), P(H^{NS}), P(H^{SS})$. On the other hand, there are at least two reasons in favor of such a choice: (i) it is an easy way to get rid of undesired factors and (ii) the correctness of the joint ranking statistic is not primordial, given that this quantity will be converted later into a FAR distribution. Also, for every (X, Y), is introduced the quantity $\mathcal{B}_{C/XY}(D_L, D_G) = P(D_L, D_G|H^C)/P(D_L, D_G|H^{XY})$, which is the likelihood ratio of the hypothesis H^C and H^{XY}. Now the association ranking statistic is written

$$\Lambda = \frac{4}{\sum_{X,Y\in\{N,S\}} \frac{1}{\mathcal{B}_{C/XY}(D_L,D_G)}}. \tag{2.16}$$

$\Theta_{\rm ASH}$ denotes the set of binary parameters. Moreover, noted by $\Theta^S_{\rm ASH}$ is the restricted set of parameters of those binaries giving rise to a signal in the GW data and a signal in the EM data, i.e. $\Theta^S_{\rm ASH} \equiv \left\{\theta \in \Theta_{\rm ASH} \text{ such that } P(\theta|H^C) > 0\right\}$. Thus, one can write $P(D_L, D_G|H^C) = \int_{\Theta^S_{\rm ASH}} P(D_L, D_G|\theta, H^C)P(\theta|H^C)d\theta$. Additionally, one can show that, for $\theta \in \Theta^S_{\rm ASH}$, the following relation holds

$$P(D_L, D_G|\theta, H^C) = \frac{P(D_L|H^C)P(\theta|D_L, H^C)}{P(\theta|H^C)}\frac{P(D_G|H^C)P(\theta|D_G, H^C)}{P(\theta|H^C)}. \tag{2.17}$$

Finally, one obtains

$$P(D_L, D_G|H^C) = P(D_L|H^C)P(D_G|H^C)\mathcal{I}^{\rm ASH}_\theta(D_L, D_G), \tag{2.18}$$

where $\mathcal{I}^{\rm ASH}_\theta(D_L, D_G) = \int_{\Theta^S_{\rm ASH}} \frac{P(\theta|D_L,H^C)P(\theta|D_G,H^C)}{P(\theta|H^C)}d\theta$ is, up to an approximation, the quantity measuring the similarities between the two separate and independent posterior distributions. The individual hypotheses H^S_L/H^N_L (respectively H^S_G/H^N_G), of having a signal/noise in the LIGO (respectively Fermi-GBM) data, are introduced. One can easily prove that, under the assumption $P(\theta|H^C) = P(\theta|H^S_L) = P(\theta|H^S_G)$ for any $\theta \in \Theta^S_{\rm ASH}$, and taking into consideration the relation $P(D_L, D_G|H^{XY}) = P(D_L|H^X_L)P(D_G|H^Y_G)$,

the following equality holds, $\frac{P(D_L,D_G|H^C)}{P(D_L,D_G|H^{XY})} = \frac{P(D_L|H_L^S)}{P(D_L|H_L^X)}\frac{P(D_G|H_G^S)}{P(D_G|H_G^Y)}$. Furthermore, by introducing the individual Bayes factor notations $Q_L(D_L) = P(D_L|H_L^N)/P(D_L|H_L^S)$ and $Q_G(D_G) = P(D_G|H_G^N)/P(D_G|H_G^S)$, one has:

$$\begin{aligned}
\mathcal{B}_{C/NN}(D_L, D_G) &= \frac{\mathcal{I}_\theta^{\rm ASH}(D_L, D_G)}{Q_L(D_L)Q_G(D_G)}, \\
\mathcal{B}_{C/SN}(D_L, D_G) &= \frac{\mathcal{I}_\theta^{\rm ASH}(D_L, D_G)}{Q_G(D_G)}, \\
\mathcal{B}_{C/NS}(D_L, D_G) &= \frac{\mathcal{I}_\theta^{\rm ASH}(D_L, D_G)}{Q_L(D_L)}, \\
\mathcal{B}_{C/SS}(D_L, D_G) &= \mathcal{I}_\theta^{\rm ASH}(D_L, D_G).
\end{aligned} \tag{2.19}$$

Now I focus on the posterior overlap $\mathcal{I}_\theta^{\rm ASH}(D_L, D_G)$. Hereafter it is considered that the binary parameters $\Theta_{\rm ASH}^S$ concern only the sky location, the coalescence time and the time of the EM signal i.e. $\Theta_{\rm ASH}^S = \{\vec{\mathbf{\Omega}}, t_c^{\rm ASH}, t_{\rm light}^{\rm ASH}\}$, where $\vec{\mathbf{\Omega}}$ represents the sky angle coordinates of the astrophysical event, $t_c^{\rm ASH}$ is the coalescence time of the binary measured at some location (for example the geocenter) and $t_{\rm light}^{\rm ASH}$ is arrival time of an EM signal at some location. One should note that $\Theta_{\rm ASH}^S$ contains only one sky location parameter and two arrival times. This is due to the fact that for an astrophysical event, the skymaps of the corresponding GW and EM signals are the same, while their arrival times are not necessarily identical. I remind that $\mathcal{I}_\theta^{\rm ASH}(D_L, D_G) = \int\int\int \frac{P(\vec{\mathbf{\Omega}},t_c^{\rm ASH},t_{\rm light}^{\rm ASH}|D_L,H_l^S)P(\vec{\mathbf{\Omega}},t_c^{\rm ASH},t_{\rm light}^{\rm ASH}|D_G,H_G^S)}{P(\vec{\mathbf{\Omega}},t_c^{\rm ASH},t_{\rm light}^{\rm ASH}|H^C)} d\vec{\mathbf{\Omega}} dt_c^{\rm ASH} dt_{\rm light}^{\rm ASH}$. By assuming the priors

$$\begin{aligned}
P(\vec{\mathbf{\Omega}}, t_c^{\rm ASH}, t_{\rm light}^{\rm ASH}|H^C) &= P(\vec{\mathbf{\Omega}}|H^C)P(t_c^{\rm ASH}, t_{\rm light}^{\rm ASH}|H^C), \\
P(\vec{\mathbf{\Omega}}|t_c^{\rm ASH}, t_{\rm light}^{\rm ASH}, D_L, H_L^S) &= P(\vec{\mathbf{\Omega}}|D_L, H_L^S), \\
P(\vec{\mathbf{\Omega}}|t_c^{\rm ASH}, t_{\rm light}^{\rm ASH}, D_G, H_L^G) &= P(\vec{\mathbf{\Omega}}|D_G, H_L^G),
\end{aligned} \tag{2.20}$$

one gets

$$\mathcal{I}_\theta^{\rm ASH}(D_L, D_G) = I_{\Delta t}(D_L, D_G) I_{\mathbf{\Omega}}(D_L, D_G), \tag{2.21}$$

where

$$\begin{aligned}
I_{\mathbf{\Omega}}(D_L, D_G) &= \int\int \frac{P(\mathbf{\Omega}|D_L, H_L^S)P(\mathbf{\Omega}|D_G, D_G^S)}{P(\mathbf{\Omega}|H^C)} d\mathbf{\Omega}, \\
I_{\Delta t}(D_L, D_G) &= \int\int \frac{P(t_c^{\rm ASH}|D_L, H_L^S)P(t_{\rm light}^{\rm ASH}|D_G, H_G^S)}{P(t_c^{\rm ASH}, t_{\rm light}^{\rm ASH}|H^C)} dt_c^{\rm ASH} dt_{\rm light}^{\rm ASH}.
\end{aligned} \tag{2.22}$$

By replacing the relations from Equation 2.21 and 2.19 in the Equation 2.16, and by ignoring the factor of 4, one obtains

$$\Lambda(D_L, D_G) = \frac{I_{\Delta t}(D_L, D_G) I_{\mathbf{\Omega}}(D_L, D_G)}{1 + Q_L(D_L) + Q_G(D_G) + Q_L(D_L)Q_G(D_G)}. \tag{2.23}$$

By dropping the factor 4, no fundamental mistake is made, because, as mentioned previously, this Λ statistic will be converted to a FAR. Here I briefly discuss the behavior of the association ranking depending on the characteristics of the input data. Given the definition of $Q_L(D_L)$ (respectively $Q_G(D_G)$), a statistical significant ***PyCBC*** (respectively *targeted-search*) trigger has $Q_L(D_L) \ll 1$ (respectively $Q_G(D_G) \gg 1$), while for a low significant candidate, $Q_L(D_L) \gg 1$ (respectively $Q_G(D_G) \gg 1$). Therefore, if very likely, both candidates are background events, then $\Lambda(D_L, D_G) \approx \frac{I_{\Delta t}(D_L,D_G) I_{\mathbf{\Omega}}(D_L,D_G)}{Q_L(D_L) Q_G(D_G)}$. If the GW trigger is statistically significant and the EM candidate is likely a noise transient (respectively the GW event is a noise transient and the EM trigger is statistical significant), then $\Lambda(D_L, D_G) \approx \frac{I_{\Delta t}(D_L,D_G) I_{\mathbf{\Omega}}(D_L,D_G)}{Q_G(D_G)}$ (respectively $\Lambda(D_L, D_G) \approx \frac{I_{\Delta t}(D_L,D_G) I_{\mathbf{\Omega}}(D_L,D_G)}{Q_L(D_L)}$). Finally if both triggers, independently, have important statistical weight, then $\Lambda(D_L, D_G) \approx I_{\Delta t}(D_L, D_G) I_{\mathbf{\Omega}}(D_L, D_G)$. Moreover $P(\mathbf{\Omega}|H^C) = \frac{1}{4\pi}$ (agnostic choice), so $I_{\mathbf{\Omega}}(D_L, D_G) = 4\pi \int P(\mathbf{\Omega}|D_L, H_L^S) P(\mathbf{\Omega}|D_G, D_G^S) d\mathbf{\Omega}$. Again if both the GW and the EM sky localizations are poorly informative, then $P(\mathbf{\Omega}|D_L, H_L^S)$, $P(\mathbf{\Omega}|D_G, H_G^S) \approx P(\mathbf{\Omega}|H^C) = \frac{1}{4\pi}$, which implies $I_{\mathbf{\Omega}}(D_L, D_G) \approx 1$. On the other hand, if the GW (respectively EM) sky localization data is very informative, i.e. it indicates with high precision the sky location (θ_L, ϕ_L) (respectively (θ_G, ϕ_G)), meaning that $P(\mathbf{\Omega}|D_L, D_L^S) \approx \vec{\delta}(\mathbf{\Omega} - (\theta_L, \phi_L))$ (respectively $P(\mathbf{\Omega}|D_G, D_G^S) \approx \vec{\delta}(\mathbf{\Omega} - (\theta_G, \phi_G))$), then the skymap overlap becomes $I_{\mathbf{\Omega}}(D_L, D_G) \approx 4\pi P(\theta_L, \phi_L|D_G, H_G^S)$ (respectively $I_{\mathbf{\Omega}}(D_L, D_G) \approx 4\pi P(\theta_G, \phi_G|D_L, H_L^S)$). In the particular case, when both skymaps are very informative, the mathematical expression of the sky localization overlap is $I_{\mathbf{\Omega}}(D_L, D_G) \approx 4\pi\delta(\theta_L - \theta_L)\delta(\phi_G - \phi_G)$. This means that if the two directions (θ_L, ϕ_L) and (θ_G, ϕ_G) are distinct, then $I_{\mathbf{\Omega}}(D_L, D_G) = 0$, while if they are identical, then mathematically speaking one has $I_{\mathbf{\Omega}}(D_L, D_G) = \infty$. In reality, in this latter case, the value of $I_{\mathbf{\Omega}}(D_L, D_G)$ is limited by the characteristics of the instruments. Indeed, when one deals with experimental physics, zero uncertainty does not exist. The discussion about the behavior of $I_{\Delta t}(D_L, D_G)$ is less obvious because, up to date, it is not clear what the prior $P(t_c^{\rm ASH}, t_{\rm light}^{\rm ASH}|H^C)$ should be. Indeed this probability accounts for the difference of the arrival times for the two signals. If the GW and the EM signal would be emitted at the same time, under the assumption of graviton propagation at the light speed, one would have $P(t_c^{\rm ASH}, t_{\rm light}^{\rm ASH}|H^C) = \delta(t_c^{\rm ASH} - t_{\rm light}^{\rm ASH})$. But such a thing is not expected. The main reason is that right after the coalescence, the matter density around the binary remnant black hole is very high, which means that the medium is optically thick. In these conditions, the optical path length is short, the photons scatter on the surrounding atoms, and so the merger remnant is invisible for an external observer. Once the ejecta expands enough and the baryon density is sufficiently low, the medium becomes transparent and the EM signal can propagate towards us. This is why one would expect $t_{\rm light}^{\rm ASH} - t_c^{\rm ASH} > 0$, when the two times are measured at the same spatial location.

Nevertheless, given that, to date, there exists only one example of a simultaneous measurement of $t^{\rm ASH}_{\rm light}$ and $t^{\rm ASH}_c$, the option $t^{\rm ASH}_{\rm light} - t^{\rm ASH}_c < 0$ should not be neglected. However, this is to say that one needs a prior for $P(t^{\rm ASH}_c, t^{\rm ASH}_{\rm light}|H^C)$. The constraints on the arrival times $t^{\rm ASH}_{\rm light}$ and $t^{\rm ASH}_c$ are, in general, very good (around 1 ms of imprecision). It means that, if $t^{\rm ASH}_{c,L}$ and $t^{\rm ASH}_{\rm light,G}$ denote the measured values, then $P(t^{\rm ASH}_c|D_L, H^S_L) \approx \delta(t^{\rm ASH}_c - t^{\rm ASH}_{c,L})$ and $P(t^{\rm ASH}_{\rm light}|D_G, H^S_G) \approx \delta(t^{\rm ASH}_{\rm light} - t^{\rm ASH}_{\rm light,G})$. Moreover, the arrival time overlap reads $I_{\Delta t}(D_L, D_G) = \int\int \frac{\delta(t^{\rm ASH}_c - t^{\rm ASH}_{c,L})\delta(t^{\rm ASH}_{\rm light} - t^{\rm ASH}_{\rm light,G})}{P(t^{\rm ASH}_c, t^{\rm ASH}_{\rm light}|H^C)} dt^{\rm ASH}_c dt^{\rm ASH}_{\rm light}$, which, after mathematical development, becomes $I_{\Delta t}(D_L, D_G) = \frac{1}{P(t^{\rm ASH}_{c,L}, t^{\rm ASH}_{\rm light,G}|H^C)}$. If in addition, it is considered that the arrival time offset should be in some range, say $t^{\rm ASH}_c - t^{\rm ASH}_{\rm light} \in [t_{\rm unr} - \frac{\Delta T_{\rm unr}}{2}, t_{\rm unr} + \frac{\Delta T_{\rm unr}}{2}]$, then $I_{\Delta t}(D_L, D_G) = \Delta T_{\rm unr}$ if $t^{\rm ASH}_{c,L} - t^{\rm ASH}_{\rm light,G} \in [t_{\rm unr} - \frac{\Delta T_{\rm unr}}{2}, t_{\rm unr} + \frac{\Delta T_{\rm unr}}{2}]$ and $I_{\Delta t}(D_L, D_G) = 0$ otherwise. One should remark the behaviour in the extreme cases: when $\Delta T_{\rm unr} \to \infty$, then $I_{\Delta t}(D_L, D_G) \to \infty$ whatever $t^{\rm ASH}_{c,L}$ and $t^{\rm ASH}_{\rm light,G}$; when $\Delta T_{\rm unr} \to 0$, then $I_{\Delta t}(D_L, D_G) \to 0$, for all $t^{\rm ASH}_{c,L}$ and $t^{\rm ASH}_{\rm light,G}$. These results are expected. Indeed, the former case corresponds to the situation where there is no constraint, so the probability is maximum for all input values. On the other hand, the latter case corresponds to the situation where the constraint is infinite.

In this paragraph, I present the method for the calculation of the FAR, given two lists of *PyCBC* and *targeted-search* triggers, noted $\{D^i_L\}$ and $\{D^i_G\}$. In the preceding set expressions, D^i_L (respectively D^i_G) stands for the detection parameters of the $i^{\rm th}$ LIGO (respectively Fermi-GBM) candidate. Among the parameters, of particular interest are the arrival time of the GW signal, $t^{i,{\rm ASH}}_{c,L} \in D^i_L$, and the arrival time of the EM signal, $t^{i,{\rm ASH}}_{\rm light,G} \in D^i_G$. Even if, as noted above, there is no absolute knowledge about what the quantity $t^{\rm ASH}_c - t^{\rm ASH}_{\rm light}$ should be, one can confidently assume an upper limit for its absolute value (for example 50 s), noted $\Delta T^{\rm upper}$. Now two processes are executed: (i) the *targeted-search* triggers is time shifted by an amount higher than $2\Delta T^{\rm upper}$, i.e. $t^{i,{\rm ASH}}_{\rm light,G} \to t^{i,{\rm ASH}}_{\rm light,G} + 2\Delta T^{\rm upper}$ and (ii) set of associations distant in time by less than $\Delta T^{\rm upper}$, i.e. $\{(D^i_L, D^j_G)$ such that $|t^{i,{\rm ASH}}_{c,L} - t^{j,{\rm ASH}}_{\rm light,G}| < \Delta T^{\rm upper}\}$, is considered. Each such association contains two triggers which, before the time shift, were distant by more than $\Delta T^{\rm upper}$, thus it is assumed as a chance coincidence. Hence, the corresponding statistics $\Lambda(D^i_L, D^j_G)$ belong to the distribution of background rankings. Thus, by repeating lots of times these two operations, a FAR distribution is derived.

2.2.3 O1 and O2 data analysis results

Here I apply the mathematical framework, presented in the previous subsection, for the O1 and O2 *PyCBC* triggers and their *targeted-search* counterpart candidates. One can easily remark from above that in order to assign a joint ranking statistic for a pair of triggers, one needs to compute $Q_L(D_L), Q_G(D_G), I_{\Delta t}(D_L, D_G)$ and $I_{\mathbf{\Omega}}(D_L, D_G)$. I make the following choices: $Q_L(D_L)$ and $Q_G(D_G)$ uniquely depend on the $\hat{\rho}_{gw}$ and the

LLR; $I_{\Delta t}(D_L, D_G)$ (respectively $I_{\mathbf{\Omega}}(D_L, D_G)$) is a function of only the ***PyCBC*** and the *targeted-search* trigger times (respectively skymaps), $t_{c,L}^{\mathrm{ASH}}$ and $t_{\mathrm{light,G}}^{\mathrm{ASH}}$ (respectively $\mathbf{\Omega}_L$ and $\mathbf{\Omega}_G$). Therefore, in order to calculate $Q_G(\mathrm{LLR}) = \frac{P(\mathrm{LLR}|H_G^N)}{P(\mathrm{LLR}|H_G^S)}$, the LLR dependence of the probability distribution functions of the background and the real short GRB signal events needs to be computed. I use the same set of real signals as in Kocevski et al. [2018]. Additionally, the Fermi-GBM team tried the *targeted-search* on a large set of random times during O2, providing thus the list of background events. I fit, by means of a kernel density estimation (KDE) procedure, the histogram of real signals (respectively noise triggers), on the range of LLR going from 5 to 2000 (respectively 170). If the choice of the lower limit was explained in Subsection 2.2.1, the upper limit selections are justified by the quality of the KDE fitting. Moreover, for real short GRBs (noise triggers) possessing $\mathrm{LLR} \geq 2000$ ($\mathrm{LLR} \geq 170$), I assume $P(\mathrm{LLR}|\mathrm{H_G^S}) \propto \mathrm{LLR}^{-4}$ ($P(\mathrm{LLR}|\mathrm{H_G^N}) \propto \mathrm{LLR}^{-4}$). While for the real events, such a power law with exponent -4 is consistent with a population of binaries which is uniformly distributed in the Universe, concerning the background distribution, this prior only represents a conservative choice. In a similar way, I realize the derivation of the $Q_L(\hat{\rho}_{gw}) = \frac{P(\hat{\rho}_{gw}|H_L^N)}{P(\hat{\rho}_{gw}|H_L^S)}$. Therefore, for the background events, the KDE fitting is done over the range $\hat{\rho}_{gw} \in [8.0, 10.6]$. Also for $\hat{\rho}_{gw} \geq 10.6$, the prior $P(\hat{\rho}_{gw}|H_L^N) \propto \hat{\rho}_{gw}^{-4}$ is used [Callister et al., 2017]. On the other hand, there is no real single interferometer compact binary coalescence event during O1 and O2. This together with consistency arguments led to the assumption $P(\hat{\rho}_{gw}|H_L^S)$ for all $\hat{\rho}_{gw} \geq 8$. The different steps used in the derivation of the four density distributions, $P(\mathrm{LLR}|H_G^N)$, $P(\mathrm{LLR}|H_G^S)$ and $P(\hat{\rho}_{gw}|H_L^N)$, are illustrated in Figure 2.6. Once these distributions are calculated, one can easily derive the LIGO and the Fermi-GBM Bayes factors $Q_L(\hat{\rho}_{gw})$ and $Q_G(\mathrm{LLR})$. These quantities are shown in Figure 2.7. Intuitively, one would expect the Bayes factors to be decreasing functions of the individual statistical significances. But in Figure 2.7, one can easily remark the presence of rapid oscillations contrary to our prior belief. It is worth mentioning that these spikes are not real representations of the observational data. Actually, they are numerical artifacts, due to the bad KDE fitting. Even if the non-monotonicity of the Bayes factors is unexpectable and probably physically wrong, given the conversion of the joint ranking Λ into a FAR, the worry of a fundamental mistake can be eliminated. Additionally, I will show later that the pipeline sensitivity is essentially not impacted by this artificial behavior of the Bayes factors.

Even if the behavior of the skymap overlap $I_{\mathbf{\Omega}}(\mathbf{\Omega}_L, \mathbf{\Omega}_G)$ was discussed in Subsection 2.2.2, I focus here on the particular features of the present work. Given that only single interferometer triggers are considered, the localization of the GW triggers is largely uninformative. Indeed, contrary to the case of coincident triggers where the difference in the arrival times of the GW signal at the different detectors is used for

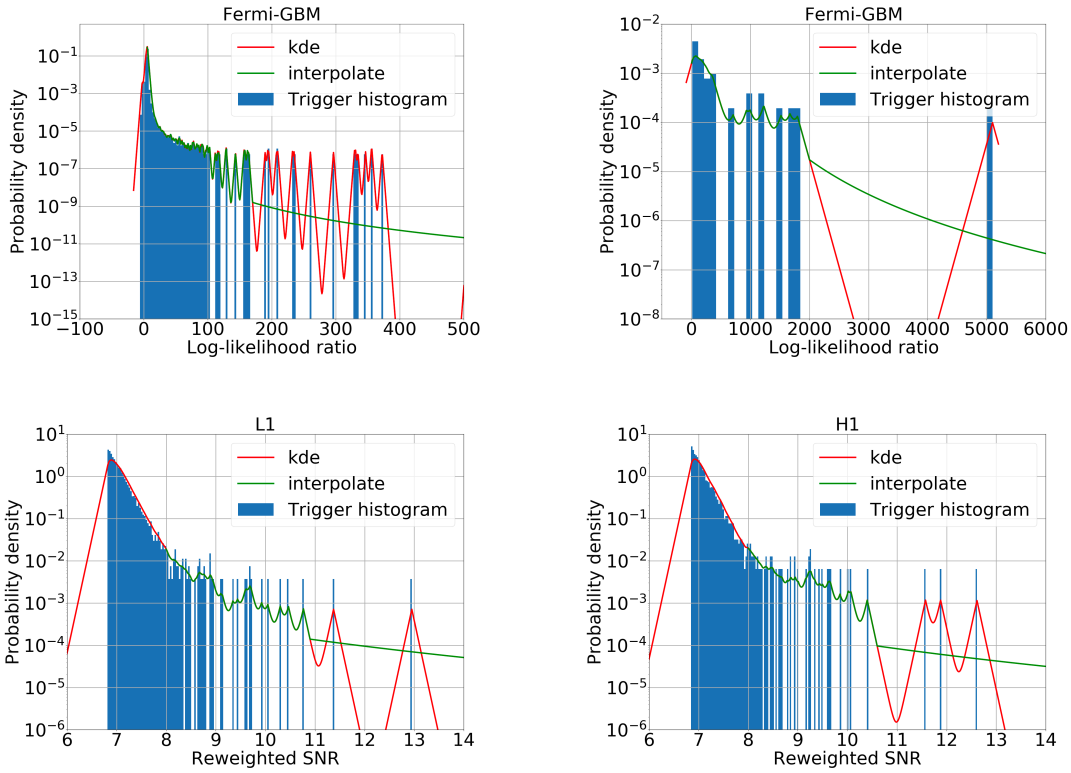

Fig. 2.6 The stages employed in the derivation of $P(\mathrm{LLR}|H_G^N)$ (top left), $P(\mathrm{LLR}|H_G^S)$ (top right), and $P(\hat{\rho}_{gw}|H_L^N)$ for the LIGO Livingston (bottom left) and LIGO Hanford (bottom right) interferometers. The histograms of the data samples are on blue, the KDE fitting appears on red. In green, the interpolation of the fitting over the ranges $\mathrm{LLR} \in [5, 170]$ (for the Fermi-GBM backgrounds), $\mathrm{LLR} \in [5, 2000]$ (for the Fermi-GBM real signals) and $\hat{\rho}_{gw} \in [8.0, 10.6]$ (for the GW noise events) with the functions LLR^{-4} and $\hat{\rho}_{gw}^{-4}$ for $\mathrm{LLR} \geq 170$ (for the EM noise transients), $\mathrm{LLR} \geq 2000$ (for the short GRB transients) and respectively $\hat{\rho}_{gw} \geq 10.6$ (for the GW backgrounds).

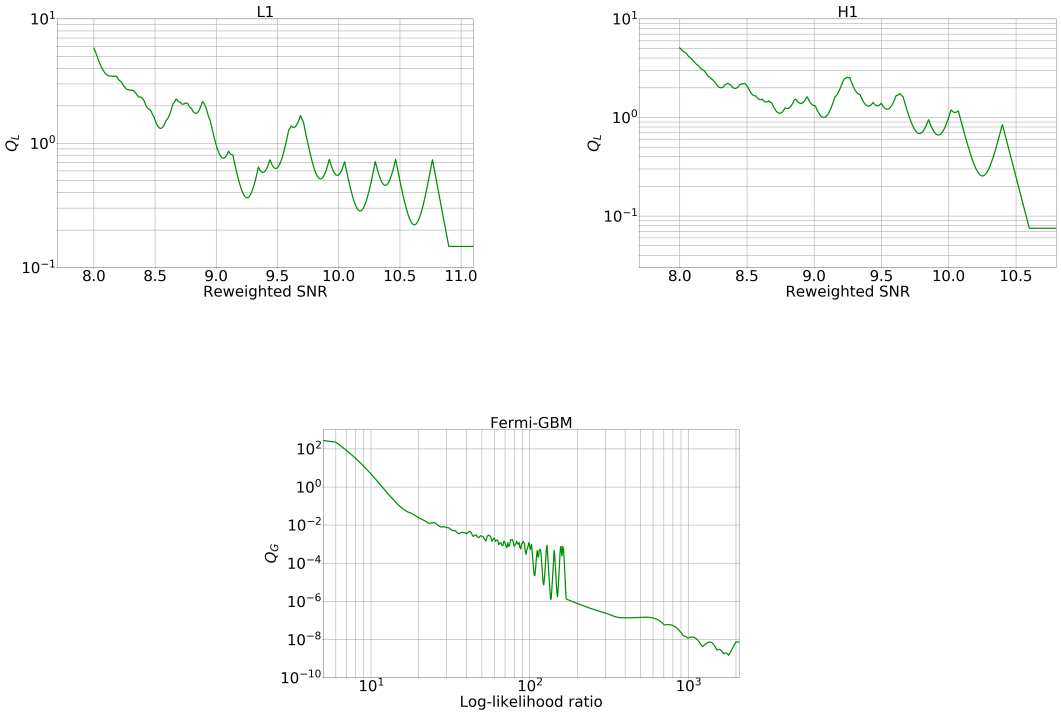

Fig. 2.7 On top, the LIGO Bayes factor Q_L as a function of $\hat{\rho}_{gw}$ for the LIGO Livingston (left) and the LIGO Hanford (right) interferometers, during O2. On bottom, the LLR dependence of the Fermi-GBM Bayes factor Q_G, over the same period of time.

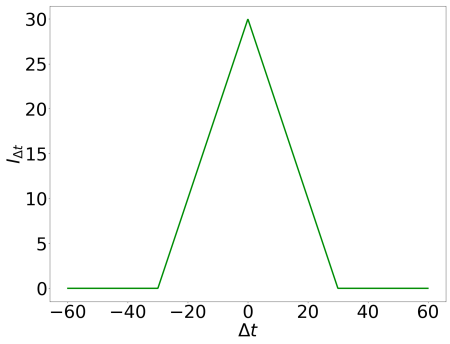

Fig. 2.8 $I_{\Delta t}$ versus Δt.

spatial triangulation, in the case of the single interferometer events, one can only use the directional response of the interferometer, whatever the sky position of the GW source. Thus, the 50% (respectively 90%) credible regions of a single interferometer trigger cover areas spread over 8000 (respectively 24000) square degrees. Finally with respect to $I_{\Delta t}(t^{\rm ASH}_{c,L}, t^{\rm ASH}_{\rm light,G})$, I recall that the value of this quantity depends on the prior $P(t^{\rm ASH}_{c}, t^{\rm ASH}_{\rm light}|H^{C})$ which is largely unconstrained. For the present study, the following assumption is used

$$I_{\Delta t}(t^{\rm ASH}_{c,L}, t^{\rm ASH}_{\rm light,G}) = \begin{cases} 30 - \left|\frac{\Delta t}{1s}\right| & \text{if } |\Delta t| < 30\,\text{s} \\ 0 & \text{otherwise} \end{cases}, \tag{2.24}$$

where $\Delta t = t^{\rm ASH}_{c,L} - t^{\rm ASH}_{\rm light,G}$ is the difference between the arrival times of the GW and the EM signals at the geocenter, and respectively the Fermi-GBM satellite. The dependence of $I_{\Delta t}$ with Δt is presented in Figure 2.8. This choice favors an association of signals close in time and forbids signals separated by more than $30\,$s. Also, by considering such a form for $I_{\Delta t}$, no arrival chronology is preferred over the others. Finally, one might consider other similar priors, but the final results are expected to be equivalent, as long as the forbidden time offsets are the same and $I_{\Delta t}$ is slowly varying.

So for each *PyCBC* trigger assigned with $(\hat{\rho}_{gw}, \mathbf{\Omega}_L, t^{\rm ASH}_{c,L})$, its *targeted-search* counterpart candidate assigned with $(\mathrm{LLR}, \mathbf{\Omega}_G, t^{\rm ASH}_{\rm light,G})$ is considered. This represents the set of foreground associations. For each pair of triggers belonging to this set, I calculate $Q_L(\hat{\rho}_{gw})$, $Q_G(\mathrm{LLR})$, $I_{\mathbf{\Omega}}(\mathbf{\Omega}_L, \mathbf{\Omega}_G)$ and $I_{\Delta t}(t^{\rm ASH}_{c,L}, t^{\rm ASH}_{\rm light,G})$, and finally the joint ranking statistic $\Lambda(\hat{\rho}_{gw}, \mathbf{\Omega}_L, t^{\rm ASH}_{c,L}, \mathrm{LLR}, \mathbf{\Omega}_G, t^{\rm ASH}_{\rm light,G})$. In order to derive the FAR distribution, one needs the set of background associations. For this I consider the same set of GW triggers, while for the set of EM candidates I run the *targeted-search* over the 23 days centered at GPS time 1180561923. This GPS time is the coalescence time of the *PyCBC* trigger of the most interesting foreground association. It should be noted that, in

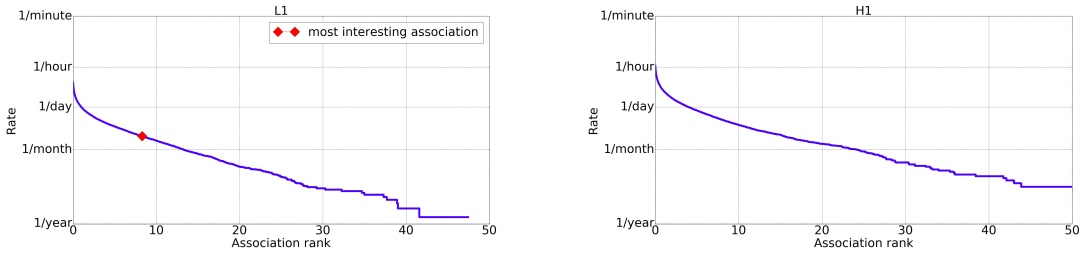

Fig. 2.9 Background FAR versus joint ranking Λ, for O2. The distribution corresponding to the background pairs of Fermi-GBM triggers and LIGO-Livingston (respectively LIGO-Hanford) triggers is on left (respectively right). On the left panel, the red diamond illustrates the position of the most interesting foreground association.

this way, the FAR value is not completely correct for each foreground pair. Indeed, the *targeted-search* should be run over the entire O1 and O2, instead of only 23 days around a particular GPS time. This choice has been done for computational cost reasons. Then, the set of Fermi-GBM triggers is time shifted by a non-zero integer multiple of $50\,\mathrm{s}$ with respect to the set of LIGO triggers. The joint ranking statistic is calculated for the new pairs. This procedure is repeated multiple times. According to Subsection 2.2.2 and the expression of $I_{\Delta t}$ from Equation 2.24, the absolute value of the time shift should be higher than $60\,\mathrm{s}$. So the case of the time shifts equals to $+50\,\mathrm{s}$ and $-50\,\mathrm{s}$ seems problematic. This inconsistency has been noted only after the publication of Stachie et al. [2020a]. However, a rapid manual verification allows to confirm that there is no real association in the foreground set, such that one messenger arrives earlier with respect to the other messenger by an amount of time situated in between $[25\,\mathrm{s}\,,\,30\,\mathrm{s}]$. After all, when the joint ranking statistic is calculated for a large number of background associations, I derive the background FAR. The two distributions, corresponding to the two LIGO interferometers, are illustrated in Figure 2.9. A comparison of the FAR from Figure 2.9 and the FAR one would obtain if the LIGO Bayes factor is completely uninformative, i.e. $Q_L(\hat{\rho}_{gw}) = 1$, for all $\hat{\rho}_{gw}$, is proposed in Figure 2.10. One can conclude, that the non-physical spikes presented in the LIGO Bayes factor function have no impact on the output results. Before having a look at the most significant associations, it is interesting to compare the FAR distributions of the background and foreground. This is realized in Figure 2.11. One can easily see that the distribution of inverse false alarm rates for the foreground associations is away from the background association corresponding distribution by less than 3σ errors. This means that most (or all) of the foreground associations are not of astrophysical origin. This behavior is expected from the beginning, given that the number of associations considered in this study is much

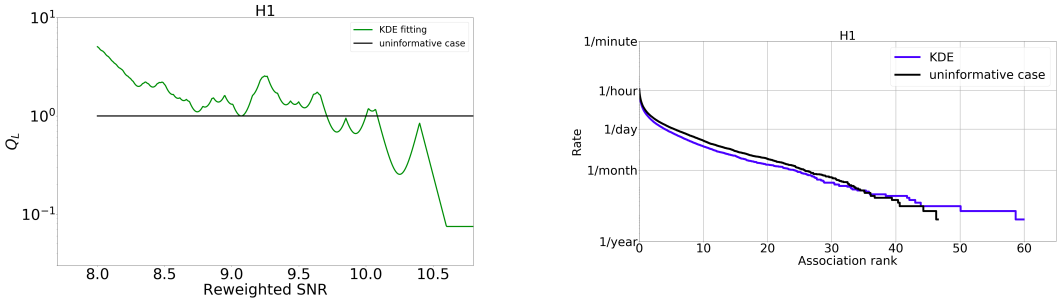

Fig. 2.10 On left, Q_L versus $\hat{\rho}_{gw}$ for both the uninformative case (on black) and the quantity obtained empirically from the distributions $P(\hat{\rho}_{gw}|H_L^S)$ and $P(\hat{\rho}_{gw}|H_L^N)$ (on green). On right, the corresponding O2 FAR distributions. These results concern the LIGO-Hanford data.

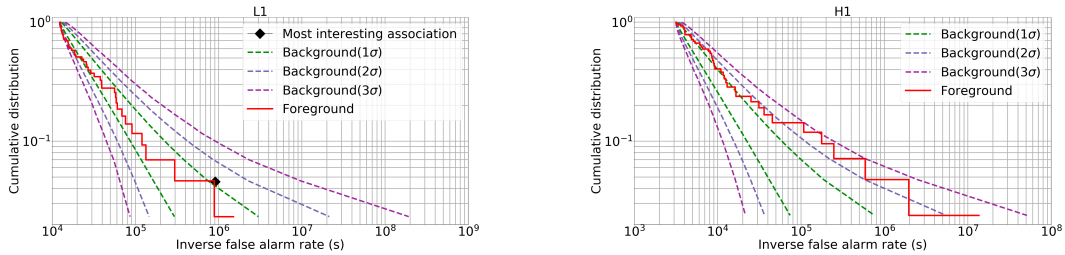

Fig. 2.11 On left (right), the cumulative density function of the inverse false alarm rate for the background and the foreground associations when the LIGO-Livingston (respectively LIGO-Hanford) GW triggers are considered. For the background associations, the 1σ, 2σ and 3σ uncertainties are provided too. On the left plot, the diagram coordinates of the most interesting foreground association is equally provided.

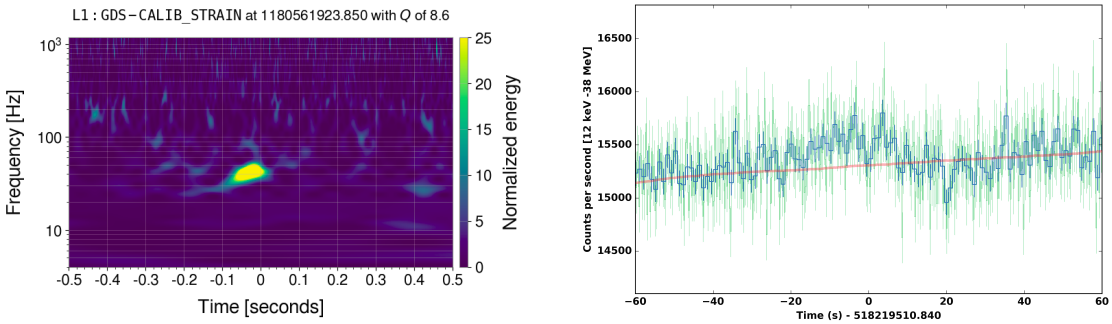

Fig. 2.12 On left, frequency-time diagram of the power measured at LIGO-Livingston near June 03, 2017 21:51:45 UTC. On right, the Fermi-GBM lightcurve (summation of all NaI detector photon counts with energies in between $12\,\mathrm{keV}$ and $38\,\mathrm{keV}$) of the *targeted-search* counterpart.

larger than the expected rate of multimessenger signals. Moreover, Figure 2.11 suggests that there is no foreground association having a $\mathrm{FAR} < \frac{1}{\mathrm{year}}$.

Once the FAR was calculated for each O2 foreground association, more focused analysis is done for the 80 pairs with the best statistic. Concerning the *PyCBC* triggers, I realize manual analysis consisting in detector characterization, realized by means of Omicron Scans and Used Percentage Vetoes [Abbott et al., 2018b, 2016b; Isogai, 2010]. This procedure led to the rejection of 64 candidates. For the GW triggers surviving this first test, parameter estimation [Veitch et al., 2015] is realized. The candidates, for which the log Bayes factor is smaller than 5, are rejected. There are 12 such triggers. If a foreground association has a GW trigger which passes also this test, analysis of the lightcurve is realized for EM counterpart. 3 associations are rejected because the *targeted-search* triggers are due to poor background fits in the low-energy detectors of the Fermi-GBM scintillators. Finally, there is still one association, for which there is no obvious reason to reject it. The individual statistics are $\hat{\rho}_{gw} = 9.04$ and $\mathrm{LLR} = 30.63$. The arrival time offset is $0.7\,\mathrm{s}$. When analyzed with offline parameter estimation, the log Bayes factor of 12.3 still indicates more likely a signal than a Gaussian noise. The Omega scan of the GW trigger and the lightcurve of the EM counterpart are offered in Figure 2.12. On the left panel, the spectrogram of the *PyCBC* trigger ressembles a high mass binary chirp. Nonetheless, it can also be a glitch. The EM counterpart, on the other hand, represents very probably an excess of high energy photons coming from outside the satellite. Despite the promising GW and EM individual candidates, there are reasons to believe that the association is not due to a same astrophysical event. Indeed, the GW trigger, if real, indicates a very high mass binary (total mass higher than $200 M_{\odot}$), which is expected to be invisible for an EM external observer. Moreover, the sky localization of the EM trigger is consistent with the galactic plane. In addition,

it lasts more than $8\,\mathrm{s}$, which is much more than the typical duration of known short GRBs. Equally, the excess photons have low energies (soft spectrum), which is not a characteristic of the short GRBs. [Stachie et al., 2020a] conclude that the *targeted-search* event is associated with the X-ray binary Scorpius X-1, because almost at the same time was observed strong occultation step resulting from this galactic source. Finally, the FAR of the association is only $1.1 \times 10^{-6}\,\mathrm{Hz}$, which is not sufficient to claim a confident detection. In conlusion, there is no real astrophysical association between a GW signal and flux of high energy photons in the datasets.

2.3 Upcoming analyses

The different studies presented in Burns et al. [2019]; Hamburg et al. [2020]; Stachie et al. [2020a] are part of a larger effort to search for coincidences of Fermi-GBM and LIGO/Virgo sub-threshold triggers. During my PhD thesis I was part of a team, regrouping people from both LVC and Fermi-GBM collaborations, whose activity is dedicated to this multimessenger endeavor. Improvements to the current methods are in progress. In particular, I worked on the method search for EM counterparts to the O3 GW sub-threshold triggers. Very probably, this analysis will be an improved version of the work from Stachie et al. [2020a]. As part of the team, I had a few task to accomplish related to this activity. More specifically, I had to generate the entire set of O3 Fermi-GBM triggers, by means of the *targeted-search*. This output set is largely dominated by noise events, but it also contains the real GRBs occurring during the O3 period. Finally it is equally the set eventually holding in the targeted EM trigger in coincidence with a GW sub-threshold candidate. In addition to be the set of EM triggers needed to realized an analysis similar to the one described in the previous section, it also has a relevant importance for the study of the Fermi-GBM data separately. Indeed given that it represents the output of almost an year of data, continuously in time, this set of triggers is very representative for the output results one can have by running the *targeted-search* at a random GPS time. Thus, not only the rate of high LLR and non-GRB events can accurately be derived, but also the Fermi-GBM data search analysis (in this case the *targeted-search*) might be improved, in order to get rid of unwanted triggers, impacting the sensitivity of the coincidence search method. More specifically, the filtering strategy might be modified to take into account other particularities (and up to now unknown) of spurious events.

CHAPTER 3

Modulated gamma-ray precursors to GW mergers

The results from this Chapter will appear in an upcoming paper (*Stachie et al. (2021)* in prep).

3.1 Real GRBs with multiple emission peaks and proposed precursor signal models

Up to now, except for the case of GRB 170817A, the GRB γ-ray prompt emissions have been detected, either alone or together with the subsequent X-ray/optical/radio afterglow. Most of the time, such a signal consists in an excess of high energy photons, appearing in the γ-ray detectors as a photon counts peak. According to the existing knowledge about both the short and long GRBs, the γ-ray flaring is believed to be triggered by specific physical mechanisms: the gravitational collapse of a massive star (for long GRBs) and the coalescence of compact objects (for short GRBs). More precisely, it is thought that the EM emission starting time is posterior to these trigger processes by a few seconds, because the matter inside the corresponding relativistic jets needs to expand enough in order for the ejecta medium to be optically transparent. However, there are situations where GRBs have several γ-ray peaks, sometimes separated in times by hundreds of seconds, as was the case for GRB 160625B [Zhang et al., 2018]. Even if the different γ-ray flashes are not equivalent, mainly because they do not have the same intensity, the attribution of the physical mechanisms responsible for these bursts is controversial. The detection of a multi-peak γ-ray emission in coincidence with the GW originating from a compact binary coalescence, would allow to address more properly the question related to the EM flaring generation mechanism. Traditionally, the convention is to consider the peak possessing the highest brightness as the γ-ray prompt emission, while the other ones as precursor, if they occur before the main peak, or successor (or extended emissions) signals, if they occur after the main peak. In this chapter, of interest is the former type of EM flaring. An example of a short GRB prompt emission preceded by a precursor is shown in Figure 3.1.

For both short and long GRBs, many searches and claimed detections of precursor emissions exist in the literature [Lazzati, 2005; Burlon et al., 2008; Murakami et al.,

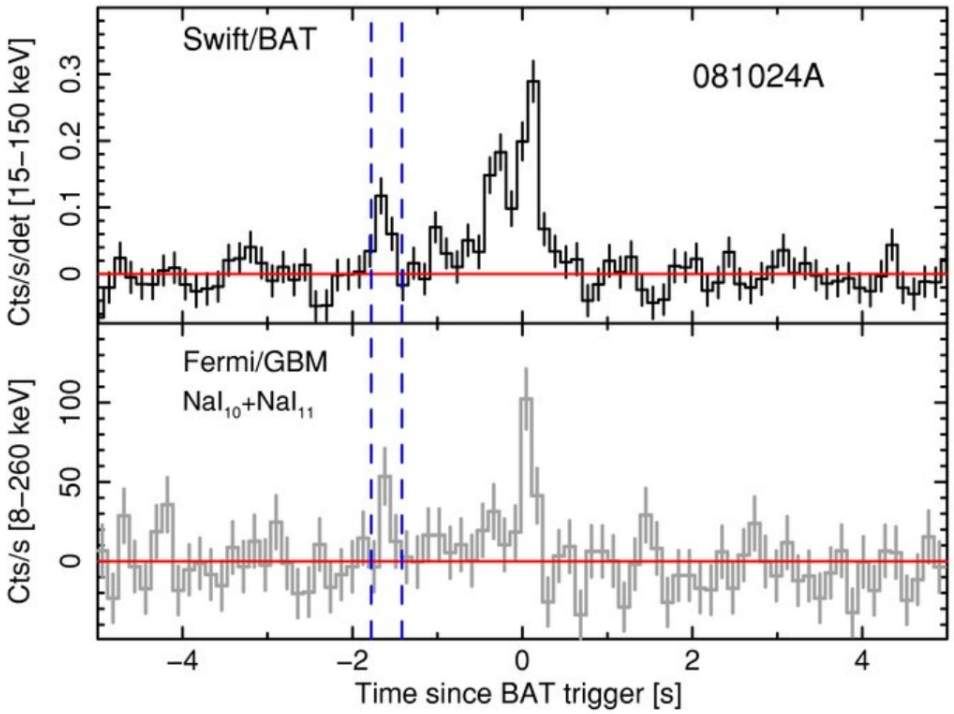

Fig. 3.1 *Swift/BAT* and Fermi-GBM lightcurves of GRB 081024A, containing two statistical significant bursts of photons. The picture is taken from Troja et al. [2010].

1991; Piro et al., 2005; Vanderspek et al., 2004; Page et al., 2007]. Because in this thesis I treat the case of EM counterparts to compact binary coalescences, in this chapter, I focus on the case of early emissions to short GRBs. Troja et al. [2010] lead a search for precursor signals to *Swift* short GRBs. More precisely, they use a wavelet transform based detection algorithm [Torrence and Compo, 1998], to search for an excess of photons into the data. Then, Troja et al. [2010] consider the EM signal candidate a GRB precursor if, in addition to the lower photon flux intensity, the candidate sky location is consistent with the localization of the main burst and if the two signals are separated by a non-zero amount of time where the detectors photon counts do not overcome the background rate. The output of the analysis indicates that $\sim 8\% - 10\%$ of the GRB samples possess early emission. Also, Troja et al. [2010] find no spectral hardness difference between the precursor and the main emission. Moreover, more than one precursor might exist, as in the case of GRB 090510 [Abdo et al., 2009]. Equally, for some GRBs, multiple detection of the precursor is realized by analyzing the data of another high energy observatory than *Swift*: Fermi-GBM detector for GRB 080124A [Stratta et al., 2008] and *Suzaku* [Mitsuda et al., 2007] detector for GRB 091117 [Hayashi et al., 2009]. Li et al. [2021] search for signal precursors in the third Swift/BAT short GRB Catalog. They find that 25 out of 124 GRBs present early emission. For some of them, a comparison of the precursor and the main peak temporal properties is done. More precisely, if one notes by $f_m^{\rm LI}$, $t_m^{\rm LI}$, $\rm FWHM^{LI}$, $t_r^{\rm LI}$, $t_d^{\rm LI}$ and $t_r^{\rm LI}/t_d^{\rm LI}$, the peak amplitude, the peak

time, the full width at half maximum, the rise time, the decay time and the asymmetry of a burst, then the conclusions of Li et al. [2021] are: a weak positive correlation in the $f_m^{\rm LI}$ indicating a same progenitor for the two (precursor and main burst) emissions; mild correlations in $t_r^{\rm LI}/t_d^{\rm LI}$, $\rm FWHM^{LI}$, $t_r^{\rm LI}$ and $t_d^{\rm LI}$ for the two flaring episodes; an order of magnitude difference in the $\rm FWHM^{LI}$ of the two EM emissions, pointing out that precursors are shorter duration signals than the main γ-ray flaring episodes.

In the literature, different physical models have been proposed to explain the existence of GRB precursor signals. Bernardini et al. [2013] assume that the GRB engine consists in a newborn magnetar. Others [Wang and Meszaros, 2007; Lipunova et al., 2009] explain the multiple signals within the more classical GRB model: generally, they consider a first collapse to a short-lived neutron star (responsible for the precursor) and then a second collapse to a black hole (responsible for the main emission). But, there are also explanations which invoke binary interaction hypotheses. For example, Most and Philippov [2020] show that one possible channel is represented by the force free interaction of the magnetospheres of the two magnetized neutron stars of a binary. In such a situation, a twist in the magnetic flux tube, powered by binary differential motion, is responsible for repeated flaring episodes. In the study of Most and Philippov [2020], the General Relativity electrodynamics equations are solved by means of numerical simulations. Thus, the neutron stars are modeled as $13\,$km spherical conductors with surface magnetic field strength $B_0^{\rm MOS}$. Therefore, inside the neutron stars, the line element is written $ds^2 = (-1+\beta_k\beta^k)dt^2 + 2\beta_k dx^k dt + \delta_{ij}dx^i dx^j$, with $\beta_i = -\epsilon_{ijk}\Omega^j x^k$. With this notation, $\mathbf{\Omega} = (0,0,0,\omega^{\rm MOS})$ is the orbital angular momentum, while t, x^k, δ_{ij}, ϵ_{ijk} are the time coordinate, the space coordinate, the Kronecker delta and the Levi-Civita tensor. In the corotating frame, the magnetohydrodynamics equation reads $E_i^{\rm MOS} = -\epsilon_i^{jk} v_j^{\rm MOS} B_k^{\rm MOS}$, where $\mathbf{E}^{\rm MOS}$, $\mathbf{B}^{\rm MOS}$ and $\mathbf{v}^{\rm MOS}$ are the electric field, the magnetic field and the spin vector of the neutron star. The EM flaring is powered by the magnetosphere interaction in a tight binary. The total EM energy writes $E_{\rm EM}^{\rm MOS} = \frac{1}{8\pi}\int((E^{\rm MOS})^2 + (B^{\rm MOS})^2)d^3\mathbf{x}$. Some part of this energy, noted $\mathcal{L}_{\rm dissipation}^{\rm MOS}$, is dissipated by Ohmic resistance due to formation of closed electrical circuit, while the remaining energy is transported away by the Poynting flux $\mathbf{S}_{\rm EM}^{\rm MOS} = \frac{1}{4\pi}\left[\mathbf{E}^{\rm MOS}\times\mathbf{B}^{\rm MOS} - \frac{1}{2}((\mathbf{E}^{\rm MOS})^2 + (\mathbf{B}^{\rm MOS})^2)\boldsymbol{\beta}\right]$. The distribution of the energy is done according to the conservation equation $\partial_t\left(\frac{1}{8\pi}((E^{\rm MOS})^2 + (B^{\rm MOS})^2)\right) + \boldsymbol{\nabla}\cdot\mathbf{S}_{\rm EM}^{\rm MOS} = \mathcal{L}_{\rm dissipation}^{\rm MOS}$. Finally the precursor peak luminosity, noted $\mathcal{L}_{\rm EM,max}^{\rm MOS}$, is estimated to be $\mathcal{L}_{\rm EM,max}^{\rm MOS} \approx \eta^{\rm MOS}\frac{(\psi^{\rm MOS})^2}{2} v_{\rm rec}^{\rm MOS}\frac{(R^{\rm MOS})^3}{(a^{\rm MOS})^4}E_0^{\rm MOS}$, where $\eta^{\rm MOS} \leq 1$, $\psi^{\rm MOS}$, $v_{\rm rec}^{\rm MOS}$, $R^{\rm MOS}$, $a^{\rm MOS}$ and $E_0^{\rm MOS}$ are the pre-factor quantifying the percentage of twisted flux energy available for reconnection, the (small) twist of the magnetic tube, the reconnection speed, the neutron star radius, the orbital separation and the unperturbed dipole configuration energy. Tsang et al. [2012] investigate the possibility of another flaring channel:

the neutron star crust shattering determined by the tidal forces of the companion binary compact object. In the study led by Tsang et al. [2012], the neutron star has a liquid core and a solid crust, the transition taking place for a baryon density $n_b^{\rm TSA} \sim 0.065\,{\rm fm}^{-3}$. At the base of the crust the shear modulus is $\mu^{\rm TSA} \sim 10^{30}\,{\rm erg\cdot cm}^{-3}$. The tidal forces of the binary companion drive several neutron star modes, but the only one investigated is the $l = 2$ spheroidal i crust-core interface mode, whose frequency is $f_{\rm mode}^{\rm TSA} \sim 100\,{\rm Hz}$ [McDermott et al., 1988]. In order to have resonance, one needs phase coherent tidal driving, which occurs for a timescale $t_{\rm res}^{\rm TSA} \sim 8 \times 10^{-2}\,{\rm s} \left(\frac{\mathcal{M}^{\rm TSA}}{1.2\,M_\odot}\right)^{-5/6} \left(\frac{f_{\rm mode}^{\rm TSA}}{100\,{\rm Hz}}\right)^{-11/6}$, with $\mathcal{M}^{\rm TSA}$ the chirp mass. The energy needed to break the crust is $E_b^{\rm TSA} \approx 5 \times 10^{46}\,{\rm erg} \left(\frac{\epsilon_b^{\rm TSA}}{0.1}\right)^2$, with $\epsilon_b^{\rm TSA}$ the crust dimensionless strain. Or the maximum energy of the i mode is $E_{\rm max}^{\rm TSA} \approx 5{\times}10^{50}\,{\rm erg} \left(\frac{f_{\rm mode}^{\rm TSA}}{188\,{\rm Hz}}\right)^{1/3} \left(\frac{Q^{\rm TSA}}{0.04}\right)^2 \left(\frac{M^{\rm TSA}}{1.4\,M_\odot}\right)^{-2/3} \left(\frac{R^{\rm TSA}}{12\,{\rm km}}\right)^2 q^{\rm TSA} \left(\frac{2}{1+q^{\rm TSA}}\right)^{5/3}$, where $Q^{\rm TSA}$ is the dimensionless overlap integral between the tidal field and the i mode [Lai, 1994], $M^{\rm TSA}$ and $R^{\rm TSA}$ are the neutron star mass and radius, while $q^{\rm TSA}$ is the binary mass ratio. Because $E_b^{\rm TSA} \ll E_{\rm max}^{\rm TSA}$, the crust breaks. The subsequent excited elastic energy is $E_{\rm elastic}^{\rm TSA} \approx 2 \times 10^{46}\,{\rm erg} \left(\frac{\epsilon_b^{\rm TSA}}{0.1}\right)^2$, while the tidal energy transfer is $\dot{E}_{\rm tidal}^{\rm TSA} = 10^{50}\,{\rm erg\cdot s}^{-1} \left(\frac{f_{\rm mode}^{\rm TSA}}{188\,{\rm Hz}}\right)^2 \left(\frac{E_b^{\rm TSA}}{10^{46}\,{\rm erg}}\right)^{1/2} \frac{Q^{\rm TSA}}{0.04}$. Given that $t_{\rm res}^{\rm TSA} \gg \frac{E_{\rm elastic}^{\rm TSA}}{\dot{E}_{\rm tidal}^{\rm TSA}} \sim 10^{-3}\,{\rm s}$, the crust shatters, determining the coupling of the elastic energy to the magnetic field. Finally, the estimated luminosity is $L^{\rm TSA} \sim 10^{48}\,{\rm erg\cdot s}^{-1}$.

A short GRB precursor, emitted by a binary compact object before the merger, would be modulated by the strong relativistic dynamics. Therefore, depending on the parameters of the binary, the EM signal would present a pattern, in the same way the GW signal resembles the theoretical modelled waveforms. An example of such a computed EM lightcurve, emitted by a NSBH binary, is proposed in Schnittman et al. [2018]. In this model, it is assumed that the surface of the neutron star emits thermal light, uniformly and isotropically. Noting by $m_{\rm NS}^{\rm SCH}$, $m_{\rm BH}^{\rm SCH}$ and $x^{\rm SCH} = \frac{D^{\rm SCH}}{G(m_{\rm NS}^{\rm SCH}+m_{\rm BH}^{\rm SCH})/c^2}$ the neutron star mass, the black hole mass and the orbital separation in units of gravitational radius ($D^{\rm SCH}$ being the binary components separation in units of meter), then the angular velocity can be expressed as

$$\Omega^{\rm SCH} = \left[64\frac{(x^{\rm SCH})^3}{(1+2x^{\rm SCH})^6} + \eta^{\rm SCH}\frac{1}{(x^{\rm SCH})^4} + \left(-\frac{5}{8\eta^{\rm SCH}} + (\eta^{\rm SCH})^2\right)\frac{1}{(x^{\rm SCH})^5}\right]^{1/2} (m_{\rm NS}^{\rm SCH}+m_{\rm BH}^{\rm SCH})^{-1}, \tag{3.1}$$

where $\eta^{\rm SCH} = \frac{m_{\rm NS}^{\rm SCH} m_{\rm BH}^{\rm SCH}}{(m_{\rm NS}^{\rm SCH}+m_{\rm BH}^{\rm SCH})^2}$. Equally, the orbital separation evolution is realized according to the 2.5 PN leading quadrupole radiation reaction terms, introduced in Peters [1964]:

$$\frac{dx^{\rm SCH}}{dt} = -\frac{64}{5}\eta^{\rm SCH}\frac{1}{(x^{\rm SCH})^3}. \tag{3.2}$$

Like in Campanelli et al. [2006b], the spacetime Riemannian metric can be put under

the diagonal form $g_{\mu\nu}^{\rm SCH} = diag(-\left(\frac{2}{1+(\psi^{\rm SCH})^4}\right)^2, (\psi^{\rm SCH})^4, (\psi^{\rm SCH})^4, (\psi^{\rm SCH})^4)$, where $\psi^{\rm SCH} = 1 + \frac{m_{\rm NS}^{\rm SCH}}{2r_{\rm NS}^{\rm SCH}} + \frac{m_{\rm BH}^{\rm SCH}}{2r_{\rm BH}^{\rm SCH}}$ is the conformal factor, expressed as a function of the Cartesian distances $r_{\rm NS}^{\rm SCH}$ and $r_{\rm BH}^{\rm SCH}$ to the neutron star and to the black hole. Finally, the photons travel in this dynamical relativistic spacetime, along geodesics parameterized by an affine variable λ and respecting the equation $\frac{d^2x^\rho}{d\lambda^2} = -\Gamma_{\mu\nu}^\rho \frac{dx^\mu}{d\lambda}\frac{dx^\nu}{d\lambda}$, with $\Gamma_{\mu\nu}^\rho$ the Christoffel symbol. The photons' path is integrated by means of the Monte Carlo radiation transport code *Pandurata* [Schnittman and Krolik, 2013], accounting for photon emission and absorption processes, Compton scattering and light polarization. Then, the subsequent EM energy, reaching a distant observer, is obtained. The EM signal is modulated by the binary orbital evolution. As the binary separation shrinks, the amplitude and the frequency of the EM power increase, in a similar way the GW signal does. In addition to that, inside an orbit, the modulation is due to the relativistic Doppler beaming and to the gravitational lensing.

Although radiation transport code is needed for a proper treatment of such a physical system, one might attempt to derive approximate output by means of analytical formulae. Indeed, concerning the relativistic Doppler beaming, following Dubus et al. [2010], if the neutron star moves with velocity $v_{\rm NS}^{\rm DUB}$ with respect to a distant observer and emits thermal radiation, whose spectral index is $\alpha^{\rm DUB} \in [0, 2]$, then the magnification factor writes

$$\left[\frac{1}{\gamma^{\rm DUB}\left(1 - \frac{v_{\rm NS}^{\rm DUB}}{c}\cos\zeta_1^{\rm DUB}\right)}\right]^{3-\alpha^{\rm DUB}}, \tag{3.3}$$

where $\gamma^{\rm DUB}$ and $\zeta_1^{\rm DUB}$ are the Lorentz factor and the angle between $\vec{v}_{\rm NS}^{\rm DUB}$ and the line of sight. Regarding the gravitational lensing effect, one might use the formulae from Narayan and Bartelmann [1996]. According to them, the neutron star emitted radiation is magnified by the gravitational field of its companion, by the factor

$$\begin{cases} \frac{(u^{\rm NAR})^2+2}{u^{\rm NAR}\sqrt{(u^{\rm NAR})^2+4}} & \text{for } \|u^{\rm NAR}\| \geq 1 \\ \\ \frac{2\sqrt{\frac{4Gm_{\rm BH}^{\rm NAR}D^{\rm NAR}}{c^2}}}{r_{\rm NS}^{\rm NAR}} & \text{for } \|u^{\rm NAR}\| \leq 1 \end{cases}, \tag{3.4}$$

where $u^{\rm NAR} = D^{\rm NAR}\sin\zeta_2^{\rm NAR}(R_{\rm E}^{\rm NAR})^{-1}$, with $D^{\rm NAR}$ the binary separation, $\zeta_2^{\rm NAR}$ the angle between the orbital separation and the line of sight, and $R_E^{\rm NAR}$ the Einstein radius. It is worth mentioning that $\zeta_2^{\rm NAR}$ depends on the binary inclination angle. The Einstein radius is defined as $R_{\rm E}^{\rm NAR} = \sqrt{\frac{4Gm_{\rm BH}^{\rm NAR}}{c^2}D^{\rm NAR}\cos\zeta_2^{\rm NAR}}$, with $m_{\rm BH}^{\rm NAR}$ the black hole mass. It should be noted that for small $\|u^{\rm NAR}\|$, i.e. when the neutron star is close or inside the Einstein ring, it is assumed that it is exactly behind its companion and its image is approximated as a ring with angular width equal to the neutron star angular diameter.

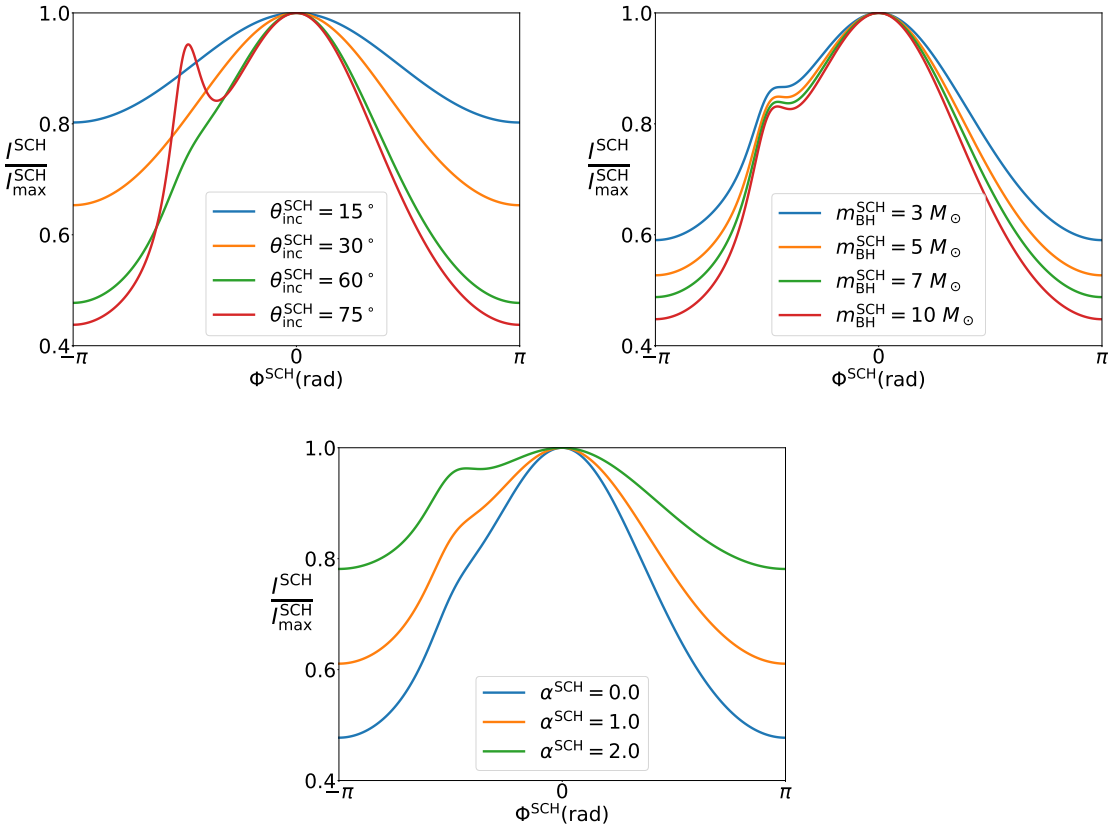

Fig. 3.2 Normalized EM intensity versus orbital phase, for EM chirps obtained as the sum of the relativistic Doppler beaming and of the gravitational lensing effects. In all simulations, the x axis covers an orbit and has its origin at the maximum of intensity. The orbital separation is, in all simulations, $\sim$ 10 gravitational radii ($G(m^{SCH}_{BH} + m^{SCH}_{NS})/c^2$). Top left: the inclination angle θ^{SCH}_{inc} is varied at constant $m^{SCH}_{NS} = 1.4\,M_\odot$, $m^{SCH}_{BH} = 10M_\odot$ and $\alpha^{SCH} = 0$; top right: the mass of the black hole m^{SCH}_{BH} varies, while $m^{SCH}_{NS} = 1.4\,M_\odot$ and $\alpha^{SCH} = 0$ are kept constant; bottom center: the binary components masses $m^{SCH}_{NS} = 1.4\,M_\odot$ and $m^{SCH}_{BH} = 10\,M_\odot$ are fixed, while the spectral index α^{SCH} varies.

In this case, one might make use of the formula proposed in Liebes [1964], and assume that the neutron star radius is $r^{NAR}_{NS} = 10$km. Finally, if one assumes orbital angular frequency evolution at the first Post-Newtonian expansion [Blanchet, 2014], the analytical expression of the EM power reaching an external observer is obtained by summing the expressions from Equations 3.3 and 3.4. In Figure 3.2, there is illustrated the variation of the normalized EM radiation intensity during an orbit. For all simulations, the origin of the orbital phase coincides with the maximum of the intensity, which corresponds to the neutron star position of maximum blueshift, i.e. when the neutron star points towards us with maximum velocity. Depending on the inclination angle θ^{SCH}_{inc} of the binary with respect to Earth, the gravitational lensing might be more or less pronounced. Indeed, the lensing amplification is favored for an aligned configuration of the neutron star - black hole - external observer geometrical system. This can be easily seen on

the top left panel of Figure 3.2, where a second local maxima (due to the gravitational lensing, and happenning when the neutron star and the Earth observer are on opposite sides with respect to the black hole) appears at high $\theta_{\rm inc}^{\rm SCH}$. The relativistic Doppler beaming increases with the velocity of the neutron star, as emphasized by Equation 3.3. This behavior is also shown on the top right panel of Figure 3.2, where the normalized intensity, outside the position of maximum blueshift, decreases with the mass of the companion black hole. Indeed, for the same orbital separation (expressed in units of gravitational radius), the higher the mass of the black hole the higher the velocity of the neutron star (in a circular orbit). The relativistic beaming factor also decreases with the spectral index $\alpha^{\rm SCH}$, as suggested by Equation 3.3, and verified by the bottom panel of Figure 3.2.

Similar predictions exist in the literature. For example, Haiman [2017] calculates the EM chirp emitted by the accretion disc photospheres of two black holes, of masses $10^4\,M_\odot \lesssim M^{\rm HAI} \lesssim 10^7\,M_\odot$, in a binary tight enough to be detectable by the future GW detector LISA [Amaro-Seoane et al., 2017]. In this thesis, I propose a method to search for EM signals, modulated by the orbital phase evolution of a binary prior to the merger. This work will be published soon in *Stachie et al. (2021) in prep.*

3.2 Search for signals modulated by the pre-merger BNS/NSBH orbital phase evolution

3.2.1 Flaring characteristics and statistical analysis of the Fermi-GBM data

This project is aimed at the detection of an excess of photons in the orbital phase space. More precisely, I am interested in those signals which, over several orbits, present the same flaring behavior, i.e. the maxima and the minima of intensity are positioned at the same place in the orbit. I assume that the evolution of the orbit is done according to the first Post-Newtonian expansion term [Blanchet, 2014]. Therefore, in the observer frame, the time dependence angular velocity is

$$\Omega(t) = \left(\frac{5}{256}\frac{1}{t_c - t}\right)^{3/8} \left(\frac{G\mathcal{M}}{c^3}\right)^{-5/8}, \tag{3.5}$$

where t_c is the coalescence time at the detector, G is the gravitational constant, c is the vacuum speed of light and $\mathcal{M}$ is the observer frame chirp mass. I also define the orbital phase by $\Phi_{\rm orbit}(t) = \int_{-30\,\rm s}^{t} \Omega(x)dx$.

In this study, I analyze the data from the Fermi-GBM instrument. I recall that Fermi-GBM has 14 detectors (12 NaI and 2 BGO scintillators) and 8 energy channels (after the collapse of the initial 128 channels). In order to search for an excess of photons occurring during some orbital phase window, and repeated for several orbits, I divide

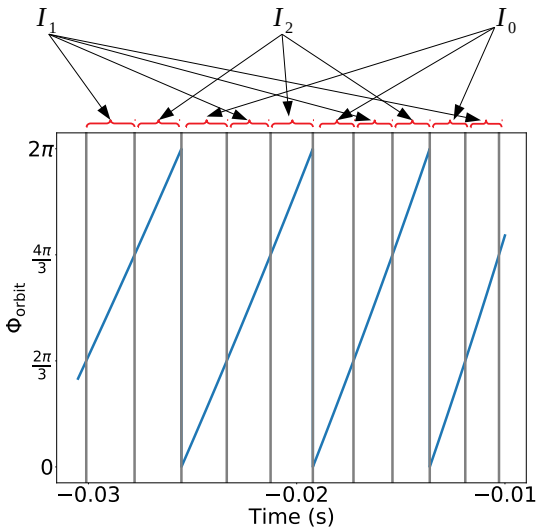

Fig. 3.3 The positions of I_0, I_1 and I_2, for $N_{\rm bins} = 3$. In blue, orbital phase $\Phi_{\rm orbit}$ versus time. The origin of the x axis corresponds to the merger time.

the orbital phase space (going from 0 to 2π) into $N_{\rm bins}$ equal intervals, as follows: $I_0 = \left[0, \frac{2\pi}{N_{\rm bins}}\right]$, $I_1 = \left[\frac{2\pi}{N_{\rm bins}}, 2\frac{2\pi}{N_{\rm bins}}\right]$, ..., $I_{N_{\rm bins}-1} = \left[(N_{\rm bins}-1)\frac{2\pi}{N_{\rm bins}}, 2\pi\right]$. The positions of the I_k intervals are illustrated in Figure 3.3. Then, an intermediate step of the statistical method is to estimate the photon background rate and to compute the foreground photons corresponding to the intervals I_k. Concerning the background, a first estimation is done in the time space, following Goldstein et al. [2019]: for a given time t_0, the total number of photon counts $N_{\rm photons}(t_0)$, corresponding to one of the 8 energy channels and to one of the 14 detectors, is summed up over a long duration T (here $T = 100\,$s) centered at t_0, and the background rate is simply evaluated as $\lambda_{\rm max}(t_0) = \frac{N_{\rm photons}(t_0)}{T}$. This procedure is repeated for several times, then the time dependence of the photon background rate, $\lambda_{\rm max}(t)$, is derived. In addition to the consideration of the Poisson uncertainty $\sigma^2_{\lambda_{\rm max}}(t_0) = \frac{\lambda_{\rm max}(t_0)}{T}$, a chi-squared χ^2 test is realized in order to analyze the quality of the fitting. The detector-energy channels, for which the fitting is bad, are discarded for the further statistical calculations. For a given $k \in [0, N_{\rm bins}]$, I obtain the I_k background photon number in the following way: first, the time space short duration intervals $[t^k_{i,\rm start}, t^k_{i,\rm end}]$ corresponding to I_k, i.e. $\Phi_{\rm orbit}([t^k_{i,\rm start}, t^k_{i,\rm end}]) \subset I_k$, are identified; secondly, the background photon number is calculated with the formula $\sum_i (t^k_{i,\rm end} - t^k_{i,\rm start}) \times \lambda_{\rm max}(\frac{t^k_{i,\rm start}+t^k_{i,\rm end}}{2})$. The I_k background photon number variance is derived in a similar way, i.e. $\sum_i (t^k_{i,\rm end} - t^k_{i,\rm start}) \times \sigma^2_{\lambda_{\rm max}}(\frac{t^k_{i,\rm start}+t^k_{i,\rm end}}{2})$. Regarding the foreground photons, for each $k \in [0, N_{\rm bins}]$, I sum up the photons corresponding to I_k. This process is easily achievable because each Fermi-GBM photon count initially assigned with a time t, might be matched with the index k, such that $\Phi_{\rm orbit}(t) \in I_k$.

Hereafter, by an excess of photons in the orbital phase space, I mean a set of adjacent intervals I_k, i.e. $\{I_i, I_{i+1}, \ldots, I_{i+j}\}$ with $0 \leq i \leq N_{\rm bins} - 1$ and $1 \leq i \leq N_{\rm bins}$, assigned

with a number of photons above the background estimation. Given that the search is designed for the detection of real astrophysical events, the set of detectors and energy channels, presenting an excess of photons, is expected to be coherent. Thus the signal is expected to indicate a reasonable (continuous function) spectrum, while the detectors with the photon surplus should point in the same direction in the sky. To a set of adjacent intervals $\{I_i, I_{i+1}, \ldots, I_{i+j}\}$, I assign a log likelihood ratio (hereafter LLR), following the same procedure as in Blackburn et al. [2015]; Kocevski et al. [2018]; Goldstein et al. [2019]. The technique was already presented in subsection 2.2.1. Nevertheless, I briefly summarize it here. Given the data $d^{\rm BLA}$, the hypothesis of noise and signal into the data $H_1^{\rm BLA}$ and the hypothesis of noise only into the data $H_0^{\rm BLA}$, then the expression of the statistical ranking is

$$\mathrm{LLR}(d^{\rm BLA}) = \ln \frac{P(d^{\rm BLA}|H_1^{\rm BLA})}{P(d^{\rm BLA}|H_0^{\rm BLA})}. \tag{3.6}$$

After some mathematical derivations and some assumptions that I do not repeat here, the same quantity might be written as

$$\mathrm{LLR}(d^{\rm BLA}) = \ln \sigma_{\mathcal{L}}^{\rm BLA} + \ln\left[1 + \mathrm{erf}\left(\frac{s_{\rm best}^{\rm BLA}}{\sqrt{2}\sigma_{\mathcal{L}}^{\rm BLA}}\right)\right] + \ln \Lambda^{\rm BLA}(d^{\rm BLA}|s_{best}^{\rm BLA}) + \tag{3.7}$$
$$\begin{cases} \ln\left[1 - \exp\left(-\frac{s_{\rm best}^{\rm BLA}}{\gamma^{\rm BLA}\sigma_{\mathcal{L}}^{\rm BLA}}\right)\right] - \beta^{\rm BLA} \ln s_{\rm best}^{\rm BLA} & \text{if } s_{\rm best}^{\rm BLA} \geq 0 \\ -\beta^{\rm BLA} \ln\left(\gamma^{\rm BLA}\sigma_{\mathcal{L}}^{\rm BLA}\right) & \text{if } s_{\rm best}^{\rm BLA} \leq 0 \end{cases}.$$

In the previous expression $\sigma_{\mathcal{L}} = \frac{1}{\sum_i \frac{(r_i^{\rm BLA})^2}{(\sigma_{d_i}^{\rm BLA})^2}}$, where $r_i^{\rm BLA}$ is the spectrally dependent sky detector response and $\sigma_{\rm d_i}^{\rm BLA}$ is the standard deviation of the expected data, the index i standing for a pair formed of a detector and an energy channel. $\Lambda^{\rm BLA}(d^{\rm BLA}|s) \equiv \frac{P(d^{\rm BLA}|H_1^{\rm BLA},s)}{P(d^{\rm BLA}|H_0^{\rm BLA})}$ designates the likelihood ratio, given the amplitude s of the signal. $s_{\rm best}^{\rm BLA}$ is the amplitude which maximizes the distribution $\ln \Lambda^{\rm BLA}(d^{\rm BLA}|s)$, obtained by the Newton iterative method. Finally $\gamma^{\rm BLA} = 2.5$ and $\beta^{\rm BLA} = 1$ are two constants, while $\mathrm{erf}(x) = \frac{2}{\sqrt{2}} \int_0^x \exp -t^2 dt$ is the error function. The last step, in this statistical method, consists in subtracting from the LLR, the quantity $\mathrm{LLR}_{\rm ref} = \beta^{\rm BLA} \ln \gamma^{\rm BLA} + (1 - \beta^{\rm BLA}) \ln \sigma_{\rm ref}^{\rm BLA}$, where $\sigma_{\rm ref}^{\rm BLA}$ is a constant that does not need to be specified, given that $1 - \beta^{\rm BLA} = 0$. The filtering techniques proposed in Goldstein et al. [2019] are still kept here. This procedure avoids among others the pollution of the background trigger set with soft events due to high energy cosmic rays interacting with the NaI detectors.

3.2.2 Pipeline sensitivity

3.2.2.1 The search method

A search attempting to detect a modelled signal should in principle be more sensitive than a search looking (blindly) just for an excess of energy/power. Therefore, a

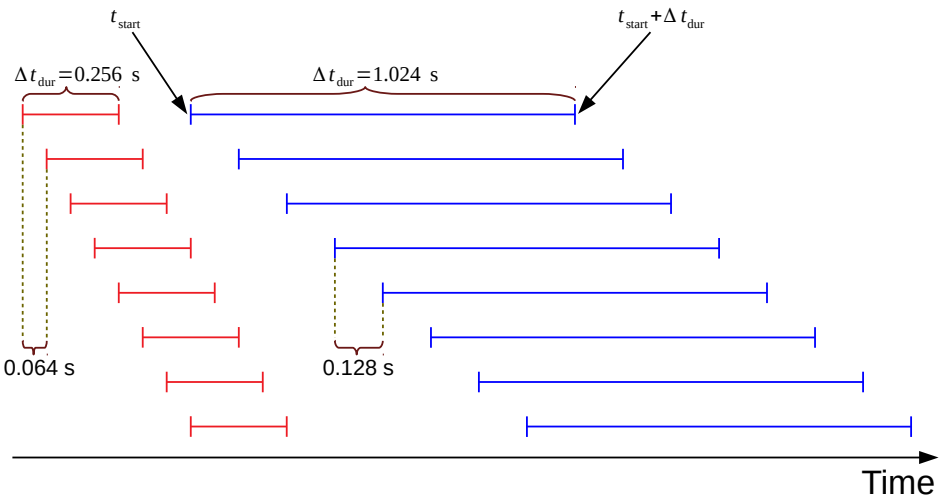

Fig. 3.4 The positions of the $[t_{\rm start}, t_{\rm start} + \Delta t_{\rm dur}]$ windows on the time axis. The time windows with $\Delta t_{\rm dur} = 0.256\,{\rm s}$ (as well as those with $\Delta t_{\rm dur} \in \{0.064\,{\rm s}, 0.128\,{\rm s}, 2.048\,{\rm s}\}$) are separated by $64\,{\rm ms}$. For the windows with $\Delta t_{\rm dur} = 1.024\,{\rm s}$ (as for those with $\Delta t_{\rm dur} \in \{2.048\,{\rm s}, 4.096\,{\rm s}, 8.192\,{\rm s}\}$), the application of the phase factor of 8 means that the time windows are separated by $\frac{1.024\,{\rm S}}{8} = 0.128\,{\rm s}$.

comparison of the proposed search (called hereafter the *chirp-search*) with the search from Goldstein et al. [2019] (called hereafter the *targeted-search*), used for the detection of un-modelled GRBs, is important. The *targeted-search* needs as input a GPS time, close enough to the compact binary merger time t_c, measured at Fermi. Indeed the *targeted-search* looks for a high energy photon excess over the $30\,{\rm s}$ preceding the input time. On the other hand, for a proper use of the *chirp-search*, one needs a good knowledge of both the merger time t_c at Fermi and the observer frame chirp mass $\mathcal{M}$. Indeed, the information concerning these two observables is essential for the conversion of the time space into orbital phase space (I_k intervals). Both searches are aimed to identify the time windows $[t_{\rm start}, t_{\rm start} + \Delta t_{\rm dur}] \subset [t_c - 30\,{\rm s}, t_c]$ where the EM signal is present, with $t_{\rm start}$ the arrival time of the first photon(s) and $\Delta t_{\rm dur}$ the duration of the signal. In both cases, the timescales $\Delta t_{\rm dur}$ over which the search is done are: $0.064\,{\rm s}$, $0.128{\rm s}$, $0.256\,{\rm s}$, $0.512\,{\rm s}$, $1.024\,{\rm s}$, $2.048\,{\rm s}$, $4.096\,{\rm s}$ and $8.192\,{\rm s}$. In order to properly cover the $30\,{\rm s}$ prior to the input GPS time, a $0.064\,{\rm s}$ phase shift is used for the four shortest timescales (i.e. $\Delta t_{\rm dur} \in \{0.064\,{\rm s}, 0.128\,{\rm s}, 0.256\,{\rm s}, 0.512\,{\rm s}\}$), while for the other timescales, the phase shift of factor 8 is used (e.g. the $1.024\,{\rm s}$ search windows are separated by $0.128\,{\rm s}$). The positions of the search time windows are also shown in Figure 3.4. It should be noted that, as mentioned in Chapter 2 for the case of the *targeted-search*, the LLR is maximized over a grid of sky positions and over three spectral Band functions, the *hard* ($\kappa = 0$), the *normal* ($\kappa = 1$) and the *soft* ($\kappa = 2$). In addition, for the *chirp-search*, for a given time window $[t_{\rm start}, t_{\rm start} + \Delta t_{\rm dur}]$, the EM signal is searched over several orbital phase space durations. More specifically, sets of adjacent intervals

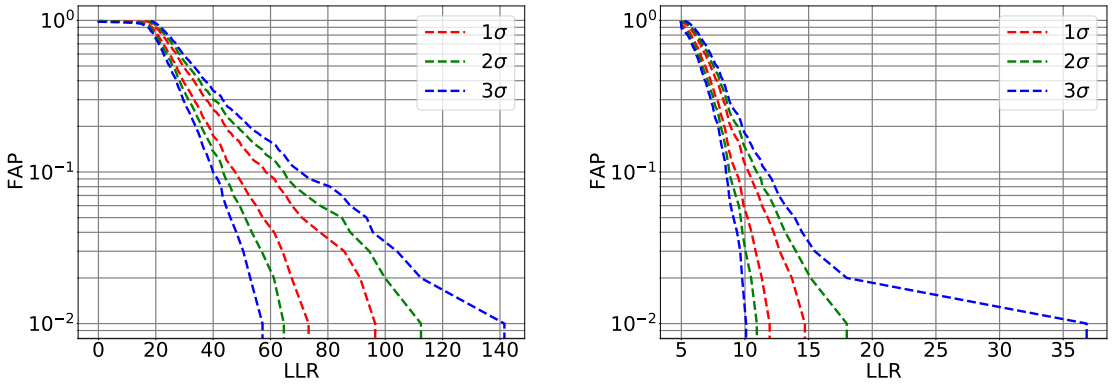

Fig. 3.5 FAP (assigned with 1σ, 2σ and 3σ uncertainties) versus LLR for background noise, for the *chirp-search* (left) and the *targeted-search* (right). The distributions have been obtained by running the two searches on the same 1000 random times distributed along the month of April 2019. For the *chirp-search*, the setting $N_{\text{bins}} = 10$ is used.

I_k of any length are considered. The coverage of the orbital phase space is realized by means of a phase factor of 2 (e.g. the subsets of length 4, 5, 7 are separated by 2, 3, 4 intervals I_k). Hereafter, for any of these searches, I assume that the output is the trigger assigned with the highest LLR. The reader of this thesis has to take some precautions: the choice of the consideration of only the highest LLR triggers is motivated in part by technical reasons. Indeed, it would be more correct to rather impose a LLR threshold motivated by the statistical significance of the background noise events. The raw output of the searches might contain several statistically significant candidates, and the true EM signal, if it exists, is not necessarily the one ranked first according to the LLR. On the other hand, such a choice would require the manual analysis of many candidates as can be seen later, and I want to avoid such a time expensive task here. Nonetheless, for the case of the few real O2/O3 GW events, presented in the next section, for the sake of clarity, the raw outputs of the two searches are investigated manually.

3.2.2.2 The case of background triggers

Before calculating the LLR of injected signals and of EM counterpart candidates to real GW events, one should know the statistical significance of the background noise. Indeed, both searches are sensitive to any coherent excess of photons, whatever its origin. Therefore, even if some prudence was taken into account by avoiding the input GPS times closer by less than 30 s to the start/end of the South Atlantic Anomaly (SAA) episodes, very high significant triggers not related to compact binary mergers survive. Some examples are: the solar flares; the γ-ray associated with galactic objects, such as pulsars; some phosphorescence events not filtered out by the code. In Figure 3.5 there is the false alarm probability (FAP) of the background noise, for both searches. I obtained

this distribution by running the code on random triggers. The FAP is calculated in the following way: given a trigger with LLR_0, then $\mathrm{FAP}(\mathrm{LLR}_0)$ represents the probability that, by running the code on a random trigger time t_{rand}, its statistical significance respects $\mathrm{LLR}(\mathrm{t_{rand}}) \geq \mathrm{LLR}_0$. One should note the similar behaviors of the FAP distributions corresponding to the two searches. Despite the resemblance, the *chirp-search* FAP is shifted to higher LLR values. Although to some extent this is normal, given that the *targeted-search* is included into the *chirp-search* (when the set of adjacent intervals I_k is the same as the entire set), some improvement of the filtering strategy is needed. Moreover, to date, the *chirp-search* is looking for signals of fixed time duration $\Delta t_{\mathrm{dur}} \in \{0.064\,\mathrm{s}, 0.128\,\mathrm{s}, 0.256\,\mathrm{s}, 0.512\,\mathrm{s}, 1.024\,\mathrm{s}, 2.048\,\mathrm{s}, 4.096\,\mathrm{s}, 8.192\,\mathrm{s}\}$, without taking care if these timescales cover an integer number of orbits. This situation is all the more problematic as the timescales are short (e.g. $0.064\,\mathrm{s}$) and situated far from the merger (where the orbital phase frequency is small). In this regime there might be durations covering a few (or less than one) orbits, which artificially create gaps in the orbital phase lightcurve. Lastly, the reader of this thesis should be aware of the fact that the *chirp-search* FAP distribution depends on the number of I_k intervals, N_{bins}. The case $N_{\mathrm{bins}} = 1$ corresponds to the case of the *targeted-search*, while a too high number of N_{bins} might artificially introduce large oscillations in the orbital phase lightcurve, generating high LLR fake triggers.

3.2.2.3 The case of injections

Once one knows the ranking statistic of background triggers, the next step for the evaluation of the sensitivity of the pipeline is to see how well injected signals are recovered. For a same light intensity amplitude of the injected EM signal, the smaller the FAP the higher the sensitivity. One should be aware that the output results depend on the choice of the injected signals. The *targeted-search* is generally used for the detection of the short GRB prompt emission and so looks for an excess of photons, whatever its pattern. On the other hand, the *chirp-search* is designed for the detection of modulated signals, i.e. those events with time dependent luminosity modelled by the orbital phase. Therefore, in order to have a chance to assess the suitability of the *chirp-search* in the case of modulated signals, one needs to avoid time independent (or similar) brightness injections. For this study, the choice consists in a set of functions, named *exotic waveforms*, parameterized by two variables: θ_{peak} and θ_{width}. More precisely, the expression of the normalized intensity of a *exotic waveform* is

$$\frac{I(\Phi_{\mathrm{orbit}})}{I_{\mathrm{max}}} = \begin{cases} 1 & \text{if } \theta_{\mathrm{peak}} - \frac{\theta_{\mathrm{width}}}{2} \leq \Phi_{\mathrm{orbit}}(t) \leq \theta_{\mathrm{peak}} + \frac{\theta_{\mathrm{width}}}{2} \\ 0 & \text{otherwise} \end{cases} . \tag{3.8}$$

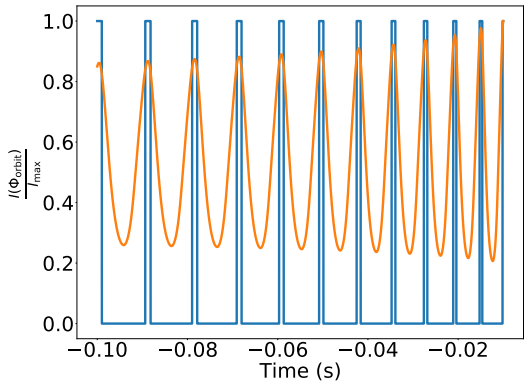

Fig. 3.6 Time dependence of the normalized lightcurve. In blue: the *exotic-waveform* parameterized by $\theta_{\rm peak} = 270°$ and $\theta_{\rm width} = 40°$; in orange: the lightcurve modulated by the relativistic beaming and the gravitational lensing. For both cases, the binary compact objects components have masses $m_1 = 10\,M_\odot$ and $m_2 = 1.4\,M_\odot$.

Based on this equation, the *exotic waveform* corresponds to an EM flaring occurring during and only during the orbital phase window $\left[\theta_{\rm peak} - \frac{\theta_{\rm width}}{2}, \theta_{\rm peak} + \frac{\theta_{\rm width}}{2}\right]$. The time evolution of the *exotic-waveform* is illustrated in Figure 3.6. For comparison purposes, in the same Figure 3.6, there is the more realistic lightcurve obtained by the summation of the relativistic Doppler beaming [Dubus et al., 2010] and the gravitational lensing [Narayan and Bartelmann, 1996], as described in the first section of this chapter (examples in Figure 3.2). While the behavior of the two types of lightcurves is similar, one should note that the *exotic-waveform* is a particular unrealistic case, where photons are not spread at all over regions of low luminosity.

Up to now, by *exotic-waveform* I meant the time evolution of the brightness. In order to completely characterize the incoming EM signal, one also needs the information related to the spectrum, i.e. the flux of photons versus the wavelength. The spectral analysis of Wang et al. [2020] indicates that the short GRB precursor spectra might be fit by blackbody, nonthermal cutoff power law and/or power-law models. For this study, I choose the spectra of the injected signals to be parameterized by $\kappa \in [0, 2]$, as follows: if $\kappa = 0, 1$ or 2, then the spectrum is *hard*, *normal* or *soft*. These templates are the same as the ones used by the *targeted-search* (and the *chirp-search*) for the recovery of the signals. The *normal* and *soft* templates are Band parameterized functions and have been introduced in Connaughton et al. [2015]. Regarding the *hard* spectrum, I make use of the comptonized version introduced in Goldstein et al. [2019]. Finally for a non-integer $\kappa \in [0, 2]$, the spectrum is assumed to be a weighted sum of two between the three *hard*, *normal* and *soft* templates. Thus, if $\kappa \in (0, 1)$, then the *hard* and *normal* templates have weights $(1 - \kappa)$ and κ, while if $\kappa \in (1, 2)$, then the *normal* and *soft* templates have weights $(2 - \kappa)$ and $(\kappa - 1)$. At this point, when both the signal amplitude and the spectrum are specified, there is a complete knowledge about

the injection. Nevertheless, in order to totally mimic the observational conditions, one should convert the time dependence brightness and the wavelength dependence photon flux distributions into Fermi-GBM detectors counts. I remind the reader of this thesis that the Fermi-GBM data consists of a list of photon counts assigned with arrival times and energies. Before deriving the histogram of photon counts, I show how the photon number rate in the detectors is computed. This conversion is possible if one knows the response of the NaI and BGO scintillators to any incoming flux of photons. It is worth mentioning that, in addition to the luminosity and the energetics related information, the direction of the incoming EM signal also plays a role. This sky localization dependency of the response is more stringent in the case of NaI crystals. For the BGO detectors, the response is relatively independent of the incoming photon flux direction. One should be aware that not only the emission directly incident on the detectors [Kippen et al., 2007] is responsible for the observed photon counts, but there is also a component accounting for the radiation originating from the Earth's atmosphere and the spacecraft scattering [Pendleton et al., 1999]. The calibration of the detectors was realized, prior to the launch of the satellite, on ground [Bissaldi et al., 2009]. Finally, the detector photon rate distributions are converted into photon counts by assuming Poisson statistic. One should note that a binning of the data is also done, the sampling being $0.5\,\mathrm{ms}$. Though, at first sight, this process might seem useless or even bad, this choice is motivated by technical reasons. Nonetheless, based on the Nyquist-Shannon sampling theorem, this binning allows the preservation of the harmonics up to $1000\,\mathrm{Hz}$, which is largely sufficient for the purpose of this project. I want to mention that the scripting tools used for the injections of signals have been largely developed by Tito Dal Canton.

From the above paragraph, to completely define an *exotic-waveform* injection, one needs the tuple $(t_c, m_1, m_2, f_{\mathrm{amp}}, t_{\mathrm{start}}, \Delta t_{\mathrm{dur}}, \theta_{\mathrm{peak}}, \theta_{\mathrm{width}}, \theta_{\mathrm{ra}}, \theta_{\mathrm{dec}}, \kappa)$, with f_{amp} the amplitude of the lightcurve, θ_{ra} the right ascension and θ_{dec} the declination angle. Moreover, I consider here a set of 1000 injections with t_c random during the month of April 2019. Additionally, $\log_2\left(\frac{\Delta t_{\mathrm{dur}}}{1\,\mathrm{ms}}\right)$, θ_{ra}, θ_{dec}, κ and θ_{peak} are chosen uniformly distributed in $[6, 13]$, $[-90°, 90°]$, $[-180°, 180°]$, $[0, 2]$ and $[0°, 360°]$. For an injection, once Δt_{dur} is fixed, then t_{start} and f_{amp} are assumed uniform in $[t_c - 30\,\mathrm{s}, t_c - \Delta t_{\mathrm{dur}}]$ and $[20\sqrt{\frac{0.064\,\mathrm{ms}}{\Delta t_{\mathrm{dur}}}}, 50\sqrt{\frac{0.064\,\mathrm{ms}}{\Delta t_{\mathrm{dur}}}}]$. The choice for t_{start} is simply the requirement to ensure $[t_{\mathrm{start}}, t_{\mathrm{start}} + \Delta t_{\mathrm{dur}}] \subset [t_c - 30\,\mathrm{s}, t_c]$, while the distribution of f_{amp} was derived empirically in order to: (i) have sufficient injections above the ranking statistic of noise triggers and (ii) have similar statistical significance among triggers of different durations. Indeed, given an amplitude, the higher the flaring duration the higher the number of incoming photons and so the bigger the LLR (and the smaller the $\mathrm{FAP(LLR)}$). Finally, for all the injections in this section, I consider $\theta_{\mathrm{width}} = 10°$.

I remind the reader that in order to effectively recover the injected signals with

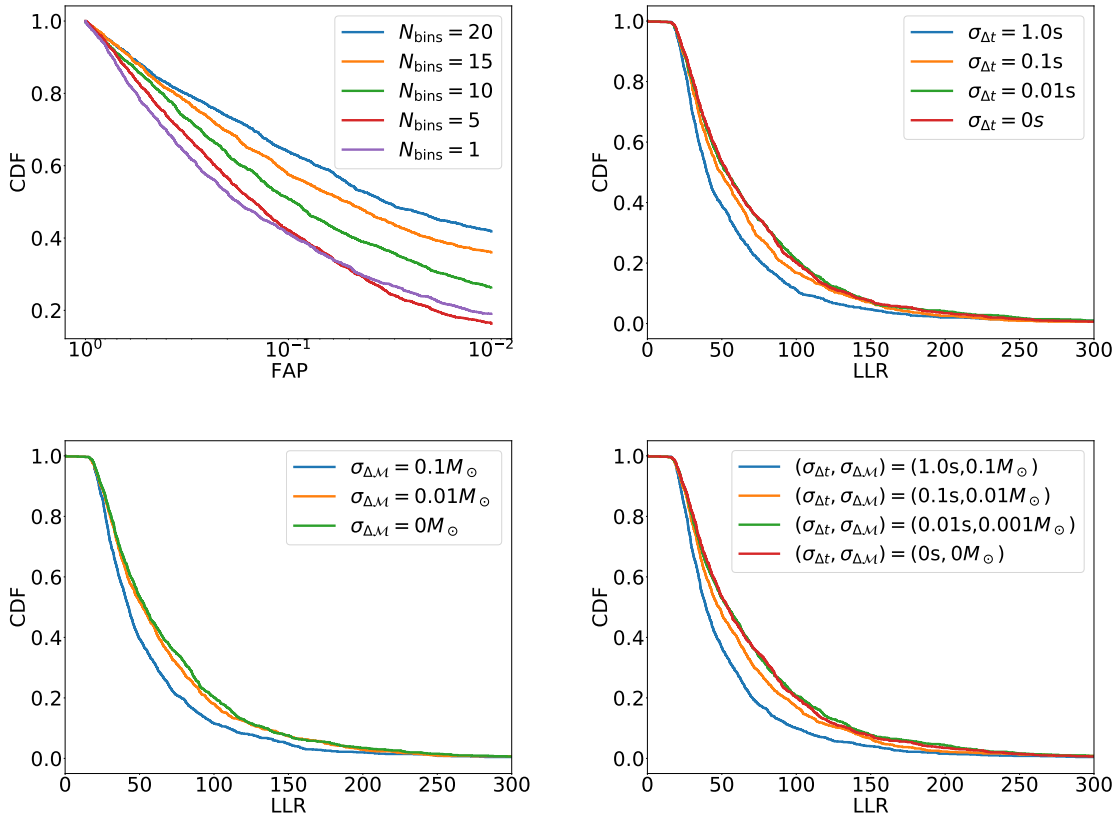

Fig. 3.7 Top left: CDF versus FAP, for the case of signals injected and recovered with the same binary parameters. Top right: CDF versus LLR for injected signals with $\sigma_{\Delta\mathcal{M}} = 0$ and different values of $\sigma_{\Delta t}$. Bottom left: CDF versus LLR for injected signals with $\sigma_{\Delta t} = 0$ and different values of $\sigma_{\Delta\mathcal{M}}$. Bottom right: CDF versus LLR for different values of $(\sigma_{\Delta t}, \sigma_{\Delta\mathcal{M}})$. For all the panels, except the top left, the setting $N_{\rm bins} = 10$ is used.

the *chirp-search*, one should have access to the observer frame chirp mass $\mathcal{M}$ and the coalescence time t_c, measured at Fermi. In this paragraph, I treat the case of perfect GW strain measurement, i.e. both $\mathcal{M}$ and t_c are known without uncertainty. More precisely for both the injection procedure and the search setting, the binary components masses $m_1 = 10\,M_\odot$ and $m_2 = 1.4\,M_\odot$ are considered. The FAP distributions for different $N_{\rm bins}$ settings are presented in the top left panel of Figure 3.7. One should remark that the pipeline sensitivity increases with $N_{\rm bins}$. Given that a signal of orbital phase duration $\theta_{\rm width} = 10°$ might be included in only one interval I_k of duration 360°, 72°, 36°, 24° or 18°, corresponding to $N_{\rm bins} = 1, 5, 10, 15$ or 20, then the narrower the I_k interval the higher the statistical significance. Indeed, for a given orbital phase interval of length l_{I_k}, containing a signal of orbital phase duration l_s and orbital phase photon rate r_s, if the orbital phase background photon rate is r_b, then the ratio between the noise only counts number and the signal plus noise counts number is $\frac{r_s l_s + r_b l_{I_k}}{r_b l_{I_k}} = 1 + \frac{1}{l_{I_k}/l_s}\frac{r_s}{r_b}$. So at fixed l_s, the higher the l_{I_k}, the lower the signal-to-noise ratio. This behavior is also

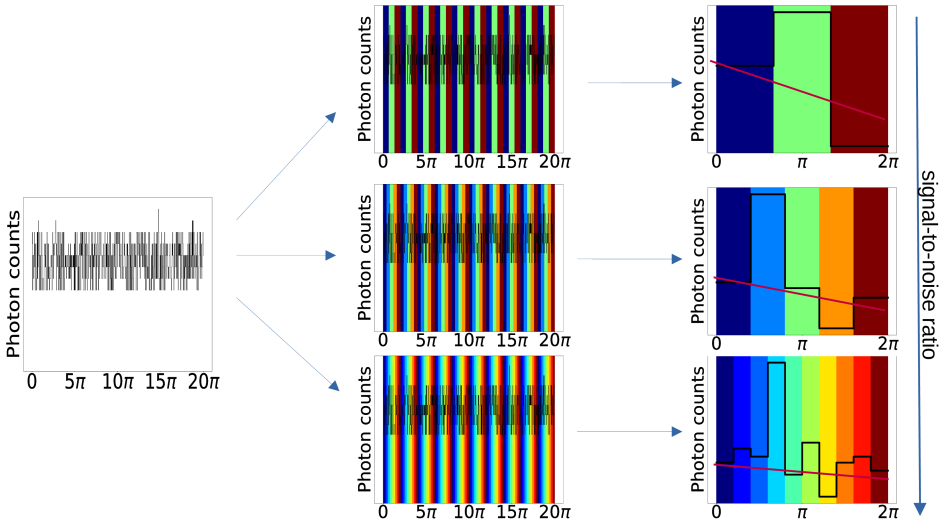

Fig. 3.8 Increase of the signal-to-noise ratio by considering more and more orbital phase intervals I_k. On the left panel is the lightcurve in the time space. The middle panels show the same time space histogram of photons arrival times as well as the positions of the orbital phase intervals I_k. The right panels represent the lightcurves in the orbital phase space after: (i) the addition of the foreground photons corresponding to each orbital phase interval I_k and (ii) the estimation of the orbital phase space photon background rate.

emphasized by the sketch proposed in Figure 3.8. One should note that the *chirp-search* with setting $N_{\rm bins} = 1$ is the same as the targeted search. Therefore the top left panel of Figure 3.7 proves the superiority of the *chirp-search* over the *targeted-search*, for the case of *exotic-waveform* signals recovery.

However, in real observational conditions, both the chirp mass and the coalescence time are assigned with uncertainties. Here, I investigate the pipeline sensitivity loss dependence on the errors affecting these two binary parameters. A $\sigma_{\Delta t}$ (respectively $\sigma_{\Delta\mathcal{M}}$) standard deviation in t_c (respectively $\mathcal{M}$) is tested by injecting signals with merger time $t_c + \delta t_c$ (respectively $\mathcal{M} + \delta\mathcal{M}$), and recovering them with the *chirp-search* set with t_c (respectively $\mathcal{M}$). In the previous expression, δt_c (respectively $\delta\mathcal{M}$) is uniform in $[-\sigma_{\Delta t}, \sigma_{\Delta t}]$ (respectively $[-\sigma_{\Delta\mathcal{M}}, \sigma_{\Delta\mathcal{M}}]$) and represents the error of the coalescence time (respectively the chirp mass) which is unknown. More precisely, I consider three situations: (i) coalescence time uncertainty only, where signals are injected with $(t_c + \delta t_c, \mathcal{M})$ and recovered with the setting $(t_c, \mathcal{M})$; (ii) chirp mass uncertainty only, where signals are injected with $(t_c, \mathcal{M} + \delta\mathcal{M})$ and recovered with the setting $(t_c, \mathcal{M})$; (iii) both coalescence time and chirp mass uncertainties, where signals are injected with the setting $(t_c + \delta t_c, \mathcal{M} + \delta\mathcal{M})$ and recovered with $(t_c, \mathcal{M})$. The mean values are the same as in the previous paragraph, i.e. t_c is random during the April 2019, while $\mathcal{M}$ is the chirp mass corresponding to a binary formed of a $10\,M_\odot$ black hole and a $1.4\,M_\odot$ neutron star. It is worth mentioning that for technical reasons, this code actually takes

as input (t_c, m_1, m_2) (instead of $(t_c, \mathcal{M})$), so when the chirp mass uncertainty is considered, I kept the total mass equal to $11.4\,M_\odot$. I vary the standard deviations $\sigma_{\Delta t}$ and $\sigma_{\Delta\mathcal{M}}$ and the results are presented in Figure 3.7. In all three related panels (top right, bottom left and bottom right), the expected behavior appears: the lower the uncertainties, the better the sensitivities, and the closer the LLR cumulative distribution functions (CDF) to the CDF corresponding to GW measurement without uncertainty ($\sigma_{\Delta t} = \sigma_{\mathcal{M}} = 0$). More precisely, for the case of coalescence time uncertainty only, the CDF relative error, between the cases $\sigma_{\Delta t} = 0.01\,\mathrm{s}$ and $\sigma_{\Delta t} = 0$, is lower than 12% for the LLR in the range $[0, 200]$. For the same LLR range, the relative error in CDF is below 12% in the case of chirp mass uncertainty only, for $\sigma_{\Delta\mathcal{M}} = 0.001\,M_\odot$ versus $\sigma_{\Delta\mathcal{M}} = 0$. Finally, when both uncertainties are considered, the case $(\sigma_{\Delta t}, \sigma_{\Delta\mathcal{M}}) = (0.01\,\mathrm{s},\, 0.001\,M_\odot)$ indicates a CDF with a relative error smaller than 21%, in the $[0, 200]\,\mathrm{LLR}$ range, with respect to the case $(\sigma_{\Delta t}, \sigma_{\Delta\mathcal{M}}) = (0, 0)$. One should be aware of the fact that *targeted-search* is not affected by uncertainty on the coalescence time, unless the EM signal is really close either to t_c or to $(t_c - 30\,\mathrm{s})$. On the other hand, concerning the *chirp-search*, an error on t_c and/or $\mathcal{M}$ implies a mixing of the true intervals I_k. Indeed, in order to derive the photon counts corresponding to the intervals I_k, one should know how the binary orbit evolves in time. And the time dependence of the orbital phase is completely known if one has both the time evolution of the angular frequency (so the chirp mass) and some point on the orbital phase axis (in present case, the merger time). Nevertheless, it is worth mentioning that this I_k mixing feature is more predominant close to the merger, because in that regime the angular frequency is higher.

3.2.3 Output results for the O2/O3 real BNS/NSBH events

According to the results derived at the end of the previous subsection, if one has a real GW measurement, and the computed coalescence time and chirp mass have uncertainties below $0.01\,\mathrm{s}$ and $0.001\,M_\odot$, then the *chirp-search* might be used confidently for the identification of EM signals modulated by the orbital phase. On the other hand, if the uncertainties are higher than these limits, say $t_c \in [t_{c,\min}, t_{c,\max}]$ and $\mathcal{M} \in [\mathcal{M}_{\min}, \mathcal{M}_{\max}]$, then the following procedure might be used: a grid of points $(t_c^i, \mathcal{M}^i)$ is introduced, such that $t_c^{i+1} - t_c^i = 0.02\,\mathrm{s}$ and $\mathcal{M}^{i+1} - \mathcal{M}^i = 0.002\,M_\odot$. It is worth mentioning that in the previous expressions i is just an index, not a power. Then, whatever the true values $t_c^{\mathrm{true}}, \mathcal{M}^{\mathrm{true}}$ of the binary parameters, there exists a grid point $(t_c^k, \mathcal{M}^k)$ such that $\|t_c^k - t_c^{\mathrm{true}}\| \leq 0.01\,\mathrm{s}$ and $\|\mathcal{M}^k - \mathcal{M}^{\mathrm{true}}\| \leq 0.001\,M_\odot$.

Now I apply the strategy, described in the previous paragraph, for: the two BNS systems GW170817 [Abbott et al., 2017e] and GW190425 [Abbott et al., 2020a]; the two NSBH systems GW200105 and GW200115 [Abbott et al., 2021b]; the event GW190814 [Abbott et al., 2020b], which is, depending on the nature of its lighter compact object, either

a NSBH or a BBH. Their binary parameters are obtained from the posteriors of offline MCMC analyses: *Bilby* [Ashton et al., 2019] for GW170817 and *LALInference* [Veitch et al., 2015] for the other four events. One should note that these posteriors provide the coalescence time measured at the center of the Earth, while in the present study, t_c measured at Fermi is needed. The conversion of the two GW arrival times might be realized if one has the position in the sky of the compact object binary. Concerning GW170817, this is simple because the galaxy (NGC 4993) hosting the binary is known. Thanks to this information, t_c at Fermi is obtained by subtracting $3.176\,\mathrm{ms}$ from the coalescence time, measured at the Earth center. Regarding the other four events, the GW based sky localization are less informative (except for GW190814). At this point of the analysis, I assume that these four events have uniform skymap distribution probability, i.e. all the directions are equally likely. For this reason, I suppose that the median value of the geocenter merger time is the same as t_c, measured at Fermi. But the Fermi satellite t_c upper/lower limits are increased/decreased by $0.023\,\mathrm{s}$, accounting for the light travel time from Fermi to the center of the Earth. One should remark that these extreme cases, where the amount of $0.023\,\mathrm{s}$ needs to be added/subtracted to/from the geocenter t_c, corresponds to the situation of an alignment of the Earth center, Fermi satellite and the EM source. In contrast, t_c is the same at the center of the Earth and at Fermi if the direction of the EM signal is perpendicular to the line defined by the geocenter and the high energy photon observatory. The median values, as well as the upper and lower limits, for the five events appear in Table 3.1. In this table, I replace t_c by MET (the

Event	MET(s)	$\mathcal{M}(M_\odot)$
GW170817	$524666469.424^{+0.001}_{-0.002}$	1.198
GW190425	$577873090.009^{+0.056}_{-0.031}$	$1.487^{+0.001}$
GW190814	$587509843.991^{+0.026}_{-0.023}$	$6.413^{+0.012}_{-0.015}$
GW200105	$599934271.05^{+0.058}_{-0.031}$	$3.62^{+0.011}_{-0.008}$
GW200115	$600754994.754^{+0.027}_{-0.055}$	$2.583^{+0.005}_{-0.005}$

Table 3.1 MET and $\mathcal{M}$ for the five O2/O3 real events. For GW170817, the posteriors from [Romero-Shaw et al., 2020] have been used, while the samples from Abbott et al. [2019a] have been preferred for both GW190814 and GW190425. Finally, for GW200105 (respectively GW200115) I have used *LALInference* with the prior waveform *SEOBNRv4 ROM NRTidalv2 NSBH* [Bohé et al., 2017] (respectively *IMRPhenomNSBH* [Thompson et al., 2020]). In the table, the reported values represent the median (50th percentile), the upper limit (90th percentile) and the lower limit (10th percentile). For the case of $\mathcal{M}$, a missing upper/lower limit means that this limit is away from the median value by less than $0.001 M_\odot$.

mission elapsed times). Then, for each of the five events, I run the *chirp-search* and the *targeted-search* on the points of the grid described in the first paragraph of this section, and the highest LLR and its associated FAP are derived. The results are summarized in Table 3.2. Based on the high values of the *targeted-search* FAP one can conclude that

Event	*chirp-search*		*targeted-search*	
	LLR	$\mathrm{FAP}^{-3\sigma}_{+3\sigma}$	LLR	$\mathrm{FAP}^{-3\sigma}_{+3\sigma}$
GW170817	28.6	$0.48^{-0.15}_{+0.15}$	8.9	$0.16^{-0.10}_{+0.12}$
GW190425	22.4	$0.76^{-0.14}_{+0.12}$	7.2	$0.47^{-0.15}_{+0.15}$
GW190814	117.4	$0.00^{-0.00}_{+0.02}$	10.3	$0.07^{-0.06}_{+0.09}$
GW200105	63.3	$0.05^{-0.05}_{+0.08}$	9.9	$0.09^{-0.07}_{+0.10}$
GW200115	70.8	$0.03^{-0.03}_{+0.07}$	8.1	$0.29^{-0.13}_{+0.14}$

Table 3.2 LLR and corresponding FAP, for the two searches, for the five O2/O3 real GW events. The *chirp-search* is used with $N_{\rm bins} = 10$. For the FAP, the mean as well as $\pm$ 3 standard deviations are provided. When the mean and/or the upper limit (-3σ) is (are) equal to 0, it means that the value(s) is (are) lower than 0.01. All the events reported in this table represent triggers with duration of $0.064\,$s and *hard* spectrum.

there is no way to claim the presence of an unambiguous excess of high energy photons emitted prior to the merger. The *chirp-search* output is similar in the case of GW170817 and GW190425. On the other hand, for GW200105, GW200115 (and respectively for GW190814) upper limits (and respectively the mean value and the upper limit) have not been derived. At first sight, this aspect can give to the reader the naive intuition that these candidates might be real GRB precursors. Nonetheless, I warn the reader of this thesis that some precautions need to be taken. The reason, for the missing upper limits, is not necessarily because the EM candidates are too statistically significant in order for these quantities to be derived. The reason is simply due to the computational expense of such operations. Moreover, the manual analysis of these three EM triggers reveal that each of them has a duration of $0.064\,$ms and possesses a hard spectrum. Given that more than 80% of the noise events (the output of the *chirp-search* when it is run on random times; previous subsection) have the same timescale and spectral features, this is a clear indication that EM candidates for GW190814, GW200105 and GW200115 are simply coincidence background triggers. Finally, I conclude that there is no modulated GRB precursor for the five GW real events examined here.

CHAPTER 4

Photometric lightcurve discrimination between kilonovae, supernovae and other transient signals

Stachie et al. [2020b] is the paper dedicated to the work contained in this Chapter.

4.1 Motivation and other proposals

Kilonovae are ultra-violet/optical/infrared transient objects, associated with the merger of two compact objects, of which at least one is a neutron star. In an Earth night, several types of transient objects might shine the sky, the majority of them being supernovae. One of the difficulties encountered in the exercise of identifying kilonovae is that their observational properties are still very uncertain. To date, these features vary depending on the models and, are mostly based on one single well-studied event, AT 2017gfo (see Figure 4.1). The photometric and spectroscopic appearance may be not universal at all, and vary depending on the merger and environment characteristics [Kasen et al., 2017], as well as on the viewing angle [Darbha and Kasen, 2020]. Furthermore, depending on the viewing angle and distance, there might be cases where the relativistic jet (GRB afterglow) will be superimposed on the kilonova [Troja et al., 2018].

Kilonovae are shorter and dimmer than the supernovae. While the supernovae are visible for the Earth telescopes on timescales of months, or even years [Fox et al., 2015], AT 2017gfo was observable for nearly one week [Coulter et al., 2017; Smartt et al., 2017], even if associated to a particular close binary merger [Abbott et al., 2017e]. For a BNS merger taking place at a few hundreds of Mpc, the optical transient is expected to fade in only one (two) day(s). Thus, while scientists might attempt to detect and identify supernovae by means of all-time all-sky observational campaigns, in the case of kilonovae such a strategy would be very challenging. Multi-wavelength and spectroscopic observations are the key for a robust KN identification, and, in any case, in order to detect kilonovae, it is preferable to be in the situation in which the search is targeted by another observation associated with the same astrophysical event. Such a trigger can be the flash of γ-ray photons or the subsequent longer wavelength afterglow originating from the relativistic jet of a short GRB, as was the case of 130603B [Tanvir et al.,

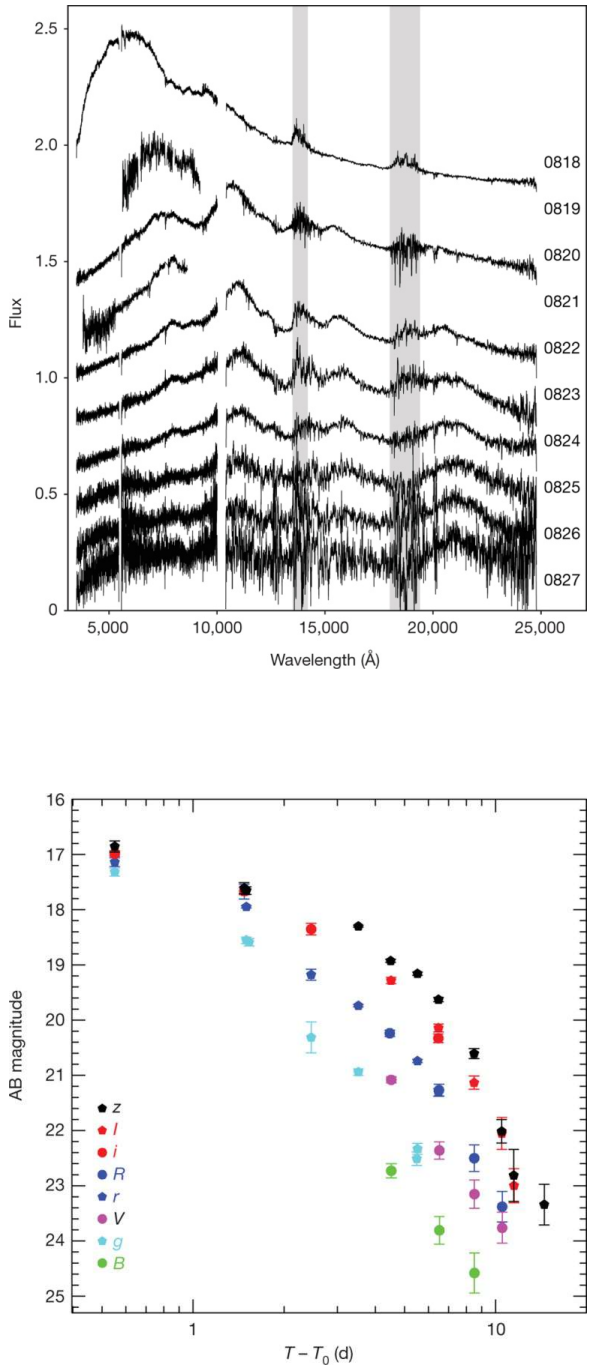

Fig. 4.1 On top: spectroscopic measurements of AT 2017gfo; on bottom: photometric measurements of AT 2017gfo. The panels are taken from Pian et al. [2017].

2013] and 150101B [Troja et al., 2018], or the GW signal emitted by a binary compact object in its last seconds of life [Abbott et al., 2017b]. Nonetheless, if the trigger is the GW strain signal, the information related to the position in the sky of the possible EM counterpart might be quite uninformative, although the luminosity distance estimation is generally quite precise and very useful. Indeed, the low-latency skymaps, during O1, O2 and O3, covered sometimes thousands of square degrees [LIGO Scientific Collaboration and Virgo Collaboration, 2019a, 2020a,b]. Not only the observational results are discouraging, but also the theoretical and numerical modelling of the compact binary coalescence GW signals indicate broad sky localizations [Röver et al., 2007; Fairhurst, 2009; Grover et al., 2014; Wen and Chen, 2010; Sidery et al., 2014; Singer et al., 2014; Berry et al., 2015; Essick et al., 2015; Cornish and Littenberg, 2015; Klimenko et al., 2016]. In the EM observing community, the sky coverage is realized by wide field of view telescopes. Depending on the sensitivity of these telescopes, a number of EM candidates are identified. Then, the promising transient objects are followed-up by smaller field of view telescopes. The problem that, in general, arises is that the number of the initial candidates is very high, which renders the selection of the potential kilonova very difficult. This is already the case for the most sensitive actual instruments, but also for the next generation facilities [Morgan et al., 2012; Tonry et al., 2018; Bellm et al., 2019; Graham et al., 2019; Bloemen et al., 2016; Ivezić et al., 2019]. One proposal to tackle this challenge is the instrument coordination within a network of telescopes [Antier et al., 2020a,b; Coughlin et al., 2019b]. For an increased synergy, skymap tiling [Coughlin et al., 2018b] and galaxy prioritization [Ducoin et al., 2020] techniques have been improved.

Nevertheless, given the large number of EM candidates, discrimination criteria should be envisaged in order to reject non interesting EM transients. In general, each type of transient has photometric lightcurves presenting particular characteristics. Thus, timescale variability, magnitude values and/or color evolution are features that might be investigated in order to assign priority weights. For example, for Type Ia supernovae, fitting formulas have been proposed in the literature. *SALT2* [Taylor et al., 2021; Guy et al., 2007, 2005] is such an example. Here the spectral flux density f^{S2} at phase p^{S2} and wavelength λ^{S2} can be expressed as

$$f^{S2}(p^{S2},\lambda^{S2}) = x_0^{S2}\times\left[M_0^{S2}(p^{S2},\lambda^{S2}) + x_1^{S2}\times M_1^{S2}(p^{S2},\lambda^{S2}) + \ldots\right]\times\exp\left[c^{S2}CL^{S2}(\lambda^{S2})\right], \tag{4.1}$$

where the fitting parameters are the amplitude x_0^{S2}, the stretch x_1^{S2} and the color c^{S2}. $M_0^{S2}(p^{S2},\lambda^{S2})$, $M_1^{S2}(p^{S2},\lambda^{S2})$ and $CL^{S2}(\lambda^{S2})$ are wavelength dependent *SALT2* parameters. $M_0^{S2}(p^{S2},\lambda^{S2})$ and $M_1^{S2}(p^{S2},\lambda^{S2})$ depend also on the phase. A more general fitting formula, convenient not only for Type Ia supernovae, but for almost all the other types including core collapse supernovae, is proposed in Bazin et al. [2009, 2011]. Ac-

cording to this model, the supernova photon flux can be written as

$$f^{\mathrm{BAZ}}(t) = A^{\mathrm{BAZ}} \frac{e^{-(t-t_0^{\mathrm{BAZ}})/\tau_{\mathrm{fall}}^{\mathrm{BAZ}}}}{1+e^{-(t-t_0^{\mathrm{BAZ}})/\tau_{\mathrm{rise}}^{\mathrm{BAZ}}}} + B^{\mathrm{BAZ}}, \tag{4.2}$$

where t is the time variable, while A^{BAZ}, B^{BAZ}, t_0^{BAZ}, $\tau_{\mathrm{fall}}^{\mathrm{BAZ}}$ and $\tau_{\mathrm{rise}}^{\mathrm{BAZ}}$ are fitting parameters. B^{BAZ} and A^{BAZ} are the constant flux value and the normalization constant of the variable part of the signal. $\tau_{\mathrm{rise}}^{\mathrm{BAZ}}$ and $\tau_{\mathrm{fall}}^{\mathrm{BAZ}}$ are the rise and fall times of the variation, while the maximum of intensity takes place at $t_0^{\mathrm{BAZ}} + \tau_{\mathrm{rise}}^{\mathrm{BAZ}} \ln\left(\frac{\tau_{\mathrm{fall}}^{\mathrm{BAZ}}}{\tau_{\mathrm{rise}}^{\mathrm{BAZ}}} - 1\right)$. But the variety of optical transients is very rich and a fitting formula may turn out to be insufficient to catch all the desired features of a lightcurve. This is why non-parametric representation can be useful. Varughese et al. [2015] makes use of wavelet decomposition based method [Timmermans and von Sachs, 2015] in order to characterize optical transients, as follows: there are N^{VAR} classes of objects possessing the unknown time dependent flux evolutions f_i^{VAR}, with $i \in \{1, 2, \ldots, N^{\mathrm{VAR}}\}$. If one notes by $x_{i,j}^{\mathrm{VAR}}$, the j^{th} measurement time argument when the i^{th} object class is considered, and by $y_{i,j}^{\mathrm{VAR}}$ and $\epsilon_{i,j}^{\mathrm{VAR}}$ the corresponding flux and uncertainty values, then

$$y_{i,j}^{\mathrm{VAR}} = f_i^{\mathrm{VAR}}(x_{i,j}^{\mathrm{VAR}}) + \epsilon_{i,j}^{\mathrm{VAR}}, \text{ for } i \in \{1, \ldots, N^{\mathrm{VAR}}\} \text{ and } j \in \{1, \ldots, n_i^{\mathrm{VAR}}\}, \tag{4.3}$$

where n_i^{VAR} is the total number of measurements. Finally similarities between wavelet decomposition coefficients of lightcurves belonging to the same class are studied. Ishida et al. [2019] propose an active learning based method for the optimization of supernova photometric classifications. More specifically, data released after the *SuperNova Photometric Classification Challenge* [Kessler et al., 2010] consisting of 20,216 supernovae observed in the g, r, i and z filters are used. For each item in the sample, feature extraction is realized by fitting every photometric band lightcurve with the expression from [Bazin et al., 2009]. A *random forest* machine learning algorithm is used as a classifier [Breiman, 2001]. Finally, in order to improve the performances of the classifier, samples are added to the training data by means of active learning procedure. Equally, Lochner et al. [2016] use machine learning approaches to classify objects. More precisely, lightcurve features extraction is initially performed by the fitting formulas proposed in Guy et al. [2007]; Newling et al. [2011]; Karpenka et al. [2012]. Then, several machine learning techniques, such as *Naive Bayes* (e.g., Zhang [2004]), *k-nearest Neighbors* (e.g., Altman [1992]), *Artificial Neural Networks* (e.g., Jeffrey and Rosner [1986]), *Support Vector Machine* (e.g., Cortes and Vapnik [1995]) and *Boosted Decision Trees* (e.g., Friedman [2002]), are used to discriminate between different object classes. Photometric lightcurves and spectroscopic data, representing the key from of the EM point of view, might be combined with high energy photons information in order to discriminate between transients. X-ray binary sources have been classified

by Wevers et al. [2017] in such a way. In a X-ray binary, matter falls in the accretion disc surrounding a white dwarf, a neutron star or a black hole releasing flashes of high energy photons. The subsequent X-rays ionize the surrounding matter, creating hydrogen Hα features in the optical range, detectable on the Earth as emission or absorption lines. This spectroscopic information, together with the photometric variability, and the ratio between the X-ray and the optical fluxes are used to identify cataclysmic variables, young stellar objects and/or low-mass X-ray binaries.

The searches for kilonovae have some specific particularities. On one hand, the inherent rapid decay of the brightness represents a disadvantage because it obliges the EM observers to have a fast identification, based on scarce information. On the other hand, astronomers can use this fast evolution feature as a flag indicating the kilonova, or other rapidly fading object such as GRB afterglows, in the large list of optical transient candidates. This kind of approach was succesfully used by Andreoni et al. [2021]. Their filtering strategy includes the decay constraint of $0.3\,\mathrm{mag}\cdot\mathrm{day}^{-1}$ in any of the g, r and i photometric filter. In this way, Andreoni et al. [2021] found several GRB afterglows, despite a serendipitous (all-time all-sky) search. In the following of this chapter, I summarize the work from Stachie et al. [2020b].

4.2 Machine-learning based method

For this study, I make use of `astrorapid` [Muthukrishna et al., 2019], a deep learning classifier based on a uni-directional recurrent neural network with Gated Recurrent Units. It is designed for time-domain astronomy, being able to analyze multi-passband photometric transients, and to discriminate among several classes of objects. As any supervised machine learning code, before it is used to classify objects, it needs to be trained on a set of already labelled astrophysical transients. To this end, the lightcurve models released by The PLAsTiCC team et al. [2018] together with the simulation code from Kessler et al. [2009, 2019] have been used in order to generate a dataset. These simulated lightcurves are representative for the "Mid Scale Innovations Program" survey at the ZTF [Bellm, 2014]. Thus, ZTF observing conditions and photometric properties have been respected. The cadence of the lightcurves has a median of 3 days in the g and r filters. `astrorapid` is designed to distinguish between the following transients types: "SNIa-norm" (the most typical thermonuclear explosion taking place when a white dwarf accretes sufficient matter from its companion star in order to reach the Chandrasekhar limit [Guy et al., 2010; Kessler et al., 2013; Pierel et al., 2018]), "SNIa-91bg" (a subtype [Perrefort et al., 2020] of Type Ia supernovae which ressemble SN 1991bg [CHENG et al., 1993]), "SNIa-x" (a subtype [Jha, 2017] of Type Ia supernovae which ressemble SN 2002cx [Li et al., 2003]), "point-Ia" (a hypothetical subtype [Shen et al., 2010] of Type Ia supernovae), "SNIbc" (the core-collapse super-

novae of Type Ibc [Kessler et al., 2010; Pierel et al., 2018; Guillochon et al.; Villar et al., 2017]), "SNII" (the Type II core-collapse supernovae [Kessler et al., 2010; Pierel et al., 2018; Guillochon et al.; Villar et al., 2017]), "Kilonova" (the r-process powered electromagnetic counterpart [Kasen et al., 2017] to BNS and NSBH), "SLSN-I" (the hydrogen-poor super-luminous supernova presumably caused by magnetars or core-collapse of very massive stars [Guillochon et al.; Nicholl et al., 2017; Kasen and Bildsten, 2010]), "PISN" (the pair instability supernovae which are believed to take place when the oxygen core of a very massive star has a so high internal energy that electron-positron annihilation reaction is possible, powering γ-ray emission [Guillochon et al.; Villar et al., 2017; Kasen et al., 2011]), "ILOT" (Intermediate Luminosity Optical Transients possessing brightnesses higher than novae and smaller than supernovae and are presumably due to either eruptions of red giants or interactions of binary systems [Guillochon et al.; Villar et al., 2017]), "CART" (CAlcium-Rich gap Transients, whose spectra show important forbidden and permitted calcium lines, and whose origin is not well understood [Guillochon et al.; Villar et al., 2017; Kasliwal et al., 2012]), "TDE" (Tidal Disruption Events designating a star which is disrupted by the tidal forces of its black hole companion [Guillochon et al.; Mockler et al., 2019; Rees, 1988]), "AGN" (Active Galactic Nuclei, resulting from the matter accretion by the supermassive black hole harbouring the center of a galaxy [Connolly et al., 2010; MacLeod et al., 2010]). An example for each of these templates is provided in Figure 4.1. More precisely, in Figure 4.1, there is: on the left panel, first line, a "SNIa-91bg" template parameterized by the stretch $x_1^{\rm PER} = 0.95$ and the color $c^{\rm PER} = 0.5$ according to Perrefort et al. [2020]; on the right panel, first line, a "SNIa-x" template parameterized by the peak optical magnitude $M_V^{\rm JHA} = -17.267$, the rising time $\tau_{\rm rise}^{\rm JHA} = 15.172$ days, the decline magnitudes after 15 days in the B- and R-band $\Delta m_{15}^{\rm JHA}(B) = 1.341$ and $\Delta m_{15}^{\rm JHA}(R) = 0.581$ according to Jha [2017]; on the left panel, second line, a "SNIa-norm" template, based on *SALT2* and extended in the ultra-violet and infrared as in Pierel et al. [2018]; on the right panel, second line, a "Kilonova" template parameterized by the mass of ejecta $M^{\rm KAS} = 10^{-1.6021}\,M_\odot$, the velocity of the ejecta $v^{\rm KAS} = 0.03\,{\rm c}$ and the lanthanide fraction $X_{lan}^{\rm KAS} = 10^{-4}$ according to Kasen et al. [2017]; on the left panel, third line, a SN 2006-like [Joubert et al., 2006] "SNIbc" template; on the right panel, third line, a SDSS-018590-like [Xavier et al., 2014] "SNII" template; on the left panel, fourth line, a "TDE" template parameterized by the radius normalization $R_{\rm phO}^{\rm MOC} = 5.739$, the viscous timescale $T_{\rm viscous}^{\rm MOC} = 0.463$ days, the scaled impact parameter $b^{\rm MOC} = 1.015$, the black hole mass $M_h^{\rm MOC} = 8.514 \times 10^5\,M_\odot$, the efficiency parameter $\epsilon^{\rm MOC} = 0.009$, the power law exponent $l^{\rm MOC} = 1.505$ and the star mass $M_*^{\rm MOC} = 1.034\,M_\odot$ according to Mockler et al. [2019]; on right panel, fourth line a "CART" template parameterized by the mass of ejecta $M_{\rm ej}^{\rm VIL} = 0.304\,M_\odot$, the velocity of the ejecta $v_{\rm ej}^{\rm VIL} = 4393.623\,{\rm km/s}$, the

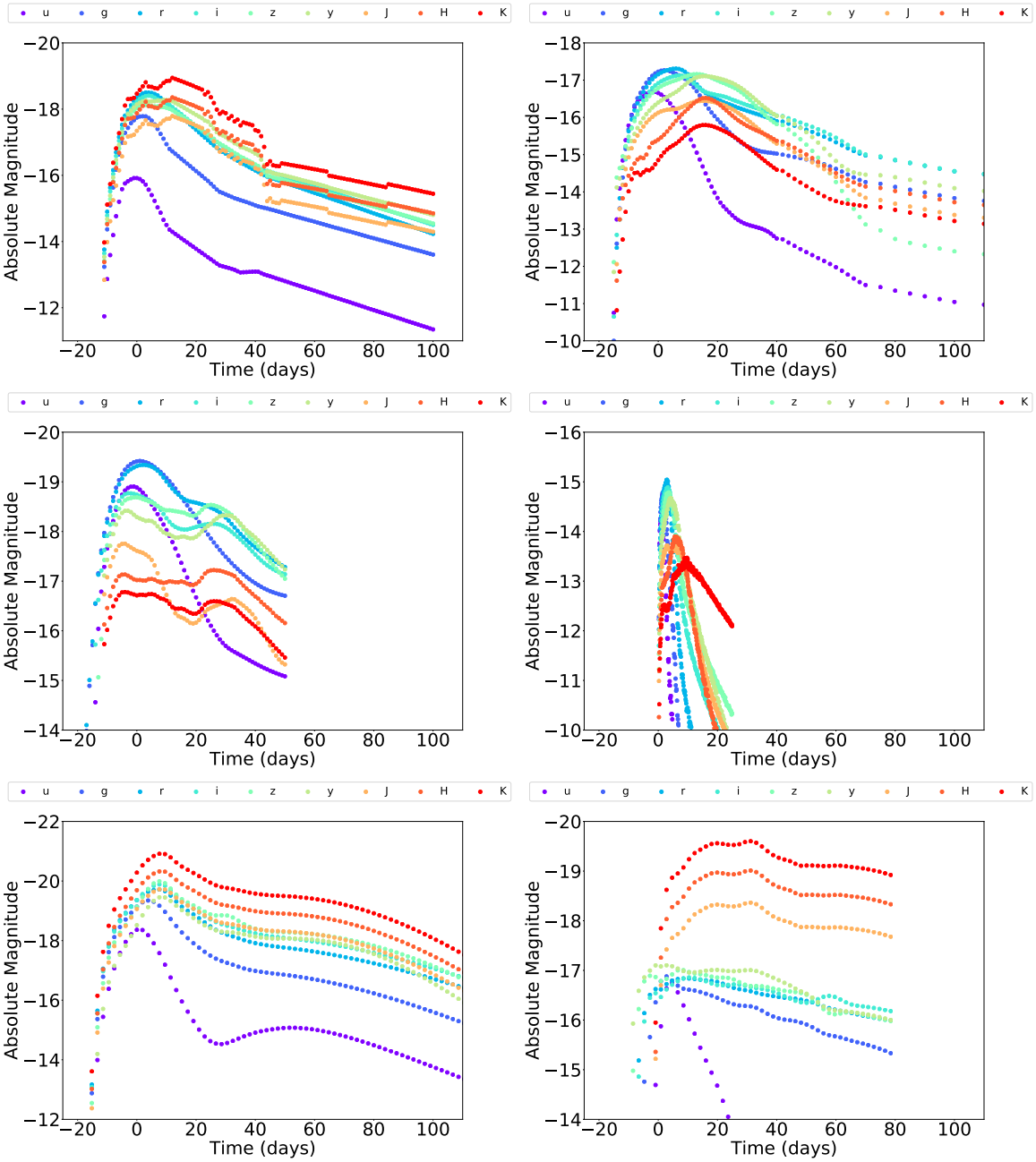
u g r i z y J H K
Absolute Magnitude
Time (days)

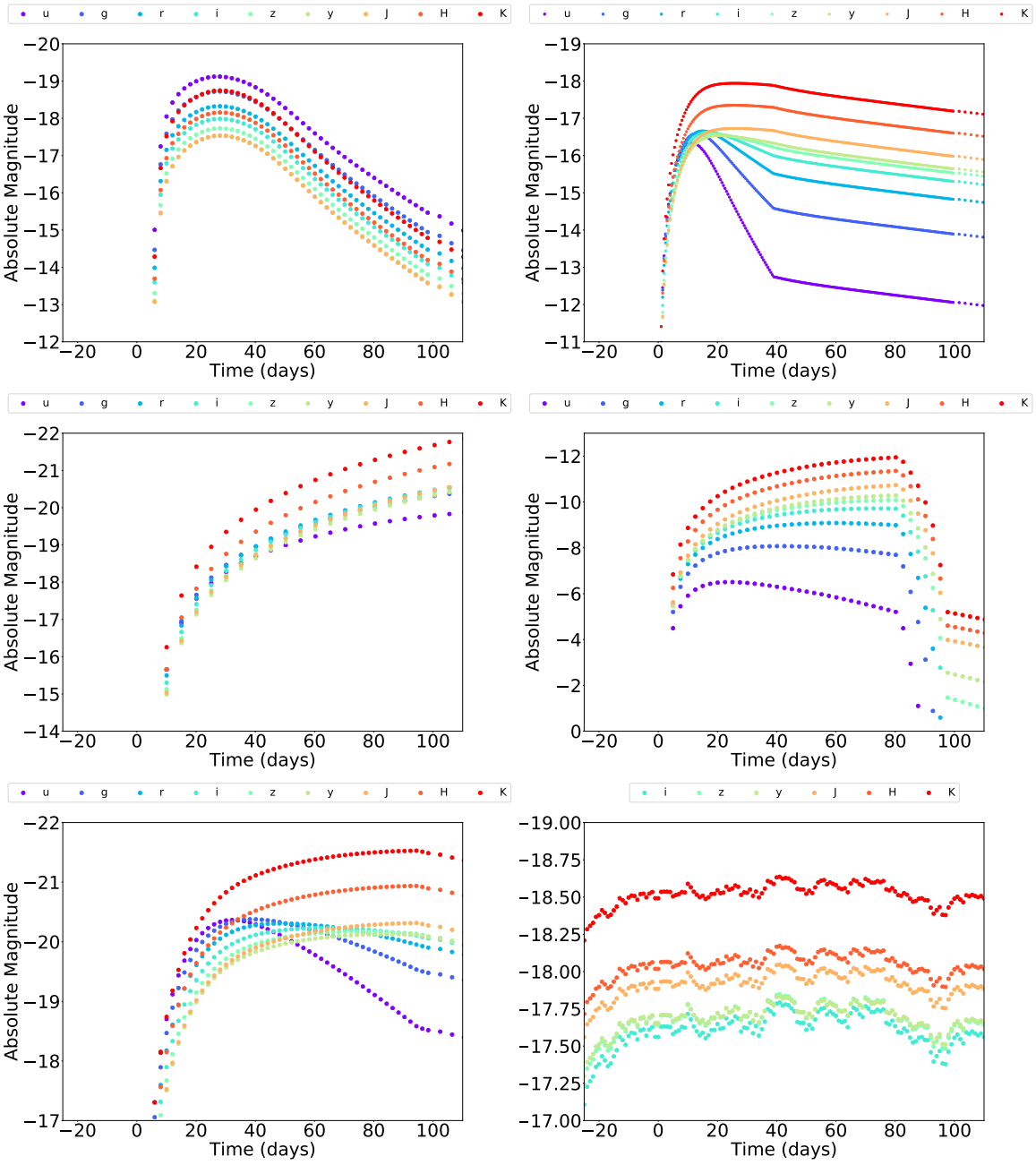

Fig. 4.1 AB magnitudes versus time for some examples of templates used in the training of `astrorapid`. The plots represent the following templates: "SNIa-91bg" (first column, first row), "SNIa-x" (second column, first row), "SNIa-norm" (first column, second row), "Kilonova" (second column, second row), "SNIbc" (first column, third row), "SNII" (second column, third row), "TDE" (first column, fourth row), "CART" (second column, fourth row), "PISN" (first column, fifth row), "ILOT" (second column, fifth row), "SLSN-I" (first column, sixth row) and "AGN" (second column, sixth row).

nickel fraction $f_{\mathrm{NI}}^{\mathrm{VIL}} = 0.220$, high energy photons opacity $\kappa_{\gamma}^{\mathrm{VIL}} = 11.195\,\mathrm{cm^2 g^{-1}}$ and temperature $T^{\mathrm{VIL}} = 2649\,\mathrm{K}$ according to Villar et al. [2017]; on the left panel, fifth line a "PISN" template parameterized by the ejecta mass $M_{\mathrm{ej}}^{\mathrm{VIL}} = 175.03\,M_{\odot}$ and kinetic energy $E_{\mathrm{KE}}^{\mathrm{VIL}} = 31.06\,\mathrm{erg}$ according to Villar et al. [2017]; on the right panel, fifth line,

a "ILOT" template parameterized by the ejecta mass $M_{\rm ej}^{\rm VIL} = 2.23\,M_\odot$, the ejecta velocity $v_{\rm ej}^{\rm VIL} = 255.097\,$km/s, the mass of the circumstellar material $M_{\rm CSM}^{\rm VIL} = 0.309\,M_\odot$, the density $\rho^{\rm VIL} = 6.312^{-15}\,{\rm cm}^{-3}$ and the initial source radius $R_0^{\rm VIL} = 33.936\,R_\odot$ according to Villar et al. [2017]; on the left panel, sixth line, a "SLSN-I" template parameterized by the magnetar mass $M_{\rm NS}^{\rm NIC} = 1.999\,M_\odot$, the spin period $P^{\rm NIC} = 7.195\,$ms, the optical opacity $\kappa^{\rm NIC} = 0.122\,{\rm cm}^2{\rm g}^{-1}$, the high energy photons opacity $\kappa_\gamma^{\rm NIC} = 22.420\,{\rm cm}^2{\rm g}^{-1}$, the ejecta mass $M_{\rm ej}^{\rm NIC} = 1.455\,M_\odot$, the final plateau temperature $T_f^{\rm NIC} = 5889.222\,$K and the velocity of the ejecta $v_{\rm ej}^{\rm NIC} = 7034.700\,$km/s according to Nicholl et al. [2017]; on the right panel, sixth line, an "AGN" template parameterized by the timescale $\tau^{\rm MAC} = 398.238\,$days and the long-term root mean square variability in the u, g, r, i, z, y equal to $SF_\infty^{\rm MAC}(u) = 0.978\,$mag, $SF_\infty^{\rm MAC}(g) = 0.865$, $SF_\infty^{\rm MAC}(r) = 0.767$, $SF_\infty^{\rm MAC}(i) = 0.697\,$mag, $SF_\infty^{\rm MAC}(z) = 0.651\,$mag, $SF_\infty^{\rm MAC}(y) = 0.610\,$mag according to [MacLeod et al., 2010]. Up to now, I discussed only about intrinsic absolute magnitude. But for an EM observer, the accessible quantity of interest is the observer frame apparent magnitude. Besides the apparent magnitude in the r and g filters, the lightcurves used for the training of the classifier also possess cosmological reshift and Milky Way dust reddening. Therefore, while the cosmological redshift is used for the conversion of the observer frame time series and the apparent photon flux into a source frame time series and intrinsic photon flux (by means of a luminosity distance), the Milky Way reddening is used for the correction of the ZTF [Bellm et al., 2018] measured wavelength. Moreover, the data preprocessing includes, for each lightcurve, a common passband time trigger $t_0^{\rm MUT}$(origin of the time axis) derivation by fitting a simple power law, $L_{\lambda;{\rm mod}}^{\rm MUT}(t; t_0^{\rm MUT}, a_\lambda^{\rm MUT}, c_\lambda^{\rm MUT}) = a_\lambda^{\rm MUT}(t-t_0^{\rm MUT})^2 H(t-t_0 MUT)+c_\lambda^{\rm MUT}$, and introducing a new template, named "Pre-explosion", accounting for the time period preceding the targeted flaring event. In the previous expression $H(t - t_0^{\rm MUT})$ stands for the Heaviside function, while $a_\lambda^{\rm MUT}$ and $c_\lambda^{\rm MUT}$ are two filter dependent fitting coefficients. $t_0^{\rm MUT}$, $\{a_\lambda^{\rm MUT}\}$ and $\{c_\lambda^{\rm MUT}\}$ are determined by means of a Markov Chain Monte Carlo procedure, using the following chi-squared metric

$$\chi^2_{\rm MUT}(t_0^{\rm MUT}, \{a_\lambda^{\rm MUT}\}, \{c_\lambda^{\rm MUT}\}) = \sum_\lambda \sum_{t=-\infty}^{t_{\rm peak}^{\rm MUT}} \frac{\left[L_{\lambda;{\rm data}}^{\rm MUT}(t) - L_{\lambda;{\rm mod}}^{\rm MUT}(t; t_0^{\rm MUT}, a_\lambda^{\rm MUT}, c_\lambda^{\rm MUT})\right]^2}{\sigma_\lambda^{\rm MUT}(t)^2}, \tag{4.4}$$

where $t_{\rm peak}^{\rm MUT}$ is the time corresponding to the peak of the lightcurve and $L_{\lambda;{\rm data}}^{\rm MUT}(t)$ is the filter input data to be fitted. Once the preprocessing is finished, the deep neural network method is setup. `astrorapid` works in the following way: at each time, based on the past observations, it provides for each of the fourteen templates (including "Pre-explosion") a probability. The sum of the probabilities is normalized to one and the probability distribution is updated at each new observation. An example of both input and output data for a transient object is proposed in Figure 4.2. I want to mention

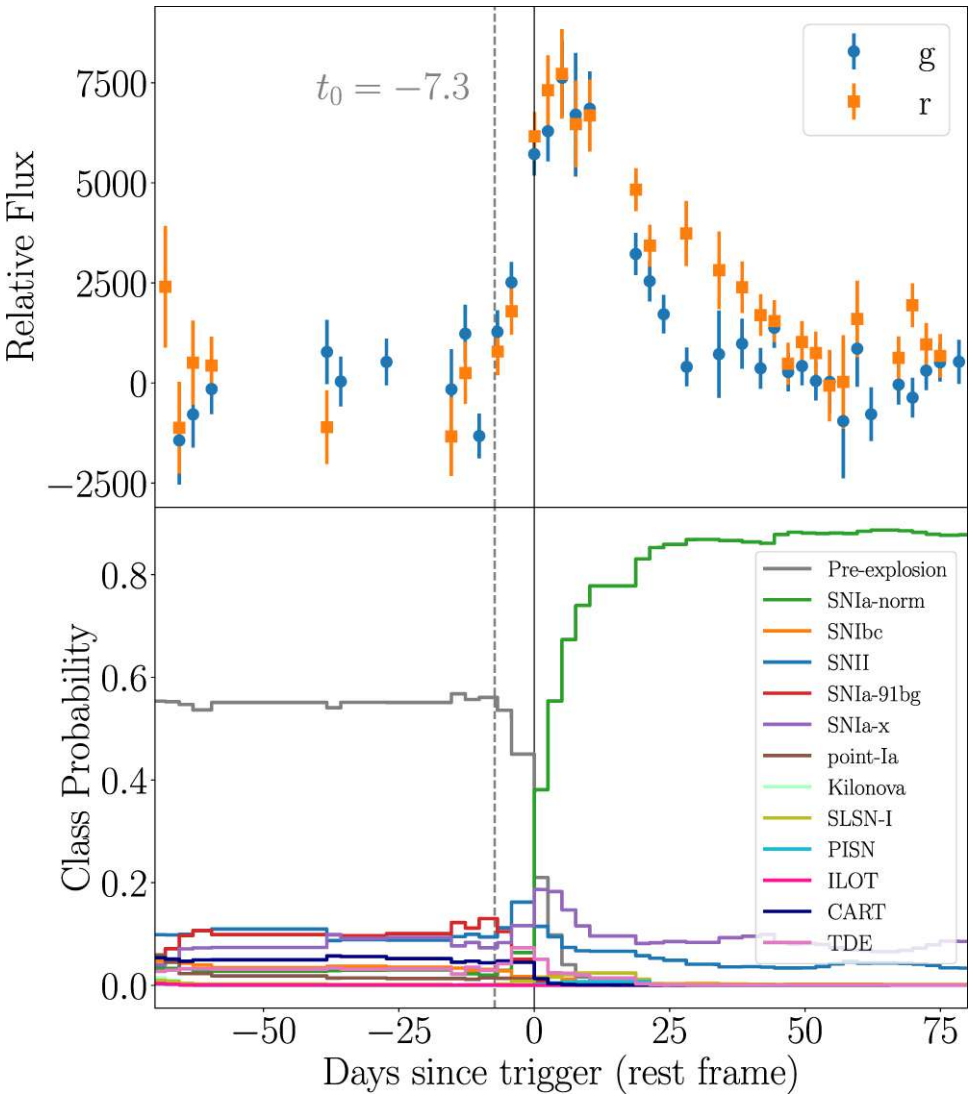

Fig. 4.2 `astrorapid` input (top panel) and output (bottom panel) data for a kilonova object. On the x axis is the time, while the y axis represents the photon flux (top panel) and the probabilities assigned to the different transient object classes (bottom panel). In this example, `astrorapid` assigns high probability to "Pre-explosion" before the increase of the light intensity, then the curve corresponding to "Kilonova" goes to higher and higher probabilities. The input data consists in r and g photometric data.

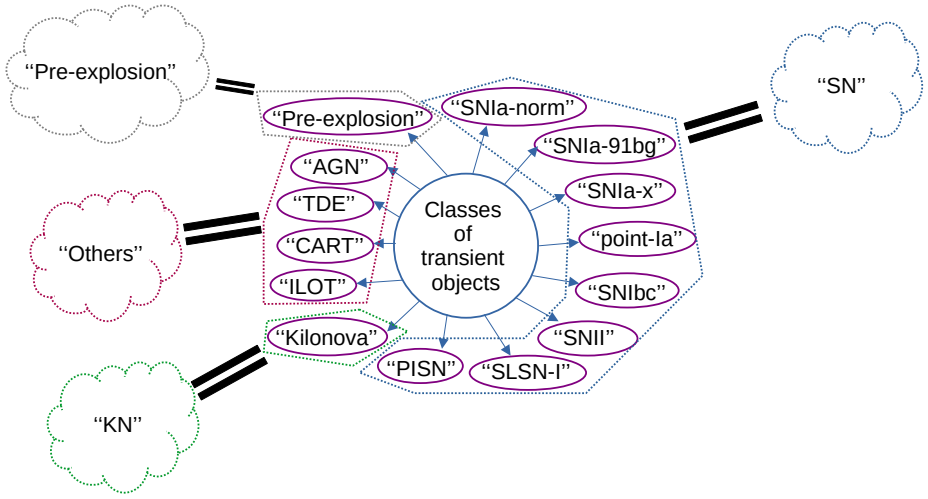

Fig. 4.3 Initial guess of the four main classes, obtained by the collapse of original `astrorapid` classes.

that I did not contribute to the development of the code described above, but I have just received it from Daniel Muthukrishna.

4.2.1 `astrorapid` output based discrimination

So far in this section, I made a summary of `astrorapid` as it is proposed in [Muthukrishna et al., 2019]. This version is designed to realize full lightcurve classification and to discriminate between many classes of objects. On the other hand, this work is destined for the kilonova follow-up. Therefore, it becomes unnecessary to distinguish between several varieties of Type Ia supernovae or to consider on equal footing as the kilonovae, rare transients such as tidal disruption events, intermediate luminosity optical transients, etc. With a real EM follow-up, the majority of the background events are represented by the supernovae. This motivates an initial choice (illustrated in Figure 4.3) of the following four main classes: “SN” (accounting for “SNIa-norm”, “SNIbc”, “SNII”, “SNIa-91bg”, “SNIa-x”, “point-Ia”, “SLSN-I”, “PISN”), “Others” (accounting for “ILOT”, “CART”, “TDE” , “AGN”), “KN” (accounting for “Kilonova”) and “Pre-explosion” (accounting for “Pre-explosion”). The first guess would be to consider that the probability assigned to each main class should be the sum of probabilities of the corresponding initial `astrorapid` templates, as follows:

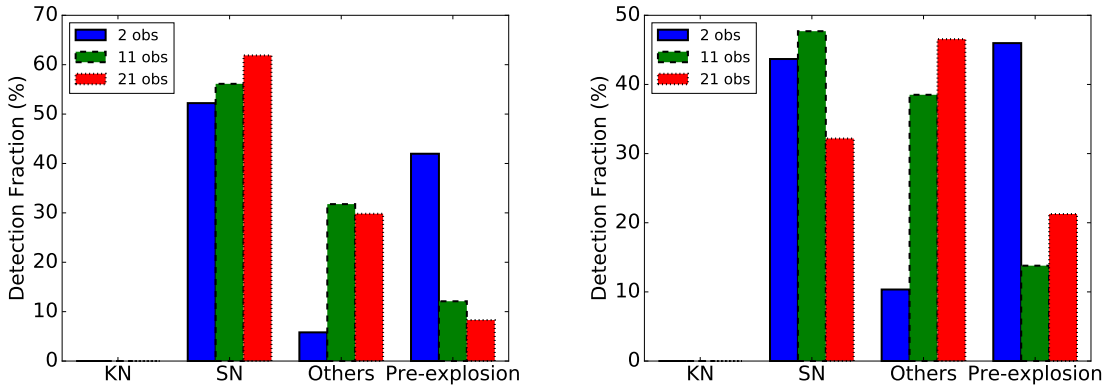

Fig. 4.4 Histogram of the preferred templates after 2, 11 and 21 observations, when the initial naive guess collapse described in Equation 4.5 is used. On the left (right) panel, the results correspond to the situation in which the input is represented by the real ZTF "SN" (respectively "Others") type transients.

$$
\begin{aligned}
P(\text{SN}) \quad &= P(\text{SNIa-norm}) + P(\text{SNIbc}) + P(\text{SNII}) + P(\text{SNIa-91bg}) + P(\text{SNIa-x}) + \\
&\quad + P(\text{point-Ia}) + P(\text{SLSN-I}) + P(\text{PISN}) \\
P(\text{Others}) \quad &= P(\text{ILOT}) + P(\text{CART}) + P(\text{TDE}) + P(\text{AGN}) \\
P(\text{KN}) \quad &= P(\text{Kilonova}) \\
P(\text{Pre-explosion}) \quad &= P(\text{Pre-explosion})
\end{aligned}
\tag{4.5}
$$

I also consider the preferred event to be the class assigned with the highest probability, i.e. $X \in \{\text{"SN"}, \text{"Others"}, \text{"KN"}, \text{"Pre-explosion"}\}$ such that $P(X) = \max(P(\text{SN}), P(\text{Others}), P(\text{KN}), P(\text{Pre-explosion}))$. Now, I show that this initial guess is not the most optimal one. To this end, I use some of the public real ZTF lightcurves. These objects have already been labelled, and thus belong to the "SN" (2,049 events among which 1450 "SNIa", 110 "SNIbc", 447 "SNII", 42 "SLSN") and "Others" (174 events among which 152 "AGN", 4 "CART", 6 "ILOT", 12 "TDE") classes. I take into consideration only the observations done on the r and g photometric bands. In Figure 4.4 there are reported the results of the classifier on these input set of real lightcurves. From Figure 4.4, one can easily remark two inconvenient behaviours: (i) the "Others" type objects are too often misclassified as "SN" type (e.g., after 11 observations more "Others" type objects are classified "SN" than "Others"); (ii) at early observations, when there is not enough information for any pertinent conclusion, the "Pre-explosion" template is too rarely selected (e.g., after two observations almost as many "Others" type objects are classified "SN" as "Pre-explosion"). Both features might be considered predictable given that "Others" and especially "SN" account for numerous initial `astrorapid` templates. These undesired features led me to make a few adjustments.

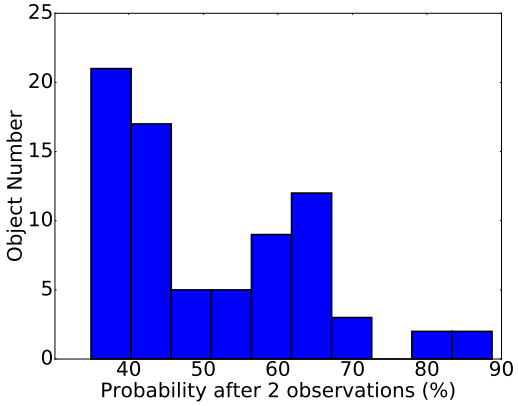

Fig. 4.5 Histogram of the percentage probabilities of the preferred template after two observations, assuming the naive guess collapse described in Equation 4.5. The input data is represented by those real ZTF "Others" lightcurves misclassified as "SN" or "KN".

Thus at the $(k_{\rm obs}+1)^{\rm th}$ observation, I penalize the "SN" class by a factor $(1-e^{-k_{\rm obs}/\beta})$, where β is a parameter to be determined. Moreover I replace the main class "Pre-explosion" by a new main class "Indistinguishable". Then for a given object, the preferred event is "Indistinguishable" if at least one of the following two scenarios holds: (i) the `astrorapid` template "Pre-explosion" is assigned with a probability higher than each of the main classes "SN", "Others" and "KN"; (ii) each class in between {"SN", "Others","KN"} has a probability lower than $p_{\rm thresh}$. The threshold probability $p_{\rm thresh}$ needs to be determined. In order to derive $p_{\rm thresh}$, the real ZTF lightcurves labelled as "Others" and misclassified, after two observations, as "SN" or "KN" have been used. In Figure 4.5, the histogram of the preferred event probabilities is plotted. One can see that a reasonable choice for the "Indistinguishable" class threshold is $p_{\rm thresh} = 0.4$. Before the determination of a value for β, the impact of the parameter might be briefly discussed. Indeed for small β, the penalty factor approaches 1 (because $\lim_{\beta\to 0} e^{-k_{\rm obs}/\beta} = 0$). This situation is equivalent to the initial guess. On the other hand, for high values of β, the penalty factor goes to zero (because $\lim_{\beta\to\infty} e^{-k_{\rm obs}/\beta} = 1$), which implies a situation in which the "SN" class is very disfavoured. As both extreme cases are undesirable, one might easily anticipate that a likeable situation represents a tradeoff between these two extreme behaviors. I use the same set of real ZTF "SN" (respectively "Others") type lightcurves, and I define the success and failure probabilities as the percentage of the objects classified as "SN" (respectively "Others"), and "Others" or "KN" (respectively "SN" or "KN"). Figure 4.6 shows the β dependence of these probabilities at the end of different number of observations. From Figure 4.6, one can conclude that $\beta = 4$ is a convenient choice. Indeed from the top (bottom) panels of Figure 4.6, one can easily remark that the higher (smaller) values of β correspond to a regime where the "SN" ("Others") class is too much disfavored. A flowchart summa-

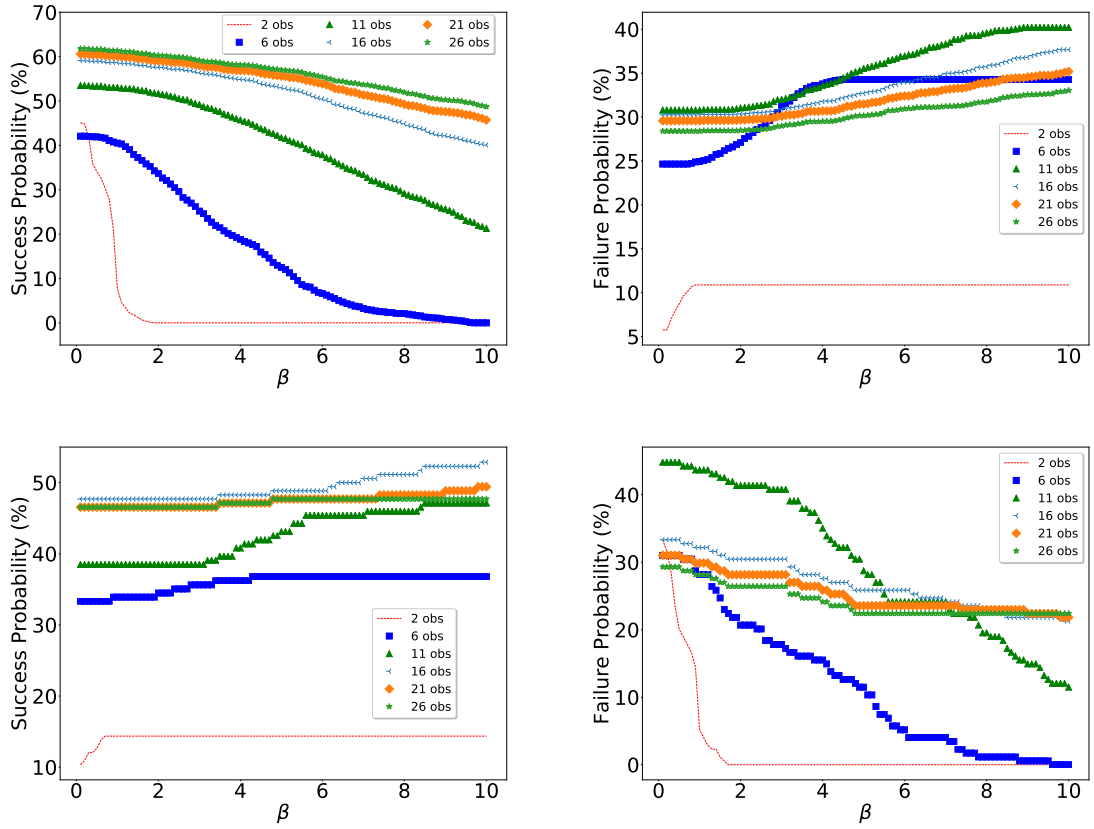

Fig. 4.6 The success (left) and failure (right) probabilities versus β. The preferred event is reported after 2, 6, 11, 16, 21 and 26 observations. The top (bottom) panels correspond to "SN" (respectively "Others") type objects.

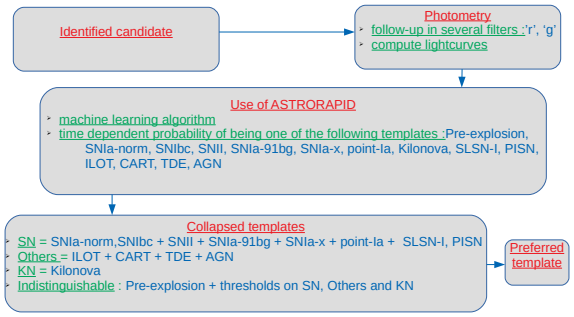

Fig. 4.7 Flowchart showing the different steps of the analysis. The photometric multi filter input data is initially analyzed by `astrorapid` which offers, after each new observation, a probability distribution over fourteen templates. The `astrorapid` output is manipulated as described in this section in order to report, at each new observation, a preferred template from {"SN", "Others", "KN", "Indistinguishable"}.

rizing the passage methodology from the input multi-passband photometric data to the report of a preferred event is proposed in Figure 4.7.

4.2.2 Performance on real events

Here I present the efficiency of the method on the same set of 2,291 public real ZTF lightcurves. As expected, all objects do not possess the same number of observation points. The top left panel of Figure 4.8 presents the histogram of the observation number for these events. While the average number of observations is 29, one can easily remark that there are events for which extensive follow-up (more than 60 measurements) was realized, as well as transients with scarce information (less than 5 observations). This non-uniformity is due to either the ZTF observation strategy, or the timescale on which a particular event is visible. For illustration purposes, on the bottom left panel of Figure 4.8 is shown the histogram of the cosmological redshifts of those real ZTF objects labelled as "SN". One can easily remark the coexistence for both objects with redshift lower than 0.03 (corresponding to $\approx 135\,$Mpc) and higher than 1 (corresponding to $\approx 475\,$Mpc). Equally, on the top right panel of Figure 4.8, the cadence of ZTF is illustrated. While most of the time, two consecutive observations, executed with the same filter, are separated by around 3 days, there is a non insignificant number of situations when the same event is either followed up in the same wavelength range, in two consecutive nights, or has no information related for around one week. While the number of observations is important to assess the effort needed in order to correctly classify astrophysical objects, the cadence is a parameter which impacts the performance of the method. Indeed, a higher cadence allows to better constrain the temporal shape of the lightcurve. On the other hand, a higher rate of photometric measurements means a higher observational effort, which might be done at the expense of other follow-up opportunities. For example, one can devote the follow-up effort to either do as many

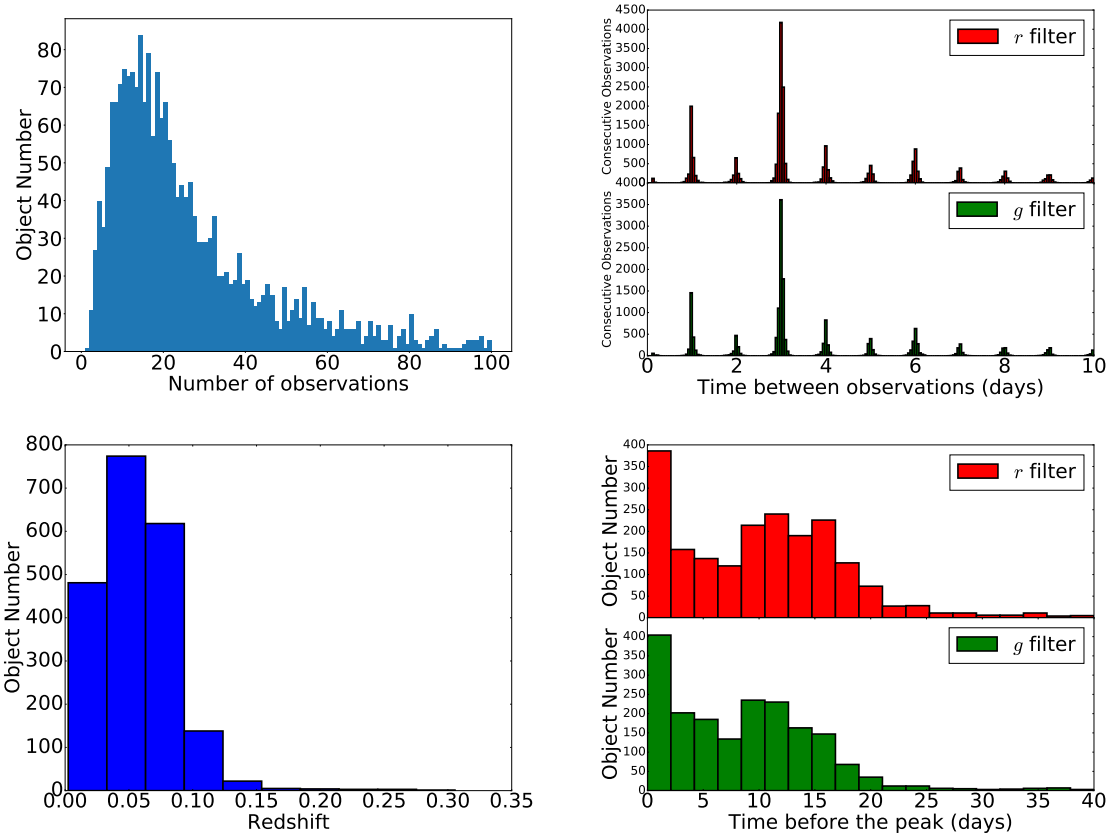

Fig. 4.8 On top left, the observations number histogram for the ZTF public data stream objects. On top right, the histogram of the time separation between two consecutive photon flux measurements realized by using the same r (on top) or g (on bottom) photometric filter. On bottom left (right), the histogram of "SN" type objects cosmological redshift (time difference between the first detection and measured global maximum).

single passband observations as possible or to detect the same astrophysical event in as many photometric filters as possible. In the former case the time evolution is better constrained, while the latter case has the advantage of investigating the color evolution. In general, the lightcurve of an optical transient has a rising and a decaying part, sometimes perturbed by fluctuations. And both portions of the lightcurve have, depending on the transient class, their characteristic timescales. However, of much importance, for the followed-up of a transient object, is the time of the first detection. Indeed, for reasons such as the observation strategy, the proximity of the EM source and/or the intrinsic luminosity, the rising side might be completely missed. In the bottom right panel of Figure 4.8, for the case of "SN" type objects, the histogram of the passband time separations, between the first detection and the observed lightcurve global maximum, is pictured. It is worth noting that there is no way to check if the measured global maximum coincides with the global maximum of the intrinsic lightcurve. So that means that even if some portion of the measured photon flux is increasing over some timescale, it might belong to the main fading regime. Nevertheless, for more than 10% of the events, the first detection is also the brightest observation, indicating thus that in a non-negligible proportion of situations, the supernovae are seen after the luminosity peak. The classification results are illustrated in Figure 4.9. The top left (right) panel corresponds to the classification results when the "SN" (respectively "Others") labelled lightcurves, with observations in both r and g filters, are used as input data. In both cases, after only 11 observations the template preferred most of the time corresponds to the correct class. However, one can remark the better efficiency of the pipeline in the case of "SN" type objects. Indeed, in the case of "SN" input, 16 observations are enough to have a detection fraction higher than 50%, while for the "Others" input, the same percentage is not reached even at the end of 26 observations. The bottom panel of Figure 4.9 shows the classifications when I consider "SN" type objects seen in only one photometric filter. The much worse detection fraction, obtained in this case, highlights the importance of the color evolution information. In this subsection, the results are presented up to 26 observations, while some events joined of less measurements, as mentioned above. In order to remediate this inconsistency, the following rule has been adopted: if an object has only N observations, the preferred template after m fictitious observations, with $m > N$, is the same as the preferred template after the only real N measurements. It is worth noting that in all cases presented here, almost no transient is misclassified as "KN", emphasizing the utility of such a tool for the kilonova follow-up.

4.2.3 Injections recovery efficiency

While in the previous section I discussed the case of real "SN" and "Others" type transients, here I consider simulated "SN" and "KN" lightcurves. The "KN" injec-

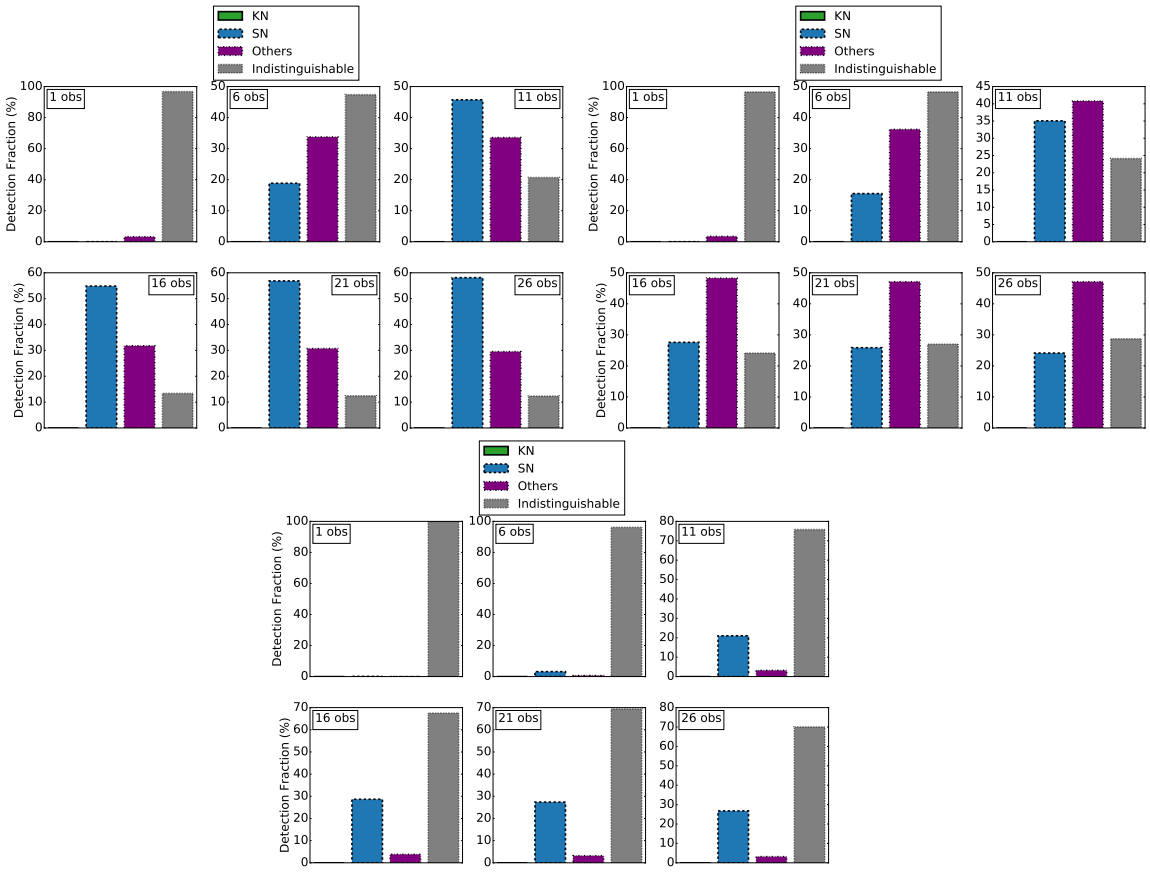

Fig. 4.9 Classification results for ZTF real events. Both r and g (respectively only r) observations are considered for the top (respectively bottom) panels. On the top left (right), "SN" (respectively "Others") labelled objects are used as input data, while for the bottom panel only "SN" type events are considered.

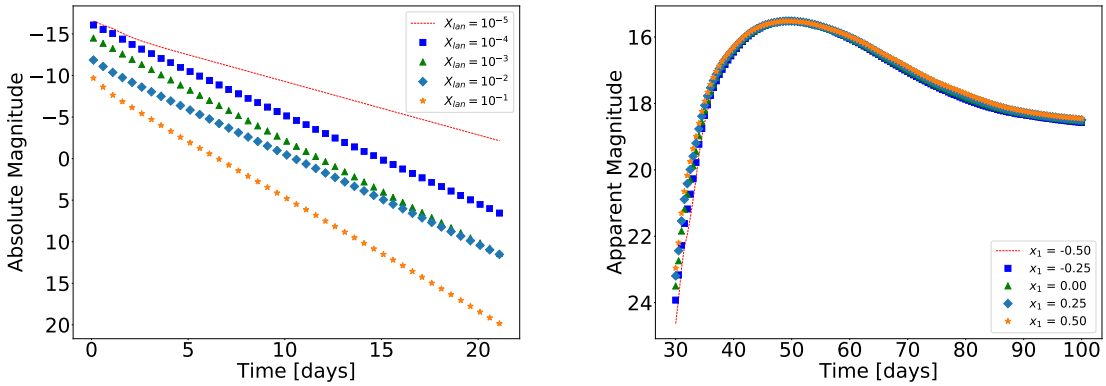

Fig. 4.10 On left, the g passband absolute magnitude for simulated kilonovae possessing $M_{ej} = 0.005\,M_{\odot}$, $v_{ej} = 0.15\,c$ and different lanthanide fractions. On right, g passband apparent magnitude for simulated supernovae with color index $c = 0$, redshift $z = 0.022$ and possessing different shape parameters x_1.

tions are clearly motivated by the scarcity of already observed kilonovae. Concerning the "SN" injections, I want to partially address the question related to how well the performances might be improved, by increasing the observational cadence. "Others" type injected objects are not considered for both technical (it needs a significant effort to collect all different simulation tools) and real EM follow-up conditions (the background transient sky is largely dominated by supernovae) reasons. The "KN" photometric lightcurve generator used here is described in Coughlin et al. [2019a, 2018a], while for the "SN" injections, "sncosmo" [Barbary et al., 2016; Guy et al., 2007] is utilized. For the "KN" simulations, the following parameter space is considered: log-uniformly distributed mass ejecta $M_{ej} \in [0.01\,M_{\odot}, 0.1\,M_{\odot}]$ and lanthanide fraction $X_{lan} \in [10^{-5}, 10^{-1}]$, and uniformly-sampled ejecta velocity $v_{ej} \in [0.01\,\mathrm{c},\ 0.3\mathrm{c}]$. Concerning the "SN" type injections, they are parameterized by the stretch $x_1 \in [-0.5, 0.5]$ and the color $c \in [-0.05, 0.05]$, both distributions being uniform. Equally, one should note that only Type Ia supernova injections are considered in this study. A few examples of "SN" and "KN" simulated lightcurves are offered in Figure 4.10. One can easily note that a heavier element kilonova ejecta renders the low wavelength photon flux dimmer, while the stretch parameter impacts on the rising and decreasing slope of the supernova lightcurve. Moreover the simulated observations are assigned with ZTF-like uncertainties, which are photometric filter dependent. In order to be consistent with the distribution of real ZTF cosmological redshifts (see Figure 4.8), the injections have distances uniformly sampled in $[40\,\mathrm{Mpc}, 300\,\mathrm{Mpc}]$. Regarding the kilonova simulations, the $300\,\mathrm{Mpc}$ boundary is almost equivalent with the ZTF apparent magnitude limit. Indeed, at such high distances, a kilonova is in general no visible in the g band, while in the r band is detectable only for a few hours. In contrast, real supernovae are detectable at much higher redshifts. Therefore, this choice for the distances might appear problem-

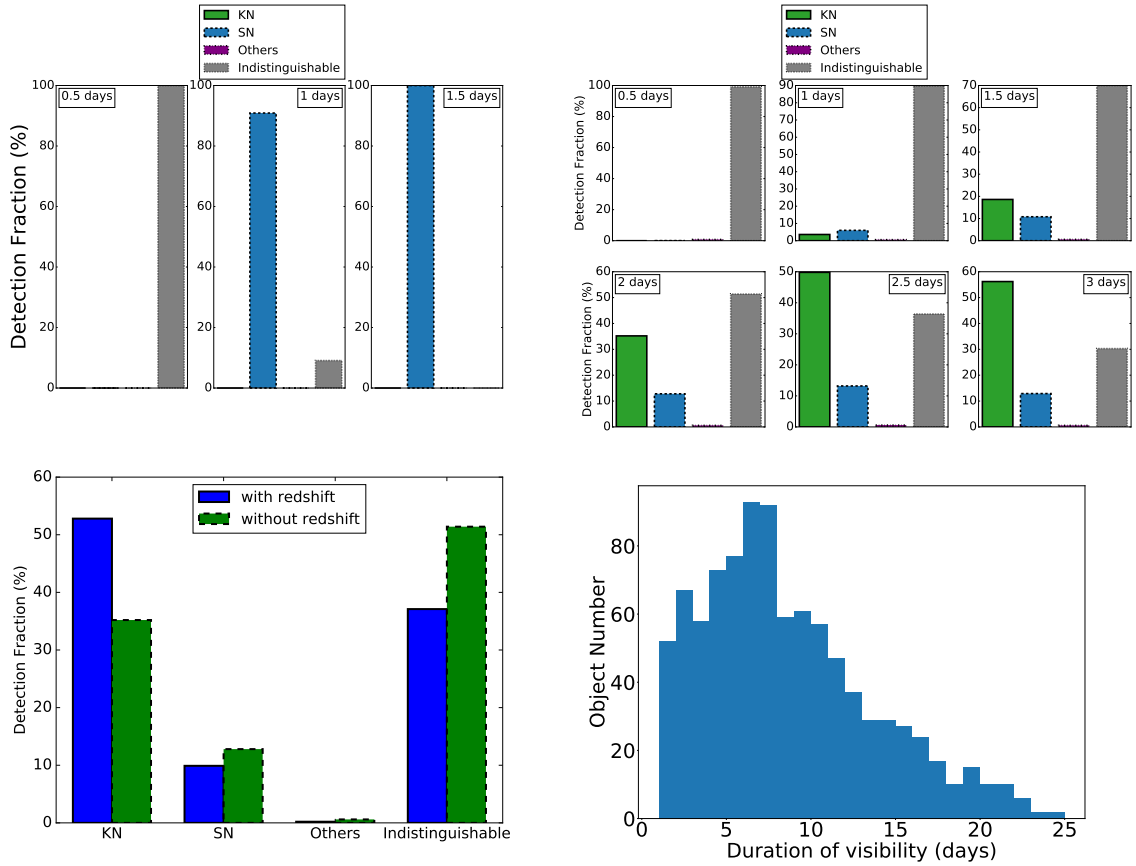

Fig. 4.11 Top left: preferred event histogram when the input is a set of 1000 injected "SN"; top right: preferred event histogram when the input is the a of 1000 injected "KN"; bottom left: classification fraction at the end of two nights, for both redshift assigned and unassigned "KN" injections; bottom-right: histogram of durations during which the simulated "KN" are visible for a ZTF-like telescope.

atic, because, in this way, the very faint objects are not considered, even if present in the real ZTF database. In the current simulation set, some supernovae might be extremely bright, remaining visible in the sky, for the telescopes, for months. On the other hand, in this section, I am interested in approximating the minimum number of observations needed for a good enough recovery efficiency of the pipeline. Therefore, the positions in time of the observations, compared to the location of the supernova peak, become relevant. Based on the bottom right panel of Figure 4.8, I choose a population of supernovae whose first detection is [-7 days, +30 days] uniformly distributed with respect to the brightness peak. Unless specified, everywhere in the rest of this section, I assume that the injections are not assigned with distance/redshift information.

Initially, well-sampled "SN" and "KN" injections are considered. More specifically, each day, there are four measurements, two for each photometric filter in $\{r, g\}$. The results classifications are presented in Figure 4.11. The top left panel shows that the pipeline needs less than 2 days to perfectly recover "SN" injections. Moreover, even for the very early observations, the well-sampled "SN" objects are not misclassified

as “KN” or “Others”, the pipeline outputting “Indistinguishable”. The main reason for which the supernovae are easily distinguishable from the other transients is that they are the brightest. The top right panel indicates that well-sampled kilonovae are recovered with an efficiency better than 50% after less than 3 days. Apart from “Indistinguishable”, the pipeline sometimes misidentifies the kilonovae as “SN”. It is worth noting that all the injected “KN” are not detectable by a ZTF-like telescope for at least 3 days as one might naively believe when looking at the top right panel of Figure 4.11. Indeed, even if the intrinsic parameters M_{ej}, v_{ej}, X_{lan} also have an impact on the brightness, the key quantity impacting the apparent magnitude is the luminosity distance. The bottom right panel of Figure 4.11 presents the timescale over which the KN is observable in at least one of the photometric filters r and g. This is why, as in the case of the real ZTF “Others” objects treated in the previous section, I consider here that, if the duration visibility of a simulated “KN” allows only N observations, the preferred template at the end of m fictitious photometric measurement, with $m > N$, is the same as the preferred template after the real N observations. Finally, in Figure 4.11, the bottom left panel displays the improvement one might obtain if, in addition of the photometric data, the cosmological redshift information is available. One can observe that more than 10% of the initially “SN” or “Indistinguishable” misclassified objects, become “KN” if luminosity distance related data is added. Additionally, for the “KN” injections, the dependence of the classifier performance on both the intrinsic parameters M_{ej}, v_{ej}, X_{lan} and cosmological reshift is provided in Figure 4.12. One can clearly remark a few behaviors. As emphasized in the top left panel, a higher (lower) lanthanide fraction favors the “Indistinguishable” (respectively “SN”) class. This is due to the fact that the heavier the ejecta, the higher the optical opacity, and then more photons are observed rather in the infrared range instead of the optical and ultra-violet bands. Therefore, given that the input data consists in r and g observations, bigger (smaller) values of X_{lan} are associated to dimmer (brighter) events. Similar behavior happens when the redshift is varied (top right panel). Indeed a higher (smaller) value of the redshift corresponds to a longer (shorter) luminosity distance, which has, as a consequence, a higher (smaller) apparent magnitude. Simultaneously, the bolometric luminosity increases with the amount of expelled matter. This is clearly emphasized by the bottom left panel, showing that the “SN” class is favored at large mass ejecta. Finally, one can see that smaller values of the ejecta velocity support the “Indistinguishable” pipeline choice. An important parameter of a photometric classifier destined to real time EM observation scheduling strategy is the event luminosity at the moment of its first correct classification. In Figure 4.13 there is the probability density of the r and g apparent magnitude at the first correct classification of a well-sampled “KN” injection. One can see that an important part of the simulated events have a magnitude smaller than 21 at the moment of their

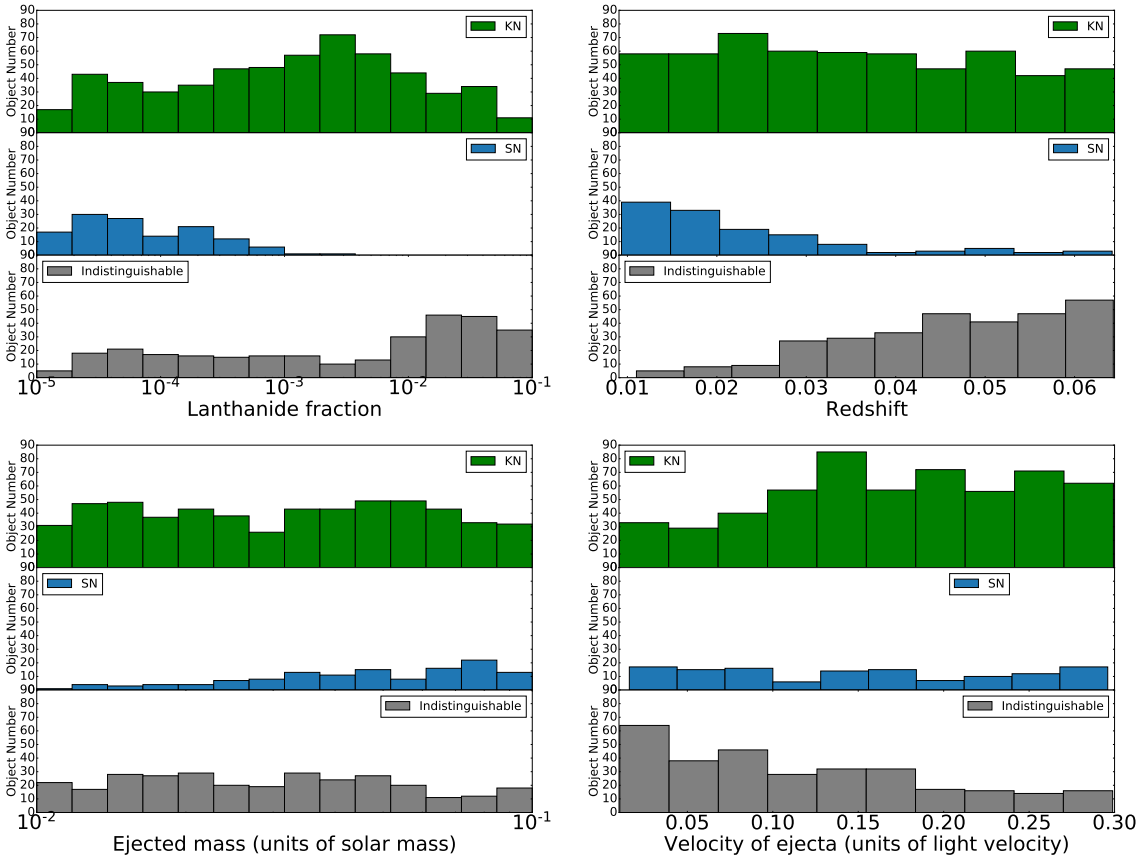

Fig. 4.12 Kilonovae injections classification results as a function of the lanthanide fraction X_{lan} (top left), cosmological redshift (top right), mass ejecta M_{ej} (bottom left) and ejecta velocity v_{ej} (bottom right). In each panel, the histogram of the number of times each template, in between {"SN", "KN", "Indistinguishable"}, is selected by the pipeline.

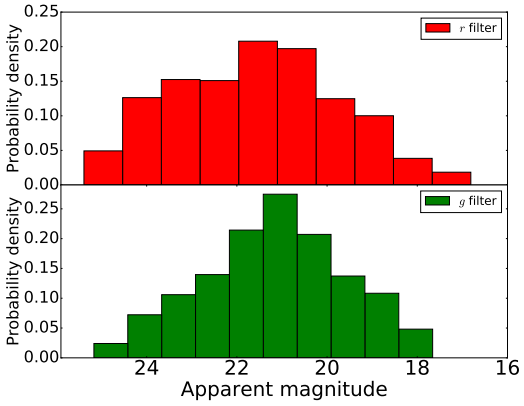

Fig. 4.13 The r (on top) and g (on bottom) apparent magnitude probability density at the moment of the first correct classification. The set of 1000 well-sampled simulated "KN" are used as input data.

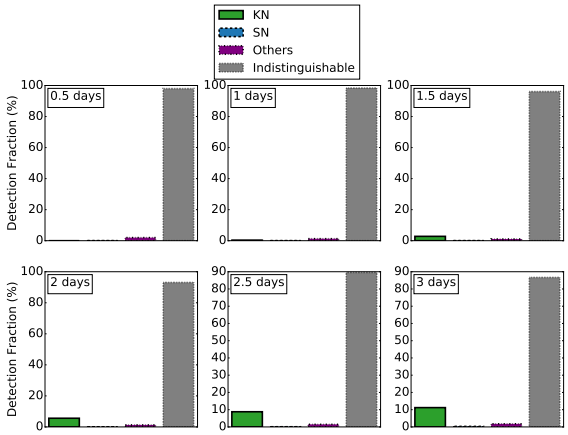

Fig. 4.14 Histogram of preferred templates when the I use the 100 realistically sampled "KN" injections.

first correct identification. Therefore for a ZTF-like instrument, as well as for the next generation telescopes, at the condition of a competitive cadence, the kilonovae would be detected early enough in order to advise the EM observing community to realize intensive follow-up too.

In the previous paragraph I considered the ideal case of a very powerful telescope cadence. However, the top right panel of Figure 4.8 suggests that this is quite unrealistic today. This is why I also choose to test the pipeline efficiency in the case of realistically-sampled kilonovae. Figure 4.14 illustrates the classification results when "KN" injections, with sampling rate of 1/(3 days) in the r and g filters, are considered. The performance of the pipeline is much worse. This is an expected behavior, given that for time evolution constraints one needs at least two observations per filter, while color information is unavailable without at least one observation per filter. The non fulfillment of these requirements favors the "Indistinguishable" class, as emphasized by Figure 4.14.

4.2.4 The case of AT2019wxt

This subsection summarizes the study, appearing in Antier et al. [2020b], of a kilonova candidate, situated at $144\,\mathrm{Mpc}$. It is about AT2019wxt, an EM counterpart candidate to the GW alert S191213g [LIGO Scientific Collaboration and Virgo Collaboration, 2019c], reported by Pan-STARRS [McBrien et al., 2019]. Inside GRANDMA collaboration, several instruments (see Figure 4.15), among which the *Lisnyky/AZT-8*, the *Tingshua-NAOC Telescope* [Wang et al., 2008; Huang et al., 2012], the *Xinglong-2.16*, the *Thai National Telescope* and some citizen astronomers, observed this transient. The present code was tried on around 20 observational points, and the output classification still indicated "Indistinguishable". This result might be the consequence of different things. Firstly, the heterogeneity of the GRANDMA observations might cause the in-

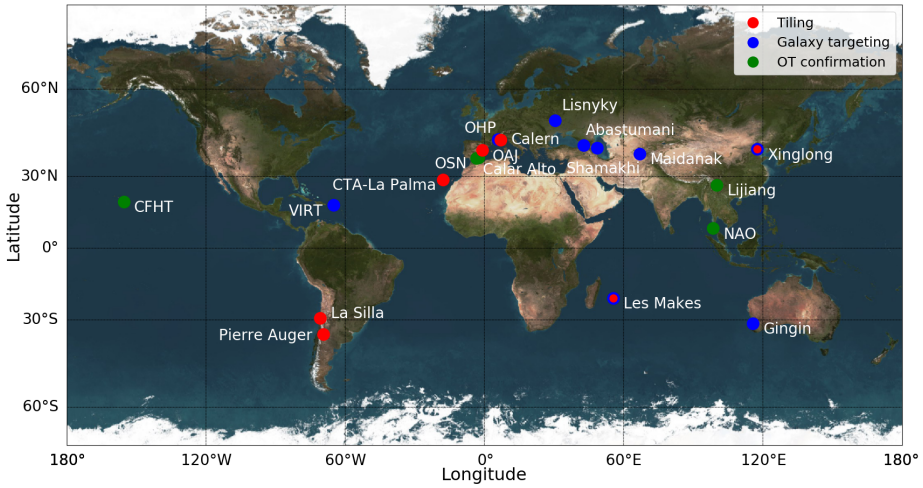

Fig. 4.15 The locations distribution of the GRANDMA network observatories. The picture is taken from Antier et al. [2020b].

conclusive output. Indeed, not only ZTF observations have not been used (as it was the case for the training of the machine learning algorithm), but measurements from different instruments, with different characteristics, were used. Secondly, the indefinite output might be an indication of the peculiarity of the EM transient. Indeed, if AT2019wxt is much different from the objects on which the classifier was trained on, it is not surprising that the present method did not recognize it. It is worth mentioning that, AT2019wxt was finally classified as Type IIb supernova by LBT [Vallely, 2019]. One should note that there was need of spectroscopic information (helium lines) in order to solve this issue.

CHAPTER 5

Kilonova photometric lightcurve prediction based on low-latency GW data

This Chapter contains the study published in Stachie et al. [2021].

5.1 Supra-nuclear density matter equation of state and kilonova lightcurve models

As explained in the previous chapter, detecting kilonovae is not an easy task. Indeed, for BNS/NSBH mergers occuring at a few hundreds Mpc away, the EM counterpart should be detectable in the sky, for the actual and near future spatial and terrestrial telescopes, only for a few nights. If in addition, the sky localization, provided by the GW signal and/or the eventual high energy photons of the corresponding GRB γ-ray prompt emission, is not very informative, the EM astronomers need to look for a needle in a haystack: indeed, in such a case, the kilonova is buried in a large set of optical transient candidates, most of them being supernovae. One might envisage several ways to tackle this issue: while in Chapter 4, the solution was to create a photometric classifier able to discriminate between kilonovae and the other type of transients, here I aim to predict the EM lightcurve, based on the GW measured data. Despite of the GW data based information, such as the masses and the spins of the binary compact objects components, there are important uncertainties regarding some binary features. Given that the equation of state of matter at supra-nuclear densities is not known with enough precision, the scenario of the binary last life moments is uncertain. For example, in a NSBH, the gravitational field of the black hole exerts tidal forces on the neutron star companion. In such a situation, two scenarios should be envisaged: either the neutron star is disrupted by the tidal forces forming a debris disc around the black hole or the neutron star plunges inside the black hole event horizon without being torn apart. A softer (stiffer) equation of state would favor the former (latter) scenario. Moreover, the properties of the matter at such high densities influence the maximum mass a object, of a given size, can support without undergoing a gravitational collapse. Indeed, the stronger the interaction between particles (accounting for the equation of state stiffness), the smaller

the maximum mass a neutron star might possess. Whereof, for instance, if the GW data indicates a compact object with mass in between two and three $M_\odot$, it is almost impossible to decide if the astrophysical object is a black hole or a neutron star. This is the case for GW190814 (where the lighter object weighs $2.6\,M_\odot$), a binary merger whose nature is unknown [Abbott et al., 2020b]. Therefore, some assumption is needed concerning the equation of state of neutron stars. By equation of state, I mean the pressure-energy density relation at a given temperature. Attempts to derive this relation exist in the literature. A famous example is the one proposed in Douchin and Haensel [2001]. In this example, the neutron star possesses a sub-nuclear density crust formed of ordinary matter (electrons, neutrons, protons) and a supra-nuclear density liquid core which, in addition to the crust particle components, also contains muons. The main interaction between particles, at such high densities, is the strong force. Unfortunately, the many-body problem (with more than two objects) is still unsolvable, even in today's era of high performance computers. Therefore, one traditional technique is to consider mean field approximation of an effective nucleon-nucleon interaction. Nonetheless some conditions are required: these approximations should verify experimental data in the regime of less dense matter [Pethick et al., 1995]. In Douchin and Haensel [2001], the *Skyrme Lyon* (SLy) type interaction is considered [Chabanat et al., 1997, 1998]. More specifically, the neutron star crust total energy is written

$$E^{\mathrm{DOU}} = E^{\mathrm{DOU}}_{\mathrm{N,bulk}} + E^{\mathrm{DOU}}_{\mathrm{N,surf}} + E^{\mathrm{DOU}}_{\mathrm{Coul}} + E^{\mathrm{DOU}}_{e}, \tag{5.1}$$

where E^{DOU}_{e} is the energy of the Fermi gas electrons (sum of the rest and kinetic energies), $E^{\mathrm{DOU}}_{\mathrm{N,bulk}}$ is the nucleon bulk energy, $E^{\mathrm{DOU}}_{\mathrm{N,surf}}$ is the surface energy due to the shapes of the denser nuclear structure immersed in the less denser neutron gas, and finally $E^{\mathrm{DOU}}_{\mathrm{Coul}}$ is the Coulomb energy, under the Wigner-Seitz approximation. For the liquid core, Coulomb contributions are negligible, and there is no more surface energy term. Indeed, given that the particle number densities are higher than $n^{\mathrm{DOU}}_{\mathrm{edge}} = 0.073\,\mathrm{fm}^{-3}$, one expects to have a homogeneous plasma of nucleons, electrons and muons. Therefore the energy density of the core plasma can be written as

$$\begin{aligned} E^{\mathrm{DOU}}(n_n^{\mathrm{DOU}}, n_p^{\mathrm{DOU}}, n_e^{\mathrm{DOU}}, n_\mu^{\mathrm{DOU}}) = E^{\mathrm{DOU}}_{\mathrm{N}}(n_n^{\mathrm{DOU}}, n_p^{\mathrm{DOU}}) + E^{\mathrm{DOU}}_{e}(n_e^{\mathrm{DOU}}) + \\ + E^{\mathrm{DOU}}_{\mu}(n_\mu^{\mathrm{DOU}}) + n_n^{\mathrm{DOU}} m_n c^2 + n_p^{\mathrm{DOU}} m_p c^2, \end{aligned} \tag{5.2}$$

where m_n and m_p are the neutron and proton rest masses, while n_e^{DOU}, n_μ^{DOU}, n_n^{DOU} and n_p^{DOU} are the electron, muon, neutron and proton number densities. Moreover, in the previous formula, E^{DOU}_{e} and E^{DOU}_{μ} are the electron and muon Fermi gas energy densities, while $E^{\mathrm{DOU}}_{\mathrm{N}}$ is the SLy based interacting nucleons energy density. If one considers the baryon number density, noted $n_b^{\mathrm{DOU}} = n_n^{\mathrm{DOU}} + n_p^{\mathrm{DOU}}$, one gets the following n_b^{DOU}

parameterized equation of state:

$$\rho^{\mathrm{DOU}}(n_b^{\mathrm{DOU}}) = \frac{E^{\mathrm{DOU}}(n_b^{\mathrm{DOU}})}{c^2}, \qquad P^{\mathrm{DOU}}(n_b^{\mathrm{DOU}}) = (n_b^{\mathrm{DOU}})^2 \frac{d}{dn_b^{\mathrm{DOU}}} \left(\frac{E^{\mathrm{DOU}}(n_b^{\mathrm{DOU}})}{n_b^{\mathrm{DOU}}} \right), \tag{5.3}$$

where ρ^{DOU} and P^{DOU} are the targeted energy density and pressure. While in Douchin and Haensel [2001] the equation of state is constructed based on nuclear physics theoretical modeling, one might try to constrain the matter properties at such high densities based on observational measurements. Examples of such endeavors exist in the literature. Miller et al. [2019a] determine the mass and radius of the millisecond pulsar PSR J0030+0451, by analyzing the rotating surface hot spot soft X-ray emission, detected by the Neutron Star Interior Composition Explorer (NICER), aboard the International Space Station. Then the neutron star mass and radius, together with the Tolman-Oppenheimer-Volkoff [Tolman, 1939; Oppenheimer and Volkoff, 1939] (TOV) equations, are used to constrain the parameterized equation of state from Lindblom [2010, 2018] and some piecewise polytropes. Equally, multimessenger observations have been used to constrain the neutron star equation of state [Dietrich et al., 2020; Landry et al., 2020; Capano et al., 2020; Essick et al., 2020].

After all, despite a good knowledge about the binary parameters, in order to predict spectra and photometric lightcurves, one needs a model for the kilonova. During the last years, several proposals have been made. For example, Barnes et al. [2016] suggest a time-dependent, multi-wavelength radiation transport simulation parameterized by the mass and the velocity of the ejecta. The chemical composition of the ejecta is derived in the following way: at first, the r-process nucleosynthesis neutron rich elements are determined by means of simulated smoothed-particle hydrodynamics trajectories [Goriely et al., 2011a]. Then, radioactive reactions such as beta decay, alpha decay and nuclear fission are considered. Therefore, the chemical elements forming the ejecta are γ-rays, β-particles, α-particles and fission fragments. The numerical simulations also take into account the influence of the residual magnetic field (created by the merger turbulence [Kiuchi et al., 2015, 2014] or inherited from the binary neutron star(s) component(s)) on the trajectories of charged particles. It is shown that the trajectories are confined inside flux tubes, because the corresponding Larmor radii are smaller than the ejecta radius. Finally the thermalized emission is computed by accounting for the energy losses of the radioactive decay products as follows: γ-rays through Compton scattering and photoionization; β-particles through Coulomb interaction based excitation and ionization of atomic electrons; α-particles and nuclear fission fragments through interactions with free and bound electrons. Korobkin et al. [2021] study the ejecta morphological shape dependence of the kilonova lightcurve. By means of a radiative transfer Monte Carlo code [Wollaeger and Van Rossum, 2014], one and

two ejecta components are considered. While in the former case, uniform chemical composition prior is adopted, in the latter case, the components ejecta are assumed to have a low- and a high-electron-fraction ($Y_e^{\rm KOR}$) abundance pattern. The geometrical shapes, chosen for this study, are Cassini ovals, noted $\rm H^{KOR}$, $\rm P^{KOR}$, $\rm B^{KOR}$, $\rm T^{KOR}$ and $\rm S^{KOR}$, corresponding, in a velocity space axisymmetric coordinates $\{v_r^{\rm KOR}, \theta^{\rm KOR}\}$, to the following time dependent density profiles

$$\rho^{\rm KOR}(v_r^{\rm KOR}, \theta^{\rm KOR}, t) = \rho_0^{\rm KOR} \left(\frac{t}{t_0^{\rm KOR}}\right)^{-3} \times$$
$$\times \begin{cases} \left(-\left(\frac{v_r^{\rm KOR}}{v_0^{\rm KOR}}\right)^4 - 2\left(\frac{v_r^{\rm KOR}}{v_0^{\rm KOR}}\right)^2 \cos 2\theta^{\rm KOR}\right)^3 & \text{if } \rm H^{KOR} \\ \left(1 - \left(\frac{v_r^{\rm KOR}}{v_0^{\rm KOR}}\right)^4 - 2\left(\frac{v_r^{\rm KOR}}{v_0^{\rm KOR}}\right)^2 \cos 2\theta^{\rm KOR}\right)^3 & \text{if } \rm P^{KOR} \\ \left(1.5 - \left(\frac{v_r^{\rm KOR}}{v_0^{\rm KOR}}\right)^4 + 2\left(\frac{v_r^{\rm KOR}}{v_0^{\rm KOR}}\right)^2 \cos 2\theta^{\rm KOR}\right)^3 & \text{if } \rm B^{KOR} \\ \left(-\left(\frac{v_r^{\rm KOR}}{v_0^{\rm KOR}}\right)^4 + 2\left(\frac{v_r^{\rm KOR}}{v_0^{\rm KOR}}\right)^2 \cos 2\theta^{\rm KOR}\right)^3 & \text{if } \rm T^{KOR} \\ \left(1 - 2\left(\frac{v_r^{\rm KOR}}{v_0^{\rm KOR}}\right)^2\right)^3 & \text{if } \rm S^{KOR} \end{cases}, \tag{5.4}$$

where $\rho_0^{\rm KOR}$, $v_0^{\rm KOR}$ and $t_0^{\rm KOR}$ are the characteristic scale density, velocity and time. One should note that $\rm S^{KOR}$ corresponds to the spherical shape. For the two components model, the two shapes are $(X, Y) \in \{\rm H^{KOR}, P^{KOR}, B^{KOR}, T^{KOR}, S^{KOR}\}^2$. The simulation output indicates large deviations from the default spherical case of the peak time and luminosity, as well as behaviors such as lanthanide curtaining, photon reprocessing and photon redirection. In the following of this chapter I present a method, also described in [Stachie et al., 2021], to convert low-latency GW data into EM photometric lightcurves.

5.2 Compact objects masses and spins conversion into photometric lightcurves

5.2.1 GW input data and neutron star matter properties prior

The binary parameters information used in this study is provided by the Multi-Band Template Analysis (MBTA) [Aubin et al., 2021; Adams et al., 2016] pipeline. MBTA is a matched filter analysis searching for modelled CBC signals in the GW data. A big difference between this pipeline and others, such as *PyCBC* presented in Section 2.2.1,

is that the data is not directly matched against a waveform spread over the entire interferometer frequency band, but uses multiple bands. Indeed, the whole frequency range, to which the GW detectors is sensitive, is split into two or more bands (hereafter two). The splitting is realized in such a way that the corresponding signal-to-noise ratio (hereafter $\mathrm{SNR}^{\mathrm{ADA}}$) is similar between different bands. For each detector, before looking for coincidences, single interferometer triggers are generated in the following way: a whole frequency range of mass and aligned spin template bank [Brown et al., 2012], whose waveforms, noted $\mathrm{VT}^{\mathrm{ADA}}$ and named "virtual" templates, with a minimal match of 97%, is considered. This set of waveforms is used to generate real templates, noted $\mathrm{RT}^{\mathrm{ADA}}$, for each of the frequency bands. Matched filtering between virtual and real templates allows the derivation of the time and phase differences, noted Δt^{ADA} and $\Delta\phi^{\mathrm{ADA}}$, between the real templates, in the two frequency bands, and the virtual templates. Then, the calibrated experimental strain data, noted h^{ADA}, is matched against each single band real waveforms. The templates for which the single band $\mathrm{SNR}^{\mathrm{ADA}}$ is higher than $5/\sqrt{2}$ are considered for further combinations with the other frequency band templates. Finally, for each such combination, the virtual template $\mathrm{SNR}^{\mathrm{ADA}}$ is computed as follows

$$\mathrm{SNR}^{\mathrm{ADA}} = \langle h^{\mathrm{ADA}}, \mathrm{VT}^{\mathrm{ADA}}\rangle(t) = \langle h^{\mathrm{ADA}}, \mathrm{RT}^{\mathrm{ADA}}_{\mathrm{LF}}\rangle(t) + e^{i\Delta\phi^{\mathrm{ADA}}}\langle h^{\mathrm{ADA}}, \mathrm{RT}^{\mathrm{ADA}}_{\mathrm{HF}}\rangle(t+\Delta t^{\mathrm{ADA}}), \tag{5.5}$$

where $\langle h^{\mathrm{ADA}}, T\rangle(t) = 4\Re\int_{\Delta f^{\mathrm{ADA}}} \frac{\tilde{h}^{\mathrm{ADA}}(f)\tilde{T}^{*}(f)}{S_h^{\mathrm{ADA}}(f)} e^{-2i\pi f t}\delta f$. Δf^{ADA} and $S_h^{\mathrm{ADA}}(f)$ are the frequency range of the band and the noise power spectral density. In Equation 5.5, the corresponding real templates are noted $\mathrm{RT}_{\mathrm{LF}}$ and $\mathrm{RT}_{\mathrm{HF}}$. A new cut consists in considering only those triggers having $\|\mathrm{SNR}^{\mathrm{ADA}}\| > 5$, then a chi-squared consistency test is done by checking the partition of the entire $\mathrm{SNR}^{\mathrm{ADA}}$ over the different frequency bands [Allen, 2005]. Then, a reweighted signal-to-noise ratio, noted ρ^{AUB}_{rw}, is calculated based on a autocorrelation least-squares test. More specifically, this new statistical quantity is defined as follows

$$\rho^{\mathrm{AUB}}_{rw} = \begin{cases} \rho^{\mathrm{AUB}} & \mathrm{if} \zeta^2_{PQ} \leq 1 \\ \rho^{\mathrm{AUB}} \left(\frac{A_1^{\mathrm{AUB}} + \zeta^2_{PQ}{}^{\alpha_1^{\mathrm{AUB}}}}{A_1^{\mathrm{AUB}}+1} \right)^{-1/\beta^{\mathrm{AUB}}} & \mathrm{otherwise} \end{cases}, \tag{5.6}$$

with $\zeta^2_{PQ} = \frac{1}{2\Delta t^{\mathrm{AUB}}} \int_{t_0^{\mathrm{AUB}} - \frac{\Delta t^{\mathrm{AUB}}}{2}}^{t_0^{\mathrm{AUB}} + \frac{\Delta t^{\mathrm{AUB}}}{2}} \left\| \begin{pmatrix} \rho_P^{\mathrm{AUB}}(t) \\ \rho_Q^{\mathrm{AUB}}(t) \end{pmatrix} - \rho^{\mathrm{AUB}} \mathcal{R}^{\mathrm{AUB}} \begin{pmatrix} A_P^{\mathrm{AUB}}(t - t_0^{\mathrm{AUB}}) \\ A_Q^{\mathrm{AUB}}(t - t_0^{\mathrm{AUB}}) \end{pmatrix} \right\|^2 dt$.

ρ^{AUB} and ϕ^{AUB} are the absolute value and the complex phase of the complex number $\mathrm{SNR}^{\mathrm{ADA}}$, ρ_P^{AUB} and ρ_Q^{AUB} are the phase and the quadrature components of the matched filter output, A_P^{AUB} and A_Q^{AUB} are the autocorrelations between the virtual combined template and its phase and quadrature components, t_0^{AUB} and Δt^{AUB} are the trigger

time and the band frequency range, $\mathcal{R}^{\mathrm{AUB}}$ is the rotation matrix associated to ϕ^{AUB}. Finally, in Equation 5.6, $A_1^{\mathrm{AUB}} = 10$, $\alpha_1^{\mathrm{AUB}} = 5$ and $\beta^{\mathrm{AUB}} = 8$ are chosen coefficients. The signal-to-noise ratio is reweighted one more time in order to account for time intervals of poor data quality. The increase in the rate of statistical significant triggers is measured with the quantity

$$\delta R^{\mathrm{AUB}}(t) = \frac{R^{\mathrm{AUB}}_{(\rho^{\mathrm{AUB}} \geq \rho^{\mathrm{AUB}}_{\mathrm{min}})} - R^{\mathrm{AUB}}_{(\rho^{\mathrm{AUB}}_{\mathrm{rw}} \geq \rho^{\mathrm{AUB}}_{\mathrm{min}})}}{R^{\mathrm{AUB}}_{(\rho^{\mathrm{AUB}} \geq \rho^{\mathrm{AUB}}_{\mathrm{min}})}}, \tag{5.7}$$

where R^{AUB} is the rate of triggers. Then, for a GW event, triggered at time t_0^{AUB} and assigned with ρ^{AUB}, a new statistical significance, noted $\rho^{\mathrm{AUB}}_{rw,E_R}$, is defined as

$$\rho^{\mathrm{AUB}}_{rw,E_R} = \begin{cases} \rho^{\mathrm{AUB}}_{rw} & \mathrm{if} E_R(t_0^{\mathrm{AUB}}) \leq 0.3 \\ \rho^{\mathrm{AUB}}_{rw}[1 - A_2^{\mathrm{AUB}}(E_R(t_0^{\mathrm{AUB}}) - 0.3)^{\alpha_2^{\mathrm{AUB}}}] & \mathrm{otherwise} \end{cases}, \tag{5.8}$$

where $E_R(t_0^{\mathrm{AUB}}) = \delta R^{\mathrm{AUB}}(\mathrm{median}_{[t_0^{\mathrm{AUB}} + t_{\mathrm{offset}}^{\mathrm{AUB}} - 10s, t_0^{\mathrm{AUB}} + t_{\mathrm{offset}}^{\mathrm{AUB}}]})$. $A_2^{\mathrm{AUB}} = 1$, $\alpha_2^{\mathrm{AUB}} = 2$ and $t_{\mathrm{offset}}^{\mathrm{AUB}} = 7\,\mathrm{s}$ are real coefficients. Coincident triggers are obtained by considering those single interferometer triggers satisfying template parameter matching and being separated in time by an interval smaller than the duration that a photon needs to go from one interferometer to the other, plus some duration accounting for the measurement uncertainty. Hereafter I note by $\mathrm{SNR}^{\mathrm{MBTA}}$, the signal-to-noise ratio of the interferometer network, defined as the square root of the sum of squares of individual interferometer $\rho^{\mathrm{AUB}}_{rw,E_R}$. In the present study, for a GW event, I consider not only the most significant trigger, i.e. having the highest $\mathrm{SNR}^{\mathrm{MBTA}}$ (noted $\mathrm{SNR}^{\mathrm{MBTA}}_{\mathrm{max}}$), but all the triggers with $\mathrm{SNR}^{\mathrm{MBTA}} > \mathrm{SNR}^{\mathrm{MBTA}}_{\mathrm{max}} - 3$. Moreover, the statistical ranking used in this study, the weight, noted w, is defined as follows: firstly, for each trigger assigned with $\mathrm{SNR}^{\mathrm{MBTA}}_i$, the quantity $\mathrm{dSNR}^{\mathrm{MBTA}}_i = \mathrm{SNR}^{\mathrm{MBTA}} - \mathrm{SNR}^{\mathrm{MBTA}}_i$ is computed; secondly the weight $w_i = \mathrm{erf}(\mathrm{dSNR}^{\mathrm{MBTA}}_{i+1}) - \mathrm{erf}(\mathrm{dSNR}^{\mathrm{MBTA}}_i)$, smoothed by taking the average of it and the two dSNR_i adjacent templates, is assigned. One should note that the weight allows in some sense the clustering of the templates, which are close in the parameter space. Indeed, for two near templates, one should expect similar $\mathrm{SNR}^{\mathrm{MBTA}}$, hence the weight of one of them approaches zero. It is worth mentioning that the indices i are attributed in such a way that $i = 0$ corresponds to the template with the highest $\mathrm{SNR}^{\mathrm{MBTA}}$, $i = 1$ to the template with the second highest $\mathrm{SNR}^{\mathrm{MBTA}}$, and so on. One should remark that the sum of the weights is 1. At the end, the low-latency GW input data consists in a list of 5-tuples (m_1, m_2, s_1, s_2, w), where m_1 and s_1 (respectively m_2 and s_2) are the mass and spin of the heavier (lighter) binary compact object. I want to make clear that I did not generate by myself this list of 5-tuples. Instead, Benoit Mours, member of the MBTA team, provided it to me.

As stated in the previous subsection, the equation of state at supra-nuclear densities determines some of the characteristics of the binary. Based on the hydrostatic equilibrium, the structure of a spherically symmetric body, of isotropic matter, is governed by the TOV equations, as follows:

$$\frac{dP(r)}{dr} = -\frac{G\rho(r)m(r)}{r^2}\left(1+\frac{P(r)}{\rho(r)c^2}\right)\left(1+\frac{4\pi P(r)r^3}{m(r)c^2}\right)\left(1-\frac{2Gm(r)}{rc^2}\right)^{-1} \quad (5.9)$$

$$\frac{dm(r)}{dr} = 4\pi r^2\rho(r), \quad (5.10)$$

$$\frac{da(r)}{dr} = 4\pi r^2 n_b\left(1-\frac{2Gm(r)}{rc^2}\right)^{-\frac{1}{2}}, \quad (5.11)$$

where r, G, c and n_b are the radial coordinate, the gravitational constant, the light speed and the baryon number density. $P(r)$ and $\rho(r)$ are the pressure and gravitational mass density evaluated at r, while $m(r)$ and $a(r)$ are the mass and the number of baryons inside the sphere of radius r. The quantum chromodynamics based equation of state, together with Equations 5.9 and 5.10, provides $m(r)$, and in particular the radius $r_{\rm NS}$ of the neutron star of mass $m_{\rm NS}$, satisfying $m(r=r_{\rm NS})=m_{\rm NS}$. Also the Equation 5.11 provides $a(r)$, and in particular the baryon mass of the neutron star which depends on $a(r=r_{\rm NS})$ and the neutron star matter components. Finally, depending on the equation of state, the TOV limit indicates the maximum mass a neutron star can have without undergoing gravitational collapse. This is equivalent to the Chandrasekhar limit for the white dwarfs. For the present study, I use the equations of state proposed in Abbott et al. [2018a], based on the GW170817 measurements. I briefly present here the method to constrain the parameters of the high density matter, inspired from the works presented in Lindblom [2010]; Lindblom and Indik [2012, 2014]. As stated above, the equation of state indicates the dependence of the energy density $\epsilon^{\rm LIN}$ on the pressure $p^{\rm LIN}$, i.e. the relation $\epsilon^{\rm LIN}(p^{\rm LIN})$. This is equivalent to knowing the pressure dependence of the adiabatic index $\Gamma^{\rm LIN}(p^{\rm LIN}) = \frac{\epsilon^{\rm LIN}+p^{\rm LIN}}{p^{\rm LIN}}\frac{dp^{\rm LIN}}{d\epsilon^{\rm LIN}}$. Indeed, if one has access to $\Gamma^{\rm LIN}(p^{\rm LIN})$, then the variation of the energy density with the pressure is obtained by means of the equation $\frac{d\epsilon^{\rm LIN}(p^{\rm LIN})}{dp^{\rm LIN}} = \frac{\epsilon^{\rm LIN}(p^{\rm LIN})+p^{\rm LIN}}{p^{\rm LIN}\Gamma^{\rm LIN}(p^{\rm LIN})}$. If one introduces the dimensionless variable $x^{\rm LIN} = \log\left(p^{\rm LIN}/p_0^{\rm LIN}\right)$, where $p_0^{\rm LIN}$ is a scale factor, then the adiabatic index admits the following spectral representation

$$\Gamma^{\rm LIN}(x^{\rm LIN}) = \exp\left(\sum_{k=0}^{\infty}\gamma_k^{\rm LIN}(x^{\rm LIN})^k\right), \quad (5.12)$$

where $\gamma_k^{\rm LIN}$ are spectral coefficients. Even if the Equation 5.12 indicates that one needs to compute an infinity of spectral coefficients, given that the adiabatic index is a slowly varying quantity, a truncated expression represents a good approximation. Hereafter

of interest are only the first coefficients $\gamma_0^{\rm LIN}$, $\gamma_1^{\rm LIN}$, $\gamma_2^{\rm LIN}$ and $\gamma_3^{\rm LIN}$. Moreover, Equation 5.12 is a local relation, while in the field of high energy astrophysics, scientists try to determine the equation of state based on macroscopic observables, such as the neutron star mass and radius, and/or the tidal deformability exerced by a companion compact object in a binary. Macroscopic quantities are obtained from the integration of equations valid at the microscopic scale, therefore in addition to the spectral coefficients, one needs to constrain the value of an internal energy related quantity at the center of the neutron star, in our case the central enthalpy, noted $h_c^{\rm LIN}$. If BNS and NSBH are detected, the masses $M_i^{\rm LIN}$ and the dimensionless tidal deformabilities $\Lambda_i^{\rm LIN}$ of the neutron stars components can be measured. The index i stands for the $i^{\rm th}$ detection. These macroscopic quantities need to be compared to the ones predicted by some central enthalpies and spectral coefficients, say $M_i^{\rm LIN}(h_{c,i}^{\rm LIN}, \gamma_k^{\rm LIN})$ and $\Lambda_i^{\rm LIN}(h_{c,i}^{\rm LIN}, \gamma_k^{\rm LIN})$. The spectral parameters as well as the central enthalpies of the stars are obtained by minimizing the following quantity

$$\chi^2_{\rm LIN}(\gamma_k^{\rm LIN}, h_{c,i}^{\rm LIN}) = \sum_i \left\{ \left[\log\left(\frac{M(h_{c,i}^{\rm LIN}, \gamma_k^{\rm LIN})}{M_i^{\rm LIN}} \right) \right]^2 + \left[\log\left(\frac{\Lambda(h_{c,i}^{\rm LIN}, \gamma_k^{\rm LIN})}{\Lambda_i^{\rm LIN}} \right) \right]^2 \right\}. \tag{5.13}$$

Based on only GW170817, the neutron star masses and tidal deformabilities allow the derivation of 2396 parameterized (by $\gamma_0^{\rm LIN}$, $\gamma_1^{\rm LIN}$, $\gamma_2^{\rm LIN}$ and $\gamma_3^{\rm LIN}$) equations of state that I use in the rest of this chapter. It is noteworthy that I had not produce the 2396 equations of state. Philippe Landry and Reed Essick offered me access to them. For each mass and spin MBTA template, a marginalization over the entire set of 2396 equations of state is realized as follows: given a GW low-latency template and a equation of state, the radii R_1 and R_2 of the binary compact objects are calculated (the radius of a black hole is assumed to be 0), before converting them to compactnesses by means of the formula $C_{1/2} = \frac{G m_{1/2}}{R_{1/2} c^2}$ (the compactness upper limit for neutron stars as well as the compactness for black holes is considered to be 4/9 according to Buchdahl's theorem); the baryonic mass $m_2^{\rm bar}$ of the lighter object is computed (if the secondary object is a black hole, the corresponding baryonic mass is 0); based on the TOV limit, the type of the compact objects and so the type of the binary is determined. At the end of this process, I get a list of 7-tuples $(q, m_{\rm chirp}, \chi_{\rm eff}, C_1, C_2, m_2^{\rm bar}, f, w)$, where $q = m_2/m_1$, $m_{\rm chirp} = \frac{(m_1 m_2)^{3/5}}{(m_1+m_2)^{1/5}}$ and $\chi_{\rm eff} = \frac{m_1 \chi_{1,z} + m_2 \chi_{2,z}}{m_1+m_2}$ are the binary mass ratio, chirp mass and effective spin, while $f \in \{0, 1, 2\}$ indicates the type of the binary as follows: BNS ($f = 0$), NSBH ($f = 1$), BBH ($f = 2$). In the following of this chapter, I show how I convert each such tuple into a kilonova lightcurve.

5.2.2 Mass ejecta and EM lightcurve computations

In order to convert binary parameters into kilonova lightcurves, a key quantity that needs to be computed is the amount of unbound mass ejecta. Traditionally, the expelled matter generating the EM signal is divided into two contributions: the dynamical ejecta, formed of heavier chemical elements, which becomes unbound during the merger of the two binary compact object components, generally due to tidal torques and dynamical shocks; the disc winds ejecta, formed of higher electron fraction atoms, that consists of matter, initially bound on the accretion disc formed around the binary merger remnant and which is subsequently driven away by the magnetic, neutrino and viscous powered winds. In order to accurately compute the amount of mass ejecta, numerical simulations must be used. Such simulations need to take into account many physical mechanisms at play in these extreme environments, such as: strong field gravity, quantum chromodynamics, general relativistic magnetohydrodynamics, neutrino transport. Several sets of simulations have been proposed in the last years by different research groups. Such an example, for the BNS mergers, is offered in Radice et al. [2018a]. For these simulations temperature-dependent nuclear equations of state have been used. Moreover, neutrino effects and viscosity have been considered, but the magnetic based physical mechanisms are omitted. More precisely, the evolution of the binary is calculated starting at the moment where the separation between the compact objects is $40\,\mathrm{km}$ (accounting for 2-3 orbits prior to the merger). The evolution takes into account matter composition and energy changes via reactions involving neutrinos [Bruenn, 1985; Ruffert et al., 1996; Burrows et al., 2006; Shapiro and Teukolsky, 2008]. The absorption and emission of neutrinos is responsible for the net energy and lepton number deposition rates, noted Q^{RAD}, R_p^{RAD} and R_n^{RAD}. For the last two quantities, the indices p and n stand for protons and neutrons. Therefore, if one notes by Y_e^{RAD}, $n_p^{\mathrm{RAD}} = Y_e^{\mathrm{RAD}} n^{\mathrm{RAD}}$, n_n^{RAD} and $n^{\mathrm{RAD}} = n_p^{\mathrm{RAD}} + n_n^{\mathrm{RAD}}$ the electron fraction, the proton number density, the neutron number density and the baryon number density, the following relation holds

$$\nabla_\mu (n_{p,n}^{\mathrm{RAD}} u_{\mathrm{RAD}}^\mu) = R_{p,n}^{\mathrm{RAD}}, \tag{5.14}$$

where u_{RAD}^μ is the fluid four-velocity. Also, if one notes by e^{RAD} and p^{RAD} the energy density and the pressure, then the stress energy tensor might be expressed as

$$T_{\mathrm{RAD}}^{\mu\nu} = (e^{\mathrm{RAD}} + p^{\mathrm{RAD}}) u_{\mathrm{RAD}}^\mu u_{\mathrm{RAD}}^\nu + p^{\mathrm{RAD}} g_{\mathrm{RAD}}^{\mu\nu}, \tag{5.15}$$

where $g_{\mathrm{RAD}}^{\mu\nu}$ is the Riemannian metric. Finally, the Euler equations write

$$\nabla_\nu T_{\mathrm{RAD}}^{\mu\nu} = Q^{\mathrm{RAD}} u_{\mathrm{RAD}}^\mu. \tag{5.16}$$

The simulations' output predicts a few $10^{-3}\,M_\odot$ dynamical ejecta and accretion discs weighing up to $\sim 0.2\,M_\odot$. Concerning the dynamical ejecta, the tidal torques component is concentrated within an angle of $\sim 60^\circ$ from the orbital plane, while the shocked heated component extends to lower latitudes. Equally, more (less) mass asymmetric binaries favor tidal (shock) outflows. Regarding the disc viscous- and neutrino-winds, the presence of unbound matter is conditioned by the survival of the rotational accretion disc for more than about one millisecond. Additionally, the amount of the remnant disc mass is correlated to its lifetime. In the case of NSBH, the kilonova signal is conditioned by the disruption of the neutron star by the black hole tidal forces. In order for the photons to escape the black hole gravity and be able to propagate towards the Earth, this phenomenon needs to occur before the neutron star reaches the black hole event horizon. Examples of NSBH merger simulations are proposed in Foucart et al. [2014]. In this study, binaries with black hole masses in $[7\,M_\odot, 10\,M_\odot]$, neutron star masses in $[1.2\,M_\odot, 1.4\,M_\odot]$ and black hole dimensionless spins in $[0.7, 0.9]$ are considered. The properties of the high density neutron star matter are assumed to be determined by the finite temperature nuclear-theory based equation of state (with incompressibility parameter $K_0^{\rm LAT} = 220\,$MeV and symmetry energy $S_\nu^{\rm LAT} = 29.3\,$MeV) introduced in Lattimer and Douglas Swesty [1991]. Finally, neutrino cooling is treated through a neutrino leakage scheme, while magnetic (such as angular momentum transport and energy dissipation caused by the magneto-rotational instability induced turbulence) and viscous (such as viscous heating) effects are omitted. The simulations attempt to solve the binary evolution starting with an initial separation of $5-8$ orbits before the merger, and considering slightly eccentric orbits (with $0.03-0.04$ eccentricity). The simulations show that when the neutron star is disrupted, unbound matter accounting for $0.05\,M_\odot - 0.20\,M_\odot$ is expelled in the form of dynamical ejecta. Given that the merger timescale is $1\,$ms, while the neutrino radiation is spread over $10\,$ms, the dynamical ejecta has a low electron fraction. Moreover, there is also bound material, in the form of a hot accretion disc ($0.04\,M_\odot - 0.14\,M_\odot$) and a cooler tidal tail. After the merger, the accretion disc cools down through the following physical mechanisms: neutrino emission, fall-back of the tail cold material into the disc; accretion of the disc hot material by the remnant black hole. Unbound matter, with higher electron fraction, might be produced subsequently from the disc by magnetic-, viscous- and/or neutrino-driven winds.

Despite that correct computations of the expelled matter require numerical simulations, such an approach is not available when aiming to make low-latency predictions. Indeed, the compact binary merger numerical simulations are computationally expensive. This is why, for our study I use fitting formulae based on numerical simulation results. Hereafter in this chapter, noted by $M_{\rm ej}^{\rm dyn}$ and $M_{\rm disc}$ are the dynamical ejecta and the mass of the accretion disc. I also consider that the total amount of unbound matter is

$m_{\rm ej} = M_{\rm ej}^{\rm dyn} + \zeta M_{\rm disc}$, with $\zeta = 0.15$ [Dietrich et al., 2020]. Now I attempt to compute, for each tuple from the list described at the end of the previous subsection, the value of $m_{\rm ej}$. If the tuple is classified as BBH, I assume $m_{\rm ej} = 0$. Concerning the BNS case, for the dynamical ejecta, I use the formula proposed by Coughlin et al. [2019a], based among others on the numerical relativity simulations of Radice et al. [2018a]:

$$\log_{10} M_{\rm ej}^{\rm dyn}(M_\odot) = \left[a \frac{(1-2C_1)m_1}{C_1} + b\, m_2 \left(\frac{m_1}{m_2}\right)^n + \frac{d}{2} \right] + [1 \leftrightarrow 2]\,, \tag{5.17}$$

with $a = -0.0719$, $b = 0.2116$, $c = 0.2116$, $d = -2.42$ and $n = -2.905$ fitting coefficients. In the previous expression, C_1 (respectively C_2) represents the compactness of the heavier (respectively lighter) neutron star. For the mass of the disc surrounding the BNS merger compact object remnant, I make use of the formula:

$$\log_{10} M_{\rm disc}(M_\odot) = \max\left(-3, a\left(1 + b \tanh\left(\frac{c - (m_1+m_2)/M_{\rm thresh}}{d}\right)\right)\right), \tag{5.18}$$

where $c = 0.953$ and $d = 0.0417$, while a and b are mass ratio parameterized coefficients. $M_{\rm thresh}$ is computed as in Bauswein et al. [2013a] and represents the binary total mass value beyond which prompt collapse takes place. The expression from Equation 5.18 is the same as in Dietrich et al. [2020] and is based on the numerical relativity datasets from Kiuchi et al. [2019]; Radice et al. [2018a]; Dietrich et al. [2017]; Hotokezaka et al. [2011]. The dependence of $m_{\rm ej}$ on the binary compact object component masses is illustrated in Figure 5.1. Equally, the two panels show the mass ejecta relative difference between our choice for the fitting formulae and the one proposed in Nedora et al. [2020], where $M_{\rm disc}$ and $M_{\rm ej}^{\rm dyn}$ are functions of the mass ratio q and the tidal deformability $\tilde{\Lambda}^{\rm NED}$. While the two models present similar behaviors (more mass ejecta for lighter and less compact neutron stars), differences of $\sim 100\%$ in the amount of predicted mass ejecta are common. Regarding the NSBH mergers, the computation of the disc mass is done in the same way as in Foucart et al. [2018] (based on the binary evolution codes from Kyutoku et al. [2015]; Foucart et al. [2014]; Brege et al. [2018]; Lovelace et al. [2013]; Foucart et al. [2012, 2011]; Kyutoku et al. [2011]; Etienne et al. [2009]; Foucart et al. [2013]), i.e.

$$M_{\rm disc}(M_\odot) = m_2^{\rm bar} \max\left(0, \alpha \frac{1-2C_2}{\eta^{1/3}} - \beta r_{\rm ISCO} \frac{C_2}{\eta} + \gamma\right)^\delta, \tag{5.19}$$

where $\eta = \frac{m_1 m_2}{m_1+m_2}$ and $r_{\rm ISCO}$ are the binary reduced mass and the innermost stable circular orbit, while $\alpha = 0.4064$, $\beta = 0.1388$, $\gamma = 0.2551$ and $\delta = 1.7612$ are the fitting coefficients. Furthermore, the fitting formula for the dynamical ejecta of NSBH mergers is taken from Krüger and Foucart [2020] (who in their turn used the numerical

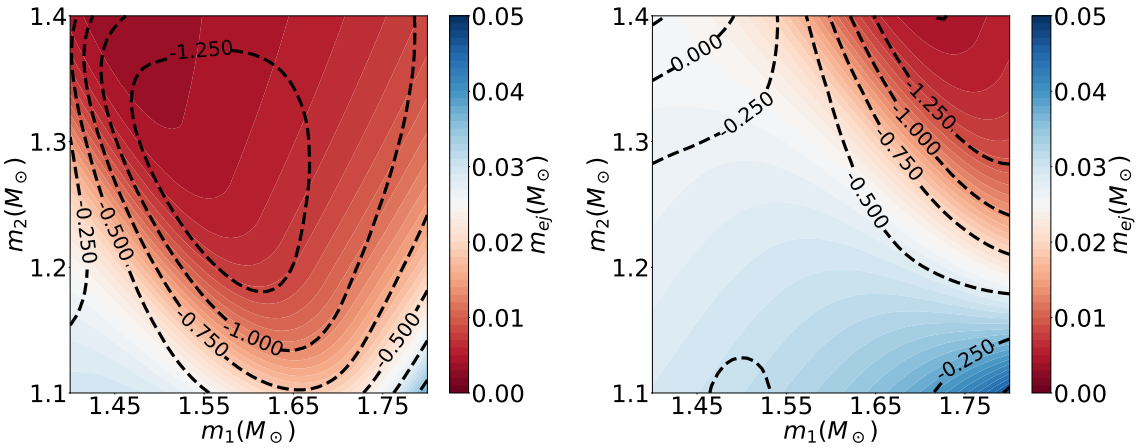

Fig. 5.1 $m_{\rm ej}(m_1, m_2)$ is plotted in color, while the level lines designate the quantity $2(m_{\rm ej} - m_{\rm ej}^{\rm NEA})/(m_{\rm ej} + m_{\rm ej}^{\rm NEA})$, where $m_{\rm ej}^{\rm NEA}$ is the predicted mass ejecta according to Nedora et al. [2020]. For the left (right) panel, the equation of state parameterized by $\gamma_0^{\rm LIN} = 0.5485$, $\gamma_1^{\rm LIN} = 0.3767$, $\gamma_2^{\rm LIN} = -0.0690$ and $\gamma_3^{\rm LIN} = 0.0035$ (respectively $\gamma_0^{\rm LIN} = 1.4777$, $\gamma_1^{\rm LIN} = -0.3225$, $\gamma_2^{\rm LIN} = 0.0694$ and $\gamma_3^{\rm LIN} = -0.0046$), predicting $11.3\,$km ($13.0\,$km) radius and 232 (663) tidal deformability for a $1.4\,M_\odot$ neutron star, as well as a $2.00\,M_\odot$ ($2.43\,M_\odot$) TOV limit, has been used.

data from Kawaguchi et al. [2015]; Foucart et al. [2019]):

$$M^{\rm dyn}(M_\odot) = m_2^{\rm bar}\left(a_1\left(\frac{m_1}{m_2}\right)^{n_1}\frac{1-2C_2}{C_2} - a_2\left(\frac{m_1}{m_2}\right)^{n_2}\frac{r_{\rm ISCO}}{m_1} + a_4\right), \qquad (5.20)$$

where $a_1 = 0.007116$, $a_2 = 0.001436$, $a_4 = -0.02762$, $n_1 = 0.8636$ and $n_2 = 1.6840$. Figure 5.2 presents the dependence of $m_{\rm ej}$ with $\chi_{\rm eff}$, $1/q$ and m_2, as well as the relative difference in the predicted dynamical mass ejecta with respect to the fitting formula from Kawaguchi et al. [2016]. One can easily remark that the amount of unbound matter is favored by higher effective spins, smaller neutron star masses and less asymmetric binaries. Also, based on Figure 5.2, on can conclude that distinct models might provide predictions being different at $\sim 100\% - 200\%$.

I also compute, based on the binary parameters, the velocity of the ejecta. Thus, for the BNS case, I use the fitting formula from Coughlin et al. [2019a], i.e.

$$v_{\rm ej} = \left[a(1 + c\,C_1\frac{m_1}{m_2} + \frac{b}{2})\right] + [1 \leftrightarrow 2], \qquad (5.21)$$

where the coefficients are $a = -0.3090$, $b = 0.657$ and $c = -1.879$, while for the NSBH case, I use the formula from Kawaguchi et al. [2016], i.e.

$$v_{\rm ej} = \alpha\frac{m_1}{m_2} + \beta, \qquad (5.22)$$

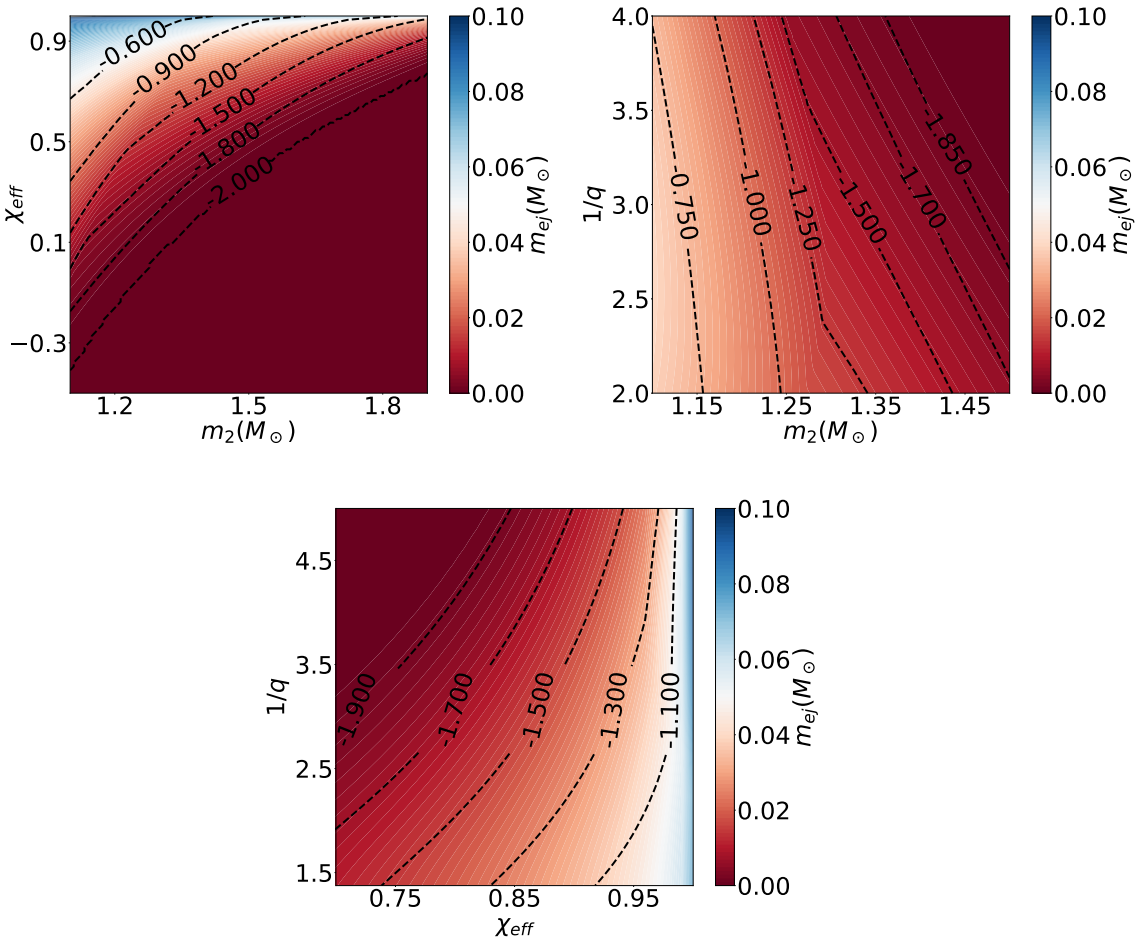

Fig. 5.2 In color: $m_{\rm ej}(\chi_{\rm eff}, m_2)$ at constant $1/q = 2$ (top left); $m_{\rm ej}(1/q, m_2)$ at constant $\chi_{\rm eff} = 0.6$ (top right); $m_{\rm ej}(1/q, \chi_{\rm eff})$ at constant $m_2 = 1.6\,M_\odot$ (bottom). The level lines designate the quantity $2(M^{\rm dyn} - M^{\rm dyn}_{\rm KAW})/(M^{\rm dyn} + M^{\rm dyn}_{\rm KAW})$, where $M^{\rm dyn}_{\rm KAW}$ is the dynamical ejecta predicted by the fitting formula from Kawaguchi et al. [2016]. For the generation of the three panels, I used the equation of state parameterized by $\gamma_0^{\rm LIN} = 0.3268$, $\gamma_1^{\rm LIN} = 0.4456$, $\gamma_2^{\rm LIN} = -0.0586$ and $\gamma_3^{\rm LIN} = 0.0016$, predicting a 12.4km radius and 458 tidal deformability, as well as a $2.37\,M_\odot$ TOV limit.

with $\alpha = 0.01533$ and $\beta = 0.1907$. At the end of this process, the 8-tuples $(q, m_{\rm chirp}, \chi_{\rm eff}, C_1, C_2, m_2^{\rm bar}, f, w)$ are converted into 3-tuples $(m_{\rm ej}, v_{\rm ej}, w)$. More precisely, the number of $(m_{\rm ej}, v_{\rm ej}, w)$ 3-tuples is equal to the size of the initial MBTA triggers set times 2396 (the number of GW170817-like equations of state used for marginalization). For computational reasons, this set is downsampled to 1000. It has been checked that such a downsampling preserves more than 80% of the mass ejecta probability distribution in the case of GW170817 and GW190425.

Now I attempt to convert the 3-tuples $(m_{\rm ej}, v_{\rm ej}, w)$ into kilonova lightcurves. To this end, I make use of two kilonova models, heareafter named *Model I* and *Model II*, based on radiative transfer simulations. *Model I* is proposed in Kasen et al. [2017], where multi-wavelength radiation transport equation is solved by a Monte Carlo code, assuming a relativistically expanding medium. According to this model, the dynamical ejecta has two components: one caused by the tidal torques situated at lower latitudes and composed of heavy elements, and eventually (if the binary is a BNS) another one caused by shocks situated closer to the poles, composed of lighter atoms. Additionally, the color of the disc winds is determined by the early fate of the binary merger remnant. Thus in the case of long lived neutron star remnant, the disc wind is optically blue, while for prompt collapse, the EM signal is predicted to be at higher wavelengths. This kilonova model is parameterized by the mass ejecta $m_{\rm ej}$, the velocity of ejecta $v_{\rm ej}$ and the lanthanide fraction $X_{\rm lan}$. While the amount of expelled neutron rich material is primordial for the existence and the brightness of the subsequent EM signal, the chemical composition of the ejecta has a relevant impact on the color and the duration. Indeed, the heavier elements have denser atomic transition bands, reducing the optical path length of photons, which undergo atomic absorption and emission transitions in addition to scattering, that happens in very dense media. Therefore, the heavier ejecta is associated to higher opacities, determining a longer-lasting flaring and photons of smaller energies. *Model II*, introduced in Bulla [2019], is also based on a Monte Carlo radiative transfer code [Bulla et al., 2016]. The ejecta chemical composition is set in a different way: the expelled material is assumed to have two components, one lanthanide-rich, situated near the plane of the initial binary and whose opening angle is Φ, and one lanthanide-free, situated at higher latitudes. Therefore, the chemical heaviness of the ejecta is fixed by Φ. On the other hand, this structure of the kilonova imposes a position dependency of the observables. This is why, in addition to $m_{\rm ej}$ and Φ, these lightcurves are also parameterized by the binary inclination angle $\theta_{\rm inc}$. Therefore, both *Model I* and *Model II* take as input parameters ejecta properties and offer as output photometric lightcurves. In order to have a quick response, and not wait for the radiative transfer codes to run every time one needs an answer, a surrogate technique has been created [Coughlin et al., 2018c] as follows: the u, g, r, i, z, y, J, H, and K photometric lightcurves output has

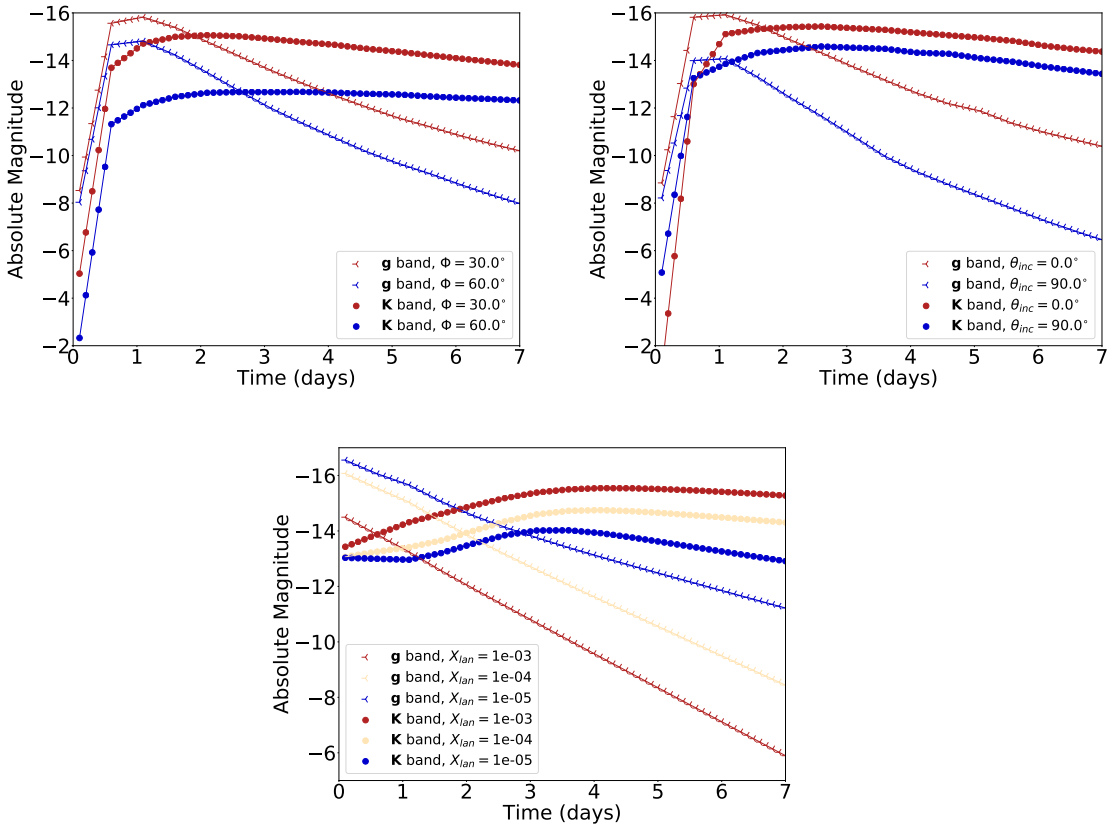

Fig. 5.3 Absolute magnitude versus time; top left: *Model II* lightcurves for $m_{\rm ej} = 0.05\,M_{\odot}$, $\theta_{\rm inc} = 45^{\circ}$ and different values of Φ; top right: *Model II* lightcurves for $m_{\rm ej} = 0.95\,M_{\odot}$, $\Phi = 45^{\circ}$ and different values of $\theta_{\rm inc}$; bottom: *Model I* lightcurves for $m_{\rm ej} = 0.05\,M_{\odot}$, $v_{\rm ej} = 0.15\,c$ and different values of $X_{\rm lan}$.

been computed by evaluating the radiative transfer codes on a set of input parameters, forming a grid. Then Gaussian Process Regression [Quadrianto et al., 2010] is used to evaluate the time dependent photometric magnitude for any input parameters in the vicinity of grid points. It is worth mentioning that, concerning the *Model II* grid, the update presented in Coughlin et al. [2020a], where the mass is varied from $10^{-6}\,M_{\odot}$ to $1\,M_{\odot}$, is used. One should also remark that, because the only binary ejecta related information I have concerns the mass $m_{\rm ej}$ and the velocity $v_{\rm ej}$ of the gravitationally unbound matter, I need to make some assumptions for the other requested parameters: $X_{\rm lan}$ in the case of *Model I*; Φ and $\theta_{\rm inc}$ in the case *Model II*. In Figure 5.3, it is shown the variation of the g and K lightcurve output with the unknown parameters. Thus, the increase of $X_{\rm lan}$ and Φ implies redder lightcurves. Concerning the inclination angle, both reddening and luminosity reduction accompany higher values of $\theta_{\rm inc}$. It is worth mentioning that from an observational point of view, at small inclination angles, the relativistic jet (GRB afterglow) will be superimposed to the kilonova radiation. Therefore, the observed lightcurve will be a combination of the two emissions, and it is possible that the relativistic jet to be the dominating part. I do not consider in this study this

situation. After some assumption concerning the ejecta chemical composition and the binary orientation with respect to an Earth observer, that I will present in the next section, the input used to generate *Model I* (respectively *Model II*) photometric lightcurve is represented by a list of 4-tuples $(m_{\rm ej}, v_{\rm ej}, X_{\rm lan}, w)$ (respectively $(m_{\rm ej}, \Phi, \theta_{\rm inc}, w)$).

In the rest of this subsection, I focus on the sources of uncertainty affecting the predicted lightcurves, in the case of *Model I*. Just before doing that, I also define *HasEjecta*, as being the weighted percentage of tuples $(m_{\rm ej}, w)$ having mass ejecta higher than $3 \times 10^{-4}\, M_\odot$. This threshold is twice the minimum disc winds mass of a BNS (according to Equation 5.18). The predicted errors of *HasEjecta* are also studied here. Therefore, the sources of uncertainty are: the GW data error measurements imprinted on the MBTA triggers; the imperfect constraint of the neutron star equation of state; the mass and the velocity ejecta fitting errors; the prior on the chemical compostion of the ejecta. On the contrary, a perfect GW strain measurement (providing unique binary parameters $m_{\rm chirp}^{\rm fixed}$, $q^{\rm fixed}$ and $X_{\rm lan}^{\rm fixed}$), a complete knowledge about the properties of matter at very high densities (providing $\rm EOS^{fixed}$) and assuming that our fitting formulae are perfect would provide unique values of $m_{\rm ej}$ and $v_{\rm ej}$, unaffected by uncertainties. If in addition, one would know exactly the chemical constituents of the ejecta (providing a unique value of $X_{\rm lan}$), then the predicted lightcurves would be without any errors. One should note that I willingly omit the uncertainty affecting the radiative transfer codes resulting in *Model I* surrogate. In order to quantify the errors due to each source of uncertainty I proceed in the following way: for the MBTA templates inaccuracy, I consider the uniform grid points $(m_{\rm chirp}, q, \chi_{\rm eff}) \in [0.99 m_{\rm chirp}^{\rm fixed}, 1.01 m_{\rm chirp}^{\rm fixed}] \times [\frac{1}{2} q^{\rm fixed}, \min(2q^{\rm fixed}, 1)] \times [-\chi_{\rm eff}^{\rm fixed}, \min(3\chi_{\rm eff}^{\rm fixed}, 1)]$ (motivated by the MBTA results for O2 and O3 real events, presented in the next section), and I assume $\rm EOS^{fixed}$, $X_{\rm lan}^{\rm fixed}$ and no fitting ejecta uncertainty; for the neutron star equation of state uncertainty, I marginalize $(m_{\rm chirp}^{\rm fixed}, q^{\rm fixed}, \chi_{\rm eff}^{\rm fixed})$ over the 2396 equations of state and I assume $X_{\rm lan}^{\rm fixed}$ and no uncertainty for the fitting formulae; for the uncertainty of the ejecta fits, I first compute the mass $m_{\rm ej}^{\rm fixed}$ and velocity $v_{\rm ej}^{\rm fixed}$ of the ejecta based on $(m_{\rm chirp}^{\rm fixed}, q^{\rm fixed}, \chi_{\rm eff}^{\rm fixed}, \rm EOS^{fixed})$, then I consider the uniform grid points $(m_{\rm ej}, v_{\rm ej}) \in [\frac{1}{3} m_{\rm ej}^{\rm fixed}, 3 m_{\rm ej}^{\rm fixed}] \times [\frac{1}{2} v_{\rm ej}^{\rm fixed}, 2 v_{\rm ej}^{\rm fixed}]$ (motivated by Figures 5.1 and 5.2) and I assume $X_{\rm lan}^{\rm fixed}$; for the missing knowledge concerning the chemical composition, I assume $(m_{\rm ej}^{\rm fixed}, v_{\rm ej}^{\rm fixed})$ and I vary uniformly $\log_{10} X_{\rm lan} \in [-9, -1]$. Table 5.1 illustrates the uncertainties on the photometric lightcurves and *HasEjecta* for five binaries. The principal sources of uncertainty turn to be the ignorance about the chemical composition and the inaccuracy of the GW strain measurement. While the variation of the lanthanide fraction primarily influences the color evolution, the imprecise MBTA templates introduce doubts about the type of the binary and thus about the existence and the subsequent brightness of an eventual EM signal. Moreover the errors assigned to

Binary					Absolute magnitude					
					1 day		2 days		3 days	
$m_1^{\rm fixed}$ ($M_\odot$)	$m_2^{\rm fixed}$ ($M_\odot$)	$\chi_{\rm eff}^{\rm fixed}$	Error	*HasEjecta* (%)	**g** band	**K** band	**g** band	**K** band	**g** band	**K** band
1.6	1.4	0.01	(i)		-13.5	-12.7	-11.9	-13.0	-10.3	-12.6
			(ii)	100	$-13.7^{-1.9}_{+0.5}$	$-12.9^{-1.1}_{+0.4}$	$-12.2^{-2.3}_{+0.7}$	$-13.4^{-1.1}_{+0.7}$	$-10.7^{-2.8}_{+0.8}$	$-13.1^{-1.9}_{+1.0}$
			(iii)	100	$-11.9^{-1.6}_{+0.3}$	$-12.1^{-0.6}_{+0.2}$	$-10.0^{-1.9}_{+0.6}$	$-11.6^{-1.5}_{+0.3}$	$-8.2^{-2.2}_{+0.8}$	$-11.2^{-1.4}_{+0.2}$
			(iv)		$-13.5^{-0.5}_{+1.5}$	$-12.9^{-0.8}_{+1.2}$	$-11.8^{-1.0}_{+2.3}$	$-12.8^{-1.0}_{+0.6}$	$-10.3^{-1.7}_{+3.1}$	$-12.1^{-0.8}_{+0.3}$
			(v)		$-14.0^{-0.3}_{+4.8}$	$-12.3^{-2.2}_{+0.3}$	$-13.0^{-0.6}_{+4.9}$	$-12.2^{-2.7}_{+0.9}$	$-12.2^{-1.0}_{+4.9}$	$-11.3^{-3.4}_{+2.2}$
			(vi)	100	$-12.9^{-2.8}_{+4.1}$	$-13.0^{-1.7}_{+2.4}$	$-11.9^{-3.0}_{+4.3}$	$-12.9^{-2.1}_{+4.7}$	$-11.1^{-3.3}_{+4.6}$	$-12.3^{-2.8}_{+6.8}$
2.0	1.4	0.10	(i)		-13.7	-13.0	-12.1	-13.2	-10.5	-12.7
			(ii)	100	$-13.7^{-1.8}_{+2.2}$	$-12.9^{-0.8}_{+1.1}$	$-12.1^{-2.2}_{+2.7}$	$-13.3^{-1.2}_{+2.1}$	$-10.6^{-2.8}_{+3.2}$	$-13.0^{-2.1}_{+2.1}$
			(iii)	96	$-13.8^{-0.3}_{+2.9}$	$-13.1^{-0.3}_{+1.8}$	$-12.2^{-0.6}_{+3.0}$	$-13.5^{-0.4}_{+2.5}$	$-10.7^{-0.8}_{+2.6}$	$-13.0^{-0.3}_{+2.5}$
			(iv)		$-13.6^{-0.3}_{+1.4}$	$-13.2^{-0.6}_{+1.3}$	$-12.1^{-0.8}_{+2.1}$	$-13.0^{-0.7}_{+0.6}$	$-10.7^{-1.4}_{+2.9}$	$-12.3^{-0.7}_{+0.3}$
			(v)		$-14.2^{-0.3}_{+4.6}$	$-12.6^{-2.2}_{+0.3}$	$-13.2^{-0.6}_{+4.6}$	$-12.3^{-2.8}_{+1.0}$	$-12.4^{-1.0}_{+4.5}$	$-11.5^{-3.4}_{+2.3}$
			(vi)	98	$-12.7^{-2.7}_{+4.0}$	$-12.8^{-1.7}_{+2.3}$	$-11.6^{-3.0}_{+4.1}$	$-12.6^{-2.3}_{+4.6}$	$-10.7^{-3.3}_{+4.3}$	$-11.8^{-3.1}_{+6.5}$
4.0	1.4	0.10	(i)		-11.5	-11.8	-9.2	-11.4	-6.9	-11.0
			(ii)	53	$-10.3^{-4.4}$	$-11.2^{-2.3}$	$-9.2^{-4.1}_{+0.1}$	$-10.3^{-3.9}$	$-8.1^{-4.0}_{+1.3}$	$-9.0^{-5.1}$
			(iii)	40	$-10.3^{-1.0}$	$-11.2^{-0.4}_{+0.1}$	$-9.2_{+1.2}$	$-10.3^{-0.8}$	$-8.1_{+2.8}$	$-8.9^{-1.8}$
			(iv)		$-11.6^{-1.1}_{+1.2}$	$-11.9^{-0.9}_{+0.6}$	$-9.7^{-1.6}_{+2.0}$	$-11.2^{-0.7}_{+0.3}$	$-7.9^{-2.3}_{+3.1}$	$-10.7^{-0.2}_{+0.2}$
			(v)		$-12.2^{-0.5}_{+4.8}$	$-11.0^{-2.7}_{+0.6}$	$-11.0^{-1.1}_{+4.9}$	$-9.8^{-3.7}_{+2.8}$	$-9.8^{-1.8}_{+5.9}$	$-9.1^{-3.7}_{+5.9}$
			(vi)	27	$-10.4^{-2.5}_{+0.1}$	$-11.2^{-1.7}$	$-9.3^{-2.5}_{+0.1}$	$-10.3^{-2.5}_{+0.1}$	$-8.2^{-2.8}_{+0.1}$	$-8.9^{-3.0}_{+0.1}$
4.0	1.4	0.70	(i)		-15.6	-13.7	-14.4	-14.6	-13.4	-15.2
			(ii)	54	$-10.7^{-5.2}_{+0.3}$	$-11.2^{-3.0}$	$-9.2^{-5.5}$	$-10.5^{-4.3}_{+0.2}$	$-8.1^{-5.8}$	$-10.1^{-4.9}_{+1.2}$
			(iii)	100	$-14.9^{-0.7}_{+1.2}$	$-13.5^{-0.3}_{+0.6}$	$-13.5^{-0.8}_{+1.4}$	$-14.2^{-0.5}_{+0.7}$	$-12.3^{-1.1}_{+1.7}$	$-14.3^{-0.9}_{+1.1}$
			(iv)		$-15.1^{-0.5}_{+0.7}$	$-13.8^{-0.6}_{+1.0}$	$-13.9^{-0.5}_{+1.2}$	$-14.6^{-0.3}_{+1.0}$	$-13.3^{-0.4}_{+1.9}$	$-14.3^{-1.1}_{+0.3}$
			(v)		$-16.1^{-0.1}_{+5.3}$	$-13.3^{-1.9}_{+0.1}$	$-15.0^{-0.4}_{+5.0}$	$-14.2^{-1.7}_{+0.2}$	$-14.4^{-0.6}_{+5.0}$	$-14.3^{-1.9}_{+0.6}$
			(vi)	44	$-10.4^{-5.2}_{+0.2}$	$-11.2^{-3.2}_{+0.1}$	$-9.3^{-5.5}_{+0.2}$	$-10.3^{-4.5}_{+0.1}$	$-8.3^{-6.0}_{+0.2}$	$-9.0^{-5.8}_{+0.2}$
4.0	2.0	0.70	(i)		-11.7	-11.9	-9.4	-11.7	-7.1	-11.3
			(ii)	16	$-10.3^{-3.2}$	$-11.2^{-1.5}$	$-9.2^{-2.7}$	$-10.3^{-2.8}$	$-8.1^{-2.2}$	$-9.0^{-3.7}$
			(iii)	46	$-10.3^{-2.7}$	$-11.2^{-1.2}$	$-9.2^{-2.1}_{+0.4}$	$-10.3^{-2.5}$	$-8.1^{-1.5}_{+1.8}$	$-9.0^{-3.3}$
			(iv)		$-11.8^{-1.2}_{+1.1}$	$-12.0^{-0.9}_{+0.8}$	$-9.9^{-1.7}_{+1.9}$	$-11.4^{-0.8}_{+0.3}$	$-8.0^{-2.4}_{+3.0}$	$-10.9^{-0.3}_{+0.2}$
			(v)		$-12.3^{-0.5}_{+4.9}$	$-11.3^{-2.4}_{+0.6}$	$-11.1^{-1.1}_{+5.1}$	$-10.2^{-3.5}_{+2.2}$	$-10.0^{-1.7}_{+6.0}$	$-9.4^{-3.7}_{+4.8}$
			(vi)	14	$-10.4^{-1.7}_{+0.1}$	$-11.2^{-1.9}$	$-9.3^{-1.7}_{+0.1}$	$-10.3^{-2.9}_{+0.1}$	$-8.2^{-2.0}_{+0.1}$	$-8.9^{-3.5}_{+0.1}$

Table 5.1 The true values of the binary parameters appear in the first three columns, as follows: $m_1^{\rm fixed} = m_{\rm chirp}^{\rm fixed}(1+q^{\rm fixed})^{1/5}/(q^{\rm fixed})^{3/5}$, $m_2^{\rm fixed} = m_{\rm chirp}^{\rm fixed}(1+q^{\rm fixed})^{1/5}(q^{\rm fixed})^{2/5})$ and $\chi_{\rm eff}^{\rm fixed}$. It is assumed that the exact lanthanide fraction is $X_{\rm lan}^{\rm fixed} = 10^{-4}$, while the exact supra-nuclear equation of state $\rm EOS^{fixed}$ is parameterized by $\gamma_0^{\rm LIN} = 1.4777$, $\gamma_1^{\rm LIN} = -0.3225$, $\gamma_2^{\rm LIN} = 0.0694$ and $\gamma_3^{\rm LIN} = -0.0046$, which associates to a $1.4\,M_\odot$ neutron star, a 13km radius and a tidal deformability of 663, and predicts a TOV limit of $2.43\,M_\odot$. In column four, the different sources of uncertainty taken into account: (i) no uncertainty; (ii) MBTA imprecise measurement only; (iii) neutron star equation of state marginalization only; (iv) ejecta fitting errors only; (v) ejecta chemical composition ignorance only; (vi) all the previous sources of uncertainty together. In the fifth column, the value of *HasEjecta*. The last sixth columns show the absolute magnitude at the end of 1, 2 and 3 days, for the g and K photometric filters. The upper and lower absolute magnitude limits are defined by the 10th and 90th percentiles.

$\chi_{\rm eff}$ have an important impact on the NSBH mass ejecta, as highlighted by Figure 5.2. The equation of state uncertainty translates in errors regarding the type of compact objects having masses $\sim 2\,M_{\odot}$. For illustration purposes, Figure 5.4 provides the time dependence of the absolute magnitude in the r photometric passband, when the different sources of uncertainty are considered. As previously shown in Table 5.1, the most negligible source of uncertainty turns to be the ejecta fitting imprecision.

The actual tool is aimed to be a useful low-latency product, destined to guide the EM observer community, in their track to catch the kilonova counterpart. Wherefore, the time needed to run this code is an important parameter. One should note that the main compilation time (more than 98%) is used for the equation of state marginalization and lightcurve generation by the surrogates. As a matter of example, a *E5-2698 v4* processor spends $6.204\,$s to marginalize an MBTA template over the 2396 equations of state, and $0.198\,$s (respectively $0.417\,$s) to convert a $(m_{\rm ej}, v_{\rm ej}, X_{\rm lan})$ (respectively $(m_{\rm ej}, \theta_{\rm inc}, \Phi)$) tuple into *Model I* (respectively *Model II*) time evolution lightcurves. Thus, the total necessary amount of time to execute these two processes is obtained by multiplying the equation of state marginalization cost duration by $n_{\rm templates}$ (the number of input MBTA templates; $\mathcal{O}(10)$ order of magnitude) and the lightcurve calculation cost duration by 1000. Nevertheless, this issue can be easily bypassed, if one has enough computational resources. Indeed, both equation of state marginalization and lightcurve computation are easily parallelizable (over the MBTA templates for the former and over the $(m_{\rm ej}, v_{\rm ej}, X_{\rm lan})$ or $(m_{\rm ej}, \theta_{\rm inc}, \Phi)$ tuples for the latter), so the computational cost might be divided by a huge factor. For instance, if one wants to convert input low-latency GW templates into *Model I* (respectively *Model II*) lightcurves, then needs $59\,{\rm s} + 0.975\,{\rm s} \times n_{\rm templates}$ (respectively $249\,{\rm s} + 0.975\,{\rm s} \times n_{\rm templates}$), if the same processor is used with 8 cores.

5.2.3 Method performance testing and outcome for some real events

In this section, I discuss the output of the present tool for some O2/O3 LIGO-Virgo confident detections. More specifically, I investigate those binary mergers, for which there is a non-negligible probability to contain at least a neutron star. Therefore, the binary systems are: the BNS merger GW170817 [Abbott et al., 2017e]; the BNS merger GW190425 [Abbott et al., 2020a]; the binary compact object GW190814 which is either a NSBH or a BBH according to Abbott et al. [2020b]; Essick and Landry [2020]; Most et al. [2020]; Tews et al. [2021]; Tan et al. [2020]; the NSBH merger GW200105 [LIGO Scientific Collaboration and Virgo Collaboration, 2020a]; the NSBH merger GW200115 [LIGO Scientific Collaboration and Virgo Collaboration, 2020b]. The preferred templates according to the MBTA offline analysis are presented in Table 5.2. But as mentioned in Section 5.2.1, for a given GW event, this tool takes as input not only

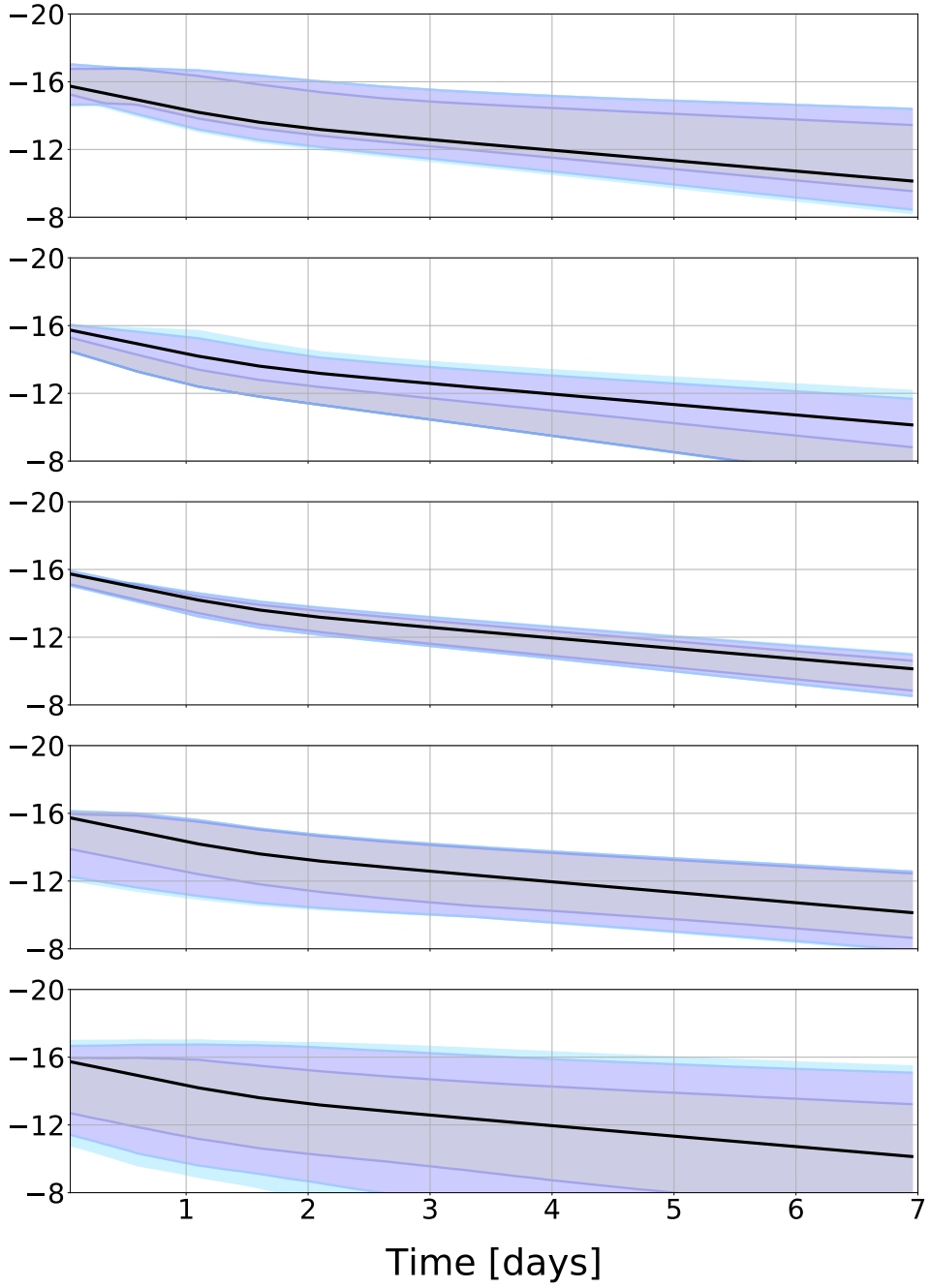

Fig. 5.4 Time evolution of the absolute magnitude. The binary parameters are $(m_1^{\rm fixed}, m_2^{\rm fixed}, \chi_{\rm eff}) = (1.6\,M_\odot, 1.4\,M_\odot, 0.001)$, the ejecta is characterized by $X_{\rm lan}^{\rm fixed} = 10^{-4}$, while the neutron star equation of state is parameterized by $(\gamma_0^{\rm LIN}, \gamma_1^{\rm LIN}, \gamma_2^{\rm LIN}, \gamma_3^{\rm LIN}) = (1.4777, -0.3225, 0.0694, -0.0046)$. From the top to the bottom panel, the considered sources of uncertainty are: the low-latency inaccurate measurement only; the equation of state marginalization only; the errors assigned to the fitting formulae only; the ejecta chemical composition uncertainty only; all the error sources put together. For each panel, the black curve represents the case of perfect predictions, while the blue shades contour plots designate the 1σ, 2σ and 3σ prediction errors.

Event	m_1 $(M_\odot)$	m_2 $(M_\odot)$	$m_{\rm chirp}$ $(M_\odot)$	q	s_1	s_2	$\chi_{\rm eff}$
GW170817	1.674	1.139	1.198	0.680	0.040	0.000	0.024
GW190425	2.269	1.305	1.487	0.575	0.080	-0.010	0.047
GW190814	36.881	2.093	6.522	0.057	0.340	0.960	0.373
GW200105	27.169	1.004	3.728	0.037	0.67	-0.05	0.644
GW200115	4.011	2.211	2.57	0.551	-0.66	-0.28	-0.525

Table 5.2 The parameters of the MBTA offline analysis preferred templates in the case of GW170817, GW190425, GW190814, GW200105 and GW200115. There are four independent parameters: the masses and the aligned/anti-aligned spins of the heavier (m_1 and s_1) and the lighter (m_2 and s_2) binary compact objects. The chirp mass $m_{\rm chirp}$, the mass ratio q and the effective spin $\chi_{\rm eff}$ might be expressed as functions of the previous parameters, as follows: $m_{\rm chirp} = (m_1 m_2)^{3/5}/(m_1 + m_2)^{1/5}$, $q = m_2/m_1$ and $\chi_{\rm eff} = (m_1 s_1 + m_2 s_2)/(m_1 + m_2)$.

the preferred template, but all the templates for which the $\mathrm{SNR}^{\mathrm{MBTA}}$ difference with respect to the preferred template is lower than 3. The weighted (by the statistical significance quantity w) binary parameters obtained from all these templates are illustrated in Table 5.3. Equally, for comparison purposes, the same quantities obtained from the long run PE posteriors are provided. At least two remarks should be made regarding the Table 5.3: (i) the low-latency output constrains well the chirp masses ($\sim 1\%$ uncertainty) and the reported values are similar to those obtained from the much more time expensively PE runs; (ii) both the mass ratio and the effective spin are assigned with large uncertainties ($> 100\%$) and, in general, are quite different from the PE reported values.

The *HasEjecta* values for both the low-latency and the offline PE input data are reported in Table 5.4. Equally, *HasRemnant*, a LIGO-Virgo low-latency data product provided during O3, is reported in Table 5.4. The similarity between low-latency and PE *HasEjecta* is valid for all the five events. On the other hand a discrepancy betweeen *HasRemnant* and *HasEjecta* appears in the case of GW200105. This is probably due to the fact that GW200105 was a sub-threshold event, being triggered only by the LIGO-Livingston interferometer, as mentioned in LIGO Scientific Collaboration and Virgo Collaboration [2020a]; Abbott et al. [2021b]. One step further, for a fair comparison of these three quantities, would be the study of a injected signals set. This investigation, although extremely motivating, would require much more work, thus it was not realized during my thesis. According to Table 5.4, the only events with non-negligible predicted mass ejecta are GW170817 and GW190425. The cumulative probability densities of $m_{\rm ej}$ for both events and for both MBTA and PE input data are provided in Figure 5.5. One should note both the resemblance of the low-latency data versus PE data based results distributions, and the fact that the GW190425 mass ejecta is predicted to be smaller that the $m_{\rm ej}$ of GW170817.

	MBTA			PE		
Event	$m_{\rm chirp}$ $(M_\odot)$	q	$\chi_{\rm eff}$	$m_{\rm chirp}$ $(M_\odot)$	q	$\chi_{\rm eff}$
GW170817	$1.198_{-0.001}$	$0.756^{+0.068}_{-0.157}$	$0.029^{+0.017}_{-0.018}$	1.186	$0.864^{+0.107}_{-0.12}$	$0.003^{+0.01}_{-0.007}$
GW190425	$1.487^{+0.001}_{-0.002}$	$0.784^{+0.121}_{-0.229}$	$0.026^{+0.024}_{-0.056}$	$1.437^{+0.018}_{-0.016}$	$0.657^{+0.266}_{-0.21}$	$0.058^{+0.079}_{-0.041}$
GW190814	$6.474^{+0.125}_{-0.134}$	$0.058^{+0.178}_{-0.008}$	$0.321^{+0.094}_{-0.817}$	$6.09^{+0.046}_{-0.043}$	$0.111^{+0.006}_{-0.007}$	$-0.003^{+0.047}_{-0.045}$
GW200105	$3.653^{+0.056}_{-0.042}$	$0.081^{+0.199}_{-0.039}$	$0.382^{+0.204}_{-0.476}$	$3.619^{+0.007}_{-0.007}$	$0.23^{+0.1}_{-0.06}$	$-0.027^{+0.135}_{-0.163}$
GW200115	$2.576^{+0.018}_{-0.012}$	$0.336^{+0.255}_{-0.243}$	$-0.264^{+0.52}_{-0.324}$	$2.582^{+0.004}_{-0.005}$	$0.195^{+0.089}_{-0.041}$	$-0.035^{+0.106}_{-0.17}$

Table 5.3 Median (50th percentile), upper limits (90th percentile) and lower limits (10th percentile) of the binary parameters $m_{\rm chirp}$, q and $\chi_{\rm eff}$, for GW170817, GW190425, GW190814, GW200105 and GW200115. While the columns 2-3-4 present the MBTA output templates results weighted by w, the columns 5-6-7 illustrate the binary parameters obtained by sampling unweighted items from the parameter estimation (hereafter PE) posteriors [Veitch et al., 2015]. More precisely, the PE samples used here are the same as in [Abbott et al., 2019a, 2021a].

Event	*HasRemnant*	MBTA *HasEjecta*	PE *HasEjecta*
GW170817	100%	100%	100%
GW190425	$> 99\%$	98%	$> 99\%$
GW190814	$< 1\%$	0%	0%
GW200105	12%	0%	0%
GW200115	9%	$< 1\%$	0%

Table 5.4 *HasRemnant*, MBTA *HasEjecta* and PE *HasEjecta*. While the *HasRemnant* values appearing here are the same as the ones reported in LIGO Scientific Collaboration and Virgo Collaboration [2019a] (for GW190425), LIGO Scientific Collaboration and Virgo Collaboration [2019b] (for GW190814), LIGO Scientific Collaboration and Virgo Collaboration [2020a] (for GW200105), LIGO Scientific Collaboration and Virgo Collaboration [2020b] (for GW200115) and Abbott et al. [2019b] (for GW170817; actually in this case I use the value reported for *EM-Bright*), the PE samples used here are identical to those reported in Abbott et al. [2019a] (for GW170817) and Abbott et al. [2021a] (for GW190425 and GW190814).

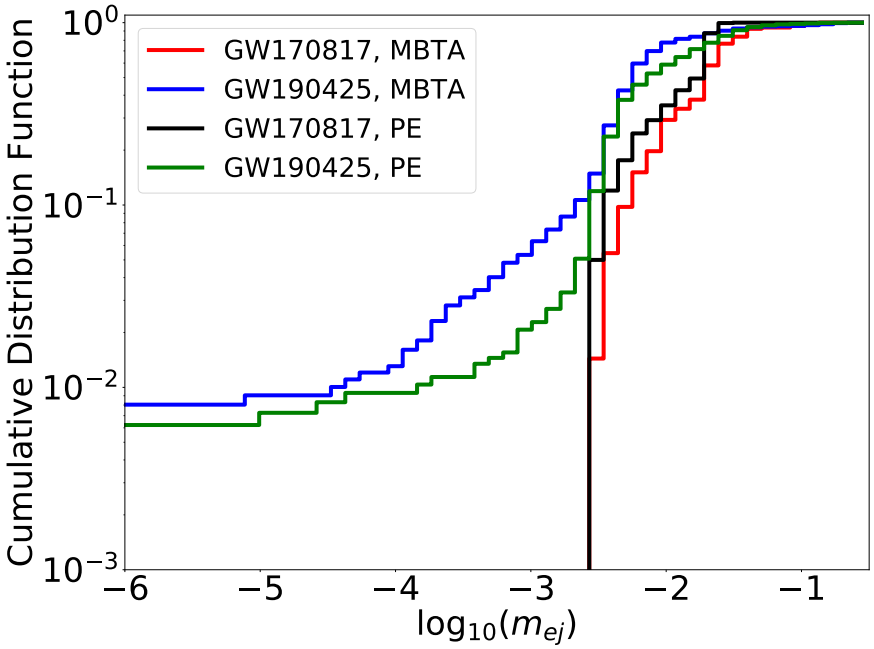

Fig. 5.5 $\log_{10} m_{\rm ej}$ cumulative distribution function for GW170817 and GW190425. One should note that this plot is slightly different than the one appearing in Figure 6 of Stachie et al. [2021]. The reason for this is the fact that here I use the PE samples from Abbott et al. [2019a] (for GW170817) and Abbott et al. [2021a] (for GW190425), while in the published paper, I used, by mistake, the PE samples corresponding to the GW waveforms priors *IMRPhenomPv2_NRTidalv2* [Dietrich et al., 2019], for GW170817, and *Taylor F2* [Damour et al., 2001], for GW190425.

The time evolution of the absolute magnitude for GW170817 and GW190425 are illustrated in Figure 5.6. One should note that the contours error bars do not contain the uncertainty of the fitting formulae and, even more important, of the chemical ejecta composition, because I use the prior $X_{\rm lan} = 10^{-4}$ (respectively $\Phi = 45^{\circ}$) for in the case of *Model I* (respectively *Model II*) lightcurves. In addition, for the *Model II* lightcurves, $\cos\theta_{\rm inc}$ is chosen to be uniform in $[0, 1]$. These assumptions are consistent with the results from Coughlin et al. [2018a]; Dietrich et al. [2020]. One should note the different behaviors of the *Model I* and *Model II* absolute magnitude in the first half day of flaring: while the *Model I* brightness decreases, the *Model II* luminosity increases. While for GW170817, one should remark the agreement between the predicted lightcurves and the observational points, for GW190425, it is worth mentioning that the EM signal is predicted to be dimmer, which, in addition to the broad sky localization and the high location distance, is indicative of the non-detection. The absolute magnitude might be converted into apparent magnitude by making use of the distance information contained in the Bayestar skymaps [Singer and Price, 2016]. The distance details might be manipulated in different ways. In this case I calculate a mean luminosity distance d_L from the Bayestar skymap and I convert the absolute magnitude M into apparent magnitude m by means of the formula $m - M = 5\log_{10} d_L - 5$, where d_L is in units of pc. One might have envisaged to derive a sky direction dependent luminosity distance, which is actually the information contained in a Bayestar skymap, but I decided to be as simple as possible for the actual study. In Figure 5.7, there are two examples of apparent magnitude for GW190425. One set of contours represents the lightcurve for $\log_{10} X_{\rm lan}$ uniform in $[-9, -1]$, while the other set designates the prior $X_{\rm lan} = 10^{-4}$. One should note that I do not include here the uncertainty, due to the distance luminosity measurement error, which I estimate to account for ~ 0.7 magnitudes.

The method used for the computation of *HasEjecta* has been used in the work related to the detection of the NSBH mergers GW200105 and GW200115 [Abbott et al., 2021b]. The input data is represented by the output posteriors of the offline MCMC runs [Ashton et al., 2019; Romero-Shaw et al., 2020; Smith et al., 2020; Speagle, 2020; Lange et al., 2018; Veitch et al., 2015]. More precisely, the GW waveform priors used in these MCMC runs are *IMRPhenomNSBH* [Thompson et al., 2020], *SEOBNRv4ROMNRTidalv2NSBH* [Matas et al., 2020]. Equally the combined parameter estimation samples obtained by using the GW waveforms, *IMRPhenomXPHM* [Pratten et al., 2021] and *SEOBNRv4PHM* [Ossokine et al., 2020], is considered like in other studies [Abbott et al., 2016a; Ashton and Khan, 2020; Abbott et al., 2020b]. The result of the method indicates that, with a probability higher than 99%, the ejected mass is below $10^{-6} M_{\odot}$ for the two binary systems.

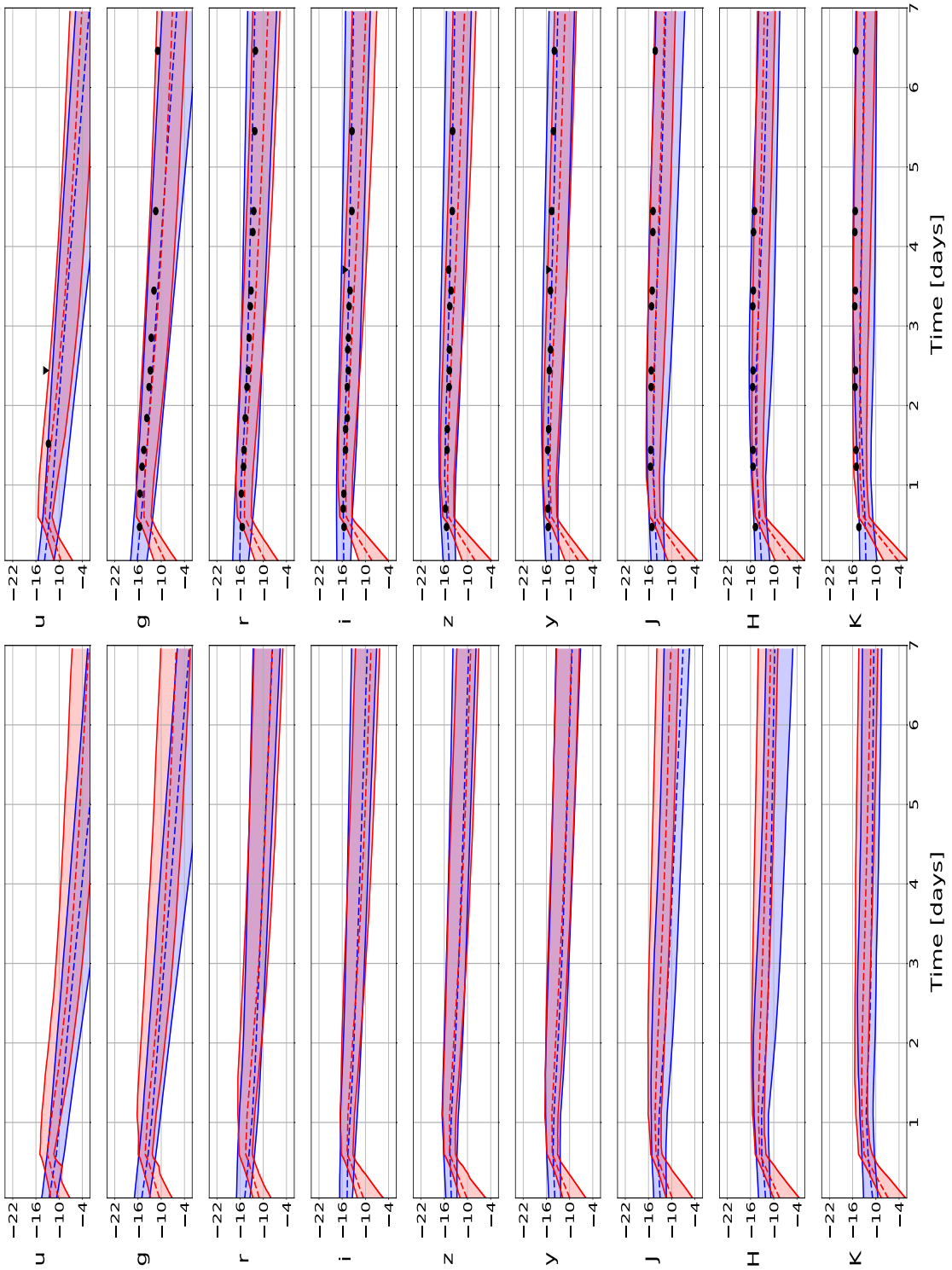

Fig. 5.6 Absolute magnitude versus time for GW170817 (on top) and GW190425 (on bottom), for the $u, g, r, i, z, y, J, H, K$ photometric filters. The *Model I* lightcurves appear in blue, while the *Model II* lightcurves are in red. For each lightcurve, the two solid lines are the upper (90th percentile) and lower (10th percentile) limits, while the dashed line corresponds to the median. Finally, regarding GW170817, the observational points appear in circles (finite uncertainty) and triangles (upper limits), and have been derived from apparent magnitude data by means of the mean Bayestar skymap luminosity distance. Only the low-latency data is used for these simulations.

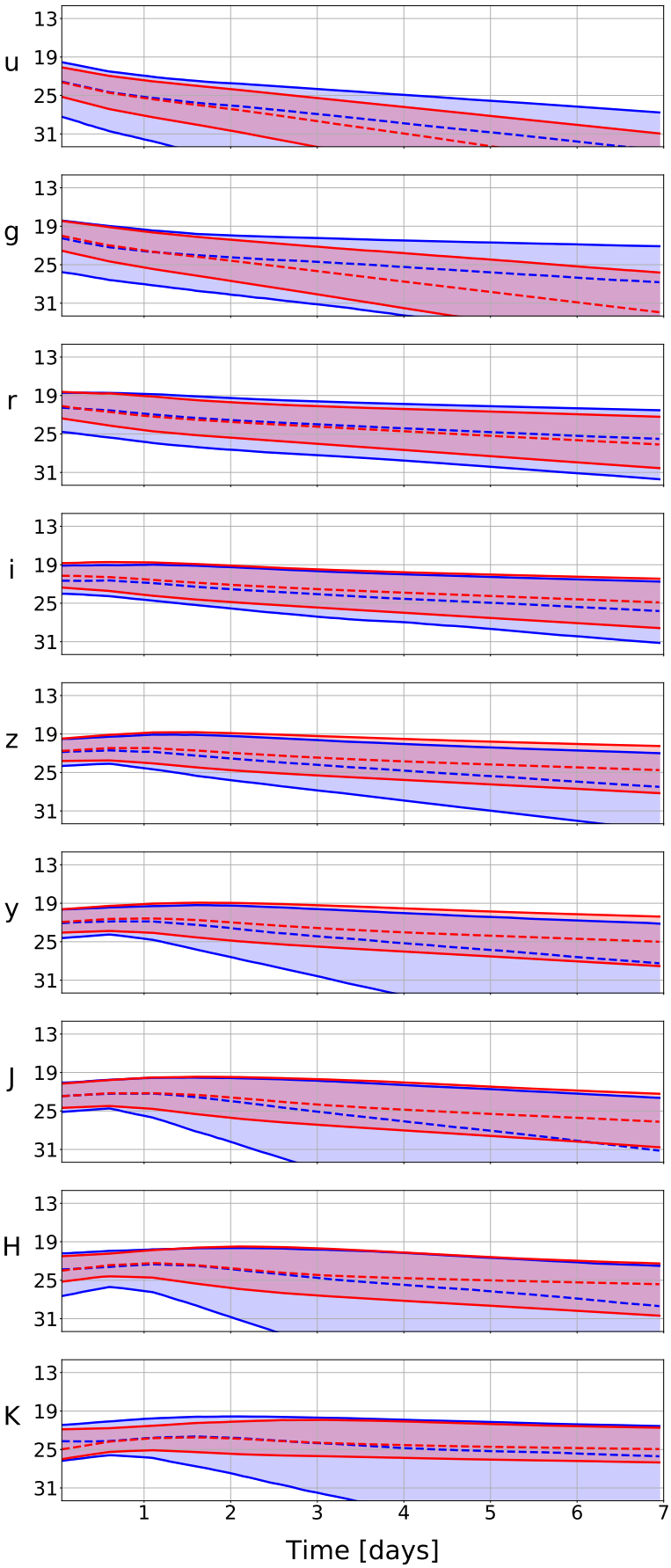

Fig. 5.7 Time evolution of the GW190425 apparent magnitude, based on the PE input data. The chemical composition ejecta priors are: $X_{\rm lan} = 10^{-4}$ for the red lightcurve and $\log_{10} X_{\rm lan}$ uniform in [-9, -1] for the blue lightcurve.

CHAPTER 6

Conclusion

During my PhD research, I participated in projects (see Figure 6.1) destined for the multimessenger detection of compact binary mergers. Except for the study presented in Chapter 4, all the other activities are assumed to require both GW and EM data. By GW data in this thesis, I always meant data from the ground based interferometers LIGO and Virgo. On the other hand, I was interested into two types of EM counterparts: the γ-rays, detected by the high energy detectors aboard space observatories (in this thesis it is always about Fermi-GBM), and interpreted as a short GRB prompt emission (in Chapter 2), or a short GRB precursor (in Chapter 3); the ultra-violet/optical/infrared emission, detectable by terrestrial telescopes (in this thesis it is always about ZTF), and representing the kilonova signal. All these studies (will) appear in published articles, as follows: Stachie et al. [2020a]; Hamburg et al. [2020] for Chapter 2, *Stachie et al. (2021) in prep.* for Chapter 3, Stachie et al. [2020b]; Antier et al. [2020b] for Chapter 4 and Stachie et al. [2021]; Abbott et al. [2021b] for Chapter 5.

Presented in Chapter 2 is a method to search for associations formed of an EM Fermi-GBM trigger and a GW LIGO single interferometer candidate, and generated by the merger of a compact object binary in the Universe. The EM and the GW triggers are found independently by two all-sky all-time pipelines: the offline *PyCBC* GW [Dal Canton et al., 2014] analysis matching the observational strain data against the modelled compact binary merger waveforms from a template bank; the *targeted-search* [Blackburn et al., 2015] aiming to coherently identify an excess of high energy photons characterized by broken power law energetics. Each trigger has assigned a ranking statistic (LLR for EM triggers and $\hat{\rho}_{gw}$ for GW triggers), a sky localization probability distribution and an arrival time (EM trigger center time measured at Fermi and GW coalescence time measured at the interferometer). The pairs of triggers are formed in the following way: for each GW candidate, the most significant (with the highest LLR) EM trigger in between $[-30\,\mathrm{s}, 30\,\mathrm{s}]$ is considered. A statistical analysis, based on Bayesian inference, is proposed. Thus, for each pair of triggers, a joint ranking statistic is derived based on the significances of the two triggers, their skymap overlap and the time separation between the arrival times of the two eventual messengers. By

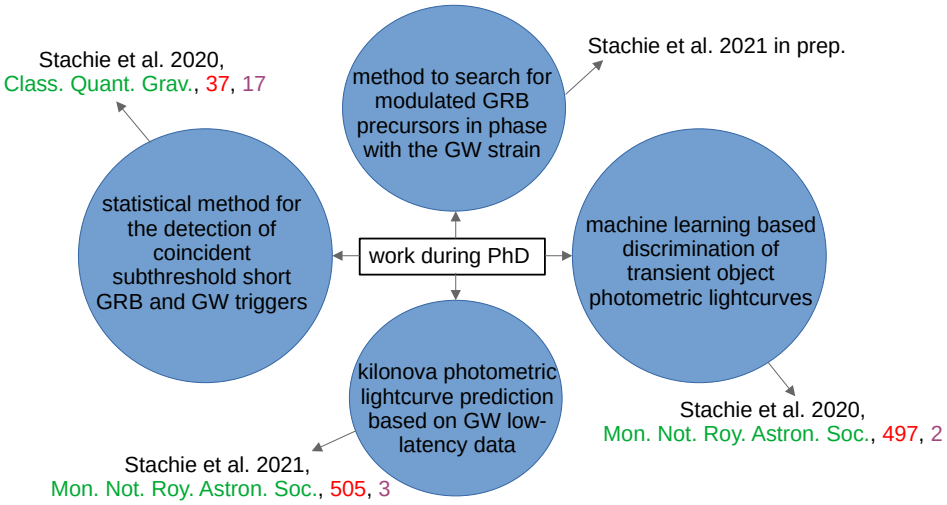

Fig. 6.1 An overview of the main projects I worked on during my PhD.

artificially creating background associations (by time slides; in a similar way the GW pipelines create artificial coincident triggers between two distinct GW interferometers), the ranking statistic distribution for noises is derived. This distribution is converted into a FAR function, which is used for the evaluation of the foreground triggers' significance. The highest ranked associations are also manually analyzed by means of Omega scans [Chatterji et al., 2004] of the GW data and EM lightcurve eye investigations. At the end of the analysis, despite the survival of an interesting pair for which there is no clear evidence for rejection, I conclude the non-existence of unambiguous astrophysical association. This method might be improved, and new solutions for the analysis of the data from the next observing runs are envisaged. For the derivation of the joint ranking statistic, unrealistic assumptions have been made. For example, it was considered that the probabilities of the different hypothesis (to have two background triggers; to have a GW noise candidate and a EM real event; to have a GW real event and a EM noise candidate; to have two non-related real events; to have two real signals generated by the same astrophysical event) are equal. This prior might be corrected easily because now, after O3, there is a good knowledge about the rate of binary mergers in the Universe as well as about the rate of GW pipeline triggering. Another aspect that needs to be treated with care is the restriction of the input data sets to those candidates which are really presumed to be in coincidence with another messenger. For example, one might restrict the list of compact object binary candidates to only those triggers for which the best template contains at least a neutron star, the existence of baryon matter being a mandatory (but not sufficient) condition for the generation of EM radiation, and the list of EM triggers to those events being shorter than 2 s and possessing a *hard* or *normal* spectrum, as the majority of short GRBs do. One should note that, if one wants to still search for less probable coincidences, such as those of BBH like signals with EM

signals, one might use trial factors. A reason motivating this restriction for the present method is to avoid the pollution of the joint ranking background distribution with unnecessary noise associations. The effect of this will be the lowering of the FAR values for the higher joint rankings.

Chapter 3 proposes a tool to search for EM signals modulated by the orbital phase of a binary prior to the merger. The only assumption I make about the structure of the signals is that for distinct orbits there are the same orbital phase windows responsible for the maximum of intensity. Therefore, the idea of the statistical analysis appears intuitively: by summing the number of photons histograms in the orbital phase, for several orbits, the maxima will add to the other maxima and the minima to the other minima. At the end of this summation process, in the orbital phase space (going from 0 to 2π), the lightcurve will present a peak, more accentuated than the peaks of the different orbits, when taken separately. Finally the technique, used in this study, to search for an excess of photons in this artificial (because it is the sum over several orbits) orbital phase is almost identical to the *targeted-search* [Blackburn et al., 2015] method used to identify a energy excess in the initial time space. An objective of this study is to prove that, in the case of orbital phase modulated signals, this new search (the *chirp-search*) is more suitable than a pipeline (in this case the *targeted-search*) aiming to simply identify an excess of power, whatever the structure of the signal. Initially both searches are tried at random times, obtaining the LLR background distributions. Then the searches are used to recover injected modulated signals, named *exotic-waveforms*. The injections represent peculiar signals, for which the flaring happens with equal intensity during the same 10° orbital phase windows, while the radiation emission is forbidden outside these windows. It is proved that the FAP distribution for the injected signals is situated at lower values in the case of the *chirp-search* than in the case of the *targeted-search*. Also investigated is the dependence of the pipeline sensitivity loss with the uncertainty of the coalescence time and the chirp mass of the binary. Finally, the two searches are used for GW170817 [Abbott et al., 2017e], GW190425 [Abbott et al., 2020a], GW190814 [Abbott et al., 2020b], GW200105 and GW200115 [Abbott et al., 2021b], and it is concluded that there is no unambiguous GRB precursor candidate for any of these events. Ways to improve the *chirp-search* might be envisaged. One important limitation of the pipeline is the high LLR of the background triggers. Some kinds of events, such as solar flaring, might not be avoided (unless one uses specific filtering for the events localized nearby the Sun) because a high intensity non-modulated signal is also identified by the *chirp-search* (as also by the *targeted-search*). However, some statistical significant spurious events are particular in the case of the *chirp-search*. Indeed, as the search is done over fixed timescales, these search durations do not necessarily cover an integer number of orbits. Therefore, the summation of the photon counts over several orbits

is biased and artificial fluctuations appear in the orbital phase lightcurve. A correction would consist in slightly changing the search duration in order to have an integer number of orbits. Other features of the search, which might impact the sensitivity of the pipeline, are related to the energetics. The *chirp-search* uses the same *hard*, *normal* and *soft* templates for the recovery of the signals. These Band functions are characteristic of the main GRB prompt emission (due to synchrotron radiation and Compton scattering), but there is less information about the flaring mechanism at play for a GRB precursor. Therefore, one might try to use other templates such as the black body distribution.

A machine learning based method for the discrimination of optical transients, based on photometric observations, is proposed in Chapter 4. The heart of the method consists of a multi-wavelength classifier, named `astrorapid` [Muthukrishna et al., 2019], which is supposed to discriminate between 13 classes of astrophysical objects plus a class accounting for the moments preceding the flaring episode. Initially, the work consisted in manipulating the time dependent distribution probability output of `astrorapid` in such a way that only four classes remain: the initial kilonova template is kept as "KN"; the different supernovae classes are collapsed in one superclass named "SN"; the other (than kilonovae and supernovae) astrophysical classes are collapsed in a superclass named "Others"; a class named "Indistinguishable" is introduced to partially account for the initial "Pre-explosion" `astrorapid` class. Then the code is tried on both ZTF real objects ("SN" and "Others" types) and injected signals ("SN" and "KN" types). Everywhere in this project, I make use of r and/or g photometric filter observations. Concerning the real ZTF events, the method needs ~ 10 observations, in both r and g filters, to have more than 40% correct identification. Regarding the injected signals, when the sampling is ideal (two observations per night in each filter), almost all supernovae are correctly identified at the end of the first day, while the kilonovae necessitate ~ 2.5 days to be identified with $\sim 50\%$ fairness. The situation is more worrying when the kilonovae are observed with a cadence similar to the one of ZTF. Finally, the color related information turn out to be primordial, as the performance of the classifier is much worse when only one photometric passband information is available. Although during my thesis, the work related to this study stopped here, this investigation is part of a larger project concerning the best observing strategy a telescope (network) should adopt. Indeed one might ask what is the compromise to be considered between the case of many observations with a same photometric filter and the case of many filters but few observations per filter. This addresses several questions: given a number of filters, how many observations an astrophysical transient needs in order to be identified with good confidence?; given a number of filters, what is the optimal observation rate?; etc. Once all these questions are answered, the EM observing community might maximize their resources in order to identify the so-rare kilonovae events.

Chapter 5 presents a method to convert GW low-latency data into kilonova lightcurves. The low-latency data contain information related to the masses and the spins of the binary compact object components. An intermediate major step, before the derivation of the photometric lightcurves, is the computation of the gravitationally unbound mass ejecta, which is assumed to be the sum of two components: the dynamical ejecta expelled during the merger by the tidal torques and the shocks, and the disc winds ejecta which consists in matter initially bound on the accretion disc surrounding the merger remnant black hole, and which subsequently becomes unbound due to, among others, neutrino radiation, magnetic and/or viscous effects. The amount of mass ejecta (as well as the velocity of the ejecta) is calculated by means of fitting formulae [Coughlin et al., 2019a; Dietrich et al., 2020; Foucart et al., 2018; Krüger and Foucart, 2020; Kawaguchi et al., 2016], derived previously based on numerical relativity simulations. Nevertheless, in order to use these fitting formulae, one needs information related to the properties of the matter inside neutron star. Given that, to date, the supra-nuclear equation of state is not completely known, the assumption used here consists in marginalizing over GW170817-like equations of state [Abbott et al., 2018a]. Then two numerical surrogates, based on two kilonovae models [Kasen et al., 2017; Bulla, 2019], are used to convert mass and velocity of ejecta into photometric lightcurve. One should note that a prior about the chemical composition of the ejecta (and for one of the kilonova model, a prior about the binary inclination angle) is also needed. The predictions match well the AT 2017gfo observational data and are consistent with the non-detection of an EM counterpart for GW190425. However the predicted error bars are significant, rendering the utility of such a tool questionable for the moment. An investigation of the sources of uncertainty has been done, and it has been concluded that the ignorance about the ejecta chemical composition, as well as the inaccuracy of the GW strain measurement, are the most prejudicial. Probably, the only way the question related to the chemical heaviness of the ejecta might be answered is by the detection, in the near future, of several other such transients. Indeed, the higher the number of detections the better the lanthanide fraction constraint. On the other hand, some improvements can be made concerning the impact of the low-latency data inaccuracy. While the low-latency chirp mass is a well measured quantity, and so does not need any modification, the information related to the mass ratio and the effective spin can be replaced with priors based on binary population. Indeed, the size of the catalog of real GW events [Abbott et al., 2021a] increased significantly during the last years and will increase even more in the next years, and so the binary parameter distributions will be more and more precise. Moreover, the improvement of the ground based GW interferometers will reduce the uncertainties on the low-latency data, while future detections of BNS/NSBH events, allowing the measurement of the tidal deformability, will represent a step further in the computation of the

neutron star equation of state. Thus, there are hopes that this tool, which is able to provide predictions with a (few) minute(s) latency, will represent a useful implementation for reporting to EM observers.

The neutron stars and black holes are astrophysical objects about which the scientific community learned a lot in the last decades. Simultaneously, the number of both short GRB and GW events has increased considerably. On the other hand, we are at the beginning of the era of multimessenger astronomy. For the next years, with the improvement of the GW detectors' sensitivity and the construction of the next generation wide field of view telescopes, there are hopes that coincident detections of EM and GW signals, generated by a same astrophysical system, to become a common thing. However, the construction of more sensitive detectors is not the only challenge that awaits scientists. Indeed, the amount of data to analyze will also be huge. Therefore not only the independent search pipelines will probably necessitate modifications, but need of strengthened coordination between GW and EM communities will be required. The research activities, I participated to during my PhD, are part of this effort. While the studies presented in Chapters 2 and 3 might be helpful for the identification of new GW, short GRB precursor and main prompt emission events, the projects from Chapters 4 and 5 are dedicated to the guidance of the EM observing community in the case of a GW detection. One should be aware that the ideas behind these projects can be slightly modified in order to address other issues. For example, the search for coincident EM and GW signals, from Chapter 2, might be easily modified in a search for coincident EM/GW and neutrino signals. Likewise, instead of searching for an EM signal modulated by the orbital phase evolution of a binary, as described in Chapter 3, one might check for modulation into a short GRB event possessing a precursor, and then correlate with the GW data, if available. Also, the studies from Chapters 4 and 5 might be updated in order to offer more ingenious ways to find the targeted kilonova event, buried in the list of identified transient objects. In the next years, low-latency tidal deformability information, as well as binary inclination angle, might be available, improving thus the precision of the kilonova lightcurve prediction. By combining early photometric/spectroscopic observations with lightcurve predictions, the discrimination between transient objects will probably be more efficient and more accurate.

REFERENCES

M. G. Aartsen et al. Multimessenger observations of a flaring blazar coincident with high-energy neutrino IceCube-170922A. *Science*, 361(6398):eaat1378, 2018. doi: 10.1126/science.aat1378.

J. Aasi et al. Enhancing the sensitivity of the LIGO gravitational wave detector by using squeezed states of light. *Nature Photon.*, 7:613–619, 2013. doi: 10.1038/nphoton.2013.177.

J. Aasi et al. Advanced LIGO. *Class. Quant. Grav.*, 32:074001, 2015a. doi: 10.1088/0264-9381/32/7/074001.

J. Aasi et al. Advanced LIGO. *Class. Quant. Grav.*, 32:074001, 2015b. doi: 10.1088/0264-9381/32/7/074001.

B. P. Abbott et al. Properties of the Binary Black Hole Merger GW150914. *Phys. Rev. Lett.*, 116(24):241102, 2016a. doi: 10.1103/PhysRevLett.116.241102.

B. P. Abbott et al. Characterization of transient noise in Advanced LIGO relevant to gravitational wave signal GW150914. *Class. Quant. Grav.*, 33(13):134001, 2016b. doi: 10.1088/0264-9381/33/13/134001.

B. P. Abbott et al. A gravitational-wave standard siren measurement of the Hubble constant. *Nature*, 551(7678):85–88, 2017a. doi: 10.1038/nature24471.

B. P. Abbott et al. Multi-messenger Observations of a Binary Neutron Star Merger. *Astrophys. J. Lett.*, 848(2):L12, 2017b. doi: 10.3847/2041-8213/aa91c9.

B. P. Abbott et al. Gravitational Waves and Gamma-rays from a Binary Neutron Star Merger: GW170817 and GRB 170817A. *Astrophys. J. Lett.*, 848(2):L13, 2017c. doi: 10.3847/2041-8213/aa920c.

B. P. Abbott et al. Gravitational Waves and Gamma-rays from a Binary Neutron Star Merger: GW170817 and GRB 170817A. *Astrophys. J. Lett.*, 848(2):L13, 2017d. doi: 10.3847/2041-8213/aa920c.

B. P. Abbott et al. GW170817: Observation of Gravitational Waves from a Binary Neutron Star Inspiral. *Phys. Rev. Lett.*, 119(16):161101, 2017e. doi: 10.1103/PhysRevLett.119.161101.

B. P. Abbott et al. GW170817: Measurements of neutron star radii and equation of state. *Phys. Rev. Lett.*, 121(16):161101, 2018a. doi: 10.1103/PhysRevLett.121.161101.

B P Abbott et al. Effects of data quality vetoes on a search for compact binary coalescences in Advanced LIGO's first observing run. *Class. Quant. Grav.*, 35(6):065010, 2018b. doi: 10.1088/1361-6382/aaaafa.

B. P. Abbott et al. GWTC-1: A Gravitational-Wave Transient Catalog of Compact Binary Mergers Observed by LIGO and Virgo during the First and Second Observing Runs. *Phys. Rev. X*, 9(3):031040, 2019a. doi: 10.1103/PhysRevX.9.031040.

B. P. Abbott et al. Low-latency Gravitational-wave Alerts for Multimessenger Astronomy during the Second Advanced LIGO and Virgo Observing Run. *Astrophys. J.*, 875 (2):161, 2019b. doi: 10.3847/1538-4357/ab0e8f.

B. P. Abbott et al. GW190425: Observation of a Compact Binary Coalescence with Total Mass $\sim 3.4 M_{\odot}$. *Astrophys. J. Lett.*, 892(1):L3, 2020a. doi: 10.3847/2041-8213/ab75f5.

R. Abbott et al. GW190814: Gravitational Waves from the Coalescence of a 23 Solar Mass Black Hole with a 2.6 Solar Mass Compact Object. *Astrophys. J. Lett.*, 896(2): L44, 2020b. doi: 10.3847/2041-8213/ab960f.

R. Abbott et al. GWTC-2: Compact Binary Coalescences Observed by LIGO and Virgo During the First Half of the Third Observing Run. *Phys. Rev. X*, 11:021053, 2021a. doi: 10.1103/PhysRevX.11.021053.

R. Abbott et al. Observation of gravitational waves from two neutron star-black hole coalescences. *Astrophys. J. Lett.*, 915:L5, 2021b. doi: 10.3847/2041-8213/ac082e.

A. A. Abdo, M. Ackermann, M. Ajello, K. Asano, W. B. Atwood, M. Axelsson, L. Baldini, J. Ballet, G. Barbiellini, M. G. Baring, D. Bastieri, K. Bechtol, R. Bellazzini, B. Berenji, P. N. Bhat, E. Bissaldi, E. D. Bloom, E. Bonamente, J. Bonnell, A. W. Borgland, A. Bouvier, J. Bregeon, A. Brez, M. S. Briggs, M. Brigida, P. Bruel, J. M. Burgess, T. H. Burnett, G. A. Caliandro, R. A. Cameron, P. A. Caraveo, J. M. Casandjian, C. Cecchi, Ö. Çelik, V. Chaplin, E. Charles, C. C. Cheung, J. Chiang, S. Ciprini, R. Claus, J. Cohen-Tanugi, L. R. Cominsky, V. Connaughton, J. Conrad, S. Cutini, C. D. Dermer, A. de Angelis, F. de Palma, S. W. Digel, B. L. Dingus, E. Do Couto E Silva, P. S. Drell, R. Dubois, D. Dumora, C. Farnier, C. Favuzzi, S. J. Fegan, J. Finke, G. Fishman,

W. B. Focke, L. Foschini, Y. Fukazawa, S. Funk, P. Fusco, F. Gargano, D. Gasparrini, N. Gehrels, S. Germani, L. Gibby, B. Giebels, N. Giglietto, F. Giordano, T. Glanzman, G. Godfrey, J. Granot, J. Greiner, I. A. Grenier, M. H. Grondin, J. E. Grove, D. Grupe, L. Guillemot, S. Guiriec, Y. Hanabata, A. K. Harding, M. Hayashida, E. Hays, E. A. Hoversten, R. E. Hughes, G. Jóhannesson, A. S. Johnson, R. P. Johnson, W. N. Johnson, T. Kamae, H. Katagiri, J. Kataoka, N. Kawai, M. Kerr, R. M. Kippen, J. Knödlseder, D. Kocevski, C. Kouveliotou, F. Kuehn, M. Kuss, J. Lande, L. Latronico, M. Lemoine-Goumard, F. Longo, F. Loparco, B. Lott, M. N. Lovellette, P. Lubrano, G. M. Madejski, A. Makeev, M. N. Mazziotta, S. McBreen, J. E. McEnery, S. McGlynn, P. Mészáros, C. Meurer, P. F. Michelson, W. Mitthumsiri, T. Mizuno, A. A. Moiseev, C. Monte, M. E. Monzani, E. Moretti, A. Morselli, I. V. Moskalenko, S. Murgia, T. Nakamori, P. L. Nolan, J. P. Norris, E. Nuss, M. Ohno, T. Ohsugi, N. Omodei, E. Orlando, J. F. Ormes, M. Ozaki, W. S. Paciesas, D. Paneque, J. H. Panetta, D. Parent, V. Pelassa, M. Pepe, M. Pesce-Rollins, V. Petrosian, F. Piron, T. A. Porter, R. Preece, S. Rainò, E. Ramirez-Ruiz, R. Rando, M. Razzano, S. Razzaque, A. Reimer, O. Reimer, T. Reposeur, S. Ritz, L. S. Rochester, A. Y. Rodriguez, M. Roth, F. Ryde, H. F. W. Sadrozinski, D. Sanchez, A. Sander, P. M. Saz Parkinson, J. D. Scargle, T. L. Schalk, C. Sgrò, E. J. Siskind, D. A. Smith, P. D. Smith, G. Spandre, P. Spinelli, M. Stamatikos, F. W. Stecker, M. S. Strickman, D. J. Suson, H. Tajima, H. Takahashi, T. Takahashi, T. Tanaka, J. B. Thayer, J. G. Thayer, D. J. Thompson, L. Tibaldo, K. Toma, D. F. Torres, G. Tosti, E. Troja, Y. Uchiyama, T. Uehara, T. L. Usher, A. J. van der Horst, V. Vasileiou, N. Vilchez, V. Vitale, A. von Kienlin, A. P. Waite, P. Wang, C. Wilson-Hodge, B. L. Winer, K. S. Wood, X. F. Wu, R. Yamazaki, T. Ylinen, M. Ziegler, and Fermi LAT Collaboration. A limit on the variation of the speed of light arising from quantum gravity effects. *Nature*, 462(7271):331–334, November 2009. doi: 10.1038/nature08574.

A. A. Abdo et al. The Second Fermi Large Area Telescope Catalog of Gamma-ray Pulsars. *Astrophys. J. Suppl.*, 208:17, 2013. doi: 10.1088/0067-0049/208/2/17.

George O. Abell. The National Geographic Society-Palomar Observatory Sky Survey. *Leaflet of the Astronomical Society of the Pacific*, 8(366):121, January 1959.

A. Abramowski et al. Acceleration of petaelectronvolt protons in the Galactic Centre. *Nature*, 531:476, 2016. doi: 10.1038/nature17147.

T. Accadia et al. Characterization of the Virgo Seismic Environment. *Class. Quant. Grav.*, 29:025005, 2012. doi: 10.1088/0264-9381/29/2/025005.

F. Acernese et al. Advanced Virgo: a second-generation interferometric gravitational wave detector. *Class. Quant. Grav.*, 32(2):024001, 2015. doi: 10.1088/0264-9381/32/2/024001.

Thomas P. Ackerman and Owen B. Toon. Absorption of visible radiation in atmosphere containing mixtures of absorbing and nonabsorbing particles. *Appl. Opt.*, 20 (20):3661–3668, Oct 1981. doi: 10.1364/AO.20.003661. URL http://ao.osa.org/abstract.cfm?URI=ao-20-20-3661.

M. Ackermann, M. Ajello, L. Baldini, J. Ballet, G. Barbiellini, D. Bastieri, J. Becerra Gonzalez, R. Bellazzini, E. Bissaldi, R. D. Blandford, E. D. Bloom, R. Bonino, E. Bottacini, J. Bregeon, P. Bruel, R. Buehler, S. Buson, R. A. Cameron, M. Caragiulo, P. A. Caraveo, E. Cavazzuti, C. Cecchi, C. C. Cheung, J. Chiang, G. Chiaro, S. Ciprini, J. Conrad, D. Costantin, F. Costanza, S. Cutini, F. D'Ammando, F. de Palma, R. Desiante, S. W. Digel, N. Di Lalla, M. Di Mauro, L. Di Venere, A. Domínguez, P. S. Drell, C. Favuzzi, S. J. Fegan, E. C. Ferrara, J. Finke, W. B. Focke, Y. Fukazawa, S. Funk, P. Fusco, F. Gargano, D. Gasparrini, N. Giglietto, F. Giordano, M. Giroletti, D. Green, I. A. Grenier, L. Guillemot, S. Guiriec, D. H. Hartmann, E. Hays, D. Horan, T. Jogler, G. Jóhannesson, A. S. Johnson, M. Kuss, G. La Mura, S. Larsson, L. Latronico, J. Li, F. Longo, F. Loparco, M. N. Lovellette, P. Lubrano, J. D. Magill, S. Maldera, A. Manfreda, L. Marcotulli, M. N. Mazziotta, P. F. Michelson, N. Mirabal, W. Mitthumsiri, T. Mizuno, M. E. Monzani, A. Morselli, I. V. Moskalenko, M. Negro, E. Nuss, T. Ohsugi, R. Ojha, N. Omodei, M. Orienti, E. Orlando, J. F. Ormes, V. S. Paliya, D. Paneque, J. S. Perkins, M. Persic, M. Pesce-Rollins, F. Piron, T. A. Porter, G. Principe, S. Rainò, R. Rando, B. Rani, M. Razzano, S. Razzaque, A. Reimer, O. Reimer, R. W. Romani, C. Sgrò, D. Simone, E. J. Siskind, F. Spada, G. Spandre, P. Spinelli, C. S. Stalin, L. Stawarz, D. J. Suson, M. Takahashi, K. Tanaka, J. B. Thayer, D. J. Thompson, D. F. Torres, E. Torresi, G. Tosti, E. Troja, G. Vianello, and K. S. Wood. Gamma-ray blazars within the first 2 billion years. *The Astrophysical Journal*, 837(1):L5, feb 2017. doi: 10.3847/2041-8213/aa5fff. URL https://doi.org/10.3847/2041-8213/aa5fff.

T. Adams, D. Buskulic, V. Germain, G. M. Guidi, F. Marion, M. Montani, B. Mours, F. Piergiovanni, and G. Wang. Low-latency analysis pipeline for compact binary coalescences in the advanced gravitational wave detector era. *Class. Quant. Grav.*, 33(17): 175012, 2016. doi: 10.1088/0264-9381/33/17/175012.

C. Akerlof et al. Observation of contemporaneous optical radiation from a gamma-ray burst. *Nature*, 398:400–402, 1999. doi: 10.1038/18837.

Mark G. Alford, Sophia Han, and Madappa Prakash. Generic conditions for stable hybrid stars. *Phys. Rev. D*, 88:083013, Oct 2013. doi: 10.1103/PhysRevD.88.083013. URL https://link.aps.org/doi/10.1103/PhysRevD.88.083013.

Bruce Allen. χ^2 time-frequency discriminator for gravitational wave detection. *Phys. Rev. D*, 71:062001, 2005. doi: 10.1103/PhysRevD.71.062001.

J. W. Allison. Gamma-Radiation Absorption Coefficients of Air in the Energy Range 0.01 to 100 Mev. *Journal of Applied Physics*, 29(8):1175–1178, August 1958. doi: 10.1063/1.1723396.

N. S. Altman. An introduction to kernel and nearest-neighbor nonparametric regression. *The American Statistician*, 46(3):175–185, 1992. doi: 10.1080/00031305.1992.10475879. URL https://www.tandfonline.com/doi/abs/10.1080/00031305.1992.10475879.

Pau Amaro-Seoane, Heather Audley, Stanislav Babak, John Baker, Enrico Barausse, Peter Bender, Emanuele Berti, Pierre Binetruy, Michael Born, Daniele Bortoluzzi, et al. Laser interferometer space antenna. *arXiv preprint arXiv:1702.00786*, 2017.

Igor Andreoni et al. Fast-transient Searches in Real Time with ZTFReST: Identification of Three Optically-discovered Gamma-ray Burst Afterglows and New Constraints on the Kilonova Rate. 4 2021.

S. Antier et al. The first six months of the Advanced LIGO's and Advanced Virgo's third observing run with GRANDMA. *Mon. Not. Roy. Astron. Soc.*, 492(3):3904–3927, 2020a. doi: 10.1093/mnras/stz3142.

S. Antier et al. GRANDMA observations of advanced LIGO's and advanced Virgo's third observational campaign. *Mon. Not. Roy. Astron. Soc.*, 497(4):5518–5539, 2020b. doi: 10.1093/mnras/staa1846.

Akito Araya, Norikatsu Mio, Kimio Tsubono, Koya Suehiro, Souichi Telada, Masatake Ohashi, and Masa-Katsu Fujimoto. Optical mode cleaner with suspended mirrors. *Applied optics*, 36:1446–53, 04 1997. doi: 10.1364/AO.36.001446.

Ubai A Arifov. *Interaction of Atomic Particles with a Solid Surface/Vzaimodeistvie Atomnykh Chastits S Poverkhnost'yu Tverdogo Tela*. Springer, 2013.

JT Armstrong, DJ Hutter, EK Baines, JA Benson, RM Bevilacqua, T Buschmann, JH CLARK III, A Ghasempour, JC Hall, RB Hindsley, et al. The navy precision optical interferometer (npoi): an update. *Journal of Astronomical Instrumentation*, 2(02): 1340002, 2013.

David Arnett. Mass dependence in gravitational collapse of stellar cores. *Canadian Journal of Physics*, 45:1621–1641, January 1967. doi: 10.1139/p67-126.

W. David Arnett, John N. Bahcall, Robert P. Kirshner, and Stanford E. Woosley. Supernova 1987a. *Annual Review of Astronomy and Astrophysics*, 27(1):629–700, 1989. doi: 10.1146/annurev.aa.27.090189.003213. URL https://doi.org/10.1146/annurev.aa.27.090189.003213.

Stefano Ascenzi et al. A luminosity distribution for kilonovae based on short gamma-ray burst afterglows. *Mon. Not. Roy. Astron. Soc.*, 486(1):672–690, 2019. doi: 10.1093/mnras/stz891.

B. Aschenbach, U. Briel, F. Haberl, H. Braeuninger, W. Burkert, A. Oppitz, P. Gondoin, and D. Lumb. Imaging performance of the xmm-newton x-ray telescopes. *Proc. SPIE Int. Soc. Opt. Eng.*, 4012:731, 2000. doi: 10.1117/12.391615.

G. Ashton, E. Burns, T. Dal Canton, T. Dent, H.-B. Eggenstein, A. B. Nielsen, R. Prix, M. Was, and S. J. Zhu. Coincident detection significance in multimessenger astronomy. *The Astrophysical Journal*, 860(1):6, jun 2018. doi: 10.3847/1538-4357/aabfd2. URL https://doi.org/10.3847/1538-4357/aabfd2.

Gregory Ashton and Sebastian Khan. Multiwaveform inference of gravitational waves. *Phys. Rev. D*, 101(6):064037, 2020. doi: 10.1103/PhysRevD.101.064037.

Gregory Ashton et al. BILBY: A user-friendly Bayesian inference library for gravitational-wave astronomy. *Astrophys. J. Suppl.*, 241(2):27, 2019. doi: 10.3847/1538-4365/ab06fc.

W. B. Atwood, A. A. Abdo, M. Ackermann, W. Althouse, B. Anderson, M. Axelsson, L. Baldini, J. Ballet, D. L. Band, G. Barbiellini, J. Bartelt, D. Bastieri, B. M. Baughman, K. Bechtol, D. Bédérède, F. Bellardi, R. Bellazzini, B. Berenji, G. F. Bignami, D. Bisello, E. Bissaldi, R. D. Blandford, E. D. Bloom, J. R. Bogart, E. Bonamente, J. Bonnell, A. W. Borgland, A. Bouvier, J. Bregeon, A. Brez, M. Brigida, P. Bruel, T. H. Burnett, G. Busetto, G. A. Caliandro, R. A. Cameron, P. A. Caraveo, S. Carius, P. Carlson, J. M. Casandjian, E. Cavazzuti, M. Ceccanti, C. Cecchi, E. Charles, A. Chekhtman, C. C. Cheung, J. Chiang, R. Chipaux, A. N. Cillis, S. Ciprini, R. Claus, J. Cohen-Tanugi, S. Condamoor, J. Conrad, R. Corbet, L. Corucci, L. Costamante, S. Cutini, D. S. Davis, D. Decotigny, M. DeKlotz, C. D. Dermer, A. de Angelis, S. W. Digel, E. do Couto e Silva, P. S. Drell, R. Dubois, D. Dumora, Y. Edmonds, D. Fabiani, C. Farnier, C. Favuzzi, D. L. Flath, P. Fleury, W. B. Focke, S. Funk, P. Fusco, F. Gargano, D. Gasparrini, N. Gehrels, F.-X. Gentit, S. Germani, B. Giebels, N. Giglietto, P. Giommi, F. Giordano, T. Glanzman, G. Godfrey, I. A. Grenier, M.-H. Grondin, J. E. Grove, L. Guillemot, S. Guiriec, G. Haller, A. K. Harding, P. A. Hart, E. Hays, S. E. Healey, M. Hirayama, L. Hjalmarsdotter, R. Horn, R. E.

Hughes, G. Jóhannesson, G. Johansson, A. S. Johnson, R. P. Johnson, T. J. Johnson, W. N. Johnson, T. Kamae, H. Katagiri, J. Kataoka, A. Kavelaars, N. Kawai, H. Kelly, M. Kerr, W. Klamra, J. Knödlseder, M. L. Kocian, N. Komin, F. Kuehn, M. Kuss, D. Landriu, L. Latronico, B. Lee, S.-H. Lee, M. Lemoine-Goumard, A. M. Lionetto, F. Longo, F. Loparco, B. Lott, M. N. Lovellette, P. Lubrano, G. M. Madejski, A. Makeev, B. Marangelli, M. M. Massai, M. N. Mazziotta, J. E. McEnery, N. Menon, C. Meurer, P. F. Michelson, M. Minuti, N. Mirizzi, W. Mitthumsiri, T. Mizuno, A. A. Moiseev, C. Monte, M. E. Monzani, E. Moretti, A. Morselli, I. V. Moskalenko, S. Murgia, T. Nakamori, S. Nishino, P. L. Nolan, J. P. Norris, E. Nuss, M. Ohno, T. Ohsugi, N. Omodei, E. Orlando, J. F. Ormes, A. Paccagnella, D. Paneque, J. H. Panetta, D. Parent, M. Pearce, M. Pepe, A. Perazzo, M. Pesce-Rollins, P. Picozza, L. Pieri, M. Pinchera, F. Piron, T. A. Porter, L. Poupard, S. Rainò, R. Rando, E. Rapposelli, M. Razzano, A. Reimer, O. Reimer, T. Reposeur, L. C. Reyes, S. Ritz, L. S. Rochester, A. Y. Rodriguez, R. W. Romani, M. Roth, J. J. Russell, F. Ryde, S. Sabatini, H. F.-W. Sadrozinski, D. Sanchez, A. Sander, L. Sapozhnikov, P. M. Saz Parkinson, J. D. Scargle, T. L. Schalk, G. Scolieri, C. Sgrò, G. H. Share, M. Shaw, T. Shimokawabe, C. Shrader, A. Sierpowska-Bartosik, E. J. Siskind, D. A. Smith, P. D. Smith, G. Spandre, P. Spinelli, J.-L. Starck, T. E. Stephens, M. S. Strickman, A. W. Strong, D. J. Suson, H. Tajima, H. Takahashi, T. Takahashi, T. Tanaka, A. Tenze, S. Tether, J. B. Thayer, J. G. Thayer, D. J. Thompson, L. Tibaldo, O. Tibolla, D. F. Torres, G. Tosti, A. Tramacere, M. Turri, T. L. Usher, N. Vilchez, V. Vitale, P. Wang, K. Watters, B. L. Winer, K. S. Wood, T. Ylinen, and M. Ziegler. THE LARGE AREA TELESCOPE ON THEFERMI GAMMA-RAY SPACE TELESCOPEMISSION. *The Astrophysical Journal*, 697(2):1071–1102, may 2009. doi: 10.1088/0004-637x/697/2/1071. URL `https://doi.org/10.1088/0004-637x/697/2/1071`.

F. Aubin et al. The MBTA pipeline for detecting compact binary coalescences in the third LIGO–Virgo observing run. *Class. Quant. Grav.*, 38(9):095004, 2021. doi: 10.1088/1361-6382/abe913.

F Badaracco and J Harms. Optimization of seismometer arrays for the cancellation of newtonian noise from seismic body waves. *Classical and Quantum Gravity*, 36(14): 145006, 2019.

Francesca Badaracco, Camilla De Rossi, Irene Fiori, Jan Harms, Kouseki Miyo, Federico Paoletti, Taiki Tanaka, Tatsuki Washimi, and Takaaki Yokozawa. The kagra underground environment and lessons for the einstein telescope. *arXiv preprint arXiv:2104.07527*, 2021.

S. Bahaadini, V. Noroozi, N. Rohani, S. Coughlin, M. Zevin, J.R. Smith, V. Kalogera, and A. Katsaggelos. Machine learning for gravity spy: Glitch classification and dataset.

Information Sciences, 444:172–186, 2018. ISSN 0020-0255. doi: https://doi.org/10.1016/j.ins.2018.02.068. URL https://www.sciencedirect.com/science/article/pii/S0020025518301634.

Sebastian Bahamonde, Konstantinos F. Dialektopoulos, Viktor Gakis, and Jackson Levi Said. Reviving Horndeski theory using teleparallel gravity after GW170817. *Phys. Rev. D*, 101(8):084060, 2020. doi: 10.1103/PhysRevD.101.084060.

John G. Baker, Joan Centrella, Dae-Il Choi, Michael Koppitz, and James van Meter. Gravitational wave extraction from an inspiraling configuration of merging black holes. *Phys. Rev. Lett.*, 96:111102, 2006a. doi: 10.1103/PhysRevLett.96.111102.

John G. Baker, Joan Centrella, Dae-Il Choi, Michael Koppitz, and James van Meter. Gravitational-wave extraction from an inspiraling configuration of merging black holes. *Phys. Rev. Lett.*, 96:111102, Mar 2006b. doi: 10.1103/PhysRevLett.96.111102. URL https://link.aps.org/doi/10.1103/PhysRevLett.96.111102.

D. Band, J. Matteson, L. Ford, B. Schaefer, D. Palmer, B. Teegarden, T. Cline, M. Briggs, W. Paciesas, G. Pendleton, G. Fishman, C. Kouveliotou, C. Meegan, R. Wilson, and P. Lestrade. BATSE Observations of Gamma-Ray Burst Spectra. I. Spectral Diversity. *The Astrophysical Journal*, 413:281, August 1993. doi: 10.1086/172995.

Kyle Barbary, Tom Barclay, Rahul Biswas, Matt Craig, Ulrich Feindt, Brian Friesen, Danny Goldstein, Saurabh Jha, Steve Rodney, Caroline Sofiatti, et al. Sncosmo: Python library for supernova cosmology. *Astrophysics Source Code Library*, pages ascl–1611, 2016.

C. Barbieri, O. S. Salafia, A. Perego, M. Colpi, and G. Ghirlanda. Electromagnetic counterparts of black hole-neutron star mergers: dependence on the neutron star properties. *Eur. Phys. J. A*, 56(1):8, 2020. doi: 10.1140/epja/s10050-019-00013-x.

Jennifer Barnes and Daniel Kasen. EFFECT OF a HIGH OPACITY ON THE LIGHT CURVES OF RADIOACTIVELY POWERED TRANSIENTS FROM COMPACT OBJECT MERGERS. *The Astrophysical Journal*, 775(1):18, aug 2013. doi: 10.1088/0004-637x/775/1/18. URL https://doi.org/10.1088/0004-637x/775/1/18.

Jennifer Barnes, Daniel Kasen, Meng-Ru Wu, and Gabriel Martínez-Pinedo. Radioactivity and thermalization in the ejecta of compact object mergers and their impact on kilonova light curves. *Astrophys. J.*, 829(2):110, 2016. doi: 10.3847/0004-637X/829/2/110.

Imre Bartos, Bence Kocsis, Zolt Haiman, and Szabolcs Márka. Rapid and Bright Stellar-mass Binary Black Hole Mergers in Active Galactic Nuclei. *Astrophys. J.*, 835 (2):165, 2017. doi: 10.3847/1538-4357/835/2/165.

A. Bauswein, T. W. Baumgarte, and H.-T. Janka. Prompt merger collapse and the maximum mass of neutron stars. *Phys. Rev. Lett.*, 111:131101, Sep 2013a. doi: 10.1103/PhysRevLett.111.131101. URL https://link.aps.org/doi/10.1103/PhysRevLett.111.131101.

Andreas Bauswein, Stéphane Goriely, and H-T Janka. Systematics of dynamical mass ejection, nucleosynthesis, and radioactively powered electromagnetic signals from neutron-star mergers. *The Astrophysical Journal*, 773(1):78, 2013b.

Andreas Bauswein, Oliver Just, Hans-Thomas Janka, and Nikolaos Stergioulas. Neutron-star radius constraints from GW170817 and future detections. *The Astrophysical Journal*, 850(2):L34, nov 2017. doi: 10.3847/2041-8213/aa9994. URL https://doi.org/10.3847/2041-8213/aa9994.

G Bazin, N Palanque-Delabrouille, J Rich, V Ruhlmann-Kleider, E Aubourg, L Le Guillou, P Astier, C Balland, S Basa, RG Carlberg, et al. The core-collapse rate from the supernova legacy survey. *Astronomy and Astrophysics*, 499(3):653–660, 2009.

G Bazin, V Ruhlmann-Kleider, N Palanque-Delabrouille, J Rich, E Aubourg, P Astier, C Balland, S Basa, RG Carlberg, A Conley, et al. Photometric selection of type ia supernovae in the supernova legacy survey. *Astronomy and Astrophysics*, 534:A43, 2011.

Jacques M. Beckers. Adaptive optics for astronomy: Principles, performance, and applications. *Annual Review of Astronomy and Astrophysics*, 31(1):13–62, 1993. doi: 10.1146/annurev.aa.31.090193.000305. URL https://doi.org/10.1146/annurev.aa.31.090193.000305.

M G Beker, J F J van den Brand, E Hennes, and D S Rabeling. Newtonian noise and ambient ground motion for gravitational wave detectors. *Journal of Physics: Conference Series*, 363:012004, jun 2012. doi: 10.1088/1742-6596/363/1/012004. URL https://doi.org/10.1088/1742-6596/363/1/012004.

Krzysztof Belczynski and Tomasz Bulik. The effect of supernova natal kicks on compact object merger rate. *Astron. Astrophys.*, 346:91, 1999.

E. Bellm. The Zwicky Transient Facility. In P. R. Wozniak, M. J. Graham, A. A. Mahabal, and R. Seaman, editors, *The Third Hot-wiring the Transient Universe Workshop*, pages 27–33, January 2014.

Eric C Bellm, Shrinivas R Kulkarni, Matthew J Graham, Richard Dekany, Roger M Smith, Reed Riddle, Frank J Masci, George Helou, Thomas A Prince, Scott M Adams, et al. The zwicky transient facility: System overview, performance, and first results. *Publications of the Astronomical Society of the Pacific*, 131(995):018002, 2018.

Eric C. Bellm, Shrinivas R. Kulkarni, Tom Barlow, Ulrich Feindt, Matthew J. Graham, Ariel Goobar, Thomas Kupfer, Chow-Choong Ngeow, Peter Nugent, Eran Ofek, Thomas A. Prince, Reed Riddle, Richard Walters, and Quan-Zhi Ye. The zwicky transient facility: Surveys and scheduler. *Publications of the Astronomical Society of the Pacific*, 131(1000):068003, apr 2019. doi: 10.1088/1538-3873/ab0c2a. URL `https://doi.org/10.1088/1538-3873/ab0c2a`.

C. L. Bennett, A. Banday, K. M. Gorski, G. Hinshaw, P. Jackson, P. Keegstra, A. Kogut, George F. Smoot, D. T. Wilkinson, and E. L. Wright. Four year COBE DMR cosmic microwave background observations: Maps and basic results. *Astrophys. J. Lett.*, 464: L1–L4, 1996. doi: 10.1086/310075.

C. L. Bennett et al. The Microwave Anisotropy Probe (MAP) mission. *Astrophys. J.*, 583:1–23, 2003. doi: 10.1086/345346.

Edo Berger. Short-Duration Gamma-Ray Bursts. *Ann. Rev. Astron. Astrophys.*, 52: 43–105, 2014. doi: 10.1146/annurev-astro-081913-035926.

Denis Bernard et al. HARPO: a TPC as a gamma-ray telescope and polarimeter. *Proc. SPIE Int. Soc. Opt. Eng.*, 9144:91441M, 2014. doi: 10.1117/12.2055307.

Maria Grazia Bernardini et al. How to switch on and off a Gamma-ray burst through a magnetar. *Astrophys. J.*, 775:67, 2013. doi: 10.1088/0004-637X/775/1/67.

Christopher P. L. Berry et al. Parameter estimation for binary neutron-star coalescences with realistic noise during the Advanced LIGO era. *Astrophys. J.*, 804(2):114, 2015. doi: 10.1088/0004-637X/804/2/114.

Swetha Bhagwat, Maria Okounkova, Stefan W. Ballmer, Duncan A. Brown, Matthew Giesler, Mark A. Scheel, and Saul A. Teukolsky. On choosing the start time of binary black hole ringdowns. *Phys. Rev. D*, 97(10):104065, 2018. doi: 10.1103/PhysRevD.97.104065.

P. Narayana Bhat, Charles A. Meegan, Andreas von Kienlin, William S. Paciesas, Michael S. Briggs, J. Michael Burgess, Eric Burns, Vandiver Chaplin, William H. Cleveland, Andrew C. Collazzi, Valerie Connaughton, Anne M. Diekmann, Gerard Fitzpatrick, Melissa H. Gibby, Misty M. Giles, Adam M. Goldstein, Jochen Greiner, Peter A. Jenke, R. Marc Kippen, Chryssa Kouveliotou, Bagrat Mailyan, Sheila McBreen,

Veronique Pelassa, Robert D. Preece, Oliver J. Roberts, Linda S. Sparke, Matthew Stanbro, Péter Veres, Colleen A. Wilson-Hodge, Shaolin Xiong, George Younes, Hoi-Fung Yu, and Binbin Zhang. THE THIRD FERMI GBM GAMMA-RAY BURST CATALOG: THE FIRST SIX YEARS. *The Astrophysical Journal Supplement Series*, 223 (2):28, apr 2016a. doi: 10.3847/0067-0049/223/2/28. URL https://doi.org/10.3847/0067-0049/223/2/28.

P. Narayana Bhat et al. The Third Fermi gbm Gamma-ray Burst Catalog: the First six Years. *Astrophys. J. Suppl.*, 223(2):28, 2016b. doi: 10.3847/0067-0049/223/2/28.

Donato Bini, Thibault Damour, and Andrea Geralico. High-order post-newtonian contributions to gravitational self-force effects in black hole spacetimes. In *Innovative Algorithms and Analysis*, pages 25–77. Springer, 2017.

Elisabetta Bissaldi, Andreas von Kienlin, G Lichti, Helmut Steinle, P Narayana Bhat, Michael S Briggs, Gerald J Fishman, Andrew S Hoover, R Marc Kippen, Michael Krumrey, et al. Ground-based calibration and characterization of the fermi gamma-ray burst monitor detectors. *Experimental Astronomy*, 24(1-3):47–88, 2009.

L. Blackburn, M. S. Briggs, J. Camp, N. Christensen, V. Connaughton, P. Jenke, R. A. Remillard, and J. Veitch. HIGH-ENERGY ELECTROMAGNETIC OFFLINE FOLLOW-UP OF LIGO-VIRGO GRAVITATIONAL-WAVE BINARY COALESCENCE CANDIDATE EVENTS. *The Astrophysical Journal Supplement Series*, 217(1):8, mar 2015. doi: 10.1088/0067-0049/217/1/8. URL https://doi.org/10.1088/0067-0049/217/1/8.

Luc Blanchet. Gravitational Radiation from Post-Newtonian Sources and Inspiralling Compact Binaries. *Living Rev. Rel.*, 17:2, 2014. doi: 10.12942/lrr-2014-2.

Luc Blanchet, Thibault Damour, Bala R. Iyer, Clifford M. Will, and Alan G. Wiseman. Gravitational-radiation damping of compact binary systems to second post-newtonian order. *Phys. Rev. Lett.*, 74:3515–3518, May 1995. doi: 10.1103/PhysRevLett.74.3515. URL https://link.aps.org/doi/10.1103/PhysRevLett.74.3515.

Steven Bloemen et al. MeerLICHT and BlackGEM: custom-built telescopes to detect faint optical transients. *Proc. SPIE Int. Soc. Opt. Eng.*, 9906:990664, 2016. doi: 10.1117/12.2232522.

Boella, G., Butler, R. C., Perola, G. C., Piro, L., Scarsi, L., and Bleeker, J. A.M. Bepposax, the wide band mission for x-ray astronomy. *Astron. Astrophys. Suppl. Ser.*, 122(2):299–307, 1997. doi: 10.1051/aas:1997136. URL https://doi.org/10.1051/aas:1997136.

Alejandro Bohé et al. Improved effective-one-body model of spinning, nonprecessing binary black holes for the era of gravitational-wave astrophysics with advanced detectors. *Phys. Rev. D*, 95(4):044028, 2017. doi: 10.1103/PhysRevD.95.044028.

C. T. Bolton. Identification of Cygnus X-1 with HDE 226868. *Nature*, 235(5336): 271–273, February 1972. doi: 10.1038/235271b0.

HE Bond, W Liller, and EJ Mannery. Uu sagittae-eclipsing nucleus of the planetary nebula abell 63. *The Astrophysical Journal*, 223:252, 1978.

KD Borne and Zooniverse Team. The zooniverse: A framework for knowledge discovery from citizen science data. In *AGU Fall Meeting Abstracts*, volume 2011, pages ED23C–0650, 2011.

S. R. Borrello, R. A. Chapman, A. Simmons, J. D. Beck, M. A. Kinch, and C. G. Roberts. HgCdTe Charge-Coupled Detectors (CCD). In William S. Chan, editor, *Advances in Focal Plane Technology*, volume 0217, pages 92 – 99. International Society for Optics and Photonics, SPIE, 1980. doi: 10.1117/12.958480. URL `https://doi.org/10.1117/12.958480`.

William J. Borucki, David Koch, Gibor Basri, Natalie Batalha, Timothy Brown, Douglas Caldwell, John Caldwell, Jørgen Christensen-Dalsgaard, William D. Cochran, Edna DeVore, Edward W. Dunham, Andrea K. Dupree, Thomas N. Gautier, John C. Geary, Ronald Gilliland, Alan Gould, Steve B. Howell, Jon M. Jenkins, Yoji Kondo, David W. Latham, Geoffrey W. Marcy, Søren Meibom, Hans Kjeldsen, Jack J. Lissauer, David G. Monet, David Morrison, Dimitar Sasselov, Jill Tarter, Alan Boss, Don Brownlee, Toby Owen, Derek Buzasi, David Charbonneau, Laurance Doyle, Jonathan Fortney, Eric B. Ford, Matthew J. Holman, Sara Seager, Jason H. Steffen, William F. Welsh, Jason Rowe, Howard Anderson, Lars Buchhave, David Ciardi, Lucianne Walkowicz, William Sherry, Elliott Horch, Howard Isaacson, Mark E. Everett, Debra Fischer, Guillermo Torres, John Asher Johnson, Michael Endl, Phillip MacQueen, Stephen T. Bryson, Jessie Dotson, Michael Haas, Jeffrey Kolodziejczak, Jeffrey Van Cleve, Hema Chandrasekaran, Joseph D. Twicken, Elisa V. Quintana, Bruce D. Clarke, Christopher Allen, Jie Li, Haley Wu, Peter Tenenbaum, Ekaterina Verner, Frederick Bruhweiler, Jason Barnes, and Andrej Prsa. Kepler planet-detection mission: Introduction and first results. *Science*, 327(5968):977–980, 2010. ISSN 0036-8075. doi: 10.1126/science.1185402. URL `https://science.sciencemag.org/content/327/5968/977`.

Luke Bovard, Dirk Martin, Federico Guercilena, Almudena Arcones, Luciano Rezzolla, and Oleg Korobkin. r-process nucleosynthesis from matter ejected in binary neutron star mergers. *Phys. Rev. D*, 96(12):124005, 2017. doi: 10.1103/PhysRevD.96.124005.

S. M. Bradbury et al. The very energetic radiation imaging telescope array system (veritas). *AIP Conf. Proc.*, 510(1):637–641, 2000. doi: 10.1063/1.1303279.

Wyatt Brege, Matthew D. Duez, Francois Foucart, M. Brett Deaton, Jesus Caro, Daniel A. Hemberger, Lawrence E. Kidder, Evan O'Connor, Harald P. Pfeiffer, and Mark A. Scheel. Black hole-neutron star mergers using a survey of finite-temperature equations of state. *Phys. Rev. D*, 98(6):063009, 2018. doi: 10.1103/PhysRevD.98.063009.

Leo Breiman. Random forests. *Machine learning*, 45(1):5–32, 2001.

Constantin Brif. Notes on anelastic effects and thermal noise in suspensions of test masses in interferometric gravitational wave detectors. 9 1999.

Omer Bromberg, Ehud Nakar, Tsvi Piran, and Re'em Sari. SHORT VERSUS LONG AND COLLAPSARS VERSUS NON-COLLAPSARS: A QUANTITATIVE CLASSIFICATION OF GAMMA-RAY BURSTS. *The Astrophysical Journal*, 764(2):179, feb 2013. doi: 10.1088/0004-637x/764/2/179. URL https://doi.org/10.1088/0004-637x/764/2/179.

Duncan A. Brown, Ian Harry, Andrew Lundgren, and Alexander H. Nitz. Detecting binary neutron star systems with spin in advanced gravitational-wave detectors. *Phys. Rev. D*, 86:084017, Oct 2012. doi: 10.1103/PhysRevD.86.084017. URL https://link.aps.org/doi/10.1103/PhysRevD.86.084017.

Robert L Brown, Wolfgang Wild, and Charles Cunningham. Alma – the atacama large millimeter array. *Advances in Space Research*, 34(3):555–559, 2004. ISSN 0273-1177. doi: https://doi.org/10.1016/j.asr.2003.03.028. URL https://www.sciencedirect.com/science/article/pii/S0273117703011979. Astronomy at IR/Submm and the Microwave Background.

Stephen W Bruenn. Stellar core collapse-numerical model and infall epoch. *The Astrophysical Journal Supplement Series*, 58:771–841, 1985.

Bernd Brügmann, José A. González, Mark D. Hannam, Sascha Husa, and Ulrich Sperhake. Numerical simulations of compact binary systems. In Siegfried Wagner, Matthias Steinmetz, Arndt Bode, and Matthias Brehm, editors, *High Performance Computing in Science and Engineering, Garching/Munich 2007*, pages 3–18, Berlin, Heidelberg, 2009. Springer Berlin Heidelberg. ISBN 978-3-540-69182-2.

Hajo Bruining. *Physics and Applications of Secondary Electron Emission: Pergamon Science Series: Electronics and Waves—a Series of Monographs*. Elsevier, 2016.

M. Bulla et al. Predicting polarization signatures for double-detonation and delayed-detonation models of Type Ia supernovae. *Mon. Not. Roy. Astron. Soc.*, 462(1):1039–1056, 2016. doi: 10.1093/mnras/stw1733.

Mattia Bulla. POSSIS: predicting spectra, light curves and polarization for multi-dimensional models of supernovae and kilonovae. *Mon. Not. Roy. Astron. Soc.*, 489 (4):5037–5045, 2019. doi: 10.1093/mnras/stz2495.

A. Buonanno and T. Damour. Effective one-body approach to general relativistic two-body dynamics. *Phys. Rev. D*, 59:084006, 1999a. doi: 10.1103/PhysRevD.59.084006.

A. Buonanno and T. Damour. Effective one-body approach to general relativistic two-body dynamics. *Phys. Rev. D*, 59:084006, Mar 1999b. doi: 10.1103/PhysRevD.59.084006. URL https://link.aps.org/doi/10.1103/PhysRevD.59.084006.

Alessandra Buonanno and Yan-bei Chen. Quantum noise in second generation, signal recycled laser interferometric gravitational wave detectors. *Phys. Rev. D*, 64:042006, 2001. doi: 10.1103/PhysRevD.64.042006.

Alessandra Buonanno and Thibault Damour. Transition from inspiral to plunge in binary black hole coalescences. *Phys. Rev. D*, 62:064015, 2000. doi: 10.1103/PhysRevD.62.064015.

Marta Burgay et al. An Increased estimate of the merger rate of double neutron stars from observations of a highly relativistic system. *Nature*, 426:531–533, 2003. doi: 10.1038/nature02124.

D. Burlon, G. Ghirlanda, G. Ghisellini, D. Lazzati, L. Nava, M. Nardini, and A. Celotti. Precursors in Swift Gamma Ray Bursts with redshift. *Astrophys. J. Lett.*, 685:L19, 2008. doi: 10.1086/592350.

E. Burns et al. A Fermi Gamma-ray Burst Monitor Search for Electromagnetic Signals Coincident with Gravitational-Wave Candidates in Advanced LIGO's First Observing Run. *Astrophys. J.*, 871(1):90, 2019. doi: 10.3847/1538-4357/aaf726.

Eric Burns. Neutron Star Mergers and How to Study Them. *Living Rev. Rel.*, 23(1):4, 2020. doi: 10.1007/s41114-020-00028-7.

Charles Burns Boyle. Mass transfer and accretion in close binaries: A review. *Vistas in Astronomy*, 27:149–169, 1984. ISSN 0083-6656. doi: https://doi.org/10.1016/0083-6656(84)90007-2. URL https://www.sciencedirect.com/science/article/pii/0083665684900072.

Adam Burrows, Sanjay Reddy, and Todd A. Thompson. Neutrino opacities in nuclear matter. *Nucl. Phys. A*, 777:356–394, 2006. doi: 10.1016/j.nuclphysa.2004.06.012.

Miriam Cabero et al. Blip glitches in Advanced LIGO data. *Class. Quant. Grav.*, 36 (15):15, 2019. doi: 10.1088/1361-6382/ab2e14.

T. A. Callister, J. B. Kanner, T. J. Massinger, S. Dhurandhar, and A. J. Weinstein. Observing Gravitational Waves with a Single Detector. *Class. Quant. Grav.*, 34(15): 155007, 2017. doi: 10.1088/1361-6382/aa7a76.

Manuela Campanelli, C. O. Lousto, P. Marronetti, and Y. Zlochower. Accurate evolutions of orbiting black-hole binaries without excision. *Phys. Rev. Lett.*, 96:111101, 2006a. doi: 10.1103/PhysRevLett.96.111101.

Manuela Campanelli, C. O. Lousto, and Y. Zlochower. Spinning-black-hole binaries: The orbital hang up. *Phys. Rev. D*, 74:041501, 2006b. doi: 10.1103/PhysRevD.74.041501.

C. G. Campbell. Tidal effects in twin-degenerate binaries. *Monthly Notices of the Royal Astronomical Society*, 207(3):433–443, 04 1984. ISSN 0035-8711. doi: 10.1093/mnras/207.3.433. URL `https://doi.org/10.1093/mnras/207.3.433`.

B. Canuel, R. Day, E. Genin, J. Marque, F. Nocera, and F. Paoletti. High Power Input Optics For Advanced VIRGO. In *46th Rencontres de Moriond on Gravitational Waves and Experimental Gravity*, Paris, France, 2011. Moriond.

Collin D. Capano, Ingo Tews, Stephanie M. Brown, Ben Margalit, Soumi De, Sumit Kumar, Duncan A. Brown, Badri Krishnan, and Sanjay Reddy. Stringent constraints on neutron-star radii from multimessenger observations and nuclear theory. *Nature Astron.*, 4(6):625–632, 2020. doi: 10.1038/s41550-020-1014-6.

B. J. Carrigan and Jonathan I. Katz. Radiation transfer in gamma-ray bursts. *Astrophys. J.*, 399:100–107, 1992. doi: 10.1086/171906.

B. Carter. Axisymmetric black hole has only two degrees of freedom. *Phys. Rev. Lett.*, 26:331–333, Feb 1971. doi: 10.1103/PhysRevLett.26.331. URL `https://link.aps.org/doi/10.1103/PhysRevLett.26.331`.

Castro-Tirado, A. J., Møller, P., García-Segura, G., Gorosabel, J., Pérez, E., de Ugarte Postigo, A., Solano, E., Barrado, D., Klose, S., Kann, D. A., Castro Cerón, J. M., Kouveliotou, C., Fynbo, J. P. U., Hjorth, J., Pedersen, H., Pian, E., Rol, E., Palazzi, E., Masetti, N., Tanvir, N. R., Vreeswijk, P. M., Andersen, M. I., Fruchter, A. S., Greiner, J., Wijers, R. A. M. J., and van den Heuvel, E. P. J. Grb 021004: Tomography of a

gamma-ray burst progenitor and its host galaxy*. *AandA*, 517:A61, 2010. doi: 10.1051/0004-6361/200913966. URL https://doi.org/10.1051/0004-6361/200913966.

Benoit Cerutti, Gregory R. Werner, Dmitri A. Uzdensky, and Mitchell C. Begelman. Gamma-ray flares in the Crab Nebula: A case of relativistic reconnection? *Phys. Plasmas*, 21:056501, 2014. doi: 10.1063/1.4872024.

E. Chabanat, P. Bonche, P. Haensel, J. Meyer, and R. Schaeffer. A skyrme parametrization from subnuclear to neutron star densities. *Nuclear Physics A*, 627 (4):710–746, 1997. ISSN 0375-9474. doi: https://doi.org/10.1016/S0375-9474(97)00596-4. URL https://www.sciencedirect.com/science/article/pii/S0375947497005964.

E. Chabanat, P. Bonche, P. Haensel, J. Meyer, and R. Schaeffer. A skyrme parametrization from subnuclear to neutron star densities part ii. nuclei far from stabilities. *Nuclear Physics A*, 635(1):231–256, 1998. ISSN 0375-9474. doi: https://doi.org/10.1016/S0375-9474(98)00180-8. URL https://www.sciencedirect.com/science/article/pii/S0375947498001808.

E. J. Chaisson and R. Villard. The science mission of the Hubble Space Telescope. *Vistas in Astronomy*, 33(2):105–141, January 1990. doi: 10.1016/0083-6656(90)90018-4.

S. Chandrasekhar and Steven L. Detweiler. The quasi-normal modes of the Schwarzschild black hole. *Proc. Roy. Soc. Lond. A*, 344:441–452, 1975. doi: 10.1098/rspa.1975.0112.

S Chatterji, L Blackburn, G Martin, and E Katsavounidis. Multiresolution techniques for the detection of gravitational-wave bursts. *Classical and Quantum Gravity*, 21(20): S1809–S1818, sep 2004. doi: 10.1088/0264-9381/21/20/024. URL https://doi.org/10.1088/0264-9381/21/20/024.

Wen-Cong Chen and Philipp Podsiadlowski. Evolution of intermediate-mass X-ray binaries driven by magnetic braking of Ap/Bp stars: I. ultracompact X-ray binaries. *Astrophys. J.*, 830(2):131, 2016. doi: 10.3847/0004-637X/830/2/131.

KP CHENG, YC KIM, and JWM PARKER. Sn 1991bg: A type ia supernova with a difference. *THE ASTRONOMICAL JOURNAL*, 105(1), 1993.

P.A. Cherenkov. Visible Emission of Clean Liquids by Action of γ Radiation. *Dokl. Akad. Nauk SSSR 2*, 451, 1934.

Sah Chih-Tang. Evolution of the mos transistor-from conception to vlsi. *Proceedings of the IEEE*, 76(10):1280–1326, 1988. doi: 10.1109/5.16328.

Lise Christensen, J. Hjorth, and J. Gorosabel. UV star-formation rates of GRB host galaxies. *Astron. Astrophys.*, 425:913–926, 2004. doi: 10.1051/0004-6361:20040361.

Stirling A. Colgate and Richard H. White. The Hydrodynamic Behavior of Supernovae Explosions. *ApJ*, 143:626, March 1966. doi: 10.1086/148549.

Gaia Collaboration et al. The gaia mission. *arXiv preprint arXiv:1609.04153*, 2016.

Planck Collaboration et al. The scientific programme of planck. *arXiv preprint astro-ph/0604069*, 2006.

Arthur H. Compton. A quantum theory of the scattering of x-rays by light elements. *Phys. Rev.*, 21:483–502, May 1923. doi: 10.1103/PhysRev.21.483. URL `https://link.aps.org/doi/10.1103/PhysRev.21.483`.

V. Connaughton et al. Localization of Gamma-Ray Bursts using the Fermi Gamma-Ray Burst Monitor. *Astrophys. J. Suppl.*, 216(2):32, 2015. doi: 10.1088/0067-0049/216/2/32.

A. J. Connolly, John Peterson, J. Garrett Jernigan, Robert Abel, Justin Bankert, Chihway Chang, Charles F. Claver, Robert Gibson, David K. Gilmore, Emily Grace, R. Lynne Jones, Zeljko Ivezic, James Jee, Mario Juric, Steven M. Kahn, Victor L. Krabbendam, Simon Krughoff, Suzanne Lorenz, James Pizagno, Andrew Rasmussen, Nathan Todd, J. Anthony Tyson, and Mallory Young. Simulating the LSST system. In George Z. Angeli and Philippe Dierickx, editors, *Modeling, Systems Engineering, and Project Management for Astronomy IV*, volume 7738 of *Society of Photo-Optical Instrumentation Engineers (SPIE) Conference Series*, page 77381O, July 2010. doi: 10.1117/12.857819.

J. M. Cordes and Ira Wasserman. Supergiant pulses from extragalactic neutron stars. *Monthly Notices of the Royal Astronomical Society*, 457(1):232–257, 01 2016. ISSN 0035-8711. doi: 10.1093/mnras/stv2948. URL `https://doi.org/10.1093/mnras/stv2948`.

Neil J. Cornish and Tyson B. Littenberg. BayesWave: Bayesian Inference for Gravitational Wave Bursts and Instrument Glitches. *Class. Quant. Grav.*, 32(13):135012, 2015. doi: 10.1088/0264-9381/32/13/135012.

Corinna Cortes and Vladimir Vapnik. Support-vector networks. *Machine learning*, 20 (3):273–297, 1995.

Juan Cortina, Florian Goebel, and Thomas Schweizer. Technical performance of the magic telescopes. *arXiv preprint arXiv:0907.1211*, 2009.

E. Costa et al. Discovery of an X-ray afterglow associated with the gamma-ray burst of 28 February 1997. *Nature*, 387:783–785, 1997. doi: 10.1038/42885.

Michael W Coughlin, Tim Dietrich, Zoheyr Doctor, Daniel Kasen, Scott Coughlin, Anders Jerkstrand, Giorgos Leloudas, Owen McBrien, Brian D Metzger, Richard O'Shaughnessy, and Stephen J Smartt. Constraints on the neutron star equation of state from AT2017gfo using radiative transfer simulations. *Monthly Notices of the Royal Astronomical Society*, 480(3):3871–3878, 08 2018a. ISSN 0035-8711. doi: 10.1093/mnras/sty2174. URL https://doi.org/10.1093/mnras/sty2174.

Michael W Coughlin, Duo Tao, Man Leong Chan, Deep Chatterjee, Nelson Christensen, Shaon Ghosh, Giuseppe Greco, Yiming Hu, Shasvath Kapadia, Javed Rana, Om Sharan Salafia, and Christopher W Stubbs. Optimizing searches for electromagnetic counterparts of gravitational wave triggers. *Monthly Notices of the Royal Astronomical Society*, 478(1):692–702, 04 2018b. ISSN 0035-8711. doi: 10.1093/mnras/sty1066. URL https://doi.org/10.1093/mnras/sty1066.

Michael W Coughlin, Tim Dietrich, Ben Margalit, and Brian D Metzger. Multimessenger Bayesian parameter inference of a binary neutron star merger. *Monthly Notices of the Royal Astronomical Society: Letters*, 489(1):L91–L96, 08 2019a. ISSN 1745-3925. doi: 10.1093/mnrasl/slz133. URL https://doi.org/10.1093/mnrasl/slz133.

Michael W. Coughlin, Sarah Antier, Tim Dietrich, Ryan J. Foley, Jack Heinzel, Mattia Bulla, Nelson Christensen, David A. Coulter, Lina Issa, and Nandita Khetan. Measuring the Hubble Constant with a sample of kilonovae. *Nature Commun.*, 11(1):4129, 2020a. doi: 10.1038/s41467-020-17998-5.

Michael W. Coughlin, Tim Dietrich, Jack Heinzel, Nandita Khetan, Sarah Antier, Mattia Bulla, Nelson Christensen, David A. Coulter, and Ryan J. Foley. Standardizing kilonovae and their use as standard candles to measure the Hubble constant. *Phys. Rev. Res.*, 2(2):022006, 2020b. doi: 10.1103/PhysRevResearch.2.022006.

Michael W. Coughlin et al. Constraints on the neutron star equation of state from AT2017gfo using radiative transfer simulations. *Mon. Not. Roy. Astron. Soc.*, 480(3): 3871–3878, 2018c. doi: 10.1093/mnras/sty2174.

Michael W. Coughlin et al. GROWTH on S190425z: Searching thousands of square degrees to identify an optical or infrared counterpart to a binary neutron star merger with the Zwicky Transient Facility and Palomar Gattini IR. *Astrophys. J. Lett.*, 885(1): L19, 2019b. doi: 10.3847/2041-8213/ab4ad8.

D. A. Coulter, R. J. Foley, C. D. Kilpatrick, M. R. Drout, A. L. Piro, B. J. Shappee, M. R. Siebert, J. D. Simon, N. Ulloa, D. Kasen, B. F. Madore, A. Murguia-Berthier, Y.-C. Pan, J. X. Prochaska, E. Ramirez-Ruiz, A. Rest, and C. Rojas-Bravo. Swope supernova survey 2017a (sss17a), the optical counterpart to a gravitational wave source. *Science*, 358(6370):1556–1558, 2017. ISSN 0036-8075. doi: 10.1126/science.aap9811. URL https://science.sciencemag.org/content/358/6370/1556.

D. A. Coulter, C. D. Kilpatrick, M. R. Siebert, R. J. Foley, B. J. Shappee, M. R. Drout, J. S. Simon, A. L. Piro, A. Rest, and One-Meter Two-Hemisphere (1M2H) Collaboration. LIGO/Virgo G298048: Potential optical counterpart discovered by Swope telescope. *GRB Coordinates Network*, 21529:1, August 2017.

C. Cuesta et al. Slow scintillation time constants in NaI(Tl) for different interacting particles. *Opt. Mater.*, 36:316, 2013. doi: 10.1016/j.optmat.2013.09.015.

F. Daigne. *GRB PROMPT EMISSION AND THE PHYSICS OF ULTRA-RELATIVISTIC OUTFLOWS*, pages 185–192. EDP Sciences, 2021. doi: doi:10.1051/978-2-7598-1002-4-030. URL https://doi.org/10.1051/978-2-7598-1002-4-030.

Tito Dal Canton and Ian W. Harry. Designing a template bank to observe compact binary coalescences in Advanced LIGO's second observing run. 5 2017.

Tito Dal Canton et al. Implementing a search for aligned-spin neutron star-black hole systems with advanced ground based gravitational wave detectors. *Phys. Rev. D*, 90(8): 082004, 2014. doi: 10.1103/PhysRevD.90.082004.

Thibault Damour and Alessandro Nagar. The Effective One Body description of the Two-Body problem. *Fundam. Theor. Phys.*, 162:211–252, 2011. doi: 10.1007/978-90-481-3015-3_7.

Thibault Damour, Bala R. Iyer, and B. S. Sathyaprakash. A Comparison of search templates for gravitational waves from binary inspiral. *Phys. Rev. D*, 63:044023, 2001. doi: 10.1103/PhysRevD.63.044023. [Erratum: Phys.Rev.D 72, 029902 (2005)].

Thibault Damour, Alessandro Nagar, and Loïc Villain. Measurability of the tidal polarizability of neutron stars in late-inspiral gravitational-wave signals. *Phys. Rev. D*, 85: 123007, Jun 2012. doi: 10.1103/PhysRevD.85.123007. URL https://link.aps.org/doi/10.1103/PhysRevD.85.123007.

Siva Darbha and Daniel Kasen. Inclination Dependence of Kilonova Light Curves from Globally Aspherical Geometries. 2 2020. doi: 10.3847/1538-4357/ab9a34.

D´Avanzo, P., Campana, S., Salafia, O. S., Ghirlanda, G., Ghisellini, G., Melandri, A., Bernardini, M. G., Branchesi, M., Chassande-Mottin, E., Covino, S., D´Elia, V., Nava, L., Salvaterra, R., Tagliaferri, G., and Vergani, S. D. The evolution of the x-ray afterglow emission of gw 170817/ grb 170817a in xmm-newton observations. *AandA*, 613:L1, 2018. doi: 10.1051/0004-6361/201832664. URL https://doi.org/10.1051/0004-6361/201832664.

M. B. Davies, W. Benz, T. Piran, and F. K. Thielemann. Merging neutron stars. 1. Initial results for coalescence of noncorotating systems. *Astrophys. J.*, 431:742, 1994. doi: 10.1086/174525.

PJ Davis, U Kolb, and C Knigge. Is the common envelope ejection efficiency a function of the binary parameters? *Monthly Notices of the Royal Astronomical Society*, 419(1): 287–303, 2012.

E. J. Daw, J. A. Giaime, D. Lormand, M. Lubinski, and J. Zweizig. Long term study of the seismic environment at LIGO. *Class. Quant. Grav.*, 21:2255–2273, 2004. doi: 10.1088/0264-9381/21/9/003.

de Mink, S. E., Cantiello, M., Langer, N., Pols, O. R., Brott, I., and Yoon, S.-Ch. Rotational mixing in massive binaries - detached short-period systems. *AandA*, 497(1): 243–253, 2009. doi: 10.1051/0004-6361/200811439. URL https://doi.org/10.1051/0004-6361/200811439.

A de Ugarte Postigo, JPU Fynbo, CC Thöne, L Christensen, J Gorosabel, B Milvang-Jensen, S Schulze, P Jakobsson, K Wiersema, R Sánchez-Ramírez, et al. The distribution of equivalent widths in long grb afterglow spectra. *Astronomy and Astrophysics*, 548:A11, 2012.

Walter Del Pozzo, Tjonnie G. F. Li, Michalis Agathos, Chris Van Den Broeck, and Salvatore Vitale. Demonstrating the feasibility of probing the neutron-star equation of state with second-generation gravitational-wave detectors. *Phys. Rev. Lett.*, 111: 071101, Aug 2013. doi: 10.1103/PhysRevLett.111.071101. URL https://link.aps.org/doi/10.1103/PhysRevLett.111.071101.

L. Dessart, C. D. Ott, A. Burrows, S. Rosswog, and E. Livne. Neutrino signatures and the neutrino-driven wind in Binary Neutron Star Mergers. *Astrophys. J.*, 690:1681, 2009. doi: 10.1088/0004-637X/690/2/1681.

Tim Dietrich and Maximiliano Ujevic. Modeling dynamical ejecta from binary neutron star mergers and implications for electromagnetic counterparts. *Classical and Quantum Gravity*, 34(10):105014, apr 2017. doi: 10.1088/1361-6382/aa6bb0. URL https://doi.org/10.1088/1361-6382/aa6bb0.

Tim Dietrich, Maximiliano Ujevic, Wolfgang Tichy, Sebastiano Bernuzzi, and Bernd Brügmann. Gravitational waves and mass ejecta from binary neutron star mergers: Effect of the mass ratio. *Phys. Rev. D*, 95:024029, Jan 2017. doi: 10.1103/PhysRevD.95.024029. URL https://link.aps.org/doi/10.1103/PhysRevD.95.024029.

Tim Dietrich, Anuradha Samajdar, Sebastian Khan, Nathan K. Johnson-McDaniel, Reetika Dudi, and Wolfgang Tichy. Improving the NRTidal model for binary neutron star systems. *Phys. Rev. D*, 100(4):044003, 2019. doi: 10.1103/PhysRevD.100.044003.

Tim Dietrich, Michael W. Coughlin, Peter T. H. Pang, Mattia Bulla, Jack Heinzel, Lina Issa, Ingo Tews, and Sarah Antier. Multimessenger constraints on the neutron-star equation of state and the Hubble constant. *Science*, 370(6523):1450–1453, 2020. doi: 10.1126/science.abb4317.

F. Fana Dirirsa, S. Razzaque, F. Piron, M. Arimoto, M. Axelsson, D. Kocevski, F. Longo, M. Ohno, and S. Zhu. Spectral analysis of Fermi-LAT gamma-ray bursts with known redshift and their potential use as cosmological standard candles. *Astrophys. J.*, 887:13, 2019. doi: 10.3847/1538-4357/ab4e11.

Richard Dodson, H. Hirabayashi, P. G. Edwards, K. Wiik, E. B. Fomalont, J. E. J. Lovell, G. A. Moellenbrock, and W. K. Scott. The VSOP 5-GHz continuum survey, recent results. In *Space Science Symposium (ISAS 2004)*, 3 2004.

F. Douchin and P. Haensel. A unified equation of state of dense matter and neutron star structure. *Astron. Astrophys.*, 380:151, 2001. doi: 10.1051/0004-6361:20011402.

M. R. Drout, A. L. Piro, B. J. Shappee, C. D. Kilpatrick, J. D. Simon, C. Contreras, D. A. Coulter, R. J. Foley, M. R. Siebert, N. Morrell, K. Boutsia, F. Di Mille, T. W. S. Holoien, D. Kasen, J. A. Kollmeier, B. F. Madore, A. J. Monson, A. Murguia-Berthier, Y. C. Pan, J. X. Prochaska, E. Ramirez-Ruiz, A. Rest, C. Adams, K. Alatalo, E. Bañados, J. Baughman, T. C. Beers, R. A. Bernstein, T. Bitsakis, A. Campillay, T. T. Hansen, C. R. Higgs, A. P. Ji, G. Maravelias, J. L. Marshall, C. Moni Bidin, J. L. Prieto, K. C. Rasmussen, C. Rojas-Bravo, A. L. Strom, N. Ulloa, J. Vargas-González, Z. Wan, and D. D. Whitten. Light curves of the neutron star merger GW170817/SSS17a: Implications for r-process nucleosynthesis. *Science*, 358(6370):1570–1574, December 2017. doi: 10.1126/science.aaq0049.

Guillaume Dubus, Benoıt Cerutti, and Gilles Henri. Relativistic doppler-boosted emission in gamma-ray binaries. *Astronomy and Astrophysics*, 516:A18, 2010.

J-G Ducoin, D Corre, N Leroy, and E Le Floch. Optimizing gravitational waves follow-up using galaxies stellar mass. *Monthly Notices of the Royal Astronomical Society*,

492(4):4768–4779, 01 2020. ISSN 0035-8711. doi: 10.1093/mnras/staa114. URL https://doi.org/10.1093/mnras/staa114.

P. P. Eggleton. Approximations to the radii of Roche lobes. *Astrophys. J.*, 268:368, 1983. doi: 10.1086/160960.

David Eichler, Mario Livio, Tsvi Piran, and David N. Schramm. Nucleosynthesis, neutrino bursts and γ-rays from coalescing neutron stars. *Nature*, 340(6229):126–128, July 1989. doi: 10.1038/340126a0.

A. Einstein. Über einen die erzeugung und verwandlung des lichtes betreffenden heuristischen gesichtspunkt. *Annalen der Physik*, 322(6):132–148, 1905. doi: https://doi.org/10.1002/andp.19053220607. URL https://onlinelibrary.wiley.com/doi/abs/10.1002/andp.19053220607.

Albert Einstein. Näherungsweise Integration der Feldgleichungen der Gravitation. *Sitzungsberichte der Königlich Preußischen Akademie der Wissenschaften (Berlin*, pages 688–696, January 1916.

Albert Einstein. Über Gravitationswellen. *Sitzungsberichte der Königlich Preußischen Akademie der Wissenschaften (Berlin*, pages 154–167, January 1918.

Julius Elster and Hans Geitel. Ueber die entladung negativ electrischer körper durch das sonnen- und tageslicht. *Annalen der Physik*, 274(12):497–514, 1889. doi: https://doi.org/10.1002/andp.18892741202. URL https://onlinelibrary.wiley.com/doi/abs/10.1002/andp.18892741202.

Reed Essick and Philippe Landry. Discriminating between Neutron Stars and Black Holes with Imperfect Knowledge of the Maximum Neutron Star Mass. *Astrophys. J.*, 904(1):80, 2020. doi: 10.3847/1538-4357/abbd3b.

Reed Essick, Salvatore Vitale, Erik Katsavounidis, Gabriele Vedovato, and Sergey Klimenko. Localization of short duration gravitational-wave transients with the early advanced LIGO and Virgo detectors. *Astrophys. J.*, 800(2):81, 2015. doi: 10.1088/0004-637X/800/2/81.

Reed Essick, Ingo Tews, Philippe Landry, Sanjay Reddy, and Daniel E. Holz. Direct astrophysical tests of chiral effective field theory at supranuclear densities. *Phys. Rev. C*, 102:055803, Nov 2020. doi: 10.1103/PhysRevC.102.055803. URL https://link.aps.org/doi/10.1103/PhysRevC.102.055803.

Zachariah B. Etienne, Yuk Tung Liu, Stuart L. Shapiro, and Thomas W. Baumgarte. General relativistic simulations of black-hole–neutron-star mergers: Effects of black-

hole spin. *Phys. Rev. D*, 79:044024, Feb 2009. doi: 10.1103/PhysRevD.79.044024. URL https://link.aps.org/doi/10.1103/PhysRevD.79.044024.

Event Horizon Telescope Collaboration, Kazunori Akiyama, Antxon Alberdi, Walter Alef, Keiichi Asada, Rebecca Azulay, Anne-Kathrin Baczko, David Ball, Mislav Baloković, John Barrett, Dan Bintley, Lindy Blackburn, Wilfred Boland, Katherine L. Bouman, Geoffrey C. Bower, Michael Bremer, Christiaan D. Brinkerink, Roger Brissenden, Silke Britzen, Avery E. Broderick, Dominique Broguiere, Thomas Bronzwaer, Do-Young Byun, John E. Carlstrom, Andrew Chael, Chi-kwan Chan, Shami Chatterjee, Koushik Chatterjee, Ming-Tang Chen, Yongjun Chen, Ilje Cho, Pierre Christian, John E. Conway, James M. Cordes, Geoffrey B. Crew, Yuzhu Cui, Jordy Davelaar, Mariafelicia De Laurentis, Roger Deane, Jessica Dempsey, Gregory Desvignes, Jason Dexter, Sheperd S. Doeleman, Ralph P. Eatough, Heino Falcke, Vincent L. Fish, Ed Fomalont, Raquel Fraga-Encinas, William T. Freeman, Per Friberg, Christian M. Fromm, José L. Gómez, Peter Galison, Charles F. Gammie, Roberto García, Olivier Gentaz, Boris Georgiev, Ciriaco Goddi, Roman Gold, Minfeng Gu, Mark Gurwell, Kazuhiro Hada, Michael H. Hecht, Ronald Hesper, Luis C. Ho, Paul Ho, Mareki Honma, Chih-Wei L. Huang, Lei Huang, David H. Hughes, Shiro Ikeda, Makoto Inoue, Sara Issaoun, David J. James, Buell T. Jannuzi, Michael Janssen, Britton Jeter, Wu Jiang, Michael D. Johnson, Svetlana Jorstad, Taehyun Jung, Mansour Karami, Ramesh Karuppusamy, Tomohisa Kawashima, Garrett K. Keating, Mark Kettenis, Jae-Young Kim, Junhan Kim, Jongsoo Kim, Motoki Kino, Jun Yi Koay, Patrick M. Koch, Shoko Koyama, Michael Kramer, Carsten Kramer, Thomas P. Krichbaum, Cheng-Yu Kuo, Tod R. Lauer, Sang-Sung Lee, Yan-Rong Li, Zhiyuan Li, Michael Lindqvist, Kuo Liu, Elisabetta Liuzzo, Wen-Ping Lo, Andrei P. Lobanov, Laurent Loinard, Colin Lonsdale, Ru-Sen Lu, Nicholas R. MacDonald, Jirong Mao, Sera Markoff, Daniel P. Marrone, Alan P. Marscher, Iván Martí-Vidal, Satoki Matsushita, Lynn D. Matthews, Lia Medeiros, Karl M. Menten, Yosuke Mizuno, Izumi Mizuno, James M. Moran, Kotaro Moriyama, Monika Moscibrodzka, Cornelia Müller, Hiroshi Nagai, Neil M. Nagar, Masanori Nakamura, Ramesh Narayan, Gopal Narayanan, Iniyan Natarajan, Roberto Neri, Chunchong Ni, Aristeidis Noutsos, Hiroki Okino, Héctor Olivares, Gisela N. Ortiz-León, Tomoaki Oyama, Feryal Özel, Daniel C. M. Palumbo, Nimesh Patel, Ue-Li Pen, Dominic W. Pesce, Vincent Piétu, Richard Plambeck, Aleksandar PopStefanija, Oliver Porth, Ben Prather, Jorge A. Preciado-López, Dimitrios Psaltis, Hung-Yi Pu, Venkatessh Ramakrishnan, Ramprasad Rao, Mark G. Rawlings, Alexander W. Raymond, Luciano Rezzolla, Bart Ripperda, Freek Roelofs, Alan Rogers, Eduardo Ros, Mel Rose, Arash Roshanineshat, Helge Rottmann, Alan L. Roy, Chet Ruszczyk, Benjamin R. Ryan, Kazi L. J. Rygl, Salvador Sánchez, David Sánchez-Arguelles, Mahito Sasada, Tuomas Savolainen, F. Peter Schloerb, Karl-Friedrich Schuster, Lijing Shao,

Zhiqiang Shen, Des Small, Bong Won Sohn, Jason SooHoo, Fumie Tazaki, Paul Tiede, Remo P. J. Tilanus, Michael Titus, Kenji Toma, Pablo Torne, Tyler Trent, Sascha Trippe, Shuichiro Tsuda, Ilse van Bemmel, Huib Jan van Langevelde, Daniel R. van Rossum, Jan Wagner, John Wardle, Jonathan Weintroub, Norbert Wex, Robert Wharton, Maciek Wielgus, George N. Wong, Qingwen Wu, Ken Young, André Young, Ziri Younsi, Feng Yuan, Ye-Fei Yuan, J. Anton Zensus, Guangyao Zhao, Shan-Shan Zhao, Ziyan Zhu, Juan-Carlos Algaba, Alexander Allardi, Rodrigo Amestica, Jadyn Anczarski, Uwe Bach, Frederick K. Baganoff, Christopher Beaudoin, Bradford A. Benson, Ryan Berthold, Jay M. Blanchard, Ray Blundell, Sandra Bustamente, Roger Cappallo, Edgar Castillo-Domínguez, Chih-Cheng Chang, Shu-Hao Chang, Song-Chu Chang, Chung-Chen Chen, Ryan Chilson, Tim C. Chuter, Rodrigo Córdova Rosado, Iain M. Coulson, Thomas M. Crawford, Joseph Crowley, John David, Mark Derome, Matthew Dexter, Sven Dornbusch, Kevin A. Dudevoir, Sergio A. Dzib, Andreas Eckart, Chris Eckert, Neal R. Erickson, Wendeline B. Everett, Aaron Faber, Joseph R. Farah, Vernon Fath, Thomas W. Folkers, David C. Forbes, Robert Freund, Arturo I. Gómez-Ruiz, David M. Gale, Feng Gao, Gertie Geertsema, David A. Graham, Christopher H. Greer, Ronald Grosslein, Frédéric Gueth, Daryl Haggard, Nils W. Halverson, Chih-Chiang Han, Kuo-Chang Han, Jinchi Hao, Yutaka Hasegawa, Jason W. Henning, Antonio Hernández-Gómez, Rubén Herrero-Illana, Stefan Heyminck, Akihiko Hirota, James Hoge, Yau-De Huang, C. M. Violette Impellizzeri, Homin Jiang, Atish Kamble, Ryan Keisler, Kimihiro Kimura, Yusuke Kono, Derek Kubo, John Kuroda, Richard Lacasse, Robert A. Laing, Erik M. Leitch, Chao-Te Li, Lupin C. C. Lin, Ching-Tang Liu, Kuan-Yu Liu, Li-Ming Lu, Ralph G. Marson, Pierre L. Martin-Cocher, Kyle D. Massingill, Callie Matulonis, Martin P. McColl, Stephen R. McWhirter, Hugo Messias, Zheng Meyer-Zhao, Daniel Michalik, Alfredo Montaña, William Montgomerie, Matias Mora-Klein, Dirk Muders, Andrew Nadolski, Santiago Navarro, Joseph Neilsen, Chi H. Nguyen, Hiroaki Nishioka, Timothy Norton, Michael A. Nowak, George Nystrom, Hideo Ogawa, Peter Oshiro, Tomoaki Oyama, Harriet Parsons, Scott N. Paine, Juan Peñalver, Neil M. Phillips, Michael Poirier, Nicolas Pradel, Rurik A. Primiani, Philippe A. Raffin, Alexandra S. Rahlin, George Reiland, Christopher Risacher, Ignacio Ruiz, Alejandro F. Sáez-Madaín, Remi Sassella, Pim Schellart, Paul Shaw, Kevin M. Silva, Hotaka Shiokawa, David R. Smith, William Snow, Kamal Souccar, Don Sousa, T. K. Sridharan, Ranjani Srinivasan, William Stahm, Anthony A. Stark, Kyle Story, Sjoerd T. Timmer, Laura Vertatschitsch, Craig Walther, Ta-Shun Wei, Nathan Whitehorn, Alan R. Whitney, David P. Woody, Jan G. A. Wouterloot, Melvin Wright, Paul Yamaguchi, Chen-Yu Yu, Milagros Zeballos, Shuo Zhang, and Lucy Ziurys. First M87 Event Horizon Telescope Results. I. The Shadow of the Supermassive Black Hole. *The Astrophysical Journal Letters*, 875(1):L1, April 2019. doi: 10.3847/2041-8213/ab0ec7.

Stephen Fairhurst. Triangulation of gravitational wave sources with a network of detectors. *New J. Phys.*, 11:123006, 2009. doi: 10.1088/1367-2630/11/12/123006. [Erratum: New J.Phys. 13, 069602 (2011)].

Yi-Zhong Fan and Tsvi Piran. High-energy γ-ray emission from gamma-ray bursts — before GLAST. *Frontiers of Physics in China*, 3(3):306–330, September 2008. doi: 10.1007/s11467-008-0033-z.

Robert P. Fender. Relativistic jets from x-ray binaries. *AIP Conf. Proc.*, 599(1):101–110, 2001. doi: 10.1063/1.1434623.

Rodrigo Fernández and Brian D. Metzger. Delayed outflows from black hole accretion tori following neutron star binary coalescence. *Mon. Not. Roy. Astron. Soc.*, 435:502, 2013. doi: 10.1093/mnras/stt1312.

Rodrigo Fernández, Eliot Quataert, Josiah Schwab, Daniel Kasen, and Stephan Rosswog. The interplay of disc wind and dynamical ejecta in the aftermath of neutron star–black hole mergers. *Mon. Not. Roy. Astron. Soc.*, 449(1):390–402, 2015. doi: 10.1093/mnras/stv238.

Rodrigo Fernández, Daniel Kasen, Brian D. Metzger, and Eliot Quataert. Outflows from accretion discs formed in neutron star mergers: effect of black hole spin. *Monthly Notices of the Royal Astronomical Society*, 446(1):750–758, 11 2014. ISSN 0035-8711. doi: 10.1093/mnras/stu2112. URL https://doi.org/10.1093/mnras/stu2112.

G. J. Fishman, C. A. Meegan, R. B. Wilson, T. A. Parnell, W. S. Paciesas, G. N. Pendleton, H. S. Hudson, J. L. Matteson, L. E. Peterson, and T. L. Cline. The BATSE experiment on the Gamma Ray Observatory: Solar flare hard X ray and gamma-ray capabilities. In *Developments in Observations and Theory for Solar Cycle 22*, pages 96–106, January 1989.

G.J. Fishman and R.W. Austin. Large-area multi-crystal nai(tl) detectors for x-ray and gamma-ray astronomy. *Nuclear Instruments and Methods*, 140(1): 193–196, 1977. ISSN 0029-554X. doi: https://doi.org/10.1016/0029-554X(77)90085-4. URL https://www.sciencedirect.com/science/article/pii/0029554X77900854.

W. Fong, R. Margutti, R. Chornock, E. Berger, B. J. Shappee, A. J. Levan, N. R. Tanvir, N. Smith, P. A. Milne, T. Laskar, D. B. Fox, R. Lunnan, P. K. Blanchard, J. Hjorth, K. Wiersema, A. J. van der Horst, and D. Zaritsky. The Afterglow and Early-type Host Galaxy of the Short GRB 150101B at z = 0.1343. *The Astrophysical Journal, Letters*, 833(2):151, December 2016. doi: 10.3847/1538-4357/833/2/151.

F. Foucart, M. D. Duez, L. E. Kidder, S. M. Nissanke, H. P. Pfeiffer, and M. A. Scheel. Numerical simulations of neutron star-black hole binaries in the near-equal-mass regime. *Phys. Rev. D*, 99:103025, May 2019. doi: 10.1103/PhysRevD.99.103025. URL https://link.aps.org/doi/10.1103/PhysRevD.99.103025.

Francois Foucart, Matthew D. Duez, Lawrence E. Kidder, and Saul A. Teukolsky. Black hole-neutron star mergers: effects of the orientation of the black hole spin. *Phys. Rev. D*, 83:024005, 2011. doi: 10.1103/PhysRevD.83.024005.

Francois Foucart, Matthew D. Duez, Lawrence E. Kidder, Mark A. Scheel, Bela Szilagyi, and Saul A. Teukolsky. Black hole-neutron star mergers for 10 solar mass black holes. *Phys. Rev. D*, 85:044015, 2012. doi: 10.1103/PhysRevD.85.044015.

Francois Foucart, M. Brett Deaton, Matthew D. Duez, Lawrence E. Kidder, Ilana MacDonald, Christian D. Ott, Harald P. Pfeiffer, Mark A. Scheel, Bela Szilagyi, and Saul A. Teukolsky. Black hole-neutron star mergers at realistic mass ratios: Equation of state and spin orientation effects. *Phys. Rev. D*, 87:084006, 2013. doi: 10.1103/PhysRevD.87.084006.

Francois Foucart, M. Brett Deaton, Matthew D. Duez, Evan O'Connor, Christian D. Ott, Roland Haas, Lawrence E. Kidder, Harald P. Pfeiffer, Mark A. Scheel, and Bela Szilagyi. Neutron star-black hole mergers with a nuclear equation of state and neutrino cooling: Dependence in the binary parameters. *Phys. Rev. D*, 90:024026, 2014. doi: 10.1103/PhysRevD.90.024026.

Francois Foucart, Tanja Hinderer, and Samaya Nissanke. Remnant baryon mass in neutron star-black hole mergers: Predictions for binary neutron star mimickers and rapidly spinning black holes. *Phys. Rev. D*, 98:081501, Oct 2018. doi: 10.1103/PhysRevD.98.081501. URL https://link.aps.org/doi/10.1103/PhysRevD.98.081501.

R. H. Fowler. On Dense Matter. *Monthly Notices of the Royal Astronomical Society*, 87 (2):114–122, 12 1926. ISSN 0035-8711. doi: 10.1093/mnras/87.2.114. URL https://doi.org/10.1093/mnras/87.2.114.

William A. Fowler and F. Hoyle. Neutrino Processes and Pair Formation in Massive Stars and Supernovae. *ApJS*, 9:201, December 1964. doi: 10.1086/190103.

Ori D. Fox, Nathan Smith, S. Mark Ammons, Jennifer Andrews, K. Azalee Bostroem, S. Bradley Cenko, Geoffrey C. Clayton, Eli Dwek, Alexei V. Filippenko, Joseph S. Gallagher, Patrick L. Kelly, Jon C. Mauerhan, Adam A. Miller, and Schuyler D. Van Dyk. What powers the 3000-day light curve of SN 2006gy? *Monthly Notices*

of the Royal Astronomical Society, 454(4):4366–4378, 10 2015. ISSN 0035-8711. doi: 10.1093/mnras/stv2270. URL https://doi.org/10.1093/mnras/stv2270.

D. A. Frail et al. Grb 010222: a burst within a starburst. *Astrophys. J.*, 565:829, 2002. doi: 10.1086/324718.

C. Freiburghaus, S. Rosswog, and F.-K. Thielemann. [CLC][ITAL]r[/ITAL][/CLC]-process in neutron star mergers. *The Astrophysical Journal*, 525(2):L121–L124, nov 1999. doi: 10.1086/312343. URL https://doi.org/10.1086/312343.

David L. Fried. Probability of getting a lucky short-exposure image through turbulence∗. *J. Opt. Soc. Am.*, 68(12):1651–1658, Dec 1978. doi: 10.1364/JOSA.68.001651. URL http://www.osapublishing.org/abstract.cfm?URI=josa-68-12-1651.

Jerome H. Friedman. Stochastic gradient boosting. *Comput. Stat. Data Anal.*, 38(4):367–378, February 2002. ISSN 0167-9473. doi: 10.1016/S0167-9473(01)00065-2. URL https://doi.org/10.1016/S0167-9473(01)00065-2.

Chris Fryer and Vassiliki Kalogera. Double neutron star systems and natal neutron star kicks. *The Astrophysical Journal*, 489(1):244, 1997.

Toshifumi Futamase and Yousuke Itoh. The post-Newtonian approximation for relativistic compact binaries. *Living Rev. Rel.*, 10:2, 2007. doi: 10.12942/lrr-2007-2.

T. J. Galama, P. M. Vreeswijk, J. van Paradijs, C. Kouveliotou, T. Augusteijn, H. Böhnhardt, J. P. Brewer, V. Doublier, J. F. Gonzalez, B. Leibundgut, C. Lidman, O. R. Hainaut, F. Patat, J. Heise, J. in't Zand, K. Hurley, P. J. Groot, R. G. Strom, P. A. Mazzali, K. Iwamoto, K. Nomoto, H. Umeda, T. Nakamura, T. R. Young, T. Suzuki, T. Shigeyama, T. Koshut, M. Kippen, C. Robinson, P. de Wildt, R. A. M. J. Wijers, N. Tanvir, J. Greiner, E. Pian, E. Palazzi, F. Frontera, N. Masetti, L. Nicastro, M. Feroci, E. Costa, L. Piro, B. A. Peterson, C. Tinney, B. Boyle, R. Cannon, R. Stathakis, E. Sadler, M. C. Begam, and P. Ianna. An unusual supernova in the error box of the γ-ray burst of 25 April 1998. *Nature*, 395(6703):670–672, October 1998. doi: 10.1038/27150.

Guillermo Gancio, Carlos Oscar Lousto, Luciano Combi, Santiago del Palacio, FG López Armengol, Jorge Ariel Combi, Federico García, Paula Kornecki, Ana Laura Müller, E Gutiérrez, et al. Upgraded antennas for pulsar observations in the argentine institute of radio astronomy. *Astronomy and Astrophysics*, 633:A84, 2020.

He Gao and Peter Mészáros. Reverse Shock Emission in Gamma-ray Bursts Revisited. *Adv. Astron.*, 2015:192383, 2015. doi: 10.1155/2015/192383.

N. Gehrels, G. Chincarini, P. Giommi, K. O. Mason, J. A. Nousek, A. A. Wells, N. E. White, S. D. Barthelmy, D. N. Burrows, L. R. Cominsky, K. C. Hurley, F. E. Marshall, P. Meszaros, P. W. A. Roming, L. Angelini, L. M. Barbier, T. Belloni, S. Campana, P. A. Caraveo, M. M. Chester, O. Citterio, T. L. Cline, M. S. Cropper, J. R. Cummings, A. J. Dean, E. D. Feigelson, E. E. Fenimore, D. A. Frail, A. S. Fruchter, G. P. Garmire, K. Gendreau, G. Ghisellini, J. Greiner, J. E. Hill, S. D. Hunsberger, H. A. Krimm, S. R. Kulkarni, P. Kumar, F. Lebrun, N. M. Lloyd-Ronning, C. B. Markwardt, B. J. Mattson, R. F. Mushotzky, J. P. Norris, J. Osborne, B. Paczynski, D. M. Palmer, H.-S. Park, A. M. Parsons, J. Paul, M. J. Rees, C. S. Reynolds, J. E. Rhoads, T. P. Sasseen, B. E. Schaefer, A. T. Short, A. P. Smale, I. A. Smith, L. Stella, G. Tagliaferri, T. Takahashi, M. Tashiro, L. K. Townsley, J. Tueller, M. J. L. Turner, M. Vietri, W. Voges, M. J. Ward, R. Willingale, F. M. Zerbi, and W. W. Zhang. TheSwiftGamma-ray burst mission. *The Astrophysical Journal*, 611(2):1005–1020, aug 2004. doi: 10.1086/422091. URL `https://doi.org/10.1086/422091`.

N. Gehrels, C. L. Sarazin, P. T. O'Brien, B. Zhang, L. Barbier, S. D. Barthelmy, A. Blustin, D. N. Burrows, J. Cannizzo, J. R. Cummings, M. Goad, S. T. Holland, C. P. Hurkett, J. A. Kennea, A. Levan, C. B. Markwardt, K. O. Mason, P. Meszaros, M. Page, D. M. Palmer, E. Rol, T. Sakamoto, R. Willingale, L. Angelini, A. Beardmore, P. T. Boyd, A. Breeveld, S. Campana, M. M. Chester, G. Chincarini, L. R. Cominsky, G. Cusumano, M. de Pasquale, E. E. Fenimore, P. Giommi, C. Gronwall, D. Grupe, J. E. Hill, D. Hinshaw, J. Hjorth, D. Hullinger, K. C. Hurley, S. Klose, S. Kobayashi, C. Kouveliotou, H. A. Krimm, V. Mangano, F. E. Marshall, K. McGowan, A. Moretti, R. F. Mushotzky, K. Nakazawa, J. P. Norris, J. A. Nousek, J. P. Osborne, K. Page, A. M. Parsons, S. Patel, M. Perri, T. Poole, P. Romano, P. W. A. Roming, S. Rosen, G. Sato, P. Schady, A. P. Smale, J. Sollerman, R. Starling, M. Still, M. Suzuki, G. Tagliaferri, T. Takahashi, M. Tashiro, J. Tueller, A. A. Wells, N. E. White, and R. A. M. J. Wijers. A short γ-ray burst apparently associated with an elliptical galaxy at redshift z = 0.225. *Nature*, 437(7060):851–854, October 2005. doi: 10.1038/nature04142.

G. Ghirlanda, G. Ghisellini, and A. Celotti. The spectra of short gamma-ray bursts. *Astron. Astrophys.*, 422:L55–L58, 2004. doi: 10.1051/0004-6361:20048008.

G Ghirlanda, L Nava, G Ghisellini, A Celotti, and C Firmani. Short versus long gamma-ray bursts: spectra, energetics, and luminosities. *Astronomy and Astrophysics*, 496(3): 585–595, 2009.

Gerry Gilmore. The short spectacular life of a superstar. *Science*, 304(5679):1915–1916, 2004. ISSN 0036-8075. doi: 10.1126/science.1100370. URL `https://science.sciencemag.org/content/304/5679/1915`.

Hila Glanz and Hagai B Perets. Efficient common-envelope ejection through dust-driven winds. *Monthly Notices of the Royal Astronomical Society: Letters*, 478(1): L12–L17, 2018.

A. Goldstein et al. An Ordinary Short Gamma-Ray Burst with Extraordinary Implications: Fermi-GBM Detection of GRB 170817A. *Astrophys. J. Lett.*, 848(2):L14, 2017. doi: 10.3847/2041-8213/aa8f41.

Adam Goldstein et al. Updates to the Fermi GBM Targeted Sub-threshold Search in Preparation for the Third Observing Run of LIGO/Virgo. 3 2019.

B. P. Gompertz et al. The Diversity of Kilonova Emission in Short Gamma-Ray Bursts. *Astrophys. J.*, 860(1):62, 2018. doi: 10.3847/1538-4357/aac206.

B. Alvarez Gonzalez. Study of the effects of radiation at the CERN gamma irradiation facility on the CMS drift tubes muon detector for the HL-LHC. *Journal of Instrumentation*, 15(04):C04012–C04012, apr 2020. doi: 10.1088/1748-0221/15/04/c04012. URL `https://doi.org/10.1088/1748-0221/15/04/c04012`.

J. Goodman. Are gamma-ray bursts optically thick? *The Astrophysical Journal, Letters*, 308:L47, September 1986. doi: 10.1086/184741.

Stephane Goriely, Andreas Bauswein, and H. Thomas Janka. R-Process Nucleosynthesis in Dynamically Ejected Matter of Neutron Star Mergers. *Astrophys. J. Lett.*, 738: L32, 2011a. doi: 10.1088/2041-8205/738/2/L32.

Stephane Goriely, Andreas Bauswein, and Hans-Thomas Janka. r -PROCESS NUCLEOSYNTHESIS IN DYNAMICALLY EJECTED MATTER OF NEUTRON STAR MERGERS. *The Astrophysical Journal*, 738(2):L32, aug 2011b. doi: 10.1088/2041-8205/738/2/l32. URL `https://doi.org/10.1088/2041-8205/738/2/l32`.

Stéphane Goriely, Nicolas Chamel, H-T Janka, and JM Pearson. The decompression of the outer neutron star crust and r-process nucleosynthesis. *Astronomy and astrophysics*, 531:A78, 2011c.

Matthew J. Graham et al. The Zwicky Transient Facility: Science Objectives. *Publ. Astron. Soc. Pac.*, 131(1001):078001, 2019. doi: 10.1088/1538-3873/ab006c.

M. Granata et al. Progress in the measurement and reduction of thermal noise in optical coatings for gravitational-wave detectors. *Appl. Opt.*, 59(5):A229–A235, 2020. doi: 10.1364/AO.377293.

Jonathan Granot, Ramandeep Gill, Dafne Guetta, and Fabio De Colle. Off-axis emission of short GRB jets from double neutron star mergers and GRB 170817A. *Mon. Not. Roy. Astron. Soc.*, 481(2):1597–1608, 2018. doi: 10.1093/mnras/sty2308.

R. L. Grasty. Atmospheric absorption of 2.62 Mev gamma-ray photons emitted from the ground. *Geophysics*, 40(6):1058–1065, 12 1975. ISSN 0016-8033. doi: 10.1190/1.1440582. URL https://doi.org/10.1190/1.1440582.

M.A. Green, J.W. Moffat, and V.T. Toth. Modified gravity (mog), the speed of gravitational radiation and the event gw170817/grb170817a. *Physics Letters B*, 780:300–302, 2018. ISSN 0370-2693. doi: https://doi.org/10.1016/j.physletb.2018.03.015. URL https://www.sciencedirect.com/science/article/pii/S0370269318302041.

Isabelle A. Grenier and Alice K. Harding. Gamma-ray pulsars: A gold mine. *Comptes Rendus Physique*, 16(6):641–660, 2015. ISSN 1631-0705. doi: https://doi.org/10.1016/j.crhy.2015.08.013. URL https://www.sciencedirect.com/science/article/pii/S1631070515001486. Gamma-ray astronomy / Astronomie des rayons gamma.

D. Grigoriev, G. Kuznetcov, I. Novoselov, P. Schotanus, B. Shavinski, S. Shepelev, V. Shlegel, and Ya Vasiliev. Incidental radioactive background in BGO crystals. In *1st International Workshop on Radiopure Scintillators for EURECA (RPScint 2008)*, Kiev, 3 2009. INR.

V. Grinberg et al. Long term variability of Cygnus X-1 V. State definitions with all sky monitors. *Astron. Astrophys.*, 554:A88, 2013. doi: 10.1051/0004-6361/201321128.

K. Grover, S. Fairhurst, B. F. Farr, I. Mandel, C. Rodriguez, T. Sidery, and A. Vecchio. Comparison of gravitational wave detector network sky localization approximations. *Phys. Rev. D*, 89:042004, Feb 2014. doi: 10.1103/PhysRevD.89.042004. URL https://link.aps.org/doi/10.1103/PhysRevD.89.042004.

D Gruber, T Krühler, S Foley, M Nardini, D Burlon, A Rau, Elisabetta Bissaldi, A Von Kienlin, S McBreen, J Greiner, et al. Fermi/gbm observations of the ultra-long grb 091024-a burst with an optical flash. *Astronomy and Astrophysics*, 528:A15, 2011.

P. W. Guilbert, A. C. Fabian, and M. J. Rees. Spectral and variability constraints on compact sources. *Monthly Notices of the Royal Astronomical Society*, 205(3):593–603, 12 1983. ISSN 0035-8711. doi: 10.1093/mnras/205.3.593. URL https://doi.org/10.1093/mnras/205.3.593.

James Guillochon, Matt Nicholl, V. Ashley Villar, Brenna Mockler, Gautham Narayan, Kaisey S. Mandel, Edo Berger, and Peter K. G. Williams. MOSFiT: Modular Open-Source Fitter for Transients. *Astrophys. J. Suppl.*, 236(1):6. doi: 10.3847/1538-4365/aab761.

Julien Guy, P. Astier, S. Nobili, N. Regnault, and R. Pain. SALT: A Spectral adaptive Light curve Template for Type Ia supernovae. *Astron. Astrophys.*, 443:781–791, 2005. doi: 10.1051/0004-6361:20053025.

Julien Guy, Mark Sullivan, A Conley, N Regnault, P Astier, C Balland, S Basa, RG Carlberg, D Fouchez, D Hardin, et al. The supernova legacy survey 3-year sample: Type ia supernovae photometric distances and cosmological constraints. *Astronomy and Astrophysics*, 523:A7, 2010.

Julien Guy et al. SALT2: Using distant supernovae to improve the use of Type Ia supernovae as distance indicators. *Astron. Astrophys.*, 466:11–21, 2007. doi: 10.1051/0004-6361:20066930.

Pierre Haguenauer, Jaime Alonso, Pierre Bourget, Stephane Brillant, Philippe Gitton, Stephane Guisard, Sébastien Poupar, Nicolas Schuhler, Roberto Abuter, Luigi Andolfato, Guillaume Blanchard, Jean-Philippe Berger, Angela Cortes, Frédéric Dérie, Françoise Delplancke, Nicola Di Lieto, Christophe Dupuy, Bruno Gilli, Andreas Glindemann, Serge Guniat, Gerhard Huedepohl, Andreas Kaufer, Jean-Baptiste Le Bouquin, Samuel Lévêque, Serge Ménardi, Antoine Mérand, Sebastien Morel, Isabelle Percheron, Than Phan Duc, Andres Pino, Andres Ramirez, Sridharan Rengaswamy, Andrea Richichi, Thomas Rivinius, Johannes Sahlmann, Markus Schoeller, Christian Schmid, Stan Stefl, Guillermo Valdes, Gerard van Belle, Stefan Wehner, and Markus Wittkowski. The very large telescope Interferometer: 2010 edition. In William C. Danchi, Françoise Delplancke, and Jayadev K. Rajagopal, editors, *Optical and Infrared Interferometry II*, volume 7734, pages 53 – 63. International Society for Optics and Photonics, SPIE, 2010. doi: 10.1117/12.857070. URL `https://doi.org/10.1117/12.857070`.

Zoltán Haiman. Electromagnetic chirp of a compact binary black hole: A phase template for the gravitational wave inspiral. *Phys. Rev. D*, 96(2):023004, 2017. doi: 10.1103/PhysRevD.96.023004.

R. Hainich, T. Shenar, A. Sander, W. R. Hamann, and H. Todt. The metallicity dependence of WR winds. In J. J. Eldridge, J. C. Bray, L. A. S. McClelland, and L. Xiao, editors, *The Lives and Death-Throes of Massive Stars*, volume 329, pages 171–175, November 2017. doi: 10.1017/S1743921317002794.

George F. Hale. The Yerkes Observatory of the University of Chicago: I.SELECTION of the Site. *The Astrophysical Journal, Letters*, 5:164, March 1897. doi: 10.1086/140327.

G. Hallinan et al. A Radio Counterpart to a Neutron Star Merger. *Science*, 358:1579, 2017. doi: 10.1126/science.aap9855.

R. Hamburg et al. A Joint Fermi-GBM and LIGO/Virgo Analysis of Compact Binary Mergers From the First and Second Gravitational-wave Observing Runs. *Astrophys. J.*, 893:100, 2020. doi: 10.3847/1538-4357/ab7d3e.

Sophia Han, M. A. A. Mamun, S. Lalit, C. Constantinou, and M. Prakash. Treating quarks within neutron stars. *Phys. Rev. D*, 100:103022, Nov 2019. doi: 10.1103/PhysRevD.100.103022. URL https://link.aps.org/doi/10.1103/PhysRevD.100.103022.

Mark Hannam, Patricia Schmidt, Alejandro Bohé, Leïla Haegel, Sascha Husa, Frank Ohme, Geraint Pratten, and Michael Pürrer. Simple Model of Complete Precessing Black-Hole-Binary Gravitational Waveforms. *Phys. Rev. Lett.*, 113(15):151101, 2014. doi: 10.1103/PhysRevLett.113.151101.

Brad M. S. Hansen and E. Sterl Phinney. The Pulsar kick velocity distribution. *Mon. Not. Roy. Astron. Soc.*, 291:569, 1997. doi: 10.1093/mnras/291.3.569.

William E. Harris. A Catalog of Parameters for Globular Clusters in the Milky Way. *The Astronomical Journal*, 112:1487, October 1996. doi: 10.1086/118116.

Ian Harry and Tanja Hinderer. Observing and measuring the neutron-star equation-of-state in spinning binary neutron star systems. *Classical and Quantum Gravity*, 35(14): 145010, jun 2018. doi: 10.1088/1361-6382/aac7e3. URL https://doi.org/10.1088/1361-6382/aac7e3.

WN Hartley. Xxi.—on the absorption of solar rays by atmospheric ozone. *Journal of the Chemical Society, Transactions*, 39:111–128, 1881.

H Hayashi, N Ohmori, A Daikyuji, E Sonoda, K Kono, K Noda, Y Nishioka, M Yamauchi, T Sugasahara, M Tashiro, et al. Grb 091117a: Suzaku wam observation of the prompt emission. *GRB Coordinates Network*, 10186:1, 2009.

A. Heger and N. Langer. Presupernova evolution of rotating massive stars. 2. - evolution of the surface properties. *Astrophys. J.*, 544:1016–1035, 2000. doi: 10.1086/317239.

J. J. Hermes, Mukremin Kilic, Warren R. Brown, D. E. Winget, Carlos Allende Prieto, A. Gianninas, Anjum S. Mukadam, Antonio Cabrera-Lavers, and Scott J. Kenyon.

Rapid Orbital Decay in the 12.75-minute Binary White Dwarf J0651+2844. *The Astrophysical Journal, Letters*, 757(2):L21, October 2012. doi: 10.1088/2041-8205/757/2/L21.

H. Hertz. Ueber einen einfluss des ultravioletten lichtes auf die electrische entladung. *Annalen der Physik*, 267(8):983–1000, 1887. doi: https://doi.org/10.1002/andp.18872670827. URL https://onlinelibrary.wiley.com/doi/abs/10.1002/andp.18872670827.

Jason W. T. Hessels, Scott M. Ransom, Ingrid H. Stairs, Paulo Cesar Carvalho Freire, Victoria M. Kaspi, and Fernando Camilo. A radio pulsar spinning at 716-hz. *Science*, 311:1901–1904, 2006. doi: 10.1126/science.1123430.

A. Hewish, S. J. Bell, J. D. H. Pilkington, P. F. Scott, and R. A. Collins. Observation of a Rapidly Pulsating Radio Source. *Nature*, 217(5130):709–713, February 1968. doi: 10.1038/217709a0.

Tanja Hinderer, Benjamin D. Lackey, Ryan N. Lang, and Jocelyn S. Read. Tidal deformability of neutron stars with realistic equations of state and their gravitational wave signatures in binary inspiral. *Phys. Rev. D*, 81:123016, Jun 2010. doi: 10.1103/PhysRevD.81.123016. URL https://link.aps.org/doi/10.1103/PhysRevD.81.123016.

Jens Hjorth, Jesper Sollerman, Palle Møller, Johan P. U. Fynbo, Stan E. Woosley, Chryssa Kouveliotou, Nial R. Tanvir, Jochen Greiner, Michael I. Andersen, Alberto J. Castro-Tirado, José María Castro Cerón, Andrew S. Fruchter, Javier Gorosabel, Páll Jakobsson, Lex Kaper, Sylvio Klose, Nicola Masetti, Holger Pedersen, Kristian Pedersen, Elena Pian, Eliana Palazzi, James E. Rhoads, Evert Rol, Edward P. J. van den Heuvel, Paul M. Vreeswijk, Darach Watson, and Ralph A. M. J. Wijers. A very energetic supernova associated with the γ-ray burst of 29 March 2003. *Nature*, 423(6942):847–850, June 2003. doi: 10.1038/nature01750.

J. B. Holberg. The discovery of the existence of white dwarf stars: 1862 to 1930. *Journal for the History of Astronomy*, 40(2):137–154, 2009. doi: 10.1177/002182860904000201. URL https://doi.org/10.1177/002182860904000201.

G. Horedt. Fast synchronization of the rotation of binaries by tidally induced turbulence. *Astronomy and Astrophysics*, 44(2):461–463, November 1975.

H. Horvath. Atmospheric light absorption—a review. *Atmospheric Environment. Part A. General Topics*, 27(3):293–317, 1993. ISSN 0960-1686. doi: https://doi.org/

10.1016/0960-1686(93)90104-7. URL https://www.sciencedirect.com/science/article/pii/0960168693901047. First Ibero-American Conference on the Atmospheric Environment, CIAMAA91/ACAE91.

Kenta Hotokezaka, Koutarou Kyutoku, Hirotada Okawa, Masaru Shibata, and Kenta Kiuchi. Binary neutron star mergers: Dependence on the nuclear equation of state. *Phys. Rev. D*, 83:124008, Jun 2011. doi: 10.1103/PhysRevD.83.124008. URL https://link.aps.org/doi/10.1103/PhysRevD.83.124008.

Kenta Hotokezaka, Kenta Kiuchi, Koutarou Kyutoku, Hirotada Okawa, Yu-ichiro Sekiguchi, Masaru Shibata, and Keisuke Taniguchi. Mass ejection from the merger of binary neutron stars. *Phys. Rev. D*, 87:024001, Jan 2013. doi: 10.1103/PhysRevD.87.024001. URL https://link.aps.org/doi/10.1103/PhysRevD.87.024001.

Kenta Hotokezaka, Ehud Nakar, Ore Gottlieb, Samaya Nissanke, Kento Masuda, Gregg Hallinan, Kunal P. Mooley, and Adam. T. Deller. A Hubble constant measurement from superluminal motion of the jet in GW170817. *Nature Astron.*, 3(10):940–944, 2019. doi: 10.1038/s41550-019-0820-1.

Fang Huang, Jun-Zheng Li, Xiao-Feng Wang, Ren-Cheng Shang, Tian-Meng Zhang, Jing-Yao Hu, Yu-Lei Qiu, and Xiao-Jun Jiang. The photometric system of the tsinghua-NAOC 80-cm telescope at NAOC xinglong observatory. *Research in Astronomy and Astrophysics*, 12(11):1585–1596, oct 2012. doi: 10.1088/1674-4527/12/11/012. URL https://doi.org/10.1088/1674-4527/12/11/012.

J.H. Hubbell. Electron–positron pair production by photons: A historical overview. *Radiation Physics and Chemistry*, 75(6):614–623, 2006. ISSN 0969-806X. doi: https://doi.org/10.1016/j.radphyschem.2005.10.008. URL https://www.sciencedirect.com/science/article/pii/S0969806X0500263X. Pair Production.

Michelle Hui, Michael S. Briggs, Peter Veres, and Rachel Hamburg. Finding untriggered gamma-ray transients in the Fermi GBM data. *PoS*, IFS2017:129, 2020. doi: 10.22323/1.312.0129.

Stanley D. Hunter. The advanced energetic pair telescope for gamma-ray polarimetry. In Jan-Willem A. den Herder, Shouleh Nikzad, and Kazuhiro Nakazawa, editors, *Space Telescopes and Instrumentation 2018: Ultraviolet to Gamma Ray*, volume 10699, pages 652 – 658. International Society for Optics and Photonics, SPIE, 2018. doi: 10.1117/12.2312732. URL https://doi.org/10.1117/12.2312732.

Jarrod R. Hurley, Christopher A. Tout, and Onno R. Pols. Evolution of binary stars and the effect of tides on binary populations. *Mon. Not. Roy. Astron. Soc.*, 329:897, 2002. doi: 10.1046/j.1365-8711.2002.05038.x.

K Hurley. Phosphorescence in cs icrystals. *Astronomy and Astrophysics*, 69:313, 1978.

Sascha Husa, Sebastian Khan, Mark Hannam, Michael Pürrer, Frank Ohme, Xisco Jiménez Forteza, and Alejandro Bohé. Frequency-domain gravitational waves from nonprecessing black-hole binaries. i. new numerical waveforms and anatomy of the signal. *Phys. Rev. D*, 93:044006, Feb 2016. doi: 10.1103/PhysRevD.93.044006. URL `https://link.aps.org/doi/10.1103/PhysRevD.93.044006`.

P. Hut. Tidal evolution in close binary systems. *Astronomy and Astrophysics*, 99:126–140, June 1981.

E. E. O. Ishida et al. Optimizing spectroscopic follow-up strategies for supernova photometric classification with active learning. *Mon. Not. Roy. Astron. Soc.*, 483(1):2–18, 2019. doi: 10.1093/mnras/sty3015.

Tomoki Isogai. Used percentage veto for LIGO and virgo binary inspiral searches. *J. Phys. Conf. Ser.*, 243:012005, 2010. doi: 10.1088/1742-6596/243/1/012005.

Željko Ivezić et al. LSST: from Science Drivers to Reference Design and Anticipated Data Products. *Astrophys. J.*, 873(2):111, 2019. doi: 10.3847/1538-4357/ab042c.

Brian Jackson, Phil Arras, Kaloyan Penev, Sarah Peacock, and Pablo Marchant. A new model of roche lobe overflow for short-period gaseous planets and binary stars. *The Astrophysical Journal*, 835(2):145, 2017.

Pierre Jacquot. Speckle interferometry: a review of the principal methods in use for experimental mechanics applications. *Strain*, 44(1):57–69, 2008.

Pall Jakobsson et al. Grb 050814 at z=5.3 and the redshift distribution of swift grbs. *AIP Conf. Proc.*, 836(1):552–557, 2006. doi: 10.1063/1.2207953.

Soumya Jana and Subhendra Mohanty. Constraints on $f(R)$ theories of gravity from GW170817. *Phys. Rev. D*, 99(4):044056, 2019. doi: 10.1103/PhysRevD.99.044056.

Agnieszka Janiuk, Szymon Charzyński, and Michał Bejger. Long Gamma Ray Bursts from binary black holes. *Astron. Astrophys.*, 560:A25, 2013. doi: 10.1051/0004-6361/201322165.

W Jeffrey and R Rosner. Optimization algorithms-simulated annealing and neural network processing. *The Astrophysical Journal*, 310:473–481, 1986.

Paul I. Jefremov, Oleg Yu. Tsupko, and Gennady S. Bisnovatyi-Kogan. Innermost stable circular orbits of spinning test particles in Schwarzschild and Kerr space-times. *Phys. Rev. D*, 91(12):124030, 2015. doi: 10.1103/PhysRevD.91.124030.

Saurabh W Jha. Type iax supernovae. *arXiv preprint arXiv:1707.01110*, 2017.

N. Joubert, W. Li, K. Itagaki, S. Nakano, and J. Frieman. Supernovae 2006ep, 2006eq, 2006er. *IAU Circulars*, 8744:2, September 2006.

Oliver Just, Andreas Bauswein, R Ardevol Pulpillo, Stephane Goriely, and H-T Janka. Comprehensive nucleosynthesis analysis for ejecta of compact binary mergers. *Monthly Notices of the Royal Astronomical Society*, 448(1):541–567, 2015.

Ervin Kafexhiu, Carlo Romoli, Andrew M. Taylor, and Felix Aharonian. Energetic gamma-ray emission from solar flares. *Astrophys. J.*, 864(2):148, 2018. doi: 10.3847/1538-4357/aad801.

Yukiko Kamata, Satoshi Miyazaki, Masaharu Muramatsu, Hisanori Suzuki, Kazuhisa Miyaguchi, Takeshi Go Tsuru, Shin ichiro Takagi, and Emi Miyata. Development of thick back-illuminated CCD to improve quantum efficiency in optical longer wavelength using high-resistivity n-type silicon. In James D. Garnett and James W. Beletic, editors, *Optical and Infrared Detectors for Astronomy*, volume 5499, pages 210 – 218. International Society for Optics and Photonics, SPIE, 2004. doi: 10.1117/12.552515. URL https://doi.org/10.1117/12.552515.

N. V. Karpenka, F. Feroz, and M. P. Hobson. A simple and robust method for automated photometric classification of supernovae using neural networks. *Monthly Notices of the Royal Astronomical Society*, 429(2):1278–1285, 12 2012. ISSN 0035-8711. doi: 10.1093/mnras/sts412. URL https://doi.org/10.1093/mnras/sts412.

Daniel Kasen and Lars Bildsten. Supernova light curves powered by young magnetars. *The Astrophysical Journal*, 717(1):245, 2010.

Daniel Kasen, SE Woosley, and Alexander Heger. Pair instability supernovae: light curves, spectra, and shock breakout. *The Astrophysical Journal*, 734(2):102, 2011.

Daniel Kasen, Brian Metzger, Jennifer Barnes, Eliot Quataert, and Enrico Ramirez-Ruiz. Origin of the heavy elements in binary neutron-star mergers from a gravitational wave event. *Nature*, 551:80, 2017. doi: 10.1038/nature24453.

Mansi M Kasliwal, SR Kulkarni, Avishay Gal-Yam, Peter E Nugent, Mark Sullivan, Lars Bildsten, Ofer Yaron, Hagai B Perets, Iair Arcavi, Sagi Ben-Ami, et al. Calcium-rich gap transients in the remote outskirts of galaxies. *The Astrophysical Journal*, 755 (2):161, 2012.

V. Kaspi, M. Bailes, R. Manchester, B. Stappers, and J. Bell. Evidence from a processing pulsar orbit for a neutron-star birth kick. *Nature*, 381:584–586, 1996.

Jonathan I. Katz. Two populations and models of gamma-ray bursts. *Astrophys. J.*, 422: 248, 1994. doi: 10.1086/173723.

Jonathan I. Katz. Yet another model of gamma-ray bursts. *Astrophys. J.*, 490:633, 1997. doi: 10.1086/304896.

Kyohei Kawaguchi, Koutarou Kyutoku, Hiroyuki Nakano, Hirotada Okawa, Masaru Shibata, and Keisuke Taniguchi. Black hole-neutron star binary merger: Dependence on black hole spin orientation and equation of state. *Phys. Rev. D*, 92:024014, Jul 2015. doi: 10.1103/PhysRevD.92.024014. URL `https://link.aps.org/doi/10.1103/PhysRevD.92.024014`.

Kyohei Kawaguchi, Kotarou Kyutoku, Masaru Shibata, and Masaomi Tanaka. Models of Kilonova/macronova Emission From Black Hole–neutron Star Mergers. *Astrophys. J.*, 825(1):52, 2016. doi: 10.3847/0004-637X/825/1/52.

Yuta Kawakubo, Takanori Sakamoto, Satoshi Nakahira, Kazutaka Yamaoka, Motoko Serino, Yoichi Asaoka, Michael L Cherry, Shohei Matsukawa, Masaki Mori, Yujin Nakagawa, Shunsuke Ozawa, Ana V Penacchioni, Sergio B Ricciarini, Akira Tezuka, Shoji Torii, Yusuke Yamada, and Atsumasa Yoshida. Detection of the thermal component in GRB 160107A. *Publications of the Astronomical Society of Japan*, 70(1), 02 2018. ISSN 0004-6264. doi: 10.1093/pasj/psx152. URL `https://doi.org/10.1093/pasj/psx152`. 6.

Bernard J. Kelly and John G. Baker. Decoding mode mixing in black-hole merger ringdown. *Phys. Rev. D*, 87(8):084004, 2013. doi: 10.1103/PhysRevD.87.084004.

R. Kessler et al. Models and Simulations for the Photometric LSST Astronomical Time Series Classification Challenge (PLAsTiCC). *Publ. Astron. Soc. Pac.*, 131(1003): 094501, 2019. doi: 10.1088/1538-3873/ab26f1.

Richard Kessler, Joseph P Bernstein, David Cinabro, Benjamin Dilday, Joshua A Frieman, Saurabh Jha, Stephen Kuhlmann, Gajus Miknaitis, Masao Sako, Matt Taylor, et al. Snana: A public software package for supernova analysis. *Publications of the Astronomical Society of the Pacific*, 121(883):1028, 2009.

Richard Kessler, Bruce Bassett, Pavel Belov, Vasudha Bhatnagar, Heather Campbell, Alex Conley, Joshua A Frieman, Alexandre Glazov, Santiago González-Gaitán, Renée Hlozek, et al. Results from the supernova photometric classification challenge. *Publications of the Astronomical Society of the Pacific*, 122(898):1415, 2010.

Richard Kessler, Julien Guy, John Marriner, Marc Betoule, Jon Brinkmann, David Cinabro, Patrick El-Hage, Joshua A Frieman, Saurabh Jha, Jennifer Mosher, et al. Testing models of intrinsic brightness variations in type ia supernovae and their impact on measuring cosmological parameters. *The Astrophysical Journal*, 764(1):48, 2013.

Sebastian Khan, Sascha Husa, Mark Hannam, Frank Ohme, Michael Pürrer, Xisco Jiménez Forteza, and Alejandro Bohé. Frequency-domain gravitational waves from nonprecessing black-hole binaries. II. A phenomenological model for the advanced detector era. *Phys. Rev. D*, 93(4):044007, 2016. doi: 10.1103/PhysRevD.93.044007.

RM Kippen, AS Hoover, MS Wallace, GN Pendleton, CA Meegan, GJ Fishman, CA Wilson-Hodge, C Kouveliotou, GG Lichti, A Von Kienlin, et al. Instrument response modeling and simulation for the glast burst monitor. In *AIP Conference Proceedings*, volume 921, pages 590–591. American Institute of Physics, 2007.

Kenta Kiuchi, Koutarou Kyutoku, Yuichiro Sekiguchi, Masaru Shibata, and Tomohide Wada. High resolution numerical relativity simulations for the merger of binary magnetized neutron stars. *Phys. Rev. D*, 90:041502, Aug 2014. doi: 10.1103/PhysRevD.90.041502. URL `https://link.aps.org/doi/10.1103/PhysRevD.90.041502`.

Kenta Kiuchi, Pablo Cerdá-Durán, Koutarou Kyutoku, Yuichiro Sekiguchi, and Masaru Shibata. Efficient magnetic-field amplification due to the kelvin-helmholtz instability in binary neutron star mergers. *Phys. Rev. D*, 92:124034, Dec 2015. doi: 10.1103/PhysRevD.92.124034. URL `https://link.aps.org/doi/10.1103/PhysRevD.92.124034`.

Kenta Kiuchi, Koutarou Kyutoku, Masaru Shibata, and Keisuke Taniguchi. Revisiting the lower bound on tidal deformability derived by AT 2017gfo. *Astrophys. J. Lett.*, 876 (2):L31, 2019. doi: 10.3847/2041-8213/ab1e45.

Ray W. Klebesadel, Ian B. Strong, and Roy A. Olson. Observations of Gamma-Ray Bursts of Cosmic Origin. *The Astrophysical Journal Letters*, 182:L85, June 1973. doi: 10.1086/181225.

S. Klimenko, G. Vedovato, M. Drago, F. Salemi, V. Tiwari, G. A. Prodi, C. Lazzaro, K. Ackley, S. Tiwari, C. F. Da Silva, and G. Mitselmakher. Method for detection and reconstruction of gravitational wave transients with networks of advanced detectors. *Phys. Rev. D*, 93:042004, Feb 2016. doi: 10.1103/PhysRevD.93.042004. URL `https://link.aps.org/doi/10.1103/PhysRevD.93.042004`.

Jürgen Knödlseder. The Cherenkov Telescope Array. In *16th Rencontres du Vietnam: Theory meeting experiment: Particle Astrophysics and Cosmology*, 4 2020.

Trevor Knuth and Lindsay Glesener. Subsecond Spikes in Fermi GBM X-ray Flux as a Probe for Solar Flare Particle Acceleration. *Astrophys. J.*, 903(1):63, 2020. doi: 10.3847/1538-4357/abb779.

HK Kobayashi. Atmospheric effects on millimeter radio waves. Technical report, ARMY ELECTRONICS RESEARCH AND DEVELOPMENT COMMAND WSMR NM ATMOSPHERIC . . . , 1980.

D. Kocevski et al. Analysis of Sub-threshold Short Gamma-ray Bursts in $Fermi$ GBM Data. *Astrophys. J.*, 862(2):152, 2018. doi: 10.3847/1538-4357/aacb7b.

O. Korobkin, S. Rosswog, A. Arcones, and C. Winteler. On the astrophysical robustness of the neutron star merger r-process. *Monthly Notices of the Royal Astronomical Society*, 426(3):1940–1949, 11 2012. ISSN 0035-8711. doi: 10.1111/j.1365-2966.2012.21859.x. URL https://doi.org/10.1111/j.1365-2966.2012.21859.x.

Oleg Korobkin et al. Axisymmetric Radiative Transfer Models of Kilonovae. *Astrophys. J.*, 910(2):116, 2021. doi: 10.3847/1538-4357/abe1b5.

C. Kouveliotou, J. P. Norris, K. S. Wood, T. L. Cline, B. R. Dennis, U. D. Desal, and L. E. Orwig. Search for Soft Gamma Repeaters in the SMM/HXRBS Data. *The Astrophysical Journal*, 392:179, June 1992. doi: 10.1086/171416.

Chryssa Kouveliotou, Charles A. Meegan, Gerald J. Fishman, Narayana P. Bhat, Michael S. Briggs, Thomas M. Koshut, William S. Paciesas, and Geoffrey N. Pendleton. Identification of Two Classes of Gamma-Ray Bursts. *The Astrophysical Journal, Letters*, 413:L101, August 1993. doi: 10.1086/186969.

K. S. Krane. *INTRODUCTORY NUCLEAR PHYSICS*. 1987.

Kyle Kremer, Sourav Chatterjee, Carl L. Rodriguez, and Frederic A. Rasio. Low-mass X-ray binaries ejected from globular clusters. 2 2018.

Kruckow, M. U., Tauris, T. M., Langer, N., Szécsi, D., Marchant, P., and Podsiadlowski, Ph. Common-envelope ejection in massive binary stars - implications for the progenitors of gw150914 and gw151226. *AandA*, 596:A58, 2016. doi: 10.1051/0004-6361/201629420. URL https://doi.org/10.1051/0004-6361/201629420.

Christian J. Krüger and Francois Foucart. Estimates for disk and ejecta masses produced in compact binary mergers. *Phys. Rev. D*, 101:103002, May 2020. doi: 10.1103/PhysRevD.101.103002. URL https://link.aps.org/doi/10.1103/PhysRevD.101.103002.

Pawan Kumar and Bing Zhang. The physics of gamma-ray bursts \and relativistic jets. *Phys. Rept.*, 561:1–109, 2014. doi: 10.1016/j.physrep.2014.09.008.

Ayaka Kumeta, Charlotte Bond, and Kentaro Somiya. Design study of the KAGRA output mode-cleaner. *Opt. Rev.*, 22:149–152, 2015. doi: 10.1007/s10043-015-0028-2.

Sun Kwok. Planetary Nebulae: New Challenges in the 21st Century. *Journal of Korean Astronomical Society*, 38(2):271–278, June 2005. doi: 10.5303/JKAS.2005.38.2.271.

Koutarou Kyutoku, Hirotada Okawa, Masaru Shibata, and Keisuke Taniguchi. Gravitational waves from spinning black hole-neutron star binaries: dependence on black hole spins and on neutron star equations of state. *Phys. Rev. D*, 84:064018, 2011. doi: 10.1103/PhysRevD.84.064018.

Koutarou Kyutoku, Kunihito Ioka, Hirotada Okawa, Masaru Shibata, and Keisuke Taniguchi. Dynamical mass ejection from black hole-neutron star binaries. *Phys. Rev. D*, 92:044028, 2015. doi: 10.1103/PhysRevD.92.044028.

Benjamin D. Lackey and Leslie Wade. Reconstructing the neutron-star equation of state with gravitational-wave detectors from a realistic population of inspiralling binary neutron stars. *Phys. Rev. D*, 91:043002, Feb 2015. doi: 10.1103/PhysRevD.91.043002. URL `https://link.aps.org/doi/10.1103/PhysRevD.91.043002`.

Dong Lai. Resonant oscillations and tidal heating in coalescing binary neutron stars. *Mon. Not. Roy. Astron. Soc.*, 270:611, 1994. doi: 10.1093/mnras/270.3.611.

Gavin P. Lamb. Reverse Shocks in Short Gamma-Ray Bursts – The case of GRB 160821B and prospects as gravitational-wave counterparts. 6 2020.

H. J. G. L. M. Lamers, E. P. J. van den Heuvel, and J. A. Petterson. Stellar winds and accretion in massive X-ray binaries. *Astronomy and Astrophysics*, 49:327–335, June 1976.

Philippe Landry, Reed Essick, and Katerina Chatziioannou. Nonparametric constraints on neutron star matter with existing and upcoming gravitational wave and pulsar observations. *Phys. Rev. D*, 101:123007, Jun 2020. doi: 10.1103/PhysRevD.101.123007. URL `https://link.aps.org/doi/10.1103/PhysRevD.101.123007`.

Jacob Lange, Richard O'Shaughnessy, and Monica Rizzo. Rapid and accurate parameter inference for coalescing, precessing compact binaries. 5 2018.

David Langlois, Ryo Saito, Daisuke Yamauchi, and Karim Noui. Scalar-tensor theories and modified gravity in the wake of GW170817. *Phys. Rev. D*, 97(6):061501, 2018. doi: 10.1103/PhysRevD.97.061501.

J. M. Lattimer and D. N. Schramm. Black-Hole-Neutron-Star Collisions. *The Astrophysical Journal, Letters*, 192:L145, September 1974. doi: 10.1086/181612.

J. M. Lattimer and D. N. Schramm. The tidal disruption of neutron stars by black holes in close binaries. *The Astrophysical Journal*, 210:549–567, December 1976. doi: 10.1086/154860.

J. M. Lattimer, F. Mackie, D. G. Ravenhall, and D. N. Schramm. The decompression of cold neutron star matter. *The Astrophysical Journal*, 213:225–233, April 1977. doi: 10.1086/155148.

James M. Lattimer and F. Douglas Swesty. A generalized equation of state for hot, dense matter. *Nuclear Physics A*, 535(2):331–376, 1991. ISSN 0375-9474. doi: https://doi.org/10.1016/0375-9474(91)90452-C. URL `https://www.sciencedirect.com/science/article/pii/037594749190452C`.

Françoise Launay. The great Paris Exhibition telescope of 1900. *Journal for the History of Astronomy*, 38(133):459–475, November 2007. doi: 10.1177/002182860703800404.

Jamie A. P. Law-Smith et al. Successful Common Envelope Ejection and Binary Neutron Star Formation in 3D Hydrodynamics. 11 2020.

Davide Lazzati. Precursor activity in bright long batse gamma-ray bursts. *Mon. Not. Roy. Astron. Soc.*, 357:722–731, 2005. doi: 10.1111/j.1365-2966.2005.08687.x.

Truong Le and Vedant Mehta. Revisiting the Redshift Distribution of Gamma Ray Bursts in the Swift Era. *Astrophys. J.*, 837(1):17, 2017. doi: 10.3847/1538-4357/aa5fa7.

William H Lee, Enrico Ramirez-Ruiz, and Diego López-Cámara. Phase transitions and he-synthesis-driven winds in neutrino cooled accretion disks: prospects for late flares in short gamma-ray bursts. *The Astrophysical Journal Letters*, 699(2):L93, 2009.

N. W. C. Leigh et al. On the rate of black hole binary mergers in galactic nuclei due to dynamical hardening. *Mon. Not. Roy. Astron. Soc.*, 474(4):5672–5683, 2018. doi: 10.1093/mnras/stx3134.

William R Leo. *Techniques for nuclear and particle physics experiments: a how-to approach*. Springer Science and Business Media, 2012.

Walter H. G. Lewin and Michiel van der Klis. *Compact Stellar X-ray Sources*, volume 39. 2006.

Li-Xin Li and Bohdan Paczynski. Transient events from neutron star mergers. *Astrophys. J. Lett.*, 507:L59, 1998. doi: 10.1086/311680.

Weidong Li et al. Sn 2002cx: the most peculiar known type ia supernova. *Publ. Astron. Soc. Pac.*, 115:453–473, 2003. doi: 10.1086/374200.

X. J. Li, Z. B. Zhang, X. L. Zhang, and H. Y. Zhen. Temporal Properties of Precursors, Main peaks and Extended Emissions of Short GRBs in the Third Swift/BAT GRB Catalog. *Astrophys. J. Suppl.*, 252(2):16, 2021. doi: 10.3847/1538-4365/abd3fd.

Sidney Liebes. Gravitational lenses. *Phys. Rev.*, 133:B835–B844, Feb 1964. doi: 10.1103/PhysRev.133.B835. URL https://link.aps.org/doi/10.1103/PhysRev.133.B835.

LIGO Scientific Collaboration and Virgo Collaboration. LIGO/Virgo S190425z: Identification of a GW compact binary merger candidate. *GRB Coordinates Network*, 24168: 1, January 2019a.

LIGO Scientific Collaboration and Virgo Collaboration. LIGO/Virgo S190814bv: Identification of a GW compact binary merger candidate. *GRB Coordinates Network*, 25324:1, August 2019b.

LIGO Scientific Collaboration and Virgo Collaboration. LIGO/Virgo S191213g: Identification of a GW compact binary merger candidate. *GRB Coordinates Network*, 26402: 1, December 2019c.

LIGO Scientific Collaboration and Virgo Collaboration. LIGO/Virgo S200105ae: A subthreshold GW compact binary merger candidate. *GRB Coordinates Network*, 26640: 1, January 2020a.

LIGO Scientific Collaboration and Virgo Collaboration. LIGO/Virgo S200115j: Identification of a GW compact binary merger candidate. *GRB Coordinates Network*, 26759: 1, January 2020b.

Lee Lindblom. Phase transitions and the mass-radius curves of relativistic stars. *Phys. Rev. D*, 58:024008, Jun 1998. doi: 10.1103/PhysRevD.58.024008. URL https://link.aps.org/doi/10.1103/PhysRevD.58.024008.

Lee Lindblom. Spectral representations of neutron-star equations of state. *Phys. Rev. D*, 82:103011, Nov 2010. doi: 10.1103/PhysRevD.82.103011. URL https://link.aps.org/doi/10.1103/PhysRevD.82.103011.

Lee Lindblom. Causal representations of neutron-star equations of state. *Phys. Rev. D*, 97:123019, Jun 2018. doi: 10.1103/PhysRevD.97.123019. URL https://link.aps.org/doi/10.1103/PhysRevD.97.123019.

Lee Lindblom and Nathaniel M. Indik. Spectral approach to the relativistic inverse stellar structure problem. *Phys. Rev. D*, 86:084003, Oct 2012. doi: 10.1103/PhysRevD.86.084003. URL https://link.aps.org/doi/10.1103/PhysRevD.86.084003.

Lee Lindblom and Nathaniel M. Indik. Spectral approach to the relativistic inverse stellar structure problem ii. *Phys. Rev. D*, 89:064003, Mar 2014. doi: 10.1103/PhysRevD.89.064003. URL https://link.aps.org/doi/10.1103/PhysRevD.89.064003.

GV Lipunova, ES Gorbovskoy, AI Bogomazov, and VM Lipunov. Population synthesis of gamma-ray bursts with precursor activity and the spinar paradigm. *Monthly Notices of the Royal Astronomical Society*, 397(3):1695–1704, 2009.

Michelle Lochner, Jason D. McEwen, Hiranya V. Peiris, Ofer Lahav, and Max K. Winter. Photometric Supernova Classification With Machine Learning. *Astrophys. J. Suppl.*, 225(2):31, 2016. doi: 10.3847/0067-0049/225/2/31.

Abraham Loeb. Electromagnetic Counterparts to Black Hole Mergers Detected by LIGO. *Astrophys. J. Lett.*, 819(2):L21, 2016. doi: 10.3847/2041-8205/819/2/L21.

Bruno Lopez, Stéphane Lagarde, Walter Jaffe, Romain Petrov, Markus Schöller, Pierre Antonelli, Udo Beckmann, Philippe Berio, Felix Bettonvil, Andreas Glindemann, et al. An overview of the matisse instrument—science, concept and current status. *The Messenger*, 157:5–12, 2014.

Geoffrey Lovelace, Matthew D. Duez, Francois Foucart, Lawrence E. Kidder, Harald P. Pfeiffer, Mark A. Scheel, and Béla Szilágyi. Massive disc formation in the tidal disruption of a neutron star by a nearly extremal black hole. *Class. Quant. Grav.*, 30:135004, 2013. doi: 10.1088/0264-9381/30/13/135004.

Geoffrey Lovelace et al. Nearly extremal apparent horizons in simulations of merging black holes. *Class. Quant. Grav.*, 32(6):065007, 2015. doi: 10.1088/0264-9381/32/6/065007.

A. G. Lyne and D. R. Lorimer. High birth velocities of radio pulsars. *Nature*, 369:127, 1994. doi: 10.1038/369127a0.

Ch L MacLeod, Ž Ivezić, CS Kochanek, S Kozłowski, B Kelly, E Bullock, A Kimball, B Sesar, D Westman, K Brooks, et al. Modeling the time variability of sdss stripe 82 quasars as a damped random walk. *The Astrophysical Journal*, 721(2):1014, 2010.

A Maeder. Evidences for a bifurcation in massive star evolution. the on-blue stragglers. *Astronomy and Astrophysics*, 178:159–169, 1987.

André Maeder and Georges Meynet. The evolution of rotating stars. *Annual Review of Astronomy and Astrophysics*, 38(1):143–190, 2000. doi: 10.1146/annurev.astro.38.1.143. URL https://doi.org/10.1146/annurev.astro.38.1.143.

Michele Maggiore. *Gravitational Waves. Vol. 1: Theory and Experiments*. Oxford Master Series in Physics. Oxford University Press, 2007. ISBN 978-0-19-857074-5, 978-0-19-852074-0.

B. Mailyan, Amitabh Nag, J. Dwyer, R. Said, M. Briggs, Oliver Roberts, M. Stanbro, and H. Rassoul. Gamma-ray and radio-frequency radiation from thunderstorms observed from space and ground. *Scientific Reports*, 10:7286, 04 2020. doi: 10.1038/s41598-020-63437-2.

Kazuo Makishima. Measuring Magnetic Fields of Neutron Stars. *Progress of Theoretical Physics Supplement*, 151:54–63, 05 2003. ISSN 0375-9687. doi: 10.1143/PTPS.151.54. URL https://doi.org/10.1143/PTPS.151.54.

C. Malacaria, P. Kretschmar, K. K. Madsen, C. A. Wilson-Hodge, Joel B. Coley, P. Jenke, A. A. Lutovinov, K. Pottschmidt, S. S. Tsygankov, and J. Wilms. The X-ray pulsar XTE J1858+034 observed with NuSTAR and Fermi/GBM: spectral and timing characterization plus a cyclotron line. *Astrophys. J.*, 909(2):153, 2021. doi: 10.3847/1538-4357/abddbc.

Rebecca G. Martin, Christopher A. Tout, and J. E. Pringle. Supernova kicks and misaligned Be star binaries. *Monthly Notices of the Royal Astronomical Society*, 397(3):1563–1576, 07 2009. ISSN 0035-8711. doi: 10.1111/j.1365-2966.2009.15031.x. URL https://doi.org/10.1111/j.1365-2966.2009.15031.x.

Andrew Matas et al. Aligned-spin neutron-star–black-hole waveform model based on the effective-one-body approach and numerical-relativity simulations. *Phys. Rev. D*, 102(4):043023, 2020. doi: 10.1103/PhysRevD.102.043023.

O. McBrien, S. J. Smartt, K. W. Smith, D. R. Young, J. Gillanders. S. Srivastav, P. Clark, D. O'Neill, M. Fulton, S. McLaughlin, K. C. Chambers, M. E. Huber, A. S. B. Schultz, T. de Boer, J. Bulger, J. Fairlamb, C. C. Lin, T. Lowe, E. Magnier, R. J. Wainscoat, M. Willman, A. Rest, C. Stubbs, T. W. Chen, and Pan-Starrs Collaboration. LIGO/Virgo S191213g: Pan-STARRS1 discovery of a potential optical counterpart. *GRB Coordinates Network*, 26485:1, December 2019.

L. McCuller et al. Frequency-Dependent Squeezing for Advanced LIGO. *Phys. Rev. Lett.*, 124(17):171102, 2020. doi: 10.1103/PhysRevLett.124.171102.

Patrick Neal McDermott, HM Van Horn, and CJ Hansen. Nonradial oscillations of neutron stars. *The Astrophysical Journal*, 325:725–748, 1988.

Gail C. McLaughlin and R. Surman. Prospects for obtaining an r-process from gamma ray burst disk winds. *Nucl. Phys. A*, 758:189–196, 2005. doi: 10.1016/j.nuclphysa.2005.05.036.

C. A. Meegan, G. J. Fishman, R. B. Wilson, W. S. Paciesas, G. N. Pendleton, J. M. Horack, M. N. Brock, and C. Kouveliotou. Spatial distribution of γ-ray bursts observed by BATSE. *Nature*, 355(6356):143–145, January 1992. doi: 10.1038/355143a0.

Charles Meegan, Giselher Lichti, P. N. Bhat, Elisabetta Bissaldi, Michael S. Briggs, Valerie Connaughton, Roland Diehl, Gerald Fishman, Jochen Greiner, Andrew S. Hoover, Alexander J. van der Horst, Andreas von Kienlin, R. Marc Kippen, Chryssa Kouveliotou, Sheila McBreen, W. S. Paciesas, Robert Preece, Helmut Steinle, Mark S. Wallace, Robert B. Wilson, and Colleen Wilson-Hodge. THEFERMIGAMMA-RAY BURST MONITOR. *The Astrophysical Journal*, 702(1):791–804, aug 2009. doi: 10.1088/0004-637x/702/1/791. URL https://doi.org/10.1088/0004-637x/702/1/791.

Cody Messick, Kent Blackburn, Patrick Brady, Patrick Brockill, Kipp Cannon, Romain Cariou, Sarah Caudill, Sydney J. Chamberlin, Jolien D. E. Creighton, Ryan Everett, Chad Hanna, Drew Keppel, Ryan N. Lang, Tjonnie G. F. Li, Duncan Meacher, Alex Nielsen, Chris Pankow, Stephen Privitera, Hong Qi, Surabhi Sachdev, Laleh Sadeghian, Leo Singer, E. Gareth Thomas, Leslie Wade, Madeline Wade, Alan Weinstein, and Karsten Wiesner. Analysis framework for the prompt discovery of compact binary mergers in gravitational-wave data. *Phys. Rev. D*, 95:042001, Feb 2017. doi: 10.1103/PhysRevD.95.042001. URL https://link.aps.org/doi/10.1103/PhysRevD.95.042001.

P. Meszaros and M. J. Rees. Relativistic Fireballs and Their Impact on External Matter: Models for Cosmological Gamma-Ray Bursts. *The Astrophysical Journal*, 405:278, March 1993. doi: 10.1086/172360.

P. Meszaros and M. J. Rees. Optical and long wavelength afterglow from gamma-ray bursts. *Astrophys. J.*, 476:232–237, 1997. doi: 10.1086/303625.

P. Meszaros, P. Laguna, and M. J. Rees. Gas dynamics of relativistically expanding gamma-ray burst sources: Kinematics, energetics, magnetic fields and efficiency. *Astrophys. J.*, 415:181–190, 1993. doi: 10.1086/173154.

P. Meszaros, M. J. Rees, and R. A. M. J. Wijers. Viewing angle and environment effects in GRB: Sources of afterglow diversity. *Astrophys. J.*, 499:301, 1998. doi: 10.1086/305635.

Peter Meszaros. Gamma-Ray Bursts. *Rept. Prog. Phys.*, 69:2259–2322, 2006. doi: 10.1088/0034-4885/69/8/R01.

B. D. Metzger, A. L. Piro, and E. Quataert. Neutron-rich freeze-out in viscously spreading accretion discs formed from compact object mergers. *Monthly Notices of the Royal Astronomical Society*, 396(1):304–314, 06 2009. ISSN 0035-8711. doi: 10.1111/j.1365-2966.2008.14380.x. URL https://doi.org/10.1111/j.1365-2966.2008.14380.x.

B. D. Metzger, G. Martínez-Pinedo, S. Darbha, E. Quataert, A. Arcones, D. Kasen, R. Thomas, P. Nugent, I. V. Panov, and N. T. Zinner. Electromagnetic counterparts of compact object mergers powered by the radioactive decay of r-process nuclei. *Monthly Notices of the Royal Astronomical Society*, 406(4):2650–2662, 08 2010a. ISSN 0035-8711. doi: 10.1111/j.1365-2966.2010.16864.x. URL https://doi.org/10.1111/j.1365-2966.2010.16864.x.

BD Metzger, G Martínez-Pinedo, S Darbha, E Quataert, Almudena Arcones, D Kasen, R Thomas, P Nugent, IV Panov, and NT Zinner. Electromagnetic counterparts of compact object mergers powered by the radioactive decay of r-process nuclei. *Monthly Notices of the Royal Astronomical Society*, 406(4):2650–2662, 2010b.

Brian D. Metzger and Rodrigo Fernández. Red or blue? A potential kilonova imprint of the delay until black hole formation following a neutron star merger. *Mon. Not. Roy. Astron. Soc.*, 441:3444–3453, 2014. doi: 10.1093/mnras/stu802.

M. R. Metzger, S. G. Djorgovski, S. R. Kulkarni, C. C. Steidel, K. L. Adelberger, D. A. Frail, E. Costa, and F. Frontera. Spectral constraints on the redshift of the optical counterpart to the γ-ray burst of 8 May 1997. *Nature*, 387(6636):878–880, June 1997. doi: 10.1038/43132.

Bradley S. Meyer. Decompression of Initially Cold Neutron Star Matter: A Mechanism for the r-Process? *The Astrophysical Journal*, 343:254, August 1989. doi: 10.1086/167702.

S. Migliari and R. P. Fender. Jets in neutron star X-ray binaries: a comparison with black holes. *Monthly Notices of the Royal Astronomical Society*, 366(1):79–91, 02 2006. ISSN 0035-8711. doi: 10.1111/j.1365-2966.2005.09777.x. URL https://doi.org/10.1111/j.1365-2966.2005.09777.x.

Andrea Miglio, Josefina Montalbán, and Arlette Noels, editors. *Proceedings, Red Giants as Probes of the Structure and Evolution of the Milky Way: Rome, Italy, November 15-17, 2010*, 2012.

M. C. Miller et al. PSR J0030+0451 Mass and Radius from $NICER$ Data and Implications for the Properties of Neutron Star Matter. *Astrophys. J. Lett.*, 887(1):L24, 2019a. doi: 10.3847/2041-8213/ab50c5.

MC Miller, Frederick K Lamb, AJ Dittmann, Slavko Bogdanov, Zaven Arzoumanian, Keith C Gendreau, S Guillot, AK Harding, WCG Ho, JM Lattimer, et al. Psr j0030+ 0451 mass and radius from nicer data and implications for the properties of neutron star matter. *The Astrophysical Journal Letters*, 887(1):L24, 2019b.

I. F. Mirabel and L. F. Rodriguez. Superluminal Sources in the Galaxy. In C. Winkler, T. J. L. Courvoisier, and Ph. Durouchoux, editors, *The Transparent Universe*, volume 382 of *ESA Special Publication*, page 151, January 1997.

Razmik Mirzoyan. Major Changes in Understanding of GRBs: Discovery of Teraelectron Volt Gamma-Ray Emission. *PoS*, ICRC2019:010, 2021. doi: 10.22323/1.358.0010.

Kazuhisa Mitsuda, Mark Bautz, Hajime Inoue, Richard L. Kelley, Katsuji Koyama, Hideyo Kunieda, Kazuo Makishima, Yoshiaki Ogawara, Robert Petre, Tadayuki Takahashi, Hiroshi Tsunemi, Nicholas E. White, Naohisa Anabuki, Lorella Angelini, Keith Arnaud, Hisamitsu Awaki, Aya Bamba, Kevin Boyce, Gregory V. Brown, Kai-Wing Chan, Jean Cottam, Tadayasu Dotani, John Doty, Ken Ebisawa, Yuichiro Ezoe, Andrew C. Fabian, Enectali Figueroa, Ryuichi Fujimoto, Yasushi Fukazawa, Tae Furusho, Akihiro Furuzawa, Keith Gendreau, Richard E. Griffiths, Yoshito Haba, Kenji Hamaguchi, Ilana Harrus, Günther Hasinger, Isamu Hatsukade, Kiyoshi Hayashida, Patrick J. Henry, Junko S. Hiraga, Stephen S. Holt, Ann Hornschemeier, John P. Hughes, Una Hwang, Manabu Ishida, Yoshitaka Ishisaki, Naoki Isobe, Masayuki Itoh, Naoko Iyomoto, Steven M. Kahn, Tuneyoshi Kamae, Hideaki Katagiri, Jun Kataoka, Haruyoshi Katayama, Nobuyuki Kawai, Caroline Kilbourne, Kenzo Kinugasa, Steve Kissel, Shunji Kitamoto, Mitsuhiro Kohama, Takayoshi Kohmura, Motohide Kokubun, Taro Kotani, Jun'ichi Kotoku, Aya Kubota, Greg M. Madejski, Yoshitomo Maeda, Fumiyoshi Makino, Alex Markowitz, Chiho Matsumoto, Hironori Matsumoto, Masaru Matsuoka, Kyoko Matsushita, Dan McCammon, Tatehiko Mihara, Kazutami Misaki, Emi Miyata, Tsunefumi Mizuno, Koji Mori, Hideyuki Mori, Mikio Morii, Harvey Moseley, Koji Mukai, Hiroshi Murakami, Toshio Murakami, Richard Mushotzky, Fumiaki Nagase, Masaaki Namiki, Hitoshi Negoro, Kazuhiro Nakazawa, John A. Nousek, Takashi Okajima, yasushi ogasaka, Takaya Ohashi, Tai Oshima,

Naomi Ota, Masanobu Ozaki, Hideki Ozawa, Arvind N. Parmar, William D. Pence, F. Scott Porter, James N. Reeves, George R. Ricker, Ikuya Sakurai, Wilton T. Sanders, Atsushi Senda, Peter Serlemitsos, Ryo Shibata, Yang Soong, Randall Smith, Motoko Suzuki, Andrew E. Szymkowiak, Hiromitsu Takahashi, Toru Tamagawa, Keisuke Tamura, Takayuki Tamura, Yasuo Tanaka, Makoto Tashiro, Yuzuru Tawara, Yukikatsu Terada, Yuichi Terashima, Hiroshi Tomida, Ken'ichi Torii, Yohko Tsuboi, Masahiro Tsujimoto, Takeshi Go Tsuru, Martin J. L. Turner, Yoshihiro Ueda, Shiro Ueno, Masaru Ueno, Shin'ichiro Uno, Yuji Urata, Shin Watanabe, Norimasa Yamamoto, Kazutaka Yamaoka, Noriko Y. Yamasaki, Koujun Yamashita, Makoto Yamauchi, Shigeo Yamauchi, Tahir Yaqoob, Daisuke Yonetoku, and Atsumasa Yoshida. The X-Ray Observatory Suzaku. *Publications of the Astronomical Society of Japan*, 59(sp1): S1–S7, 01 2007. ISSN 0004-6264. doi: 10.1093/pasj/59.sp1.S1. URL `https://doi.org/10.1093/pasj/59.sp1.S1`.

Robert Mochkovitch, Frédéric Daigne, Raphaël Duque, and Hannachi Zitouni. Prospects for kilonova signals in the gravitational-wave era. *Astron. Astrophys.*, 651: A83, 2021. doi: 10.1051/0004-6361/202140689.

Brenna Mockler, James Guillochon, and Enrico Ramirez-Ruiz. Weighing Black Holes using Tidal Disruption Events. *Astrophys. J.*, 872(2):151, 2019. doi: 10.3847/1538-4357/ab010f.

Thomas Andrew Moore. *A general relativity workbook*. University Science Books Mill Valley, California, 2013.

Jeffrey S. Morgan, Nicholas Kaiser, Vincent Moreau, David Anderson, and William Burgett. Design Differences between the Pan-STARRS PS1 and PS2 Telescopes. *Proc. SPIE Int. Soc. Opt. Eng.*, 8444:0H, 2012. doi: 10.1117/12.926646.

Elias R. Most and Alexander A. Philippov. Electromagnetic precursors to gravitational wave events: Numerical simulations of flaring in pre-merger binary neutron star magnetospheres. *Astrophys. J. Lett.*, 893(1):L6, 2020. doi: 10.3847/2041-8213/ab8196.

Elias R. Most, L. Jens Papenfort, Lukas R. Weih, and Luciano Rezzolla. A lower bound on the maximum mass if the secondary in GW190814 was once a rapidly spinning neutron star. *Mon. Not. Roy. Astron. Soc.*, 499(1):L82–L86, 2020. doi: 10.1093/mnrasl/slaa168.

S. Mukherjee, R. Obaid, and B. Matkarimov. Classification of glitch waveforms in gravitational wave detector characterization. *J. Phys. Conf. Ser.*, 243:012006, 2010. doi: 10.1088/1742-6596/243/1/012006.

Nikhil Mukund, Sheelu Abraham, Shivaraj Kandhasamy, Sanjit Mitra, and Ninan Sajeeth Philip. Transient Classification in LIGO data using Difference Boosting Neural Network. *Phys. Rev. D*, 95(10):104059, 2017. doi: 10.1103/PhysRevD.95.104059.

T. Murakami, H. Inoue, J. Nishimura, J. van Paradijs, and E. E. Fenimore. A γ-ray burst preceded by X-ray activity. *Nature*, 350(6319):592–594, April 1991. doi: 10.1038/350592a0.

Norman Murray. Star formation efficiencies and lifetimes of giant molecular clouds in the milky way. *The Astrophysical Journal*, 729, 07 2010. doi: 10.1088/0004-637X/729/2/133.

Daniel Muthukrishna, Gautham Narayan, Kaisey S. Mandel, Rahul Biswas, and Renée Hložek. RAPID: Early Classification of Explosive Transients using Deep Learning. *Publ. Astron. Soc. Pac.*, 131(1005):118002, 2019. doi: 10.1088/1538-3873/ab1609.

Ehud Nakar. Short-hard gamma-ray bursts. *Physics Reports*, 442(1-6):166–236, April 2007. doi: 10.1016/j.physrep.2007.02.005.

Ehud Nakar. Short-Hard Gamma-Ray Bursts. *Phys. Rept.*, 442:166–236, 2007. doi: 10.1016/j.physrep.2007.02.005.

Yoshiyuki Nakashima, Susumu Minato, Minoru Kawano, Tadashi Tsujimoto, and Kousuke Katsurayama. Gamma-ray Energy Spectra Observed around a Nuclear Reactor. *Journal of Radiation Research*, 12(3-4):138–147, 09 1971. ISSN 0449-3060. doi: 10.1269/jrr.12.138. URL `https://doi.org/10.1269/jrr.12.138`.

P.J. Napier, D.S. Bagri, B.G. Clark, A.E.E. Rogers, J.D. Romney, A.R. Thompson, and R.C. Walker. The very long baseline array. *Proceedings of the IEEE*, 82(5):658–672, 1994. doi: 10.1109/5.284733.

Ramesh Narayan and Matthias Bartelmann. Lectures on gravitational lensing. In *13th Jerusalem Winter School in Theoretical Physics: Formation of Structure in the Universe*, 6 1996.

Ramesh Narayan, Shoji Kato, and Fumio Honma. Global structure and dynamics of advection-dominated accretion flows around black holes. *The Astrophysical Journal*, 476(1):49–60, feb 1997. doi: 10.1086/303591. URL `https://doi.org/10.1086/303591`.

Vsevolod Nedora, Federico Schianchi, Sebastiano Bernuzzi, David Radice, Boris Daszuta, Andrea Endrizzi, Albino Perego, Aviral Prakash, and Francesco Zappa. Map-

ping dynamical ejecta and disk masses from numerical relativity simulations of neutron star mergers. 11 2020.

F. J. Neubauer. A short history of the Lick Observatory. *Popular Astronomy*, 58:201, May 1950.

Torsten Neubert, Nikolai Ostgaard, Victor Reglero, O. Chanrion, Matthias Heumesser, Krystallia Dimitriadou, F. Christiansen, Carl budtz jørgensen, Irfan Kuvvetli, Ib Rasmussen, Andrew Mezentsev, Martino Marisaldi, Kjetil Ullaland, Georgi Genov, shiming yang, Pavlo Kochkin, Javier Navarro-González, Paul Connell, and Chris Eyles. A terrestrial gamma-ray flash and ionospheric ultraviolet emissions powered by lightning. *Science*, 367:eaax3872, 12 2019. doi: 10.1126/science.aax3872.

J. Newling, M. Varughese, B. Bassett, H. Campbell, R. Hlozek, M. Kunz, H. Lampeitl, B. Martin, R. Nichol, D. Parkinson, and M. Smith. Statistical classification techniques for photometric supernova typing. *Monthly Notices of the Royal Astronomical Society*, 414(3):1987–2004, 06 2011. ISSN 0035-8711. doi: 10.1111/j.1365-2966.2011.18514.x. URL https://doi.org/10.1111/j.1365-2966.2011.18514.x.

Matt Nicholl, James Guillochon, and Edo Berger. The Magnetar Model for Type I Superluminous Supernovae. I. Bayesian Analysis of the Full Multicolor Light-curve Sample with MOSFiT. *Astrophys. J.*, 850(1):55, 2017. doi: 10.3847/1538-4357/aa9334.

Tetsuo Nishimura. Infrared detector for mid-infrared astronomy. In T. Kogure and A. T. Tokunaga, editors, *Japanese National Large Telescope and Related Engineering Developments*, pages 325–332, Dordrecht, 1989. Springer Netherlands. ISBN 978-94-017-2003-8.

Atsushi Nishizawa, Masa-aki Sakagami, and Seiji Kawamura. Quantum noise in differential-type gravitational-wave interferometer and signal recycling. *Phys. Rev. D*, 76:042002, 2007. doi: 10.1103/PhysRevD.76.042002.

Alexander Harvey Nitz. Distinguishing short duration noise transients in LIGO data to improve the PyCBC search for gravitational waves from high mass binary black hole mergers. *Class. Quant. Grav.*, 35(3):035016, 2018. doi: 10.1088/1361-6382/aaa13d.

Shin'ichi Nojiri and Sergei D. Odintsov. Cosmological bound from the neutron star merger gw170817 in scalar–tensor and f(r) gravity theories. *Physics Letters B*, 779: 425–429, 2018. ISSN 0370-2693. doi: https://doi.org/10.1016/j.physletb.2018.01.078. URL https://www.sciencedirect.com/science/article/pii/S0370269318300960.

Ken'ichi Nomoto. The fate of accreting white dwarfs: Type i supernovae vs. collapse. *Progress in Particle and Nuclear Physics*, 17:249–266, 1986. ISSN 0146-6410. doi: https://doi.org/10.1016/0146-6410(86)90020-7. URL https://www.sciencedirect.com/science/article/pii/0146641086900207.

Melania Nynka, John J. Ruan, Daryl Haggard, and Phil A. Evans. Fading of the x-ray afterglow of neutron star merger GW170817/GRB 170817a at 260 days. *The Astrophysical Journal*, 862(2):L19, jul 2018. doi: 10.3847/2041-8213/aad32d. URL https://doi.org/10.3847/2041-8213/aad32d.

Roland Oechslin, H. T. Janka, and A. Marek. Relativistic neutron star merger simulations with non-zero temperature equations of state. 1. Variation of binary parameters and equation of state. *Astron. Astrophys.*, 467:395, 2007. doi: 10.1051/0004-6361:20066682.

Ryan M. O'Leary, Bence Kocsis, and Abraham Loeb. Gravitational waves from scattering of stellar-mass black holes in galactic nuclei. *Mon. Not. Roy. Astron. Soc.*, 395 (4):2127–2146, 2009. doi: 10.1111/j.1365-2966.2009.14653.x.

J. R. Oppenheimer and G. M. Volkoff. On massive neutron cores. *Phys. Rev.*, 55:374–381, Feb 1939. doi: 10.1103/PhysRev.55.374. URL https://link.aps.org/doi/10.1103/PhysRev.55.374.

Serguei Ossokine et al. Multipolar Effective-One-Body Waveforms for Precessing Binary Black Holes: Construction and Validation. *Phys. Rev. D*, 102(4):044055, 2020. doi: 10.1103/PhysRevD.102.044055.

B. Paczynski. Gamma-ray bursters at cosmological distances. *Astrophysical Journal, Letters*, 308:L43–L46, September 1986. doi: 10.1086/184740.

Bohdan Paczynski. Super-Eddington Winds from Neutron Stars. *The Astrophysical Journal, Letters*, 363:218, November 1990. doi: 10.1086/169332.

Bohdan Paczyński. Are Gamma-Ray Bursts in Star-Forming Regions? *The Astrophysical Journal, Letters*, 494(1):L45–L48, February 1998. doi: 10.1086/311148.

Bohdan Paczynski and James E. Rhoads. Radio transients from gamma-ray bursters. *Astrophys. J. Lett.*, 418:L5, 1993. doi: 10.1086/187102.

K. L. Page et al. GRB 061121: Broadband spectral evolution through the prompt and afterglow phases of a bright burst. *Astrophys. J.*, 663:1125–1138, 2007. doi: 10.1086/518821.

David M. Palmer et al. Gamma-ray observations of a giant flare from the magnetar SGR 1806-20. *Nature*, 434:1107–1109, 2005. doi: 10.1038/nature03525.

Geoffrey N Pendleton, Michael S Briggs, R Marc Kippen, William S Paciesas, Mark Stollberg, Pete Woods, Charles A Meegan, Gerald J Fishman, Mike L McCollough, and Valerie Connaughton. The structure and evolution of locburst: The batse burst location algorithm. *The Astrophysical Journal*, 512(1):362, 1999.

A. Perego, S. Rosswog, R. M. Cabezón, O. Korobkin, R. Käppeli, A. Arcones, and M. Liebendörfer. Neutrino-driven winds from neutron star merger remnants. *Monthly Notices of the Royal Astronomical Society*, 443(4):3134–3156, 08 2014. ISSN 0035-8711. doi: 10.1093/mnras/stu1352. URL https://doi.org/10.1093/mnras/stu1352.

Daniel Perrefort, Yike Zhang, Lluís Galbany, WM Wood-Vasey, and Santiago González-Gaitán. A template-based approach to the photometric classification of sn 1991bg-like supernovae in the sdss-ii supernova survey. *The Astrophysical Journal*, 904(2):156, 2020.

P. C. Peters. Gravitational radiation and the motion of two point masses. *Phys. Rev.*, 136:B1224–B1232, Nov 1964. doi: 10.1103/PhysRev.136.B1224. URL https://link.aps.org/doi/10.1103/PhysRev.136.B1224.

C.J. Pethick, D.G. Ravenhall, and C.P. Lorenz. The inner boundary of a neutron-star crust. *Nuclear Physics A*, 584(4):675–703, 1995. ISSN 0375-9474. doi: https://doi.org/10.1016/0375-9474(94)00506-I. URL https://www.sciencedirect.com/science/article/pii/037594749400506I.

E. Pian et al. Spectroscopic identification of r-process nucleosynthesis in a double neutron star merger. *Nature*, 551:67–70, 2017. doi: 10.1038/nature24298.

J. D. R. Pierel et al. Extending Supernova Spectral Templates for Next-Generation Space Telescope Observations. *Publ. Astron. Soc. Pac.*, 130(993):114504, 2018. doi: 10.1088/1538-3873/aadb7a.

GL Pilbratt, JR Riedinger, T Passvogel, G Crone, D Doyle, U Gageur, AM Heras, C Jewell, L Metcalfe, S Ott, et al. Herschel space observatory-an esa facility for far-infrared and submillimetre astronomy. *Astronomy and Astrophysics*, 518:L1, 2010.

Tsvi Piran. The physics of gamma-ray bursts. *Rev. Mod. Phys.*, 76:1143–1210, Jan 2005. doi: 10.1103/RevModPhys.76.1143. URL https://link.aps.org/doi/10.1103/RevModPhys.76.1143.

Tsvi Piran, Ehud Nakar, and Stephan Rosswog. The electromagnetic signals of compact binary mergers. *Monthly Notices of the Royal Astronomical Society*, 430(3):2121–2136, 02 2013. ISSN 0035-8711. doi: 10.1093/mnras/stt037. URL https://doi.org/10.1093/mnras/stt037.

Luigi Piro et al. Probing the environment in gamma-ray bursts: The Case of an x-ray precursor, afterglow late onset and wind vs constant density profile in GRB 011121 and GRB 011211. *Astrophys. J.*, 623:314–324, 2005. doi: 10.1086/428377.

M. H. Poincaré. Sur la dynamique de l'électron. *Rendiconti del Circolo Matematico di Palermo (1884-1940)*, 21(1):129–175, Dec 1906. ISSN 0009-725X. doi: 10.1007/BF03013466. URL https://doi.org/10.1007/BF03013466.

Eric Poisson. Gravitational waves from inspiraling compact binaries: The quadrupole-moment term. *Phys. Rev. D*, 57:5287–5290, Apr 1998. doi: 10.1103/PhysRevD.57.5287. URL https://link.aps.org/doi/10.1103/PhysRevD.57.5287.

Eric Poisson and Clifford M Will. *Gravity: Newtonian, post-newtonian, relativistic*. Cambridge University Press, 2014.

Jade Powell, Daniele Trifirò, Elena Cuoco, Ik Siong Heng, and Marco Cavaglià. Classification methods for noise transients in advanced gravitational-wave detectors. *Classical and Quantum Gravity*, 32(21):215012, oct 2015. doi: 10.1088/0264-9381/32/21/215012. URL https://doi.org/10.1088/0264-9381/32/21/215012.

Geraint Pratten et al. Computationally efficient models for the dominant and subdominant harmonic modes of precessing binary black holes. *Phys. Rev. D*, 103(10):104056, 2021. doi: 10.1103/PhysRevD.103.104056.

William H. Press. Long Wave Trains of Gravitational Waves from a Vibrating Black Hole. *The Astrophysical Journal, Letters*, 170:L105, December 1971. doi: 10.1086/180849.

Frans Pretorius. Evolution of binary black hole spacetimes. *Phys. Rev. Lett.*, 95:121101, 2005. doi: 10.1103/PhysRevLett.95.121101.

M Prijatelj, J Degallaix, H Grote, J Leong, C Affeldt, S Hild, H Lück, J Slutsky, H Wittel, K Strain, and K Danzmann. The output mode cleaner of GEO 600. *Classical and Quantum Gravity*, 29(5):055009, feb 2012. doi: 10.1088/0264-9381/29/5/055009. URL https://doi.org/10.1088/0264-9381/29/5/055009.

Stephen Privitera, Satyanarayan R. P. Mohapatra, Parameswaran Ajith, Kipp Cannon, Nickolas Fotopoulos, Melissa A. Frei, Chad Hanna, Alan J. Weinstein, and John T.

Whelan. Improving the sensitivity of a search for coalescing binary black holes with nonprecessing spins in gravitational wave data. *Phys. Rev. D*, 89(2):024003, 2014. doi: 10.1103/PhysRevD.89.024003.

Brian Punsly. EVIDENCE OF THE DYNAMICS OF RELATIVISTIC JET LAUNCHING IN QUASARS. *The Astrophysical Journal*, 806(1):47, jun 2015. doi: 10.1088/0004-637x/806/1/47. URL https://doi.org/10.1088/0004-637x/806/1/47.

Michael Pürrer. Frequency domain reduced order models for gravitational waves from aligned-spin compact binaries. *Class. Quant. Grav.*, 31(19):195010, 2014. doi: 10.1088/0264-9381/31/19/195010.

A. F. Pérez-Sánchez, W. H. T. Vlemmings, D. Tafoya, and J. M. Chapman. A synchrotron jet from a post-asymptotic giant branch star. *Monthly Notices of the Royal Astronomical Society: Letters*, 436(1):L79–L83, 09 2013. ISSN 1745-3925. doi: 10.1093/mnrasl/slt117. URL https://doi.org/10.1093/mnrasl/slt117.

Novi Quadrianto, Kristian Kersting, and Zhao Xu. *Gaussian Process*, pages 428–439. Springer US, Boston, MA, 2010. ISBN 978-0-387-30164-8. doi: 10.1007/978-0-387-30164-8_324. URL https://doi.org/10.1007/978-0-387-30164-8_324.

Volker Quetschke. Electro-optic modulators and modulation for enhanced ligo and beyond. *Coherent Optical Technologies and Applications, COTA 2008*, 07 2008. doi: 10.1364/COTA.2008.CMC1.

David Radice, Filippo Galeazzi, Jonas Lippuner, Luke F. Roberts, Christian D. Ott, and Luciano Rezzolla. Dynamical mass ejection from binary neutron star mergers. *Monthly Notices of the Royal Astronomical Society*, 460(3):3255–3271, 05 2016. ISSN 0035-8711. doi: 10.1093/mnras/stw1227. URL https://doi.org/10.1093/mnras/stw1227.

David Radice, Albino Perego, Kenta Hotokezaka, Steven A. Fromm, Sebastiano Bernuzzi, and Luke F. Roberts. Binary Neutron Star Mergers: Mass Ejection, Electromagnetic Counterparts and Nucleosynthesis. *Astrophys. J.*, 869(2):130, 2018a. doi: 10.3847/1538-4357/aaf054.

David Radice, Albino Perego, Francesco Zappa, and Sebastiano Bernuzzi. GW170817: Joint constraint on the neutron star equation of state from multimessenger observations. *The Astrophysical Journal*, 852(2):L29, jan 2018b. doi: 10.3847/2041-8213/aaa402. URL https://doi.org/10.3847/2041-8213/aaa402.

Bhoomika Rajput, C. S. Stalin, and Suvendu Rakshit. Long term γ-ray variability of blazars. *Astron. Astrophys.*, 634:A80, 2020. doi: 10.1051/0004-6361/201936769.

Salvatore Rampone, Vincenzo Pierro, Luigi Troiano, and Innocenzo M Pinto. Neural network aided glitch-burst discrimination and glitch classification. *International Journal of Modern Physics C*, 24(11):1350084, 2013.

F. A. Rasio, C. A. Tout, S. H. Lubow, and M. Livio. Tidal decay of close planetary orbits. *Astrophys. J.*, 470:1187, 1996. doi: 10.1086/177941.

Frederic A. Rasio and Mario Livio. On the formation and evolution of common envelope systems. *Astrophys. J.*, 471:366, 1996. doi: 10.1086/177975.

Jocelyn S. Read, Charalampos Markakis, Masaru Shibata, K ōji Uryū, Jolien D. E. Creighton, and John L. Friedman. Measuring the neutron star equation of state with gravitational wave observations. *Phys. Rev. D*, 79:124033, Jun 2009. doi: 10.1103/PhysRevD.79.124033. URL https://link.aps.org/doi/10.1103/PhysRevD.79.124033.

Jocelyn S. Read, Luca Baiotti, Jolien D. E. Creighton, John L. Friedman, Bruno Giacomazzo, Koutarou Kyutoku, Charalampos Markakis, Luciano Rezzolla, Masaru Shibata, and Keisuke Taniguchi. Matter effects on binary neutron star waveforms. *Phys. Rev. D*, 88:044042, Aug 2013. doi: 10.1103/PhysRevD.88.044042. URL https://link.aps.org/doi/10.1103/PhysRevD.88.044042.

R. C. Reedy. Backgrounds in Bismuth Germanate (BGO) Gamma-Ray Spectrometers in Space. In *Lunar and Planetary Science Conference*, Lunar and Planetary Science Conference, page 1917, March 2010.

M. J. Rees and P. Meszaros. Unsteady outflow models for cosmological gamma-ray bursts. *Astrophys. J. Lett.*, 430:L93–L96, 1994. doi: 10.1086/187446.

M. J. Rees and P. Mészáros. Relativistic fireballs: energy conversion and time-scales. *Monthly Notices of the Royal Astronomical Society*, 258(1):41P–43P, 09 1992. ISSN 0035-8711. doi: 10.1093/mnras/258.1.41P. URL https://doi.org/10.1093/mnras/258.1.41P.

Martin J. Rees. Tidal disruption of stars by black holes of 10^6-10^8 solar masses in nearby galaxies. *Nature*, 333(6173):523–528, June 1988. doi: 10.1038/333523a0.

Daniel E. Reichart. The redshift of grb 970508. *Astrophys. J. Lett.*, 495:L99, 1998. doi: 10.1086/311222.

N. Remoue, K. Lacombe, C. Amoros, D. Barret, P. Mandrou, and R. Pons. Selection of cdte detectors for the detection plane of the eclairs gamma-ray burst detector. *Nuclear Instruments and Methods in Physics Research Section A: Accelerators, Spectrometers, Detectors and Associated Equipment*, 610(1): 287–290, 2009. ISSN 0168-9002. doi: https://doi.org/10.1016/j.nima.2009.05.162. URL https://www.sciencedirect.com/science/article/pii/S0168900209011012. New Developments In Photodetection NDIP08.

W. Rindler. Visual Horizons in World Models. *Monthly Notices of the Royal Astronomical Society*, 116(6):662–677, 12 1956. ISSN 0035-8711. doi: 10.1093/mnras/116.6.662. URL https://doi.org/10.1093/mnras/116.6.662.

L. F. Roberts, D. Kasen, W. H. Lee, and E. Ramirez-Ruiz. ELECTROMAGNETIC TRANSIENTS POWERED BY NUCLEAR DECAY IN THE TIDAL TAILS OF COALESCING COMPACT BINARIES. *The Astrophysical Journal*, 736(1):L21, jul 2011. doi: 10.1088/2041-8205/736/1/l21. URL https://doi.org/10.1088/2041-8205/736/1/l21.

Antoni Rogalski. History of infrared detectors. *Opto-Electronics Review*, 20(3):279–308, 2012.

A. Romero-Rodríguez, A. Allocca, A. Chiummo, M. Martínez, Ll M. Mir, and H. Yamamoto. Determination of the light exposure on the photodiodes of a new instrumented baffle for the Virgo input mode cleaner end-mirror. *Class. Quant. Grav.*, 38(4):045002, 2021. doi: 10.1088/1361-6382/abce6b.

I. M. Romero-Shaw et al. Bayesian inference for compact binary coalescences with bilby: validation and application to the first LIGO–Virgo gravitational-wave transient catalogue. *Mon. Not. Roy. Astron. Soc.*, 499(3):3295–3319, 2020. doi: 10.1093/mnras/staa2850.

Matts Roos. Sources of gamma radiation in a reactor core. *Journal of Nuclear Energy. Part B. Reactor Technology*, 1(2):98–104, 1959. ISSN 0368-3273. doi: https://doi.org/10.1016/S0368-3273(15)30005-5. URL https://www.sciencedirect.com/science/article/pii/S0368327315300055.

Andrea Rossi et al. The peculiar short-duration GRB 200826A and its supernova. 5 2021.

S. Rosswog, M. Liebendoerfer, F. K. Thielemann, M. B. Davies, W. Benz, and T. Piran. Mass ejection in neutron star mergers. *Astron. Astrophys.*, 341:499–526, 1999.

Stephan Rosswog. The dynamic ejecta of compact object mergers and eccentric collisions. *Philosophical transactions. Series A, Mathematical, physical, and engineering sciences*, 371:20120272, 06 2013. doi: 10.1098/rsta.2012.0272.

Christian Röver, Renate Meyer, Gianluca M Guidi, Andrea Viceré, and Nelson Christensen. Coherent bayesian analysis of inspiral signals. *Classical and Quantum Gravity*, 24(19):S607, 2007.

M. Ruderman. Theories of gamma -ray bursts. In P. G. Bergman, E. J. Fenyves, and L. Motz, editors, *Seventh Texas Symposium on Relativistic Astrophysics*, volume 262, pages 164–180, October 1975. doi: 10.1111/j.1749-6632.1975.tb31430.x.

M. H. Ruffert, H. T. Janka, and Gerhard Schaefer. Coalescing neutron stars: A Step towards physical models. 1: Hydrodynamic evolution and gravitational wave emission. *Astron. Astrophys.*, 311:532–566, 1996.

George B. Rybicki and Alan P. Lightman. *Radiative processes in astrophysics*. 1979.

C Sailer, B Lubsandorzhiev, C Strandhagen, and J Jochum. Low temperature light yield measurements in nai and nai (tl). *The European Physical Journal C*, 72(6):1–4, 2012.

Jeremy Sakstein and Bhuvnesh Jain. Implications of the Neutron Star Merger GW170817 for Cosmological Scalar-Tensor Theories. *Phys. Rev. Lett.*, 119(25): 251303, 2017. doi: 10.1103/PhysRevLett.119.251303.

L. Santamaría, F. Ohme, P. Ajith, B. Brügmann, N. Dorband, M. Hannam, S. Husa, P. Mösta, D. Pollney, C. Reisswig, E. L. Robinson, J. Seiler, and B. Krishnan. Matching post-newtonian and numerical relativity waveforms: Systematic errors and a new phenomenological model for nonprecessing black hole binaries. *Phys. Rev. D*, 82:064016, Sep 2010. doi: 10.1103/PhysRevD.82.064016. URL `https://link.aps.org/doi/10.1103/PhysRevD.82.064016`.

Reem Sari and Tsvi Piran. Hydrodynamic time scales and temporal structure of GRBs. *Astrophys. J. Lett.*, 455:L143, 1995. doi: 10.1086/309835.

Re'em Sari, Ramesh Narayan, and Tsvi Piran. Cooling time scales and temporal structure of gamma-ray bursts. *Astrophys. J.*, 473:204, 1996. doi: 10.1086/178136.

Re'em Sari, Tsvi Piran, and Jules Halpern. Jets in GRBs. *Astrophys. J. Lett.*, 519:L17, 1999. doi: 10.1086/312109.

V. Savchenko et al. INTEGRAL Detection of the First Prompt Gamma-Ray Signal Coincident with the Gravitational-wave Event GW170817. *Astrophys. J. Lett.*, 848(2): L15, 2017. doi: 10.3847/2041-8213/aa8f94.

Bradley E. Schaefer, D. Palmer, B. L. Dingus, E. J. Schneid, V. Schoenfelder, J. Ryan, C. Winkler, L. Hanlon, R. M. Kippen, and A. Connors. Gamma-Ray–Burst Spectral Shapes from 2 keV to 500 MeV. *The Astrophysical Journal*, 492(2):696–702, January 1998. doi: 10.1086/305058.

Gerhard Schäfer and Piotr Jaranowski. Hamiltonian formulation of general relativity and post-Newtonian dynamics of compact binaries. *Living Rev. Rel.*, 21(1):7, 2018. doi: 10.1007/s41114-018-0016-5.

Goran B. Scharmer, Klas Bjelksjo, Tapio K. Korhonen, Bo Lindberg, and Bertil Petterson. The 1-meter Swedish solar telescope. In Stephen L. Keil and Sergey V. Avakyan, editors, *Innovative Telescopes and Instrumentation for Solar Astrophysics*, volume 4853 of *Society of Photo-Optical Instrumentation Engineers (SPIE) Conference Series*, pages 341–350, February 2003. doi: 10.1117/12.460377.

WOLFGANG KH Schmidt. Distance limit for a class of model γ-ray burst sources. *Nature*, 271(5645):525–527, 1978.

Jeremy D. Schnittman and Julian H. Krolik. A Monte Carlo Code for Relativistic Radiation Transport Around Kerr Black Holes. *Astrophys. J.*, 777:11, 2013. doi: 10.1088/0004-637X/777/1/11.

Jeremy D. Schnittman, Tito Dal Canton, Jordan Camp, David Tsang, and Bernard J. Kelly. Electromagnetic Chirps from Neutron Star–Black Hole Mergers. *Astrophys. J.*, 853(2):123, 2018. doi: 10.3847/1538-4357/aaa08b.

Sophie Lund Schrøder, Morgan MacLeod, Abraham Loeb, Alejandro Vigna-Gómez, and Ilya Mandel. Explosions Driven by the Coalescence of a Compact Object with the Core of a Massive-Star Companion Inside a Common Envelope: Circumstellar Properties, Light Curves, and Population Statistics. 6 2019. doi: 10.3847/1538-4357/ab7014.

Yuichiro Sekiguchi, Kenta Kiuchi, Koutarou Kyutoku, Masaru Shibata, and Keisuke Taniguchi. Dynamical mass ejection from the merger of asymmetric binary neutron stars: Radiation-hydrodynamics study in general relativity. *Phys. Rev. D*, 93:124046, Jun 2016. doi: 10.1103/PhysRevD.93.124046. URL `https://link.aps.org/doi/10.1103/PhysRevD.93.124046`.

T. Shahbaz, M. Livio, K. A. Southwell, and P. A. Charles. T pyxidis: the first cataclysmic variable with a collimated jet. *Astrophys. J. Lett.*, 484:L59, 1997. doi: 10.1086/310765.

Yong Shao and Xiang-Dong Li. On the role of supernova kicks in the formation of Galactic double neutron star systems. *Astrophys. J.*, 867(2):124, 2018. doi: 10.3847/1538-4357/aae648.

Stuart L. Shapiro and Saul A. Teukolsky. *Black holes, white dwarfs, and neutron stars : the physics of compact objects*. 1983.

Stuart L Shapiro and Saul A Teukolsky. *Black holes, white dwarfs, and neutron stars: The physics of compact objects*. John Wiley and Sons, 2008.

Amotz Shemi and Tsvi Piran. The Appearance of Cosmic Fireballs. *The Astrophysical Journal, Letters*, 365:L55, December 1990. doi: 10.1086/185887.

Ken J Shen, Dan Kasen, Nevin N Weinberg, Lars Bildsten, and Evan Scannapieco. Thermonuclear. ia supernovae from helium shell detonations: explosion models and observables. *The Astrophysical Journal*, 715(2):767, 2010.

Zhaoyi Shen, Yi Ming, and Isaac M. Held. Using the fast impact of anthropogenic aerosols on regional land temperature to constrain aerosol forcing. *Science Advances*, 6(32), 2020. doi: 10.1126/sciadv.abb5297. URL `https://advances.sciencemag.org/content/6/32/eabb5297`.

Lijuan Shi, Yubao Qiu, Jiancheng Shi, Juha Lemmetyinen, and Shaojie Zhao. Estimation of microwave atmospheric transmittance over china. *IEEE Geoscience and Remote Sensing Letters*, 14(12):2210–2214, 2017. doi: 10.1109/LGRS.2017.2756111.

Gregory A. Shields. A brief history of agn. *Publ. Astron. Soc. Pac.*, 111:661, 1999. doi: 10.1086/316378.

Sakae Shimizu. Gamma-ray spectrum of the radiaoctive dust produced by the super-hydrogen bomb test explosion on march 1, 1954. *Nuclear Instruments and Methods in Physics Research Section A, Accelerators, Spectrometers, Detectors and Associated Equipment*, 255(1/2):177–182, Mar 1987. ISSN 0168-9002.

S. Shirouzu, T. Tsuji, N. Harada, T. Sado, S. Aihara, R. Tsunoda, and T. Kanno. 64 x 64 InSb Focal Plane Array With Improved Two Layer Structure. In C. P. Grover, editor, *Optical testing and metrology*, volume 661 of *Society of Photo-Optical Instrumentation Engineers (SPIE) Conference Series*, pages 419–425, November 1986. doi: 10.1117/12.938647.

Trevor Sidery, Ben Aylott, Nelson Christensen, Ben Farr, Will Farr, Farhan Feroz, Jonathan Gair, Katherine Grover, Philip Graff, Chad Hanna, et al. Reconstructing the sky location of gravitational-wave detected compact binary systems: methodology for testing and comparison. *Physical Review D*, 89(8):084060, 2014.

Thomas Siegert. Gamma-ray line diagnostics of supernova explosions - SN2014j and cas a. *Journal of Physics: Conference Series*, 940:012008, jan 2018. doi: 10.1088/

1742-6596/940/1/012008. URL https://doi.org/10.1088/1742-6596/940/1/012008.

Leo P. Singer and Larry R. Price. Rapid bayesian position reconstruction for gravitational-wave transients. *Phys. Rev. D*, 93:024013, Jan 2016. doi: 10.1103/PhysRevD.93.024013. URL https://link.aps.org/doi/10.1103/PhysRevD.93.024013.

Leo P. Singer et al. The First Two Years of Electromagnetic Follow-Up with Advanced LIGO and Virgo. *Astrophys. J.*, 795(2):105, 2014. doi: 10.1088/0004-637X/795/2/105.

Ashok Sinha and John E. Harries. Water vapour and greenhouse trapping: The role of far infrared absorption. *Geophysical Research Letters*, 22(16):2147–2150, 1995. doi: https://doi.org/10.1029/95GL01891. URL https://agupubs.onlinelibrary.wiley.com/doi/abs/10.1029/95GL01891.

A. Skumanich. Time scales for ca ii emission decay, rotational braking, and lithium depletion. *The Astrophysical Journal*, 171:565, 1971.

S. J. Smartt et al. A kilonova as the electromagnetic counterpart to a gravitational-wave source. *Nature*, 551(7678):75–79, 2017. doi: 10.1038/nature24303.

Michael D. Smith. *The Origin of Stars*. 2004. doi: 10.1142/p353.

Rory J. E. Smith, Gregory Ashton, Avi Vajpeyi, and Colm Talbot. Massively parallel Bayesian inference for transient gravitational-wave astronomy. *Mon. Not. Roy. Astron. Soc.*, 498(3):4492–4502, 2020. doi: 10.1093/mnras/staa2483.

M. V. Smolsky and V. V. Usov. Relativistic Beam–Magnetic Barrier Collision and Nonthermal Radiation of Cosmological γ-Ray Bursters. *The Astrophysical Journal, Letters*, 461:858, April 1996. doi: 10.1086/177107.

Noam Soker. Wind accretion by a binary stellar system and disk formation. *Mon. Not. Roy. Astron. Soc.*, 350:1366, 2004. doi: 10.1111/j.1365-2966.2004.07731.x.

Noam Soker. Merger by migration at the final phase of common envelope evolution. *New Astronomy*, 18:18–22, 2013. ISSN 1384-1076. doi: https://doi.org/10.1016/j.newast.2012.05.001. URL https://www.sciencedirect.com/science/article/pii/S1384107612000383.

HF Song, G Meynet, A Maeder, S Ekström, and P Eggenberger. Massive star evolution in close binaries-conditions for homogeneous chemical evolution. *Astronomy and Astrophysics*, 585:A120, 2016.

Joshua S Speagle. dynesty: a dynamic nested sampling package for estimating bayesian posteriors and evidences. *Monthly Notices of the Royal Astronomical Society*, 493(3): 3132–3158, 2020.

C. Stachie et al. Search for advanced LIGO single interferometer compact binary coalescence signals in coincidence with Gamma-ray events in Fermi-GBM. *Class. Quant. Grav.*, 37(17):175001, 2020a. doi: 10.1088/1361-6382/aba28a.

Cosmin Stachie, Michael W. Coughlin, Nelson Christensen, and Daniel Muthukrishna. Using machine learning for transient classification in searches for gravitational-wave counterparts. *Mon. Not. Roy. Astron. Soc.*, 497(2):1320–1331, 2020b. doi: 10.1093/mnras/staa1776.

Cosmin Stachie, Michael W Coughlin, Tim Dietrich, Sarah Antier, Mattia Bulla, Nelson Christensen, Reed Essick, Philippe Landry, Benoit Mours, Federico Schianchi, and Andrew Toivonen. Predicting electromagnetic counterparts using low-latency gravitational-wave data products. *Monthly Notices of the Royal Astronomical Society*, 505(3):4235–4248, 06 2021. ISSN 0035-8711. doi: 10.1093/mnras/stab1492. URL https://doi.org/10.1093/mnras/stab1492.

Steven W. Stahler and Francesco Palla. *The Formation of Stars*. 2004.

Nicholas C. Stone, Brian D. Metzger, and Zoltán Haiman. Assisted inspirals of stellar mass black holes embedded in AGN discs: solving the 'final au problem'. *Mon. Not. Roy. Astron. Soc.*, 464(1):946–954, 2017. doi: 10.1093/mnras/stw2260.

G Stratta, WH Baumgartner, N Gehrels, EA Hoversten, CB Markwardt, M Perri, and L Vetere. Grb 081024: Swift detection of a burst. *GRB Coordinates Network*, 8398:1, 2008.

T Straume. High-energy gamma rays in hiroshima and nagasaki: implications for risk and wr. *Health physics*, 69(6):954—956, December 1995. ISSN 0017-9078. doi: 10.1097/00004032-199512000-00010. URL https://doi.org/10.1097/00004032-199512000-00010.

R Sturani, S Fischetti, L Cadonati, G M Guidi, J Healy, D Shoemaker, and A Viceré. Complete phenomenological gravitational waveforms from spinning coalescing binaries. *Journal of Physics: Conference Series*, 243:012007, aug 2010. doi: 10.1088/1742-6596/243/1/012007. URL https://doi.org/10.1088/1742-6596/243/1/012007.

Mutsumi Sugizaki, Motoki Oeda, Nobuyuki Kawai, Tatehiro Mihara, Kazuo Makishima, and Motoki Nakajima. X-Ray Emission Evolution of the Galactic Ultralumi-

nous X-Ray Pulsar Swift J0243.6+6124 during the 2017–2018 Outburst Observed by the MAXI GSC. *Astrophys. J.*, 896(2):124, 2020. doi: 10.3847/1538-4357/ab93c7.

Lunan Sun, Milton Ruiz, and Stuart L. Shapiro. Magnetic braking and damping of differential rotation in massive stars. *Phys. Rev. D*, 99:064057, Mar 2019. doi: 10.1103/PhysRevD.99.064057. URL https://link.aps.org/doi/10.1103/PhysRevD.99.064057.

R. Surman, G. C. McLaughlin, M. Ruffert, H.-Th. Janka, and W. R. Hix. r -process nucleosynthesis in hot accretion disk flows from black hole-neutron star mergers. *The Astrophysical Journal*, 679(2):L117–L120, may 2008. doi: 10.1086/589507. URL https://doi.org/10.1086/589507.

Rebecca Surman, G. C. McLaughlin, and W. R. Hix. Nucleosynthesis in the outflow from gamma-ray burst accretion disks. *Astrophys. J.*, 643:1057–1064, 2006. doi: 10.1086/501116.

E. Symbalisty and D. N. Schramm. Neutron Star Collisions and the r-Process. *Astrophysics Letters*, 22:143, January 1982.

Ronald E. Taam and Eric L. Sandquist. Common envelope evolution of massive binary stars. *Annual Review of Astronomy and Astrophysics*, 38(1):113–141, 2000. doi: 10.1146/annurev.astro.38.1.113. URL https://doi.org/10.1146/annurev.astro.38.1.113.

Hiromichi Tagawa, Zoltan Haiman, Imre Bartos, and Bence Kocsis. Spin Evolution of Stellar-mass Black Hole Binaries in Active Galactic Nuclei. *Astrophys. J.*, 899(1):26, 2020a. doi: 10.3847/1538-4357/aba2cc.

Hiromichi Tagawa, Zoltan Haiman, and Bence Kocsis. Formation and Evolution of Compact Object Binaries in AGN Disks. *Astrophys. J.*, 898(1):25, 2020b. doi: 10.3847/1538-4357/ab9b8c.

Hiromichi Tagawa, Bence Kocsis, Zoltan Haiman, Imre Bartos, Kazuyuki Omukai, and Johan Samsing. Eccentric Black Hole Mergers in Active Galactic Nuclei. *Astrophys. J. Lett.*, 907(1):L20, 2021. doi: 10.3847/2041-8213/abd4d3.

Hung Tan, Jacquelyn Noronha-Hostler, and Nico Yunes. Neutron Star Equation of State in light of GW190814. *Phys. Rev. Lett.*, 125(26):261104, 2020. doi: 10.1103/PhysRevLett.125.261104.

Masaomi Tanaka and Kenta Hotokezaka. RADIATIVE TRANSFER SIMULATIONS OF NEUTRON STAR MERGER EJECTA. *The Astrophysical Journal*, 775(2):113, sep

2013. doi: 10.1088/0004-637x/775/2/113. URL https://doi.org/10.1088/0004-637x/775/2/113.

N. R. Tanvir, A. J. Levan, A. S. Fruchter, J. Hjorth, R. A. Hounsell, K. Wiersema, and R. L. Tunnicliffe. A 'kilonova' associated with the short-duration γ-ray burst GRB 130603B. *Nature*, 500(7464):547–549, August 2013. doi: 10.1038/nature12505.

V. Tatischeff et al. The e-ASTROGAM gamma-ray space mission. *Proc. SPIE Int. Soc. Opt. Eng.*, 9905:99052N, 2016. doi: 10.1117/12.2231601.

G Taylor, C Lidman, B E Tucker, D Brout, S R Hinton, and R Kessler. A revised SALT2 surface for fitting Type Ia supernova light curves. *Monthly Notices of the Royal Astronomical Society*, 504(3):4111–4122, 04 2021. ISSN 0035-8711. doi: 10.1093/mnras/stab962. URL https://doi.org/10.1093/mnras/stab962.

GB Taylor, P Charlot, RC Vermeulen, and N Pradel. Monitoring the bidirectional relativistic jets of the radio galaxy 1946+ 708. *The Astrophysical Journal*, 698(2):1282, 2009.

Ingo Tews, Peter T. H. Pang, Tim Dietrich, Michael W. Coughlin, Sarah Antier, Mattia Bulla, Jack Heinzel, and Lina Issa. On the Nature of GW190814 and Its Impact on the Understanding of Supranuclear Matter. *Astrophys. J. Lett.*, 908(1):L1, 2021. doi: 10.3847/2041-8213/abdaae.

The PLAsTiCC team, Jr. Allam, Tarek, Anita Bahmanyar, Rahul Biswas, Mi Dai, Lluís Galbany, Renée Hložek, Emille E. O. Ishida, Saurabh W. Jha, David O. Jones, Richard Kessler, Michelle Lochner, Ashish A. Mahabal, Alex I. Malz, Kaisey S. Mandel, Juan Rafael Martínez-Galarza, Jason D. McEwen, Daniel Muthukrishna, Gautham Narayan, Hiranya Peiris, Christina M. Peters, Kara Ponder, Christian N. Setzer, The LSST Dark Energy Science Collaboration, The LSST Transients, and Variable Stars Science Collaboration. The Photometric LSST Astronomical Time-series Classification Challenge (PLAsTiCC): Data set. *arXiv e-prints*, art. arXiv:1810.00001, September 2018.

Christopher Thompson. A model of gamma-ray bursts. *Monthly Notices of the Royal Astronomical Society*, 270(3):480–498, 10 1994. ISSN 0035-8711. doi: 10.1093/mnras/270.3.480. URL https://doi.org/10.1093/mnras/270.3.480.

Jonathan E. Thompson, Edward Fauchon-Jones, Sebastian Khan, Elisa Nitoglia, Francesco Pannarale, Tim Dietrich, and Mark Hannam. Modeling the gravitational wave signature of neutron star black hole coalescences. *Phys. Rev. D*, 101(12):124059, 2020. doi: 10.1103/PhysRevD.101.124059.

Catherine Timmermans and Rainer von Sachs. A novel semi-distance for measuring dissimilarities of curves with sharp local patterns. *Journal of Statistical Planning and Inference*, 160:35–50, 2015.

Richard C. Tolman. Static solutions of einstein's field equations for spheres of fluid. *Phys. Rev.*, 55:364–373, Feb 1939. doi: 10.1103/PhysRev.55.364. URL https://link.aps.org/doi/10.1103/PhysRev.55.364.

M. F. Tompsett, G. F. Amelio, and G. E. Smith. Charge coupled 8-bit shift register. *Applied Physics Letters*, 17(3):111–115, 1970. doi: 10.1063/1.1653327. URL https://doi.org/10.1063/1.1653327.

J. L. Tonry, L. Denneau, A. N. Heinze, B. Stalder, K. W. Smith, S. J. Smartt, C. W. Stubbs, H. J. Weiland, and A. Rest. ATLAS: A high-cadence all-sky survey system. *Publications of the Astronomical Society of the Pacific*, 130(988):064505, may 2018. doi: 10.1088/1538-3873/aabadf. URL https://doi.org/10.1088/1538-3873/aabadf.

Christopher Torrence and Gilbert P Compo. A practical guide to wavelet analysis. *Bulletin of the American Meteorological society*, 79(1):61–78, 1998.

Alejandro Torres-Forné, Elena Cuoco, José A. Font, and Antonio Marquina. Application of dictionary learning to denoise LIGO's blip noise transients. *Phys. Rev. D*, 102 (2):023011, 2020. doi: 10.1103/PhysRevD.102.023011.

Christopher A. Tout, Sverre J. Aarseth, Onno R. Pols, and Peter P. Eggleton. Rapid binary star evolution for N-body simulations and population synthesis. *Monthly Notices of the Royal Astronomical Society*, 291(4):732–748, 11 1997. ISSN 0035-8711. doi: 10.1093/mnras/291.4.732. URL https://doi.org/10.1093/mnras/291.4.732.

Piotr Tracz. Eli-np gamma beam system — new facility for nuclear physics research. pages 1–4, 06 2017. doi: 10.1109/PPC.2017.8291290.

A. A. Trani, A. Tanikawa, M. S. Fujii, N. W. C. Leigh, and J. Kumamoto. Spin misalignment of black hole binaries from young star clusters: implications for the origin of gravitational waves events. 2 2021. doi: 10.1093/mnras/stab967.

E. Troja et al. A luminous blue kilonova and an off-axis jet from a compact binary merger at z=0.1341. *Nature Commun.*, 9:4089, 2018. doi: 10.1038/s41467-018-06558-7.

Eleonora Troja, Stephan Rosswog, and Neil Gehrels. Precursors of short gamma-ray bursts. *The Astrophysical Journal*, 723(2):1711, 2010.

David Tsang, Jocelyn S Read, Tanja Hinderer, Anthony L Piro, and Ruxandra Bondarescu. Resonant shattering of neutron star crusts. *Physical Review Letters*, 108(1): 011102, 2012.

A. Tsvetkova, D. Frederiks, D. Svinkin, R. Aptekar, T. L. Cline, S. Golenetskii, K. Hurley, A. Lysenko, A. Ridnaia, and M. Ulanov. The Konus–Wind Catalog of Gamma-Ray Bursts with Known Redshifts. II. Waiting-Mode Bursts Simultaneously Detected by Swift/BAT. *Astrophys. J.*, 908(1):83, 2021. doi: 10.3847/1538-4357/abd569.

Miroslav Tugolukov, Yuri Levin, and Sergey Vyatchanin. Thermal noise computation in gravitational wave interferometers from first principles. *Physics Letters A*, 382(33): 2181–2185, 2018. ISSN 0375-9601. doi: https://doi.org/10.1016/j.physleta.2017.07.001. URL `https://www.sciencedirect.com/science/article/pii/S0375960117304851`. Special Issue in memory of Professor V.B. Braginsky.

Samantha A. Usman et al. The PyCBC search for gravitational waves from compact binary coalescence. *Class. Quant. Grav.*, 33(21):215004, 2016. doi: 10.1088/0264-9381/33/21/215004.

Vladimir V Usov. On the nature of non-thermal radiation from cosmological γ-ray bursters. *Monthly Notices of the Royal Astronomical Society*, 267(4):1035–1038, 1994.

P. Vallely. LIGO/Virgo S191213g: LBT spectrum of AT2019wxt (PS19hgw) reveals a type IIb supernova. *GRB Coordinates Network*, 26508:1, December 2019.

G. T. van Belle, M. J. Creech-Eakman, and A. Hart. Supergiant Temperatures and Linear Radii from Near-Infrared Interferometry. *Mon. Not. Roy. Astron. Soc.*, 394: 1925–1935, 2009. doi: 10.1111/j.1365-2966.2008.14146.x.

J. Th. van Loon. On the metallicity dependence of the winds from red supergiants and Asymptotic Giant Branch stars. In Henny J. G. L. M. Lamers, Norbert Langer, Tiit Nugis, and Kalju Annuk, editors, *Stellar Evolution at Low Metallicity: Mass Loss, Explosions, Cosmology*, volume 353 of *Astronomical Society of the Pacific Conference Series*, page 211, December 2006.

J. van Paradijs, P. J. Groot, T. Galama, C. Kouveliotou, R. G. Strom, J. Telting, R. G. M. Rutten, G. J. Fishman, C. A. Meegan, M. Pettini, N. Tanvir, J. Bloom, H. Pedersen, H. U. Nørdgaard-Nielsen, M. Linden-Vørnle, J. Melnick, G. Van der Steene, M. Bremer, R. Naber, J. Heise, J. in't Zand, E. Costa, M. Feroci, L. Piro, F. Frontera, G. Zavattini, L. Nicastro, E. Palazzi, K. Bennett, L. Hanlon, and A. Parmar. Transient optical emission from the error box of the γ-ray burst of 28 February 1997. *Nature*, 386(6626): 686–689, April 1997. doi: 10.1038/386686a0.

R. Vanderspek et al. Hete observations of the gamma-ray burst grb030329: evidence for an underlying soft x-ray component. *Astrophys. J.*, 617:1251–1257, 2004. doi: 10.1086/423923.

Melvin M Varughese, Rainer von Sachs, Michael Stephanou, and Bruce A Bassett. Non-parametric transient classification using adaptive wavelets. *Monthly Notices of the Royal Astronomical Society*, 453(3):2848–2861, 2015.

J. Veitch, V. Raymond, B. Farr, W. Farr, P. Graff, S. Vitale, B. Aylott, K. Blackburn, N. Christensen, M. Coughlin, W. Del Pozzo, F. Feroz, J. Gair, C.-J. Haster, V. Kalogera, T. Littenberg, I. Mandel, R. O'Shaughnessy, M. Pitkin, C. Rodriguez, C. Röver, T. Sidery, R. Smith, M. Van Der Sluys, A. Vecchio, W. Vousden, and L. Wade. Parameter estimation for compact binaries with ground-based gravitational-wave observations using the lalinference software library. *Phys. Rev. D*, 91:042003, Feb 2015. doi: 10.1103/PhysRevD.91.042003. URL `https://link.aps.org/doi/10.1103/PhysRevD.91.042003`.

M. Viana, J. Pey, X. Querol, A. Alastuey, F. de Leeuw, and Anke Lükewille. Natural sources of atmospheric aerosols influencing air quality across europe. *Science of The Total Environment*, 472:825–833, 2014. ISSN 0048-9697. doi: https://doi.org/10.1016/j.scitotenv.2013.11.140. URL `https://www.sciencedirect.com/science/article/pii/S0048969713014447`.

V. Ashley Villar, Edo Berger, Brian D. Metzger, and James Guillochon. Theoretical Models of Optical Transients. I. A Broad Exploration of the Duration-Luminosity Phase Space. *Astrophys. J.*, 849:70, 2017. doi: 10.3847/1538-4357/aa8fcb.

Jorick S. Vink. Very Massive Stars: a metallicity-dependent upper-mass limit, slow winds, and the self-enrichment of Globular Clusters. *Astron. Astrophys.*, 615:A119, 2018. doi: 10.1051/0004-6361/201832773.

C. V. Vishveshwara. Scattering of Gravitational Radiation by a Schwarzschild Blackhole. *Nature*, 227(5261):936–938, August 1970. doi: 10.1038/227936a0.

Andreas von Kienlin, Charles A. Meegan, William S. Paciesas, P. N. Bhat, Elisabetta Bissaldi, Michael S. Briggs, J. Michael Burgess, David Byrne, Vandiver Chaplin, William Cleveland, Valerie Connaughton, Andrew C. Collazzi, Gerard Fitzpatrick, Suzanne Foley, Melissa Gibby, Misty Giles, Adam Goldstein, Jochen Greiner, David Gruber, Sylvain Guiriec, Alexander J. van der Horst, Chryssa Kouveliotou, Emily Layden, Sheila McBreen, Sinéad McGlynn, Veronique Pelassa, Robert D. Preece, Arne Rau, Dave Tierney, Colleen A. Wilson-Hodge, Shaolin Xiong, George Younes, and Hoi-Fung Yu. THE SECOND FERMI GBM GAMMA-RAY BURST CATALOG: THE

FIRST FOUR YEARS. *The Astrophysical Journal Supplement Series*, 211(1):13, feb 2014. doi: 10.1088/0067-0049/211/1/13. URL https://doi.org/10.1088/0067-0049/211/1/13.

Leslie Wade, Jolien D. E. Creighton, Evan Ochsner, Benjamin D. Lackey, Benjamin F. Farr, Tyson B. Littenberg, and Vivien Raymond. Systematic and statistical errors in a bayesian approach to the estimation of the neutron-star equation of state using advanced gravitational wave detectors. *Phys. Rev. D*, 89:103012, May 2014. doi: 10.1103/PhysRevD.89.103012. URL https://link.aps.org/doi/10.1103/PhysRevD.89.103012.

NiR Walborn. The obn and obc stars. *The Astrophysical Journal*, 205:419–425, 1976.

Shinya Wanajo and Hans-Thomas Janka. Ther-PROCESS IN THE NEUTRINO-DRIVEN WIND FROM a BLACK-HOLE TORUS. *The Astrophysical Journal*, 746 (2):180, feb 2012. doi: 10.1088/0004-637x/746/2/180. URL https://doi.org/10.1088/0004-637x/746/2/180.

Jie-Shuang Wang, Zong-Kai Peng, Jin-Hang Zou, Bin-Bin Zhang, and Bing Zhang. Stringent Search for Precursor Emission in Short GRBs from Fermi/GBM data and Physical Implications. *Astrophys. J. Lett.*, 902(2):L42, 2020. doi: 10.3847/2041-8213/abbfb8.

Xiang-Yu Wang and Peter Meszaros. GRB Precursors in the Fallback Collapsar Scenario. *Astrophys. J.*, 670:1247–1253, 2007. doi: 10.1086/522820.

Xiaofeng Wang et al. Optical and Near-Infrared Observations of the Highly Reddened, Rapidly Expanding Type Ia Supernova 2006X in M100. *Astrophys. J.*, 675:626–643, 2008. doi: 10.1086/526413.

Darach Watson et al. Identification of strontium in the merger of two neutron stars. *Nature*, 574(7779):497–500, 2019. doi: 10.1038/s41586-019-1676-3.

E. Waxman, S. R. Kulkarni, and D. A. Frail. Implications of the radio afterglow from the gamma-ray burst of 1997 may 8. *The Astrophysical Journal*, 497(1):288–293, apr 1998. doi: 10.1086/305467. URL https://doi.org/10.1086/305467.

Eli Waxman. Gamma-ray burst afterglow: Confirming the cosmological fireball model. *Astrophys. J. Lett.*, 489:L33–L36, 1997a. doi: 10.1086/310960.

Eli Waxman. GRB afterglow: Supporting the cosmological fireball model, constraining parameters, and making predictions. *Astrophys. J. Lett.*, 485:L5, 1997b. doi: 10.1086/310809.

R. F. Webbink. The formation and evolution of symbiotic stars. In Joanna Mikolajewska, Michael Friedjung, Scott J. Kenyon, and Roberto Viotti, editors, *The Symbiotic Phenomenon*, pages 311–321, Dordrecht, 1988. Springer Netherlands. ISBN 978-94-009-2969-2.

J. Weber. Detection and generation of gravitational waves. *Phys. Rev.*, 117:306–313, Jan 1960. doi: 10.1103/PhysRev.117.306. URL https://link.aps.org/doi/10.1103/PhysRev.117.306.

J. Weber. Gravitational-wave-detector events. *Phys. Rev. Lett.*, 20:1307–1308, Jun 1968. doi: 10.1103/PhysRevLett.20.1307. URL https://link.aps.org/doi/10.1103/PhysRevLett.20.1307.

B Louise Webster and Paul Murdin. Cygnus x-1—a spectroscopic binary with a heavy companion? *Nature*, 235(5332):37–38, 1972.

J. M. Weisberg, D. J. Nice, and J. H. Taylor. Timing Measurements of the Relativistic Binary Pulsar PSR B1913+16. *Astrophys. J.*, 722:1030–1034, 2010. doi: 10.1088/0004-637X/722/2/1030.

M. C. Weisskopf, H. D. Tananbaum, L. P. van Speybroeck, and S. L. O'Dell. Chandra x-ray observatory (cxo):overview. *Proc. SPIE Int. Soc. Opt. Eng.*, 4012:2, 2000. doi: 10.1117/12.391545.

Linqing Wen and Yanbei Chen. Geometrical Expression for the Angular Resolution of a Network of Gravitational-Wave Detectors. *Phys. Rev. D*, 81:082001, 2010. doi: 10.1103/PhysRevD.81.082001.

M. W. Werner et al. The Spitzer Space Telescope mission. *Astrophys. J. Suppl.*, 154:1–9, 2004. doi: 10.1086/422992.

T. Wevers et al. Spectroscopic classification of X-ray sources in the Galactic Bulge Survey. *Mon. Not. Roy. Astron. Soc.*, 470(4):4512–4529, 2017. doi: 10.1093/mnras/stx1303.

Ralph A. M. J. Wijers, Martin J. Rees, and Peter Mészáros. Shocked by GRB 970228: the afterglow of a cosmological fireball. *Monthly Notices of the Royal Astronomical Society*, 288(4):L51–L56, 07 1997. ISSN 0035-8711. doi: 10.1093/mnras/288.4.L51. URL https://doi.org/10.1093/mnras/288.4.L51.

James R. Wilson. A Numerical Study of Gravitational Stellar Collapse. *The Astrophysical Journal*, 163:209, January 1971. doi: 10.1086/150759.

Ryan T Wollaeger and Daniel R Van Rossum. Radiation transport for explosive outflows: Opacity regrouping. *The Astrophysical Journal Supplement Series*, 214(2):28, 2014.

Edward L Wright, Peter RM Eisenhardt, Amy K Mainzer, Michael E Ressler, Roc M Cutri, Thomas Jarrett, J Davy Kirkpatrick, Deborah Padgett, Robert S McMillan, Michael Skrutskie, et al. The wide-field infrared survey explorer (wise): mission description and initial on-orbit performance. *The Astronomical Journal*, 140(6):1868, 2010.

Wyrzykowski, Lukasz and Mandel, Ilya. Constraining the masses of microlensing black holes and the mass gap with gaia dr2. *AandA*, 636:A20, 2020. doi: 10.1051/0004-6361/201935842. URL https://doi.org/10.1051/0004-6361/201935842.

Henrique S. Xavier, L. Raul Abramo, Masao Sako, Narciso Benítez, Maurício O. Calvão, Alessandro Ederoclite, Antonio Marín-Franch, Alberto Molino, Ribamar R. R. Reis, Beatriz B. Siffert, and Laerte. Sodré. Photometric Type Ia supernova surveys in narrow-band filters. *Monthly Notices of the Royal Astronomical Society*, 444 (3):2313–2332, 09 2014. ISSN 0035-8711. doi: 10.1093/mnras/stu1611. URL https://doi.org/10.1093/mnras/stu1611.

Sheng Yang, Stefano Valenti, David Sand, Leonardo Tartaglia, Enrico Cappellaro, Dan Reichart, Josh Haislip, and Kouprianov Vladimir. LIGO/Virgo G298048: DLT40 optical candidate. *GRB Coordinates Network*, 21531:1, August 2017.

Min Jet Yap et al. Broadband reduction of quantum radiation pressure noise via squeezed light injection. *Nature Photon.*, 14(1):19–23, 2020. doi: 10.1038/s41566-019-0527-y.

Jean-Paul Zahn. Tidal dissipation in binary systems. *EAS Publ. Ser.*, 29:67, 2008. doi: 10.1051/eas:0829002.

B. B. Zhang et al. Transition from fireball to Poynting-flux-dominated outflow in the three-episode GRB 160625B. *Nature Astron.*, 2(1):69–75, 2018. doi: 10.1038/s41550-017-0309-8.

Bing Zhang. Gamma-Ray Burst Prompt Emission. *Int. J. Mod. Phys. D*, 23:1430002, 2014. doi: 10.1142/S021827181430002X.

Bing Zhang and Peter Meszaros. Gamma-ray bursts: Progress, problems \and prospects. *Int. J. Mod. Phys. A*, 19:2385–2472, 2004. doi: 10.1142/S0217751X0401746X.

Harry Zhang. The optimality of naive bayes. volume 2, 01 2004.